Design and synthesis of Ni-rich and low/no-Co layered oxide cathodes for Li-ion batteries

Zhijie Yang

Dissertation submitted to the faculty of the Virginia Polytechnic Institute and State University in partial fulfillment of the requirements for the degree of

Doctor of Philosophy
In
Chemistry

Feng Lin (Chair)
Amanda Morris
John Morris
Rui Qiao

December 12, 2022
Blacksburg, VA

Keywords: Li-ion batteries, Ni-rich cathode, Co-free cathode, layered oxide, synchrotron characterizations, single crystal

Design and synthesis of Ni-rich and low/no-Co layered oxide cathodes for Li-ion batteries

Zhijie Yang

Abstract

Li-ion batteries (LIBs) have achieved remarkable success in electric vehicles (EVs), consumer electronics, grid energy storage, and other applications thanks to a wide range of electrode materials that meet the performance requirements of different application scenarios. Cathodes are an essential component of LIBs, which governs the performance of commercial LIBs. Layered transition metal oxide, i.e., $LiNi_xCo_yMn_{1-x-y}O_2$ (NMC), is one family of cathodes that are widely applied in the prevailing commercial LIBs. With increasing demand for high energy density, the development of layered oxide cathodes is towards high Ni content because Ni redox couples majorly contribute to the battery capacity. Meanwhile, the battery community has been making tremendous efforts to eliminate Co in layered cathodes due to its high cost, high toxicity, and child labor issues during Co mining. However, these Ni-rich Co-free cathodes usually suffer from low electrochemical and structural stability. Several strategies are adopted to enhance the stability of Ni-rich Co-free cathodes, such as doping, coating, and synthesizing single crystal particles. However, the design principles and synthesis mechanisms of these approaches have not been fully understood. Herein, we design and synthesize stable Ni-rich and low/no-Co layered oxide cathodes by manipulating the chemical and structural properties of cathode particles. Our studies reveal the cathode formation mechanisms and shed light on the cathode design through complementary synchrotron microscopic and spectroscopic characterization methods.

In **Chapter 1**, the motivation for LIB research is introduced from the perspective of its indispensable role in achieving carbon neutrality. We then comprehensively introduce the status of LIBs at present, including assessing their sustainability, worldwide supply chain and manufacturing, and cathode materials. Subsequently, we focus on the Co-free layered oxide cathodes and discuss their structure, limitations, and strategies to address the challenges. Finally, we discuss single crystal Ni-rich layered oxide cathodes and the challenges and strategies associated with their synthesis.

In **Chapter 2**, we investigate the dopant redistribution, phase propagation, and local chemical changes of layered oxides at multiple length scales using a multielement-doped $LiNi_{0.96}Mg_{0.02}Ti_{0.02}O_2$ (Mg/Ti-LNO) as a model platform. We observed that dopants Mg and Ti diffuse from the surface to the bulk of cathode particles below 300 °C long before the formation of any layered phase, using a range of synchrotron spectroscopic and imaging diagnostic tools. After calcination, Ti is still enriched at the cathode particle surface, while Mg has a relatively uniform distribution throughout cathode particles. Our findings provide experimental guidance for manipulating the dopant distribution upon cathode synthesis.

In **Chapter 3**, we synthesized $Mn(OH)_2$-coated single crystal $LiNiO_2$ (LNO) and used it as the platform to monitor the Mn redistribution and the structural and chemical evolution of the LNO cathode. We use *in situ* transmission X-ray microscopy (TXM) to track the Mn tomography inside the LNO particle and Ni oxidation state evolution at various temperatures below 700 °C. We further reveal chemical and structural changes induced by different extents of Mn diffusion at ensemble-averaged scale, which validates the results at the single particle scale. The ion diffusion behavior in the cathode is highly

temperature dependent. Our study provides guidance for ion distribution manipulation during cathode modification.

In **Chapter 4**, we successfully fabricated a surface passivation layer for NMC particles via a feasible quenching approach. A combination of bulk and surface structural characterization methods show the correlation of surface layer with bulk chemistry including valence state and charge distribution. Our design enables high interfacial stability and homogeneous charge distribution, impelling superior electrochemical performance of NMC cathode materials. This study provides insights into the cathode surface layer design for modifying other high-capacity cathodes in LIBs.

In **Chapter 5**, we use statistical tools to identify the significance of multiple synthetic parameters in the molten salt synthesis of single crystal Ni-rich NMC cathodes. We also create a prediction model to forecast the performance of synthesized single crystal Ni-rich NMC cathodes from the input of synthetic parameters with relatively high prediction accuracy. Guided by the models, we synthesize single crystal $LiNi_{0.9}Co_{0.05}Mn_{0.05}O_2$ (SC-N90) with different particle sizes. We find large single crystals show worse capacity and cycle life than small single crystals especially at high current rates due to slower Li kinetics. However, large single crystal has higher thermal stability potentially because of smaller specific surface area. The findings of particle size effect on the performance provide insights into size engineering while developing next-generation single crystal Ni-rich NMC cathodes. The statistical and prediction models developed in this study can guide the molten salt synthesis of Ni rich cathodes and simplify the optimization process of synthetic parameters.

Chapter 6 summarizes our efforts on the novel design and fundamental understanding of the state-of-the-art cathodes. We also provide our future perspectives for the development of LIBs.

Design and synthesis of Ni-rich and low/no-Co layered oxide cathodes for Li-ion batteries

Zhijie Yang

General audience abstract

Lithium-ion batteries (LIBs) have been studied for decades and are widely applied in electronics and vehicles because of their high energy density and long lifetime. With the increasing demand for higher energy density, particularly in electric vehicles, the development of Ni-based layered oxide cathode materials has been focused on increasing the Ni content. Meanwhile, decreasing or eliminating Co has become a consensus due to its high cost, toxicity, and human rights issues during mining. Enhancing the stability of these Ni-rich and low/no-Co layered oxide cathodes is challenging yet crucial to their practical applications. Herein, we design and synthesize multiple Ni-rich and low/no-Co layered cathodes through ion distribution engineering and structure modification at various length scales. We also investigate the dopant redistribution, phase propagation, and local chemical changes during layered oxides cathode formation through a combination of complementary characterization methods at different length scales. In addition, we provide guidance for synthesis optimization by statistical correlations and performance prediction models with the input of synthetic conditions. Overall, this dissertation provides insights into the design and synthesis principles of Ni-rich low/no-Co layered oxide cathode, which can facilitate the transition to a sustainable future with next-generation LIBs.

Acknowledgements

First, I want to thank my advisor Dr. Feng Lin sincerely. I started from knowing little about research four years ago to independently conducting research projects thanks to his professional education and guidance. More importantly for my Ph.D. journey, I learned how to learn and think critically from him. These give me the confidence to start any work in a new field and will benefit my whole life. I am also grateful for his valuable advice during my life milestones. He is not only a scientific advisor but also a lifetime mentor and friend to me. Dr. Lin sets a role model for the whole group with his enthusiasm and integrity in research. I feel grateful for joining the Lin lab and wish all the best for the future of the lab and his future career.

I also want to thank my committee members, Dr. Amanda Morris, Dr. John Morris, and Dr. Rui Qiao for their extensive support and guidance throughout my doctoral program. The constructive feedback and comments that I received from each of my committee meetings guided me to think more deeply about fundamental science and more comprehensively from different perspectives. Their high standards motivate me to be more professional in my research.

I would like to express my deep gratitude to my grandmother Tianqiao Feng, my late grandfather Ximing Yang, my mother Jinhua Jia, and my late father Weimin Yang for bringing me up to be a better individual and for their unconditional love. I also want to thank my uncle Weichun Yang for being extremely supportive to my decision of pursuing my dream and being responsible to our family. You insisted that I should go for my Ph.D. abroad and told me not to worry about the family when I hesitated at my father's funeral.

None of my achievements so far can be accomplished without you taking the responsibilities of the whole family on your shoulder.

I would like to extend my gratitude to my wife-to-be Dajun Yu for her love and accompany. Your encouragement keeps me moving forward every time I feel frustrated. We have been through tough times together during the COVID-19 pandemic. We share precious memories, which are contributed a lot by our cats, Curry and Rice. I feel fortunate to have you in the most memorable four years of my life, and it is my great pleasure to be part of your Ph.D. journey as well.

I want to thank my undergraduate research mentor Dr. Cailong Zhou for his guidance. I also want to thank all my lab mates for their tremendous support. I value our friendship and all the academic and personal activities we have experienced over the years at Virginia Tech. I am deeply grateful to our first postdoc Dr. Linqin Mu. She is my first research mentor during my Ph.D. who passed me the knowledge and skills that benefit my entire Ph.D. I want to thank Dr. Dong Hou, Dr. Lei Tao, Dr. Zhengrui Xu, Dr. Huabin Sun, Yuxin Zhang, Anyang Hu, Zhao Li, Yumeng Zhu for their great support of my research and personal life. I also want to thank Dr. Chunguang Kuai, Dr. Xuerong Zheng, Dr. Xiaona Pan, Dr. Muhammad Mominur Rahman, Dr. David J. Kautz, Dr. Crystal K. Waters, Stephanie Spence, Mingyu Yuan, Dawei Xia, Jungki Min, and Anika Promi.

I appreciate the support from my collaborators Dr. Xianghui Xiao at Brookhaven National Laboratory, Dr. Cheng-Jun Sun at Argonne National Laboratory, Dr. Yijin Liu at SLAC national accelerator laboratory, and Dr. Jue Liu at Oak Ridge National Laboratory. Lastly, I want to thank Virginia Tech Chemistry department faculty and staff, especially

our Graduate Program Coordinator Joli Huynh, for their tremendous help throughout my doctoral program.

Table of Contents

Abstract .....

General audience abstract .....

Acknowledgements vii

Table of Contents x

Attribution xiii

1. Introduction 1

1.1. Motivation for Li-ion battery research 1

1.2. Status of Li-ion battery 4

1.2.1. Sustainability assessment 4

1.2.2. Supply chain and manufacturing 8

1.2.3. Cathode materials 13

1.3. $LiNiO_2$ and $LiNiO_2$-derived Ni-rich low/no-Co layered oxide cathodes 15

1.3.1. Hierarchical and heterogeneous layered cathode architecture 15

1.3.2. Crystal structure and thermodynamics of $LiNiO_2$ 20

1.3.3. Instability issues of $LiNiO_2$ 22

1.3.4. Strategies to design stable Ni-rich Co-free layered oxide cathodes 25

1.4. References 31

2. Probing Dopant Redistribution, Phase Propagation, and Local Chemical Changes in the Synthesis of Layered Oxide Battery Cathodes 46

2.1. Abstract 47

2.2. Introduction 48

2.3. Materials and methods 51

2.4. Results 54

2.5. Discussion 73

2.6. Acknowledgements 74

2.7. References 76

2.8. Supplementary information 85

3. Revealing and manipulating particle level Mn distribution upon thermal treatment in Ni-rich Co-free layered cathodes 103

3.1. Abstract 104

3.2. Introduction 105

3.3. Materials and methods 108

3.4. Results 110

3.5. Discussion 121
3.6. Acknowledgements 123
3.7. References 124
3.8. Supplementary information 129
4. Surface layer formation enabling high interfacial stability and homogeneous charge distribution in Ni-rich layered oxides 141
4.1. Abstract 142
4.2. Introduction 142
4.3. Materials and methods 144
4.4. Results 147
4.4.1. Surface layer formation on NMC particles 147
4.4.2. Similarity of bulk properties on NMC and NMC-L materials. 151
4.4.3. Enhanced cycling stability by a passivation layer on NMC surface 153
4.4.4. Better interfacial stability NMC-L upon cycling. 155
4.4.5. Homogeneous charge distribution in NMC-L particles after long-term cycling. 157
4.5. Discussion 159
4.6. Acknowledgements 159
4.7. References 160
4.8. Supplementary information 164
5. Synthesis and Size Control of Single Crystal Ni-Rich Layered Oxide Cathodes Using Statistical Analysis-Guided Molten Salt Method 171
5.1. Abstract 172
5.2. Introduction 173
5.3. Materials and methods 176
5.4. Results 179
5.4.1. Statistical analyses and model for performance prediction 179
5.4.2. Morphology and performance 185
5.4.3. Origin of size effect on the performance difference 188
5.5. Discussion 192
5.6. Acknowledgements 194
5.7. References 194
6. Conclusions and future perspective 200
6.1. Conclusions 200
6.2. Perspective of future work 202

6.3. Perspective of future battery and electrical vehicle evolution 205
6.4. References 209

Attribution

Chapter 1 combined a reprint manuscript published in *Advanced Energy Materials*, a reprint manuscript published in *the Journal of Physical Chemistry C*, and a reprint manuscript published in *Encyclopedia of Energy Storage*. Dr. Feng Lin conceived and led the projects for all manuscripts. Zhijie Yang and Dr. Feng Lin reviewed all the papers. Zhijie Yang and Dr. Feng Lin wrote the manuscripts with assistance from Dr. Haibo Huang.

Chapter 2 is a reprint of a manuscript published in *Advanced Energy Materials*. Dr. Feng Lin conceived and led the project. Zhijie Yang performed synthesis, synchrotron measurements, TGA, SEM-EDS. Dr. Linqin Mu performed the electrochemical measurements. Zhijie Yang and Dr. Xianghui Xiao performed the TXM measurement. Zhijie Yang analyzed the data with the assistance of Dr. Xianghui Xiao and Dr. Dong Hou. Zhijie Yang, Dr. Zhengrui Xu, and Dr. Chengjun Sun performed the hard XAS measurement. Dr. Muhammad Mominur Rahman performed the synchrotron XRD measurement. Dr. Dennis Nordlund performed the soft XAS measurements. Zhijie Yang collected and analyzed the XPS data. Dr. Jue Liu performed the ND. Zhijie Yang analyzed the ND data with assistance from Dr. Dong Hou. Zhijie Yang and Dr. Feng Lin analyzed the data and wrote the manuscript with the help of all coauthors.

Chapter 3 is a manuscript prepared for submission for peer review in a scientific journal. Dr. Feng Lin conceived and led the project. Zhijie Yang performed the synthesis and characterization. Zhijie Yang, Jungki Min, and Dr. Xianghui Xiao performed TXM experiments. Zhijie Yang performed synchrotron data analyses with the assistance of Dr. Dong Hou, Dr. Xianghui Xiao, and Dr. Zhengrui Xu. Dr. Dennis Nordlund performed the

soft XAS measurements. Dr. Dong Hou performed the synchrotron XRD measurement. Dr. Chengjun Sun performed the hard XAS measurement. Zhijie Yang and Dr. Feng Lin analyzed the data and wrote the manuscript with assistance from all coauthors.

Chapter 4 is a manuscript prepared for submission for peer review in a scientific journal. Dr. Feng Lin conceived and led the project. Dr. Huabin Sun performed the synthesis, characterization, and electrochemical measurements. Zhijie Yang assisted in the synthesis. Zhijie Yang performed TXM experiments with the assistance of Dr. Xianghui Xiao. Zhijie Yang performed TXM data analyses. Anyang Hu performed SEM. Yuxin Zhang assisted in the TXM analyses. Dr. Jue Liu performed neutron diffraction measurements. Dr. Dennis Nordlund and Dr. Sami Sainio performed the soft XAS measurements. Dr. Chengjun Sun performed the hard XAS measurement. Dr. Yijin Liu, Dr. Wei Luo, and Dr. Yunhui Huang participated in scientific discussions. Dr. Huabin Sun, Zhijie Yang and Dr. Feng Lin analyzed the data and wrote the manuscript with the assistance of all coauthors.

Chapter 5 is a manuscript prepared for submission for peer review in a scientific journal. Dr. Feng Lin conceived and led the project. Dr. Feng Lin and Zhijie Yang designed the experiments. Zhijie Yang performed the synthesis, characterization, and electrochemical measurements. Dajun Yu performed the statistical analyses. Ryan Ragasa and Paul Roark assisted in the synthesis. Dr. Jue Liu performed neutron diffraction measurements. Zhijie Yang and Dr. Feng Lin analyzed the data and wrote the manuscript with assistance from all coauthors.

1. Introduction

1.1. Motivation for Li-ion battery research

Recently, Li-ion batteries (LIBs) have received extensive attention with the skyrocketing growth of the electric vehicle (EV) market. Multiple countries have announced that they will progressively replace internal combustion engine vehicles (ICEVs) with EVs over the next few decades to satisfy the net-zero carbon emission criteria.[1,2] Examining the lifetime carbon emissions of EVs and ICEVs is imperative to demonstrate the validity of switching from ICEVs to EVs. Vehicle lifetime emissions include emissions during battery raw materials processing and battery manufacturing for EVs, vehicle manufacturing, and the well-to-wheel (WtW) process. For ICEVs, the WtW process relates to fuel production and vehicle use, whereas for EVs, it refers to electricity generation and distribution. The International Energy Agency (IEA) established the Stated Policies Scenario (STEPS) and the Sustainable Development Scenario (SDS) to evaluate the emissions under different circumstances.[3] The STEPS reflects the legislated or announced policies and targets for emissions by governments around the world.[3] It performs evaluations based on accomplished emission reduction goals. The STEPS is relatively conservative and does not presume all announced goals to be reached. In contrast, the SDS has set stricter emission standards and assumes all net-zero emission pledges are achieved. We chose the STEPS in the following comparison to avoid overstating the benefits of EVs.

Based on the STEPS, the global WtW greenhouse gas (GHG) emissions for EVs are all lower than their replaced ICEV counterparts for light-duty vehicles (LDVs), buses, trucks, and two/three wheelers (Figure 1a). By replacing ICEVs with EVs, the global net

GHG emissions avoided during the WtW process are predicted to be 51.9 million tonnes of carbon dioxide equivalent (Mt CO_2-eq), 55.1 Mt CO_2-eq, 58.5 Mt CO_2-eq, 69.3 Mt CO_2-eq, 91.5 Mt CO_2-eq, and 120.9 Mt CO_2-eq, respectively, at every two-year interval from 2020 to 2030 (Figure 1a).[4] The benefits of emission reduction offered by EVs will be more prominent in the SDS.[4] Taking into account vehicle manufacturing, mineral processing, and battery production, mid-size EVs still have lower GHG emissions than ICEVs throughout the life cycle (Figure 1b).[5] However, electricity generation leads to large variations of the total lifetime emissions (Figure 1b).[5] Specifically, the electricity generation source can greatly affect total emissions (Figure 1c).[5] As of 2019, renewable energy sources account for 65% of power generation in Canada, and nuclear energy accounts for 17%, resulting in comparatively low CO_2 emissions of 132 gCO_2/kWh (Figure 1c). In Indonesia, however, fossil fuels account for 83% of electrical generation. The emission during electricity generation in Indonesia was 761 gCO_2/kWh, which was nearly six times higher than that of Canada (Figure 1c).[5] The total emissions during electricity generation increase as the countries or regions rely more on fossil fuels (Figure 1c). To summarize, EVs generate lower lifetime emissions than their ICEV counterparts do. This is in good agreement with the literature.[6] In addition, increasing the share of renewable energy sources in the electricity generation mix can further enhance the environmental benefits of vehicle electrification. LIBs, being one of the most critical components of EVs, play a significant role in determining the long-term sustainability of the EV industry. The development of LIBs needs to be driven in a more sustainable direction to satisfy the rising energy demand and simultaneously meet the criteria for net-zero carbon emissions.

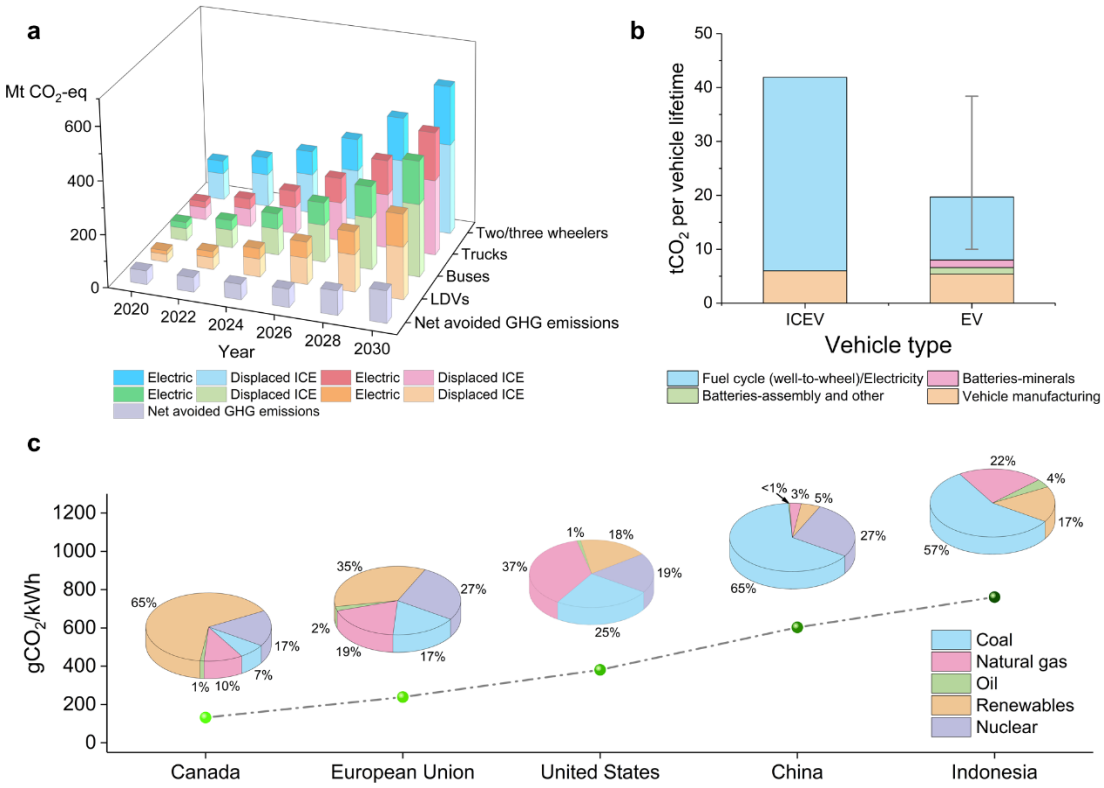

Figure 1. Environmental impact of EVs and ICEVs. (a) GHG emissions of EVs and displaced ICEVs and net avoided GHG emissions from 2020-2030 in the Stated Policies Scenario.[4] (b) Comparison of life-cycle GHG emissions of a mid-size EV and ICEV.[5] (c) Electricity generation mix and emissions from electricity generation in selected regions in 2019.[5] Overall, EVs have less GHG emissions than displaced ICEVs, after considering the processes of mineral mining, battery assembling, vehicle manufacturing, and vehicle operation. However, the emissions of EVs largely depend on the source of electricity generation. The countries that heavily rely on fossil fuels have more emissions. To reduce the emissions of EVs, optimizing the electricity generation mix and developing renewable energy are of crucial importance. The figure is made based on the data from references 4 and 5.

1.2. Status of Li-ion battery

1.2.1. Sustainability assessment

The capability of LIBs to power EVs and store electricity generated from renewable energy sources have led to the erroneous public perception that LIBs are 'zero-emission' technologies. In reality, LIBs, just like other batteries, are essentially tools to store and release electrical energy. The fact that LIB production is energy- and resource-intensive, and that current electricity generation still heavily relies on fossil fuels, can potentially cause environmental concerns. Moreover, disposal of spent LIBs without recycling could be detrimental to the environment. Life cycle assessment (LCA) is a systematic analysis of the potential environmental impacts of products, processes, or services throughout their entire life cycle.[7] It is generally accepted as a standard methodology to quantify the environmental influences of the production, usage, and recycling of LIBs.

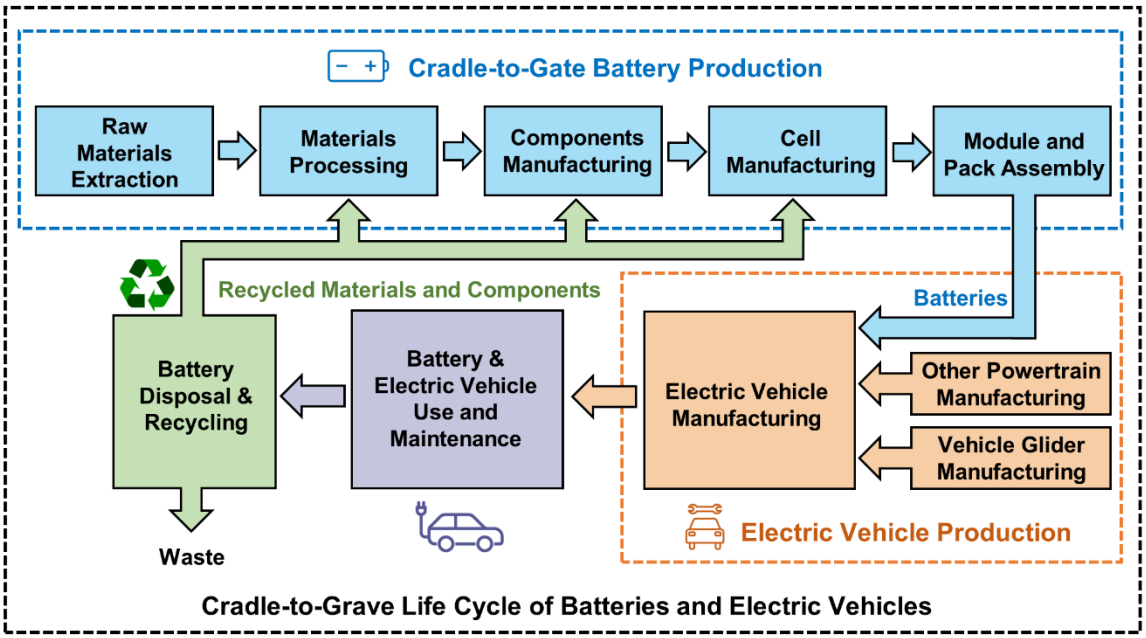

Figure 2. Major cradle-to-grave life cycle stages for batteries and EVs, including cradle-to-gate battery production, EV production, the use and maintenance of batteries and EVs,

and battery disposal and recycling. The color-coded dashed rectangles show different system boundaries.

Many LCA studies have been conducted to assess the environmental impacts of the production of different LIB chemistries including $LiFePO_4$ (LFP), $LiNi_xMn_yCo_{1-x-y}O_2$ (NMC), $LiMn_2O_4$ (LMO), and $LiNi_xCo_yAl_{1-x-y}O_2$ (NCA), but their results are far from agreement.[8–18] The reported cradle-to-gate GHG emissions for battery production (including raw materials extraction, materials production, cell and component manufacturing, and battery assembling as shown in Figure 2) range from 39 to 196 kg CO_2-eq per kWh of battery capacity with an average value of 110 kg CO_2-eq per kWh of battery capacity.[9,11–18] The discrepancies in GHG emissions in prior studies can be attributed to a variety of reasons such as different battery chemistries, regions of manufacturers, assumptions in LCA models, and modeling approaches to estimating energy demand in battery manufacturing.[15,17] LFP, NMC, and LMO are the most studied battery chemistries in LCA mainly due to their popularity in the current EV market and availability of the manufacturing data from the battery industry. Peters *et al.* critically analyzed a wide array of LCA studies of battery production and found that LMO has the lowest GHG emissions among the three battery chemistries, followed by NMC and LFP based on the averages of results from published studies.[15] Hao *et al.* examined GHG emissions from LIB production in China and reported a similar conclusion that the production of LMO automotive LIBs leads to the lowest GHG emissions and the production of LFP leads to the highest GHG emissions.[14] GHG emissions of LIB production could also vary with the locations of manufacturers due to different quality of electricity used and electricity generation source.[14] For example, the production of LFP, NMC, and LMO batteries in China has

nearly three times higher emissions than that in the US because electricity generation in China relies more on coal (Figure 1c).[14] Besides battery chemistries and regions of manufacturers, the approach for modeling the battery manufacturing process to estimate energy demand also contributes to the wide discrepancies of the LCA results.[19] Prior studies used two modeling approaches to estimate the total energy demand in battery manufacturing: (1) the bottom-up approach which uses data from theoretical simulations or lab-scale experiments of the critical processes in the manufacturing line, and (2) the top-down approach which uses data from a real manufacturing plant. It was found that the latter approach usually results in a much higher estimated energy demand in battery manufacturing compared to the bottom-up approach. For example, using the top-down approach, Kim *et al.* assessed the cradle-to-gate GHG emissions from mass-produced LIB used in the Ford Focus EVs based on the primary energy data from the battery cell and pack industries.[11] In Kim *et al.*'s study, the estimated GHG emission from the cell and pack manufacturing process is 65 kg CO_2-eq per kWh of battery capacity, which is over one order of magnitude higher than the range of 1.5-1.9 kg CO_2-eq estimated by other studies using the bottom-up approach.[11] Furthermore, the real industrial manufacturing data is critical in LCA to obtain legitimate and practically informative results.

Prior LCA studies agreed that battery electric vehicle (BEV) production generates more GHG emissions than ICEV production does. Hawkins *et al.* found that the cradle-to-gate GHG emissions associated with EV production are almost twice that associated with ICEV production, and battery production contributes 35% to 41% of the GHG emissions from EV production.[9] This finding is supported by Kim *et al.*, who reported a 39% increase in GHG emissions switching from ICEV to EV in vehicle production.[11] Hao *et al.* also

indicated that there is around 30% increase in GHG emissions for EV production compared to that of traditional vehicles.[14] The higher GHG emissions associated with EV production in comparison to ICEV production is mainly because of the high GHG emissions from the production of battery, generator, and motor, i.e., the electric powertrain system. Although EV production has higher environmental impacts, extending the system boundary to include the use phase of EV (as shown in Figure 2) leads to a clear advantage of EV compared to ICEV because EVs offer higher powertrain efficiency and zero tailpipe emissions. Hawkins *et al.* found that light-duty EVs powered by the present European electricity mix offer a 10% to 24% decrease in GHG emissions relative to ICEVs assuming 150,000 km lifetime of EVs, and extending the lifetime of EVs to 200,000 km boosts the environmental benefits of 27% to 29% decrease in GHG emissions.[9] In another study of the comparison between EVs and ICEVs, it was found that transport services with an EV result in a 35.6% (in percentage of the EV, 37,700 kg CO_2-eq) decrease in GHG emissions compared to an ICEV,[8] which is in general agreement with Hawkins *et al.*'s study. In addition, electricity generation source plays a vital role in GHG emissions. EVs powered by coal electricity can lead to an increase in GHG emissions compared to ICEVs.[16] Therefore, it is vital to promote clean electricity sources to power EVs to maximize their environmental benefits. Although global warming potential (GWP), as expressed in GHG emissions, is the most frequently assessed environmental impact category (EIC) in the majority of LCA studies, other critical EIC, such as abiotic depletion (ADP), acidification (AP), eutrophication (EP), human toxicity (HTP) and ozone depletion (ODP), are equally, sometimes even more, important to assess the environmental impacts of EV technology.

Studies have raised concerns that production and use of EVs could potentially lead to increases in HTP, EP, and ADP categories, mainly emanating from the EV supply chain.[20]

1.2.2. Supply chain and manufacturing

The LIB supply chain can be tracked back to the extraction and processing of raw minerals. A volatile supply chain or inefficient manufacturing may offset the performance benefit promoted by electrode materials. The mining and processing of LIB raw materials are more scattered across the world, compared with the procedures of fossil fuels (Figure 3). The uneven distribution of essential raw minerals may potentially give rise to geopolitical challenges and impact the global LIB industry. For example, Ni is a predominant metal in commercial cathodes for LIBs. Russia is one of the major countries that extract and refine Ni mines (Figure 3a,b). Due to the Russia-Ukraine war, the price of Ni almost doubled within one week from late February to early March in 2022.[21] The IEA reported that the total battery cost could increase by 6% if the prices of Ni or Li were doubled.[5] Contemporary Amperex Technology Co. Ltd (CATL), the largest LIB manufacturer in the world, has announced to raise prices for some battery products due to raw materials cost increase.[22] Accordingly, some EV companies, such as Tesla, Rivian, and BYD, have raised the prices of their EVs due to the increasing supply chain cost.[23] Therefore, evaluating the global supply chain and manufacturing capability is vital to gaining a comprehensive understanding and reasonable forecast of LIB development.

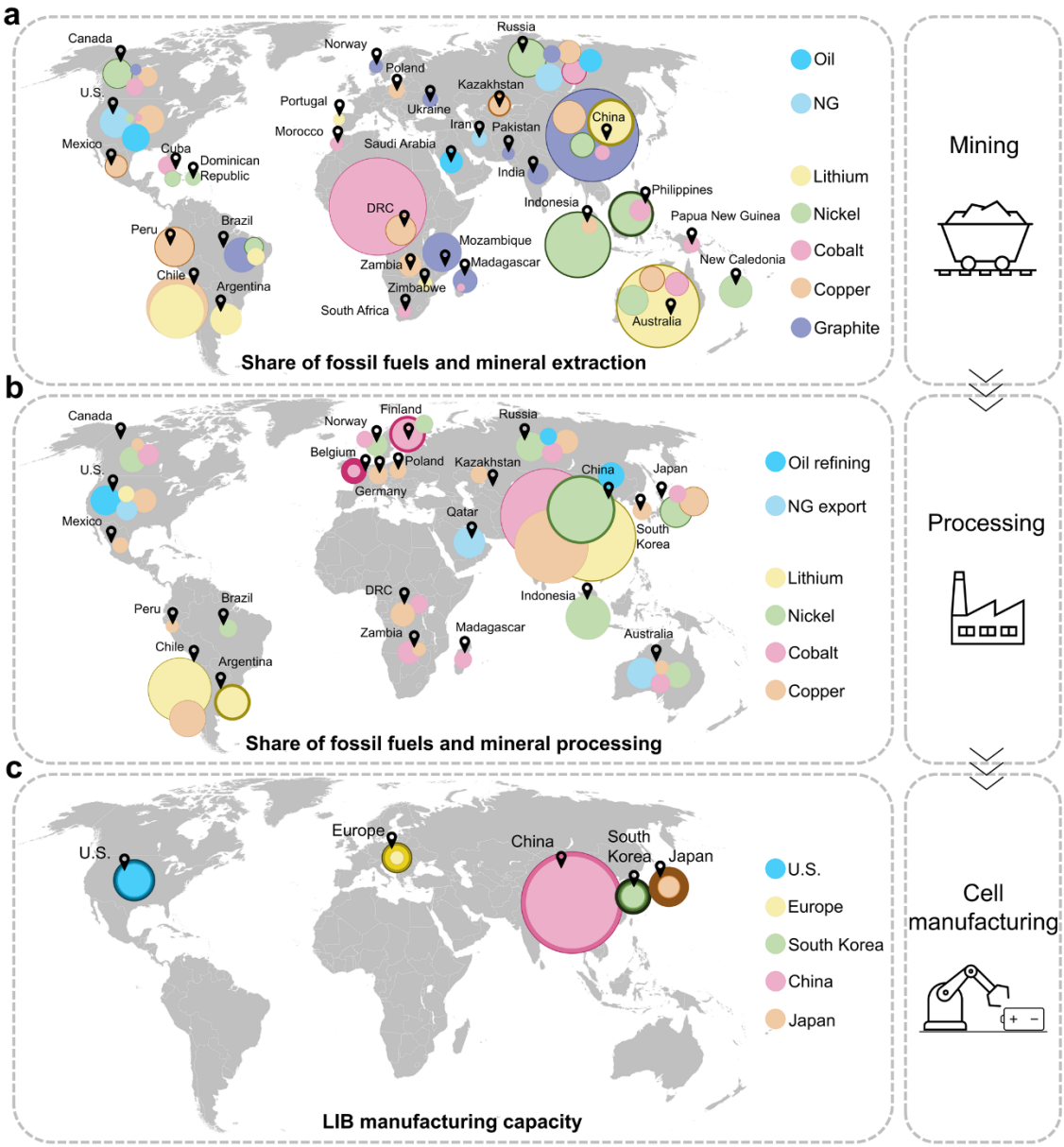

Figure 3. The worldwide distribution of LIB cradle-to-gate processes. (a) Share of fossil fuels and mineral extraction in 2019 and 2020.[5,24–26] (b) Share of fossil fuels and mineral processing in 2018, 2019, and 2020.[5,24,25,27–29] (c) LIB manufacturing capacity by country in 2016, 2019, and 2020.[30–33] The area of the color-coded circles is proportional to the share (percentage) or capacity (GWh). NG: Natural gas. DRC: The Democratic Republic of the Congo. The shaded rings around specific circles are "error rings" calculated based on

collecting data from different references. This figure only displays the top three countries for fossil fuel extraction and processing and the major contributing countries/regions in LIB cradle-to-gate processes for visualization. The distribution of LIB raw mineral materials is sporadic across the world, but raw material processing and LIB manufacturing are mainly in Asia.

The fossil fuel supply chain has been established and remained relatively stable, whereas the LIB supply chain is under development and evolving rapidly. The primary oil producers are the United States (US), Russia, and Saudi Arabia, and the top three oil refining countries are the US, China, and Russia (Figure 3a,b).[5] Regarding the natural gas production and distribution, the major producing countries are the US, Russia, and Iran, and the top three exporting countries are Qatar, Australia, and the US (Figure 3a,b).[5] In contrast, the global competition for the LIB supply chain has just begun. The distribution of the essential minerals for producing LIBs is scattered globally. In 2019 and 2020, three major Ni mine extraction countries are Indonesia, the Philippines, and Russia, which accounted for the global share of 29.8-33.0%, 12.0-15.7%, 10.1-11.3%, respectively (Figure 3a, Table S1).[5,24,25] For the global share of Co mine extraction, the Democratic Republic of the Congo (DRC) dominates with 69.0-70.4%, and Australia and Russia contribute 4.0-4.2%, 4.0-4.7%, respectively (Figure 3a, Table S1).[5,24] The top three contributing countries to the global share of Li mining are Australia (48.7-52.0%), Chile (21.9-22.0%), and China (13.0-17.0%).[5,24] Given the dispersed distribution of raw materials, the LIB supply chain requires worldwide collaborations. Moreover, the leading countries for the mining of certain materials may change as new minerals are discovered

and mining technology improves. For example, a recent assessment of worldwide metal reserves indicated that the top-reserve countries for Li_2CO_3, Ni, and Co mines are Chile, Indonesia, and DRC, which possess 52670 1000 metric tons, 28750 1000 metric tons, and 2970 1000 metric tons, respectively.[34] However, unexplored regions that have considerable potential for mineral resources can potentially be a game-changer.

Mineral processing capability also plays a crucial role in the LIB supply chain besides mineral reserves. The mineral reserves may not necessarily reflect the exact demand in the LIB industry. The reason is that LIB production normally needs high purity precursors, which require further processing after mining and specific mineral sources.[30] For example, Class 1 Ni sulfate (Ni impurity of 99.8% or greater) that is eligible for LIBs is mostly produced from Ni sulfide ores, which only accounts for around 40% of available Ni reserves.[30,35] Such strict requirements on raw materials also bring challenges to recycling. The fact that many essential metals for LIBs are mainly produced as byproducts of other metal mining further complicates the LIB supply chain.[30] For instance, over 80% of Co is produced as byproducts of Ni and Cu.[36] The worldwide distribution of mineral processing is relatively concentrated. China has the largest processing volumes for multiple essential metals. The global share of China for Li, Ni, Co, and Cu processing is 55.0-58.0%, 29.9-35.0%, 63.6-65.0%, and 39.8-40.0%, respectively (Figure 3b). Other major processing countries are distributed in the rest of Asia, Europe, and South America. Separators are another critical component of LIBs, which serve as a physical barrier to prevent cell short-circuiting and electrolyte reservoir for Li transport. The major LIB separator manufacturers are located in Asia. China, Korea, Japan, and the US accounted for 43%, 28%, 21%, and 6% of the global separator manufacturing, respectively.[31] The

separator market of Asia-pacific region is forecasted to undergo a rapid growth and will still be dominant in the next five years.[37]

LIB manufacturing is the next key step. Regarding the share of the global LIB production in the past few years, China, the US, Europe, South Korea, and Japan accounted for 62.3-76.9%, 7.9-13.1%, 1.4-7.0%, 4.0-9.8%, and 3.2-11.8%, respectively (Figure 3c). The statistics show that LIB manufacturing is dominated by Asia, especially China. More facilities will be established in Europe, North America, Australia, and Asia considering those under construction or planned.[38] China, Japan, and South Korea are rated first, second, and third in the 2020 LIB supply chain ranking, which is evaluated based on raw materials, manufacturing, battery demand, etc.[39] Europe and North America are progressing and their gap with Asia is narrowing. In 2021, the US and Germany moved up to second and third place, respectively, which is predicted to be maintained in 2026.[40] Additionally, Asian countries, including China, South Korea, and Japan, have vertically integrated the supply chain from raw materials processing to battery manufacturing.[40] In the 1990s, Japan determined to develop its LIB industry. The Japanese government supported the research and development (R&D) of private sectors and helped them establish low-cost manufacturing plants.[30] China and South Korea have copied the success of Japan through developing partnerships between the government and LIB industry and providing subsidies since the late 2000s.[30] The mature LIB supply chain and accumulated technology and production experience gave the Asian countries advantages in the EV era. The US and Europe did not focus on domestic LIB manufacturing until the late 2010s. Therefore, the supply chain is not as robust, and manufacturers are relatively inexperienced.[30] Overall,

Asia has the edge on raw materials processing and LIB manufacturing at present, but Europe and North America are accelerating the construction of their supply chains.

In all, the diversified mineral types and their concentrated geographical distributions bring more uncertainties to the supply chain. A stable supply chain is critical for the sustainable development of LIBs. Major LIB producing countries have been attempting to establish their domestic supply chains and gain an edge on the LIB manufacturing. A sustainable supply of raw materials is needed as a prerequisite. In this regard, developing local mining and processing abilities are essential for boosting domestic LIB manufacturing capacity. The competition between leading countries can accelerate the advancement of LIBs and the establishment of a global LIB industry ecosystem. On the other hand, a closer collaboration (e.g., multiyear agreement on supply) across the world and associated legislation are needed to achieve a sustainable supply chain.

1.2.3. Cathode materials

LIBs were first commercialized by Sony Corporation in 1991, adopting $LiCoO_2$ (LCO) as the cathode and graphite as the anode.[41] As graphite remains the primary anode in most commercial LIBs at present, the bottleneck regarding energy density is still cathodes. From 1991 to the 2010s, the price of LIBs has dropped by nearly 97%.[42] The cathode is the largest cost contributor among all battery components according to the cost model Ziegler *et al.* developed.[42] Efforts to boost cell charge density and lower cathode prices accounted for 38% and 14% of the LIB cost reduction, respectively.[42] Therefore, manipulating cathode design at the materials level is essential to the sustainability of the LIB industry. Several factors need to be considered when evaluating a cathode material, including but not limited to electrochemical performance (e.g., energy density, cycle life),

raw material abundance, cost, and carbon emissions during production. These factors are largely dependent on the transition metals in cathodes. Here, we categorize the state-of-the-art cathodes by their chemical compositions, especially their transition metals (Table 1). LCO is widely applied in consumer electronics due to its high energy density, good conductivity, and high discharge voltage. However, LCO is unsuitable for large-scale applications due to the toxicity, scarcity, and high cost of Co. Shortly after the successful commercialization of LCO in the 1990s, the Ni-based cathode $LiNiO_2$ (LNO) received much attention.[43,44] LNO is an isostructural compound to LCO and has a similar theoretical capacity (275 mAh g^{-1}) but avoids the problematic Co. However, severe Li/Ni cation mixing and phase transformation issues in LNO lead to its low stability.[45] The inherent low stability brings about durability and safety concerns, which hinder its commercialization even today. The battery community has made great efforts in enhancing the performance of LNO and other Ni-rich variants.

Introducing several other metal cations (e.g., Mn, Al, Co) to partially substitute Ni is one of the most successful practices to optimize LNO. This is how NMC and NCA came into play.[46–48] NMC and NCA are families of cathodes that have various ratios of Ni to other metal cations in the chemical formula. The cycling and thermal stability are enhanced, but the energy density is limited with lower Ni content. NMC and NCA have promoted the development of the automotive battery industry in the past decade. Moving towards higher Ni contents has become the trend of the Ni-based layered cathode development as the demand for high energy density increases. However, this is not simply traveling back to LNO. Various approaches have been applied to balance the energy density and stability, such as doping and coating.[49] In the meantime, decreasing or

eliminating Co in NMC and NCA has become more pressing. Co contributes a significant portion to the entire cost and carbon emissions of cathode production.[16] Besides, the child labor and human rights issues during the Co mining have drawn criticism widely. Therefore, Ni-rich Co-free cathodes have gained extensive attention recently. A variety of metal cations were selected to replace Co to improve the stability of Ni-rich cathodes.[50–53] Ni-based cathodes will persist due to the advantage of high energy density before more appealing cathodes appear.

Table 1. Selected LIB cathodes categorized by elements

Category		Advantages	Disadvantages	Status	References
Co dominating	$LiCoO_2$ (LCO)	High energy density; high conductivity; high discharge voltage	Expensive and toxic Co; low accessible capacity compared to the theoretical value	Consumer electronics	54
Ni and Co containing	$LiNi_xMn_yCo_{1-x-y}O_2$ (NMC)/ $LiNi_xCo_yAl_{1-x-y}O_2$ (NCA)	Increasing energy density with higher Ni content; lower cost and less toxicity than LCO	Low thermal and cycling stability and safety concern with higher Ni content	EVs, stationary energy storage	46–48
Ni-rich and Co-free	$LiNi_xM_{1-x}O_2$ (M=Mg, Al, Ti, etc.)	High energy density; low cost; environmentally friendly	Low thermal and cycling stability	Research	50–53

1.3. $LiNiO_2$ and $LiNiO_2$-derived Ni-rich low/no-Co layered oxide cathodes

1.3.1. Hierarchical and heterogeneous layered cathode architecture

1.3.1.1. Hierarchical structure

A well-functioning Li ion battery with superior electrochemical performance requires the coordination of each component at different length scales. The architecture of Li ion batteries is hierarchical, ranging from the battery-assembly scale in centimeters

down to atomic scale in nanometers (Figure 4). Taking a commercial cylindrical battery as an example, the main components include a cathode, separator, electrolyte, and an anode (Figure 4a). Generally, the cathode has more choices of materials and the structure is more complicated than other components. The cathode assembly consists of active materials, conductive additives, and binder (Figure 4b). The active materials are composed of numerous micron-sized particles, which can be either single crystal particles or polycrystalline secondary particles comprising nanosized single crystal primary particles oriented randomly or in a certain pattern (Figure 4c, d). Zooming into single crystal grains, Li ions and transition metal ions are arranged in an ordered and repeated manner in the lattice. For example, Figure 4e shows the lattice structure of a layered cathode with alternate layers of Li ions and transition metal ions. Throughout different length scales, many of the local chemical and structural heterogeneities may interfere with global electrode properties and electrochemical performance. Therefore, a comprehensive understanding of the heterogeneity at different length scales is crucial.

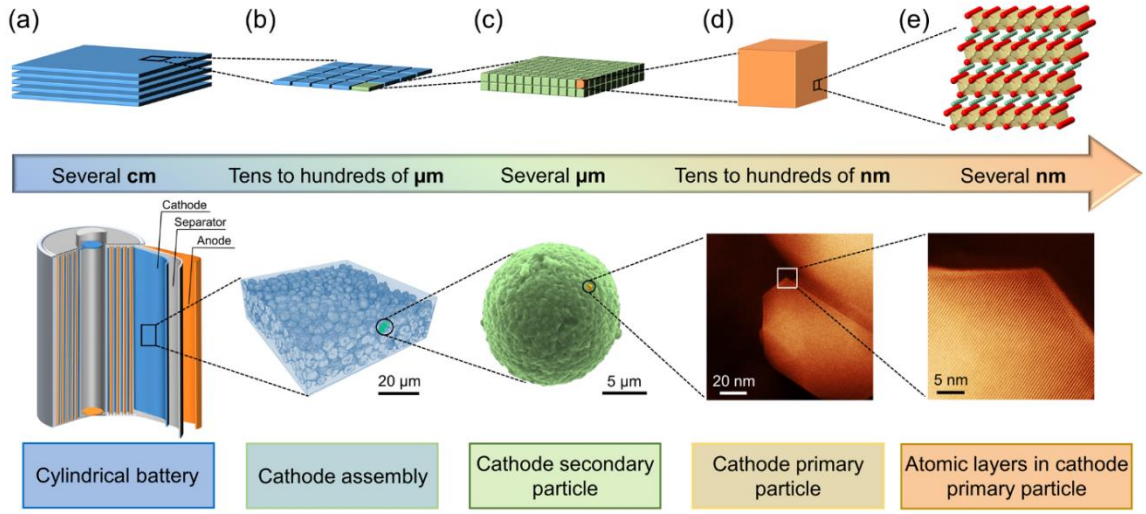

Figure 4. Schematic illustration of the length scales and corresponding battery components. (a) A cylindrical battery of several centimeters. (b) Cathode assembly from tens of to

hundreds of micrometers.[55] Copyright 2019. Elsevier. (c) Polycrystalline cathode secondary particle of several micrometers. (d) Cathode primary particle from tens to hundreds of nanometers. (e) Atomic layers in cathode primary particle within several nanometers.

1.3.1.2. Compositional heterogeneity

A homogeneous transition metal ion distribution in cathode particles has been considered as a critical criterion to achieve decent electrochemical performance of alkali ion batteries. However, our recent studies show that sodium layered cathode materials with highly 3D heterogeneous transition metal distributions exhibited good performance.[56,57] Three cathode materials with the same chemical formula of $Na_{0.9}Cu_{0.2}Fe_{0.28}Mn_{0.52}O_2$ but different transition metal distributions were synthesized (CFM-Cu, CFM-Mn, CFM-Fe, respectively). Among these cathodes, CFM-Cu showed the best performance in Na ion cells with an initial discharge capacity of 125 mAh g^{-1} at 0.1C between 2-4 V and no capacity fading after 100 cycles.[56] 3D full-field transmission X-ray microscopy (TXM) was used to quantify elemental distributions. TXM is powerful to probe elemental distribution and electronic state (e.g., oxidation state) distribution at a fast data acquisition speed with a resolution of tens of nanometers.[58] However, potential pitfalls in data analyses should be addressed to avoid data misinterpretation, which will be discussed in the next section. Herein, the elemental association maps of CFM-Cu based on TXM suggested the elemental distribution in a large number of nanodomains deviates from the global stoichiometry ($Na_{0.9}Cu_{0.2}Fe_{0.28}Mn_{0.52}O_2$). Specifically, the surface is dominated by single and binary metal associations (Figure 5a), while the bulk mostly comprises ternary metal associations (Figure 5b). This study really opens up a few questions. Are great performing

materials in the literature always homogeneous in elemental distributions? This question can essentially be applied to any multi-element oxide cathodes. Does the elemental heterogeneity create different charge distributions in battery particles? Can the elemental heterogeneity be designed to benefit battery performance?

We applied the elemental 3D distribution approach to Li ion batteries by introducing dopants as point defects to nanosized single crystal grains. The dopant distribution can be modulated during the cathode synthesis. We used a multielement-doped cathode material $LiNi_{0.96}Mg_{0.02}Ti_{0.02}O_2$ (Mg/Ti-LNO) as a platform to investigate the dopant redistribution during synthesis. A combination of X-ray photoelectron spectroscopy (XPS) and Ni K-edge extended X-ray absorption fine structure (EXAFS) wavelet transform analysis suggests that both Mg and Ti are enriched at the surface of the mixed metal hydroxide precursor (schematically represented in Figure 5c). Upon calcination, both Mg and Ti diffuse into the nickel hydroxide matrix.[59] After the calcination protocol completes, Mg distributes homogeneously throughout the cathode particle while Ti is enriched at the particle surface (Figure 5d). The resulting cathode material Mg/Ti-LNO with a 3D hierarchical dopant distribution showed smoother charge and discharge profiles (due to less phase transformation), and higher capacity retention than pure $LiNiO_2$ under the same operating conditions (Figure 5e).[52] The homogeneously distributed Mg may suppress phase transformations and thereby enhance the bulk structural stability. Meanwhile, the surface-enriched Ti may mitigate the surface oxygen loss by forming strong ionic bonds with O and reducing the hybridization between transition metal 3d and oxygen 2p orbitals.[52] By applying the 3D dopant distribution approach, we also observed stability enhancement in other cathode materials such as Ti doped $LiNi_{0.8}Mn_{0.1}Co_{0.1}O_2$ (NMC811-Ti).[60] The STEM-

energy dispersive X-ray spectroscopy (EDS) mapping of NMC811-Ti implied that Ti was enriched at the cathode particle surface (Figure 5f). The bulk of the particles had a layered structure while the surface had a deactivated reconstruction layer (Figure 5g). Similar to that observed in Mg/Ti-LNO, the surface-enriched Ti in NMC811-Ti particles also reduced the covalency between transition metals and oxygen.[60] The chemical environment of Ti is highly reversible upon charging and discharging, which contributes to excellent oxygen reversibility and electrochemical cycling stability (Figure 5h).[60] Overall, our results showed engineering the elemental distribution in individual cathode particles can modulate global electrochemical performance. However, the electrochemistry within individual particles, such as local charge distribution, was not fully understood. Therefore, we extended our work to further investigate the chemical-electrochemical correlation at the mesoscale.

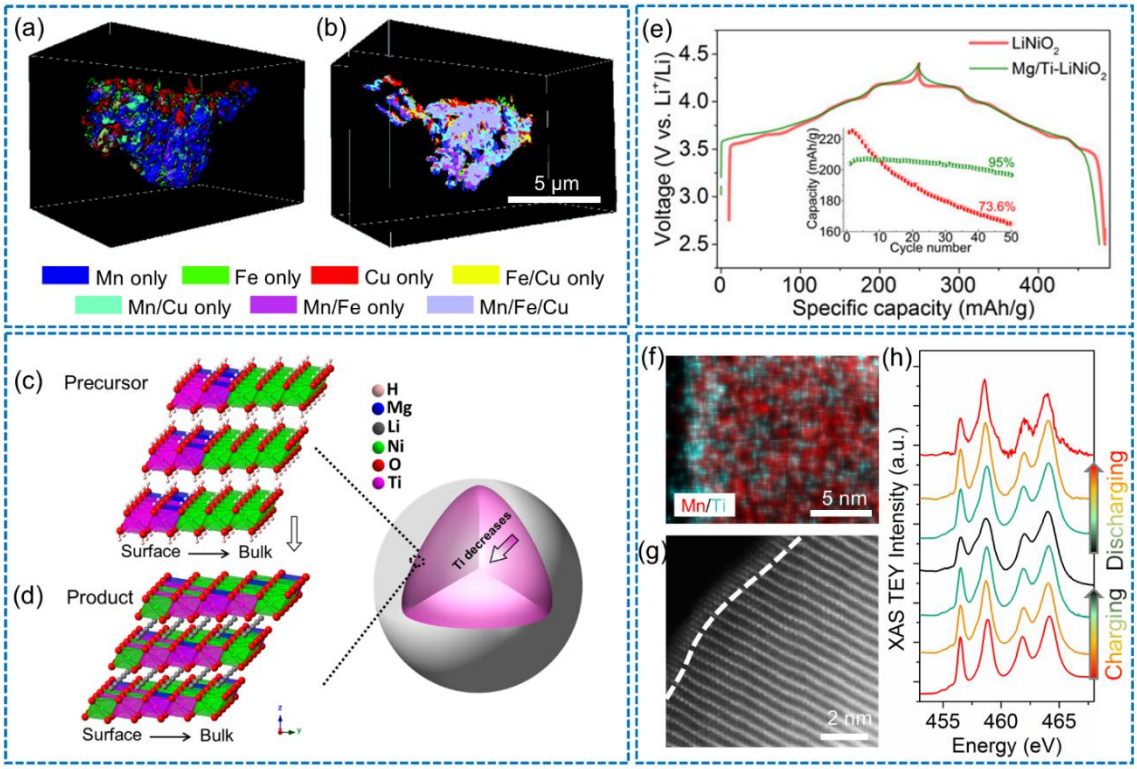

Figure 5. Elemental distribution heterogeneity in various cathode particles at different length scales. (a) 3D elemental association map of pristine $Na_{0.9}Cu_{0.2}Fe_{0.28}Mn_{0.52}O_2$ (CFM-Cu) at the particle surface. (b) a selected virtual slice cut through the bulk of the same CFM-Cu particle in (a), the bottom of (a) and (b) shows the color-coded elemental association.[56] Copyright 2018. Royal Society of Chemistry. Schematic illustration of elemental distribution in (c) precursor and (d) product of the Mg/Ti-LNO cathode material.[59] Copyright 2020. John Wiley and Sons. (e) Voltage profiles of Li cells containing $LiNiO_2$ and Mg/Ti-LNO at 0.1C (20 mA g^{-1}) and 22 °C within 2.5-4.4 V, where the inset shows the discharge capacity change as a function of cycle number.[52] Copyright 2019. American Chemical Society. (f) STEM-EDS mapping of NMC811-Ti after 300 cycles at 1C within 2.5-4.5 V. (g) STEM image of pristine NMC811-Ti. The dashed line indicates the distinction between the surface reconstruction layer and bulk layered structure. (h) Ti L-edge soft XAS spectra at different SOCs.[60] Copyright 2019. American Chemical Society.

1.3.2. Crystal structure and thermodynamics of $LiNiO_2$

Ni-rich and low/no-Co layered oxide cathodes are based on the structure of $LiNiO_2$, with low content of other metal cations occupying Ni site or Li site. $LiNiO_2$ has a hexagonal structure with trigonal symmetry ($R\bar{3}m$ space group), which is isostructural with α-$NaFeO_2$. For the ideal stoichiometric $LiNiO_2$, Ni and Li cations occupy the octahedral 3a (0 0 0) sites and 3b (0 0 1/2) sites, respectively. Oxygen anions reside in a cubic close-packed (ccp) 6c (0 0 z) sites (Figure 6). Transition metal planes and Li planes are alternately arranged along the [001] direction of a hexagonal structure (equivalent to the [111]

direction of the rock-salt cubic structure). Thus, the chemical formula can be denoted as $[Li]_{3b}[Ni]_{3a}[O_2]_{6c}$.

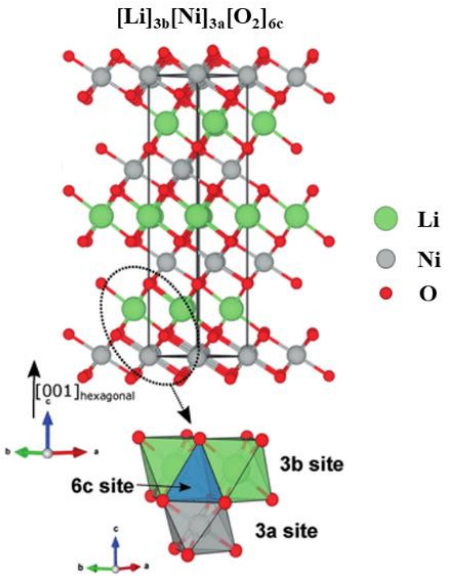

Figure 6. Schematic showing the crystal structure of $LiNiO_2$. The green, gray and red spheres indicate Li, Ni, and O atoms, respectively. (Figure reproduced from ref.49)

However, the $LiNiO_2$ is prone to be off-stoichiometric and more Ni ions are accommodated in the Li planes. The off-stoichiometry can be attributed to the low stability of the trivalent Ni ion, and the Li ion loss at high temperature during calcination.[43] Therefore, the chemical formula of $LiNiO_2$ in practice can be denoted as $[Li_{1-z}Ni_y]_{3b}[Li_zNi_{1-y}]_{3a}[O_2]_{6c}$ ($y \geq z$), where y represents the content of excess Ni^{2+} in the Li planes, and z denotes the amount of Li^+ in the Ni plane. Based on the Extended X-ray Absorption Fine Structure (EXAFS) technique, Rougier *et al.* observed the distortion of octahedral NiO_6 in the $LiNiO_2$ due to the Jahn-Teller distortion.[61] The distortion induces the formation of two Ni-O bonds with a bond length of 2.09 Å and four Ni-O bonds with a bond length of 1.91 Å.

In the off-stoichiometry $LiNiO_2$, the excess Ni^{2+} in the Li site can enlarge the distance between Ni and O, while shortening the distance between Li and O. It can be attributed to the increasing ionic radius from Ni^{3+} to Ni^{2+} and from Ni^{2+} to Li^{+}. Upon charging, Li ions in the inter-slab layer are deintercalated, and more Ni^{2+} are oxidized to Ni^{3+}. That leads to a slight decrease of lattice parameter since the ion radius of Ni^{3+} is smaller than that of Ni^{2+}.[62] Lattice parameter c increases during the initial charging because of the electrostatic effect and the repulsion between oxygen anions in the neighboring layers, and decreases eventually at the highly charged state due to the lattice structure collapse induced by the extensive Li ion removal. Moreover, a sequential crystal structural change takes place from hexagonal phase H1 to monoclinic phase M, and subsequently from monoclinic phase M back to hexagonal phases H2 and H3.

The enthalpy of $LiNiO_2$ formation ΔH_f is reported to be -54.8 kJ/mol from oxides (Li_2O and NiO) and O_2 at 298 K based on calorimetry measurement.[63] From elements, ΔH_f is -593.0 kJ/mol at 298 K.[63] The change of Gibbs energy for the formation of $LiNiO_2$ from elements ΔG_f is -514.96 kJ/mol at 300 K, indicating a spontaneous reaction.[64]

1.3.3. Instability issues of $LiNiO_2$

1.3.3.1. Chemical and electrochemical instability

The highly delithiated $LiNiO_2$ is unstable and prone to decompose, which can lead to the O_2 release (equation 2 and 3) and parasitic reaction with the electrolyte. The highly reactive Ni^{4+} formed at highly delithiated state tends to be reduced to Ni^{2+} and form the NiO-like rock-salt structure, which is resistive to the ionic conduction. Thus, the accumulation of the rock-salt phase consequently induces the increasing impedance and the capacity decay. The rock-salt structure mainly forms on the surface since the O_2 is

easier to evolve.[65] Depending on the state of charge, the spinel structure can also be formed (equation (1)).

$$3Li_xNiO_2\ (\text{layered}) \rightarrow\ Li_xNi_2\ O_4\ (\text{spinel}) +\ NiO(\text{rocksalt}) +\ x\ Li_2O \qquad (1)$$

$$Li_xNi_2\ O_4\ (\text{spinel}) \rightarrow\ 2\ NiO(\text{rocksalt})\ +\ \frac{x}{2}\ Li_2O + \frac{4-x}{2} O_2 \qquad (2)$$

$$3Li_xNiO_2\ (\text{layered}) \rightarrow 3\ NiO(\text{rocksalt}) + \frac{3x}{2}\ Li_2O + \frac{6-3x}{4} O_2 \qquad (3)$$

The theoretical specific capacity of $LiNiO_2$ is about 274 mAh/g. In practice, the reversible capacity can reach more than 150 mAh/g in the voltage window of 2 V to 4.2 V.[66] The electrochemical activity is highly related to the stoichiometry of $LiNiO_2$. The Ni ion in the Li planes induced by the off-stoichiometry results in the loss of reversible capacity during the first cycle.[67] Various factors can influence the stoichiometry, including but not limited to the O_2 partial pressure, the reactivity of the precursor and Li content during synthesis.[68]

1.3.3.2. Thermal instability

Thermal instability is a typical limit of $LiNiO_2$, which can result in severe safety issues during cycling. Dahn and coworkers observed the cathode material decomposition and the O_2 release upon heating.[69] By using thermal gravimetric analyzer (TGA), they compared the thermal stability of three cathode materials, namely $LiCoO_2$, $LiNiO_2$, and $LiMn_2O_4$. The results suggested that $LiMn_2O_4$ is the most thermally stable material while $LiNiO_2$ is the least one among the three cathode materials. The high temperature-induced cathode decomposition and O_2 evolution lead to a violent parasitic reaction with the electrolyte, which consequently causes vent and safety issues.[70] Zhang *et al.* also

investigated that the most heat release corresponds to the reaction with the electrolyte instead of the cathode itself.[71]

$LiNiO_2$ is observed to be thermally stable in the pristine state,[69] but unstable at the highly charged state.[72] With more Li ion deintercalated, more O_2 is liberated and the maximum O_2 release in the $LiNiO_2$ takes place at a lower temperature. The reversibility of $LiNiO_2$ is poor at 40 °C upon cycling, and an exothermic heat is observed at 200 °C for the highly delithiated state $Li_{0.2}NiO_2$.[73] The mechanism of the cathode decomposition and O_2 release at highly delithiated state is interpreted by a two-step process. The layered structure transforms to the spinel structure with heat release at about 200 °C, and phase transformation continues from the spinel structure to the rock-salt structure with more O_2 release when heating up to about 300 °C. The crystal structure evolution can be expressed by the equation (1) to (2) and the overall reaction (3).[74]

1.3.3.3. Structural instability

It is commonly accepted that $LiNiO_2$ undergoes sequential phase transformation during charging (Li ion deintercalation) in the order of hexagonal phase H1, monoclinic phase M, hexagonal phase H2 and hexagonal phase H3.[49] Assuming the chemical formula is $Li_xNi_{1+z}O_2$, where $0 < x < 1-z$. As Li ion deintercalated up to x=0.85, the hexagonal phase H1 is well retained. When x keeps decreasing to 0.8, the monoclinic phase M appears, and single monoclinic phase M is obtained until x decreases to about 0.75, which is driven by Li vacancy ordering.[75] As x decreases to 0.5, hexagonal phase H2 arises until x reaches 0.25 when hexagonal phase H3 begins to form. During the phase transformation from hexagonal phase H2 to H3, the lattice shrinkage induces a 7% volume decrease, which induces strain in the particles and consequently generates cracks. The cracks provide

channels for electrolyte infiltration, and parasitic reactions between the exposed cathode particle surface and electrolyte play a critical role in the eventual cycling failure. Such parasitic reactions can lead to the cathode particle surface reconstruction that involves the phase transformation from $R\bar{3}m$ layered structure to $Fm\bar{3}m$ rock-salt structure.[76] Our recent study indicated that the cracks can increase the electron diffusion length significantly, while electrolyte infiltration can shorten the diffusion distance of ions but not electrons. The mismatch gives rise to the heterogeneous distribution of ionic and electronic traffic load eventually.[77] To address the issue of cracks, Mao *et al.* indicated that engineering the as-made particle morphology carefully can tune the degree of crack formation.[78]

1.3.4. Strategies to design stable Ni-rich Co-free layered oxide cathodes

1.3.4.1. Surface engineering through coating, core-shell, and concentration-gradient designs

The surface coating of the $LiNiO_2$ is to form a passivated layer on the surface of the cathode particles, which can suppress the side reactions with the electrolyte. Therefore, the O_2 release and continuous accumulation of cathode electrolyte interface (CEI) can be mitigated. Various metal oxides have been investigated for the coating of $LiNiO_2$, such as ZrO_2, La_2O_3.[79,80] Both of the metal oxide coated $LiNiO_2$ yield larger capacity retention since the surface coating layered well suppress the phase transformation.

Another strategy to modify the surface of cathode materials is to form a core-shell structure, which is commonly achieved by coating the cathode surface with specific metal-containing compound, followed by thermal treatment to facilitate the diffusion of coating elements into the cathode structure. A thermally more stable shell, say NMC material, can be constructed in the synthesis process of the high capacity $LiNiO_2$ core. Tuning the

synthesis parameters is essential in the process of shell structure growth. Different shell structures have been reported, including but not limited to $LiNi_{0.8}Co_{0.1}Mn_{0.1}O_2$ (NMC811),[81] $LiCo_{1-y}Mn_yO_2$.[82] A chemical concentration gradient is created if the transformation from the core to the shell is continuous. NMC materials are good examples to form a concentration gradient.[83,84] The Mn-rich surface provides the thermal stability while the Ni-rich bulk maintains high capacity. Benefit from these strategies, better capacity retention and less structural degradation are obtained.

1.3.4.2. Doping chemistry

As an alternative to the surface coating, which requires extra processing and leads to high cost, doping has been becoming one of the most investigated strategies to improve the cycling stability of the cathode material. Doping is to substitute the transition metal cation (non-metal anions) in the cathode material with a slight amount of foreign metal cations (non-metal anions). Although various non-metal anion doping methods are reported,[85,86] metal cation doping remains the focus of the doping study. The discussion in this review will be based on the metal cation doping.

The role that different dopants play is dependent on not only the electrochemical properties of themselves but also the sublattice site that they reside on. In general, the electrochemical inactive metal cations staying on the Li ion sites function as pillars and maintain the structural integrity.[87] The dopants residing on the transition metal sites contribute to the increasing lattice spacing and higher Ni-O bond strength, which leads to fewer O vacancies.[88] In the layered oxide cathode materials, it is widely accepted that most monovalent and divalent ion dopants are prone to reside on Li site, while trivalent and tetravalent ion dopants prefer to stay on transition metal ion site.[87,89–91] It is also reported

that the preference of dopants staying on the Li ion site or transition metal ion site is related to the charge and spin states of the dopants, and the local lattice environment.[92] The substitutional preference of several dopants in the $LiNiO_2$ has been investigated based on the first principle calculations. According to the analysis, Mn, Co, Fe, and Al prefer to reside on Ni sublattice. Mg can stay on either Li sublattice or Ni sublattice, despite it is favorable to the Li sublattice when the fraction of the Mg dopant is more than 10%.

Various dopants have been investigated. Co doping is observed to mitigate the Ni/Li cation mixing which then increase the stoichiometry, thermal stability and mechanical stability are also slightly increased.[93–95] Mn is demonstrated to enhance the thermal stability of the cathode material,[96] but with some capacity penalty.[97] Mg resides in the Li planes that can function as pillars and thereby mitigate the structural collapse. Al doping and Ti doping are reported to contribute to the stability improvement of the cathode material.[98,73]

To obtain better electrochemical performance and take advantage of different dopants, multi-element doping has been investigated. Gao *et al.* reported Mg and Ti co-doped $LiNiO_2$ with different dopant content and obtained both higher thermal stability and capacity retention.[99] However, the effect of each dopant on the improved electrochemical performance is not well understood yet, especially in the multi-dopant system. It is commonly believed that the distribution of the dopants in the primary particle is relatively homogeneous. However, a recent study based on Ti-Mg-Al co-doped $LiCoO_2$ cathode material shows that the Ti dopant may segregate onto the surface and form a gradient distribution,[100] which is confirmed by our recent study based on NMC811-Ti. As shown in Figure 7, Ti is more enriched at the surface (5.8 at%) than the bulk (1.9 at%). To better

understand how the concentration of dopants and their distribution influence the materials properties in the multi-element doping system, we have been probing the cathode material formation process.

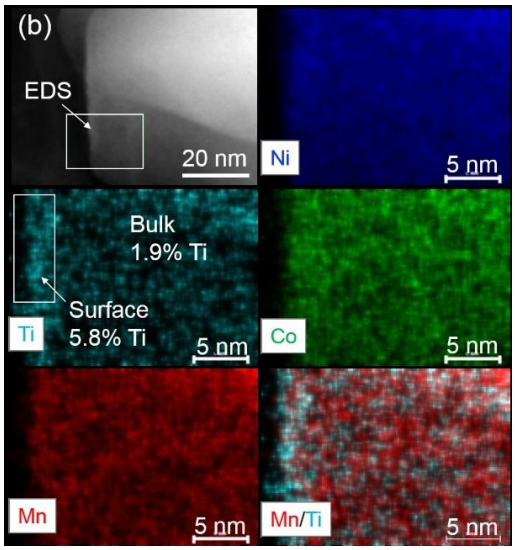

Figure 7. STEM-EDS mapping of the Ti-doped NMC811 material after 300 cycles at 1C between 2.5-4.5 V versus Li^+/Li. (Figure reproduced from ref.60)

1.3.4.3. Single crystal synthesis

At present, most commercial LIB NMC cathodes are produced with spherical polycrystalline particle morphology (Figure 8a). The reason is sphere has the smallest surface area among all shapes with the same volume. Small surface areas can minimize the parasitic reactions between the electrolyte and cathode surface, thereby enhancing the battery cycle life. However, the polycrystalline secondary particles are composed of numerous primary grains, as shown in Figure 8a. These single grains can still significantly contribute to larger specific surface area even with a spherical shape. In addition, the phase transformations upon charging and discharging cycles can cause lattice volume change and stress accumulation. The stress can lead to intergranular crack formation at the grain boundaries. The cracks expose fresh cathode surface to the electrolyte, which results in

more cathode-electrolyte side reactions and faster performance degradation. In contrast, single crystal layered oxide cathodes can be synthesized to address the instability issues of their polycrystalline counterparts. Single crystal layered cathode particles are at similar length scale with polycrystalline secondary particles but without sub-units of single grains at nanometer scale or grain boundaries (Figure 8b). Therefore, the intergranular crack issues in polycrystalline cathodes can be mitigated, and the cycling stability of single crystal cathode is increased due to its enhanced structural integrity.[101]

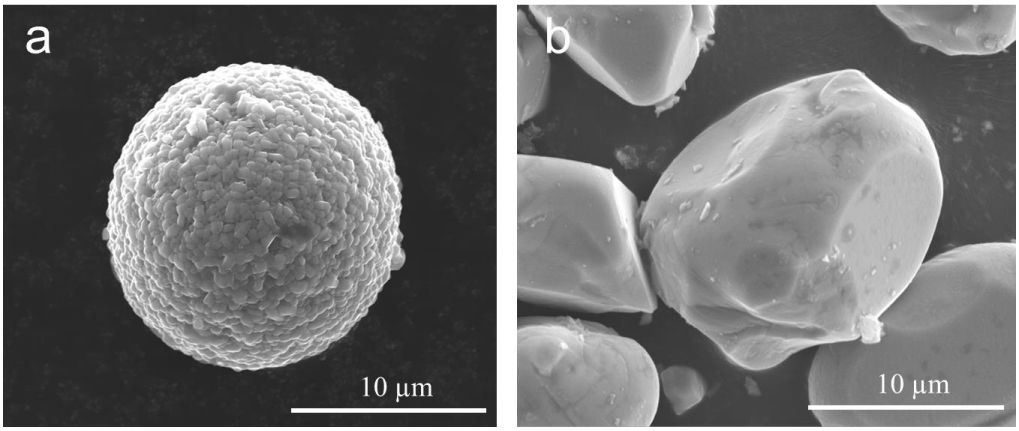

Figure 8. Scanning electron microscopy (SEM) images of (a) polycrystalline and (b) single crystal $LiNi_{0.8}Mn_{0.1}Co_{0.1}O_2$ (NMC811) cathodes.

The synthesis methods of single crystal layered cathodes can be majorly categorized into three approaches (Figure 9). High-temperature synthesis is the most direct approach to obtaining single crystal layer cathodes (Figure 9a). The increasing calcination temperature and duration can promote the ion mobility and grain growth of single crystals. However, severe particle agglomerations can readily form at high temperatures. Therefore, additional pulverization steps are required to optimize the particle size. Furthermore, the thermal stability of Ni-rich cathodes is low. High-temperature synthesis is challenging for

Ni-rich layered cathodes due to Li loss. Another approach is multi-step synthesis, which decouples the grain growth and layered phase formation by dividing the calcination into multiple steps (Figure 9b). For instance, Li *et al.* synthesized $LiNi_{0.33}Mn_{0.33}Co_{0.33}O_2$ (NMC111) by a first-step calcination at 1000 °C for 10 hours with a sub-stoichiometric amount of lithium carbonate to promote single crystal growth, followed by a second-step calcination at 900 °C for 10 hours with the remaining Li source to form the final layered phase.[102] Nevertheless, the synthesis of single crystals through multi-step approach also suffers from materials instability at high temperatures. Molten-salt synthesis is another method to obtain single crystal cathodes (Figure 9c). Specific salts, which can melt at relatively low temperatures, are added to the precursors to provide a liquid medium for the crystal to form and Li intercalation at low temperatures. The size and morphology of single crystals can be better controlled, and the particle agglomeration issues can be mitigated through molten-salt synthesis. Water washing is required to remove the residue salt from the cathode product, which can be detrimental to the performance of Ni-rich cathodes.[103] Proper processing of the cathode after washing, such as recalcination, is normally needed.

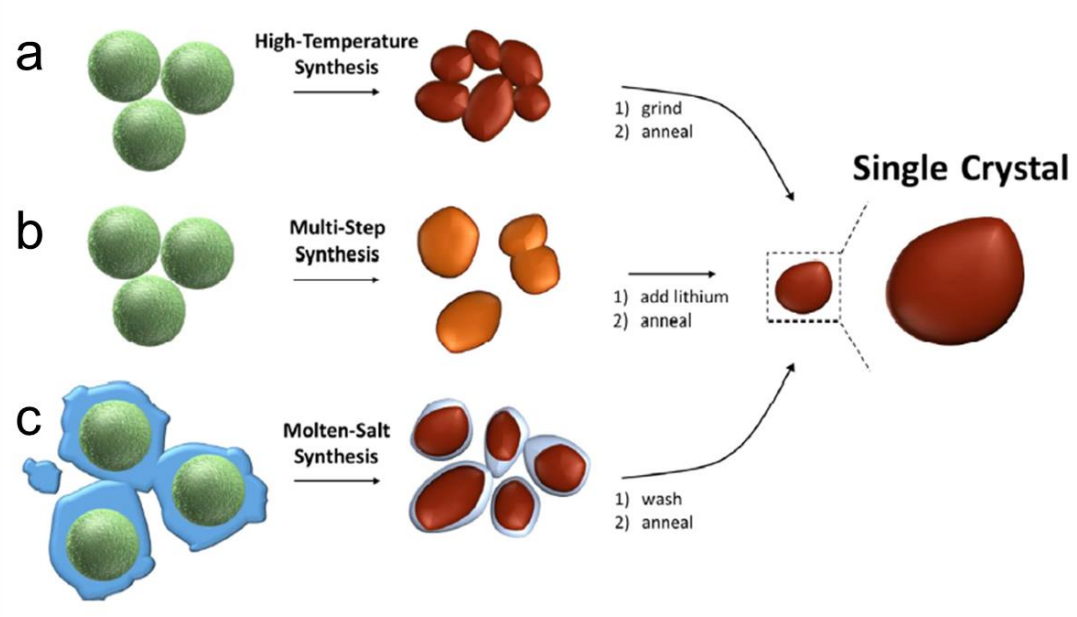

Figure 9. Three main approaches to synthesizing single crystal layered cathodes, (a) high-temperature synthesis, (b) multi-step synthesis, (c) molten-salt synthesis. (Figure reproduced from ref.101)

1.4. References

(1) General Office of the State Council. *Notice of the General Office of the State Council on Printing and Distributing the New Energy Vehicle Industry Development Plan (2021-2035)*. http://www.gov.cn/zhengce/content/2020-1/02/content_5556716.htm (accessed 2022-01-10).

(2) European Commission. *Mobility Strategy*. https://transport.ec.europa.eu/transport-themes/mobility-strategy_en (accessed 2022-01-12).

(3) International Energy Agency. *World Energy Model* . https://www.iea.org/reports/world-energy-model (accessed 2022-01-10).

(4) International Energy Agency. *Global EV Outlook 2021*. https://www.iea.org/reports/global-ev-outlook-2021 (accessed 2022-01-10).

(5) International Energy Agency. *The Role of Critical Minerals in Clean Energy*

Transitions. https://www.iea.org/reports/the-role-of-critical-minerals-in-clean-energy-transitions (accessed 2022-01-12).

(6) Nealer, R.; Hendrickson, T. P. Review of Recent Lifecycle Assessments of Energy and Greenhouse Gas Emissions for Electric Vehicles. *Curr. Sustain. Energy Reports* **2015**, *2* (3), 66–73.

(7) Finnveden, G.; Hauschild, M. Z.; Ekvall, T.; Guinée, J.; Heijungs, R.; Hellweg, S.; Koehler, A.; Pennington, D.; Suh, S. Recent Developments in Life Cycle Assessment. *J. Environ. Manage.* **2009**, *91* (1), 1–21.

(8) Notter, D. A.; Gauch, M.; Widmer, R.; Wäger, P.; Stamp, A.; Zah, R.; Althaus, H. J. Contribution of Li-Ion Batteries to the Environmental Impact of Electric Vehicles. *Environ. Sci. Technol.* **2010**, *44* (17), 6550–6556.

(9) Hawkins, T. R.; Singh, B.; Majeau-Bettez, G.; Strømman, A. H. Comparative Environmental Life Cycle Assessment of Conventional and Electric Vehicles. *J. Ind. Ecol.* **2013**, *17* (1), 53–64.

(10) Dunn, J. B.; Gaines, L.; Sullivan, J.; Wang, M. Q. Impact of Recycling on Cradle-to-Gate Energy Consumption and Greenhouse Gas Emissions of Automotive Lithium-Ion Batteries. *Environ. Sci. Technol.* **2012**, *46* (22), 12704–12710.

(11) Kim, H. C.; Wallington, T. J.; Arsenault, R.; Bae, C.; Ahn, S.; Lee, J. Cradle-to-Gate Emissions from a Commercial Electric Vehicle Li-Ion Battery: A Comparative Analysis. *Environ. Sci. Technol.* **2016**, *50* (14), 7715–7722.

(12) Majeau-Bettez, G.; Hawkins, T. R.; StrØmman, A. H. Life Cycle Environmental Assessment of Lithium-Ion and Nickel Metal Hydride Batteries for Plug-in Hybrid and Battery Electric Vehicles. *Environ. Sci. Technol.* **2011**, *45* (10), 4548–4554.

(13) Ellingsen, L. A. W.; Majeau-Bettez, G.; Singh, B.; Srivastava, A. K.; Valøen, L. O.; Strømman, A. H. Life Cycle Assessment of a Lithium-Ion Battery Vehicle Pack. *J. Ind. Ecol.* **2014**, *18* (1), 113–124.

(14) Hao, H.; Mu, Z.; Jiang, S.; Liu, Z.; Zhao, F. GHG Emissions from the Production of Lithium-Ion Batteries for Electric Vehicles in China. *Sustain.* **2017**, *9* (4), 504.

(15) Peters, J. F.; Baumann, M.; Zimmermann, B.; Braun, J.; Weil, M. The Environmental Impact of Li-Ion Batteries and the Role of Key Parameters – A Review. *Renew. Sustain. Energy Rev.* **2017**, *67*, 491–506.

(16) Dunn, J. B.; Gaines, L.; Kelly, J. C.; James, C.; Gallagher, K. G. The Significance of Li-Ion Batteries in Electric Vehicle Life-Cycle Energy and Emissions and Recycling's Role in Its Reduction. *Energy Environ. Sci.* **2014**, *8* (1), 158–168.

(17) Ciez, R. E.; Whitacre, J. F. Examining Different Recycling Processes for Lithium-Ion Batteries. *Nat. Sustain.* **2019**, *2* (2), 148–156.

(18) Yang, Y.; Okonkwo, E. G.; Huang, G.; Xu, S.; Sun, W.; He, Y. On the Sustainability of Lithium Ion Battery Industry – A Review and Perspective. *Energy Storage Mater.* **2021**, *36*, 186–212.

(19) Porzio, J.; Scown, C. D. Life-Cycle Assessment Considerations for Batteries and Battery Materials. *Adv. Energy Mater.* **2021**, *11* (33), 2100771.

(20) de Souza, L. L. P.; Lora, E. E. S.; Palacio, J. C. E.; Rocha, M. H.; Renó, M. L. G.; Venturini, O. J. Comparative Environmental Life Cycle Assessment of Conventional Vehicles with Different Fuel Options, Plug-in Hybrid and Electric Vehicles for a Sustainable Transportation System in Brazil. *J. Clean. Prod.* **2018**, *203*, 444–468.

(21) Trading Economics. *Nickel Price*. https://tradingeconomics.com/commodity/nickel (accessed 2022-04-06).

(22) Reuters. *China's CATL says raised prices for some battery products due to rising raw material costs*. https://www.reuters.com/article/china-autos-catl/chinas-catl-says-raised-prices-for-some-battery-products-due-to-rising-raw-material-costs-idINB9N2VI00I (accessed 2022-04-06).

(23) Reuters. *Analysis: Ukraine invasion sets back Musk's dream for cheaper EVs, for now*. https://www.reuters.com/technology/ukraine-invasion-sets-back-musks-dream-cheaper-evs-now-2022-03-07/ (accessed 2022-04-06).

(24) U.S. Geological Survey. *Mineral commodity summaries 2021*. https://pubs.er.usgs.gov/publication/mcs2021 (accessed 2022-01-12).

(25) Government of Canada. *Nickel facts*. https://www.nrcan.gc.ca/our-natural-resources/minerals-mining/minerals-metals-facts/nickel-facts/20519 (accessed 2022-01-12).

(26) Government of Canada. *Copper facts*. https://www.nrcan.gc.ca/our-natural-resources/minerals-mining/minerals-metals-facts/copper-facts/20506 (accessed 2022-01-12).

(27) Infinity Lithium. *Infinity Delivers Exceptional Lithium Hydroxide Pre-feasibility Study and Declares Maiden Jorc Ore Reserve*. https://www.miningnewsfeed.com/reports/San_Jose_Lithium_PFS_08222019.pdf (accessed 2022-01-12).

(28) Knoema. *Nickel Price Forecasts: Long-Term 2021 to 2030* . https://cn.knoema.com/ydolvrc/nickel-price-forecasts-long-term-2021-to-2030-

data-and-charts (accessed 2022-01-12).

(29) U.S. Geological Survey. *Cobalt Statistics and Information*. https://www.usgs.gov/centers/national-minerals-information-center/cobalt-statistics-and-information (accessed 2022-01-12).

(30) Mayyas, A.; Steward, D.; Mann, M. The Case for Recycling: Overview and Challenges in the Material Supply Chain for Automotive Li-Ion Batteries. *Sustain. Mater. Technol.* **2018**, *19* (C).

(31) Department of Energy. *National Blueprint for Lithium Batteries*. https://www.energy.gov/eere/vehicles/articles/national-blueprint-lithium-batteries (accessed 2022-01-10).

(32) S&P Global Market Intelligence. *Top electric vehicle markets dominate lithium-ion battery capacity growth*. https://www.spglobal.com/marketintelligence/en/news-insights/blog/top-electric-vehicle-markets-dominate-lithium-ion-battery-capacity-growth (accessed 2022-01-12).

(33) Horowitz, J.; Coffin, D.; Taylor, B. *Supply Chain for EV Batteries: 2020 Trade and Value-added Update*. https://papers.ssrn.com/abstract=3980828 (accessed 2022-01-12).

(34) China Geological Survey. *Assessment Report for Lithium, Cobalt, Nickel, Tin, and Potash Reserves in the World(2021)*. https://geocloudproducts.cgs.gov.cn/dzzlfw/idx/fileView.do?dzcp_id=8a8889ba7c69ff0a017c9dfd363b0896&path=https%3A%2F%2Fgeocloudproducts.cgs.gov.cn%2Fdzxxcp%2Fadmin_file%2Fcore%2Ffile%2FtoView.do%3Fid%3Df01fa73cc44e46a5aa4bde54bfd9d030&providerid=4028803a518fe41c0151a47891240027

(accessed 2022-01-12).

(35) McKinsey. *The future of nickel: A class act* . https://www.mckinsey.com/industries/metals-and-mining/our-insights/the-future-of-nickel-a-class-act (accessed 2022-04-06).

(36) Nassar, N. T.; Graedel, T. E.; Harper, E. M. By-Product Metals Are Technologically Essential but Have Problematic Supply. *Sci. Adv.* **2015**, *1* (3).

(37) Mordor Intelligence. *Lithium-Ion Battery Separator Market - Growth, Trends, COVID-19 Impact, and Forecasts (2022-2027))* . https://www.mordorintelligence.com/industry-reports/lithium-ion-battery-separator-market (accessed 2022-04-06).

(38) Department of Energy. *Energy Storage Market Report 2020*. https://www.energy.gov/energy-storage-grand-challenge/downloads/energy-storage-market-report-2020 (accessed 2022-01-10).

(39) BloombergNEF. *China Dominates the Lithium-ion Battery Supply Chain, but Europe is on the Rise*. https://about.bnef.com/blog/china-dominates-the-lithium-ion-battery-supply-chain-but-europe-is-on-the-rise/ (accessed 2022-01-10).

(40) Bloomberg. *U.S. Loosens China Grip on $46 Billion Lithium-Battery Industry*. https://www.bloomberg.com/news/articles/2021-10-07/u-s-loosens-china-grip-on-46-billion-lithium-battery-industry (accessed 2022-01-10).

(41) Nagaura, T.; Tozawa, K. Lithium Ion Rechargeable Battery. *Prog. Batter. Sol. Cells* **1990**, *9*, 209–219.

(42) Ziegler, M. S.; Song, J.; Trancik, J. E. Determinants of Lithium-Ion Battery Technology Cost Decline. *Energy Environ. Sci.* **2021**, *14* (12), 6074–6098.

(43) Dahn, J. R. R.; von Sacken, U.; Michal, C. A. A. Structure and Electrochemistry of $Li_{1\pm y}NiO_2$ and a New Li_2NiO_2 Phase with the $Ni(OH)_2$ Structure. *Solid State Ionics* **1990**, *44* (1–2), 87–97.

(44) Dahn, J. R.; von Sacken, U.; Juzkow, M. W.; Al-Janaby, H. Rechargeable $LiNiO_2$/ Carbon Cells. *J. Electrochem. Soc.* **1991**, *138* (8), 2207–2211.

(45) Chien, P. H.; Wu, X.; Song, B.; Yang, Z.; Waters, C. K.; Everett, M. S.; Lin, F.; Du, Z.; Liu, J. New Insights into Structural Evolution of $LiNiO_2$ Revealed by Operando Neutron Diffraction. *Batter. Supercaps* **2021**, *4* (11), 1701–1707.

(46) Yoshio, M.; Noguchi, H.; Itoh, J. ichi; Okada, M.; Mouri, T. Preparation and Properties of $LiCo_yMn_xNi_{1-x-y}O_2$ as a Cathode for Lithium Ion Batteries. *J. Power Sources* **2000**, *90* (2), 176–181.

(47) Lu, Z.; MacNeil, D. D.; Dahn, J. R. Layered $Li[Ni_xCo_{1-2x}Mn_x]O_2$ Cathode Materials for Lithium-Ion Batteries. *Electrochem. Solid-State Lett.* **2001**, *4* (12), A200.

(48) Lee, K. K.; Yoon, W. S.; Kim, K. B.; Lee, K. Y.; Hong, S. T. Characterization of $LiNi_{0.85}Co_{0.10}M_{0.05}O_2$ (M = Al, Fe) as a Cathode Material for Lithium Secondary Batteries. *J. Power Sources* **2001**, *97–98*, 308–312.

(49) Bianchini, M.; Roca-Ayats, M.; Hartmann, P.; Brezesinski, T.; Janek, J. There and Back Again—The Journey of $LiNiO_2$ as a Cathode Active Material. *Angew. Chemie Int. Ed.* **2019**, *58* (31), 10434–10458.

(50) Kim, J.; Amine, K. A Comparative Study on the Substitution of Divalent, Trivalent and Tetravalent Metal Ions in $LiNi_{1-x}M_xO_2$ (M = Cu^{2+}, Al^{3+} and Ti^{4+}). *J. Power Sources* **2002**, *104* (1), 33–39.

(51) Kim, Y.; Seong, W. M.; Manthiram, A. Cobalt-Free, High-Nickel Layered Oxide

Cathodes for Lithium-Ion Batteries: Progress, Challenges, and Perspectives. *Energy Storage Mater.* **2021**, *34*, 250–259.

(52) Mu, L.; Zhang, R.; Kan, W. H.; Zhang, Y.; Li, L.; Kuai, C.; Zydlewski, B.; Rahman, M. M.; Sun, C.-J. J.; Sainio, S.; Avdeev, M.; Nordlund, D.; Xin, H. L.; Lin, F. Dopant Distribution in Co-Free High-Energy Layered Cathode Materials. *Chem. Mater.* **2019**, *31* (23), 9769–9776.

(53) Mu, L.; Kan, W. H.; Kuai, C.; Yang, Z.; Li, L.; Sun, C. J.; Sainio, S.; Avdeev, M.; Nordlund, D.; Lin, F. Structural and Electrochemical Impacts of Mg/Mn Dual Dopants on the $LiNiO_2$ Cathode in Li-Metal Batteries. *ACS Appl. Mater. Interfaces* **2020**, *12* (11), 12874–12882.

(54) Mizushima, K.; Jones, P. C.; Wiseman, P. J.; Goodenough, J. B. Li_xCoO_2 ($0<x<-1$): A new cathode material for batteries of high energy density. *Mater. Res. Bull.* **1980**, *15* (6), 783–789.

(55) Xu, R.; Yang, Y.; Yin, F.; Liu, P.; Cloetens, P.; Liu, Y.; Lin, F.; Zhao, K. Heterogeneous Damage in Li-Ion Batteries: Experimental Analysis and Theoretical Modeling. *J. Mech. Phys. Solids* **2019**, *129*, 160–183.

(56) Rahman, M. M.; Xu, Y.; Cheng, H.; Shi, Q.; Kou, R.; Mu, L.; Liu, Q.; Xia, S.; Xiao, X.; Sun, C.-J.; Sokaras, D.; Nordlund, D.; Zheng, J.-C.; Liu, Y.; Lin, F. Empowering Multicomponent Cathode Materials for Sodium Ion Batteries by Exploring Three-Dimensional Compositional Heterogeneities. *Energy Environ. Sci.* **2018**, *11* (9), 2496–2508.

(57) Rahman, M. M.; Zhang, Y.; Xia, S.; Kan, W. H.; Avdeev, M.; Mu, L.; Sokaras, D.; Kroll, T.; Du, X.-W.; Nordlund, D.; Liu, Y.; Lin, F. Surface Characterization of Li-

Substituted Compositionally Heterogeneous $NaLi_{0.045}Cu_{0.185}Fe_{0.265}Mn_{0.505}O_2$ Sodium-Ion Cathode Material. *J. Phys. Chem. C* **2019**, *123* (18), 11428–11435.

(58) Lin, F.; Liu, Y.; Yu, X.; Cheng, L.; Singer, A.; Shpyrko, O. G.; Xin, H. L.; Tamura, N.; Tian, C.; Weng, T.-C.; Yang, X.-Q.; Meng, Y. S.; Nordlund, D.; Yang, W.; Doeff, M. M. Synchrotron X-Ray Analytical Techniques for Studying Materials Electrochemistry in Rechargeable Batteries. *Chem. Rev.* **2017**, *117* (21), 13123–13186.

(59) Yang, Z.; Mu, L.; Hou, D.; Rahman, M. M.; Xu, Z.; Liu, J.; Nordlund, D.; Sun, C.; Xiao, X.; Lin, F. Probing Dopant Redistribution, Phase Propagation, and Local Chemical Changes in the Synthesis of Layered Oxide Battery Cathodes. *Adv. Energy Mater.* **2020**, 2002719.

(60) Steiner, J. D.; Cheng, H.; Walsh, J.; Zhang, Y.; Zydlewski, B.; Mu, L.; Xu, Z.; Rahman, M. M.; Sun, H.; Michel, F. M.; Sun, C.-J.; Nordlund, D.; Luo, W.; Zheng, J.-C.; Xin, H. L.; Lin, F. Targeted Surface Doping with Reversible Local Environment Improves Oxygen Stability at the Electrochemical Interfaces of Nickel-Rich Cathode Materials. *ACS Appl. Mater. Interfaces* **2019**, *11* (41), 37885–37891.

(61) Rougier, A.; Delmas, C.; Chadwick, A. V. Non-Cooperative Jahn-Teller Effect in $LiNiO_2$: An EXAFS Study. *Solid State Commun.* **1995**, *94* (2), 123–127.

(62) Yamada, S.; Fujiwara, M.; Kanda, M. Synthesis and Properties of $LiNiO_2$ as Cathode Material for Secondary Batteries. *J. Power Sources* **1995**, *54* (2), 209–213.

(63) Wang, M.; Navrotsky, A. Enthalpy of Formation of $LiNiO_2$, $LiCoO_2$ and Their Solid Solution, $LiNi_{1-x}Co_xO_2$. *Solid State Ionics* **2004**, *166* (1–2), 167–173.

(64) Yokokawa, H.; Sakai, N.; Yamaji, K.; Horita, T.; Ishikawa, M. Thermodynamic Determining Factors of the Positive Electrode Potential of Lithium Batteries. *Solid State Ionics* **1998**, *113–115*, 1–9.

(65) Xu, J.; Lin, F.; Nordlund, D.; Crumlin, E. J.; Wang, F.; Bai, J.; Doeff, M. M.; Tong, W. Elucidation of the Surface Characteristics and Electrochemistry of High-Performance $LiNiO_2$. *Chem. Commun.* **2016**, *52* (22), 4239–4242.

(66) Ohzuku, T.; Ueda, A.; Nagayama, M. Electrochemistry and Structural Chemistry of $LiNiO_2$ (R3m) for 4 Volt Secondary Lithium Cells; *J. Electrochem. Soc.* **1993**, *140* (7), 1862.

(67) Peres, J. P.; Delmas, C.; Rougier, A.; Broussely, M.; Perton, F.; Biensan, P.; Willmann, P. The Relationship between the Composition of Lithium Nickel Oxide and the Loss of Reversibility during the First Cycle. *J. Phys. Chem. Solids* **1996**, *57* (6–8), 1057–1060.

(68) Xu, J.; Lin, F.; Doeff, M. M.; Tong, W. A Review of Ni-Based Layered Oxides for Rechargeable Li-Ion Batteries. *J. Mater. Chem. A* **2017**, *5* (3), 874–901.

(69) Dahn, J. R.; Fuller, E. W.; Obrovac, M.; von Sacken, U. Thermal Stability of Li_xCoO_2, Li_xNiO_2 and λ-MnO_2 and Consequences for the Safety of Li-Ion Cells. *Solid State Ionics* **1994**, *69* (3–4), 265–270.

(70) Wainwright, D. Method of Evaluating Relative Safety of Porous Electrode/Electrolyte Combinations to Spot Heating. *J. Power Sources* **1995**, *54* (2), 192–197.

(71) Zhang, Z.; Fouchard, D.; Rea, J. R. Differential Scanning Calorimetry Material Studies: Implications for the Safety of Lithium-Ion Cells. *J. Power Sources* **1998**,

70 (1), 16–20.

(72) Morales, J.; Pérez-Vicente, C.; Tirado, J. L. Thermal Behaviour of Chemically Deintercalated $Li_{1-x}Ni_{1+x}O_2$. *J. Therm. Anal.* **1992**, *38* (3), 295–301.

(73) Arai, H.; Tsuda, M.; Sakurai, Y. Lithium Nickelate Electrodes with Enhanced High-Temperature Performance and Thermal Stability. *J. Power Sources* **2000**, *90* (1), 76–81.

(74) Wang L.; Maxisch T., Ceder, G. A First-Principles Approach to Studying the Thermal Stability of Oxide Cathode Materials. *Chem. Mater.* 2007, 19 (3), 543–552.

(75) Peres, J. P.; Weill, F.; Delmas, C. Lithium/Vacancy Ordering in the Monoclinic Li_xNiO_2 ($0.50 \leq x \leq 0.75$) Solid Solution. *Solid State Ionics* **1999**, *116* (1–2), 19–27.

(76) Xu, Z.; Rahman, M. M.; Mu, L.; Liu, Y.; Lin, F. Chemomechanical Behaviors of Layered Cathode Materials in Alkali Metal Ion Batteries. *J. Mater. Chem. A* **2018**, *6* (44), 21859–21884.

(77) Xia, S.; Mu, L.; Xu, Z.; Wang, J.; Wei, C.; Liu, L.; Pianetta, P.; Zhao, K.; Yu, X.; Lin, F.; Liu, Y. Chemomechanical Interplay of Layered Cathode Materials Undergoing Fast Charging in Lithium Batteries. *Nano Energy* **2018**, *53*, 753–762.

(78) Mao, Y.; Wang, X.; Xia, S.; Zhang, K.; Wei, C.; Bak, S.; Shadike, Z.; Liu, X.; Yang, Y.; Xu, R.; Pianetta, P.; Ermon, S.; Stavitski, E.; Zhao, K.; Xu, Z.; Lin, F.; Yang, X.; Hu, E.; Liu, Y. High-Voltage Charging-Induced Strain, Heterogeneity, and Micro-Cracks in Secondary Particles of a Nickel-Rich Layered Cathode Material. *Adv. Funct. Mater.* **2019**, *29* (18), 1900247.

(79) Cho, J.; Kim, T.-J.; Kim, Y. J.; Park, B. High-Performance ZrO_2-Coated $LiNiO_2$ Cathode Material. *Electrochem. Solid-State Lett.* **2001**, *4* (10), A159.

(80) Mohan, P.; Kalaignan, G. P. Electrochemical Performance of La_2O_3-Coated Layered $LiNiO_2$ Cathode Materials for Rechargeable Lithium-Ion Batteries. *Ionics (Kiel).* **2013**, *19* (6), 895–902.

(81) Jun, D.-W.; Yoon, C. S.; Kim, U.-H.; Sun, Y.-K. High-Energy Density Core–Shell Structured $Li[Ni_{0.95}Co_{0.025}Mn_{0.025}]O_2$ Cathode for Lithium-Ion Batteries. *Chem. Mater.* **2017**, *29* (12), 5048–5052.

(82) Deng, X.; Hu, G.; Du, K.; Peng, Z.; Gao, X.-G.; Yang, Y.-N. Synthesis and Electrochemical Properties of Co,Mn-Coated $LiNiO_2$ Lithium-Ion Battery Cathode Materials. *Mater. Chem. Phys.* **2008**, *109* (2–3), 469–474.

(83) Sun, Y.-K.; Chen, Z.; Noh, H.-J.; Lee, D.-J.; Jung, H.-G.; Ren, Y.; Wang, S.; Yoon, C. S.; Myung, S.-T.; Amine, K. Nanostructured High-Energy Cathode Materials for Advanced Lithium Batteries. *Nat. Mater.* **2012**, *11* (11), 942–947.

(84) Li, J.; Doig, R.; Camardese, J.; Plucknett, K.; Dahn, J. R. Measurements of Interdiffusion Coefficients of Transition Metals in Layered Li–Ni–Mn–Co Oxide Core–Shell Materials during Sintering. *Chem. Mater.* **2015**, *27* (22), 7765–7773.

(85) Kong, F.; Liang, C.; Longo, R. C.; Yeon, D.-H.; Zheng, Y.; Park, J.-H.; Doo, S.-G.; Cho, K. Conflicting Roles of Anion Doping on the Electrochemical Performance of Li-Ion Battery Cathode Materials. *Chem. Mater.* **2016**, *28* (19), 6942–6952.

(86) Binder, J. O.; Culver, S. P.; Pinedo, R.; Weber, D. A.; Friedrich, M. S.; Gries, K. I.; Volz, K.; Zeier, W. G.; Janek, J. Investigation of Fluorine and Nitrogen as Anionic Dopants in Nickel-Rich Cathode Materials for Lithium-Ion Batteries. *ACS Appl. Mater. Interfaces* **2018**, *10* (51), 44452–44462.

(87) Min, K.; Seo, S.-W.; Song, Y. Y.; Lee, H. S.; Cho, E. A First-Principles Study of

the Preventive Effects of Al and Mg Doping on the Degradation in $LiNi_{0.8}Co_{0.1}Mn_{0.1}O_2$ Cathode Materials. *Phys. Chem. Chem. Phys.* **2017**, *19* (3), 1762–1769.

(88) Sharifi-Asl, S.; Lu, J.; Amine, K.; Shahbazian-Yassar, R. Oxygen Release Degradation in Li-Ion Battery Cathode Materials: Mechanisms and Mitigating Approaches. *Adv. Energy Mater.* **2019**, 1900551.

(89) Xie, Q.; Li, W.; Manthiram, A. A Mg-Doped High-Nickel Layered Oxide Cathode Enabling Safer, High-Energy-Density Li-Ion Batteries. *Chem. Mater.* **2019**, acs.chemmater.8b03900.

(90) Dixit, M.; Markovsky, B.; Aurbach, D.; Major, D. T. Unraveling the Effects of Al Doping on the Electrochemical Properties of $LiNi_{0.5}Co_{0.2}Mn_{0.3}O_2$ Using First Principles. *J. Electrochem. Soc.* **2017**, *164* (1), A6359–A6365.

(91) Weigel, T.; Schipper, F.; Erickson, E. M.; Susai, F. A.; Markovsky, B.; Aurbach, D. Structural and Electrochemical Aspects of $LiNi_{0.8}Co_{0.1}Mn_{0.1}O_2$ Cathode Materials Doped by Various Cations. *ACS Energy Lett.* **2019**, *4* (2), 508–516.

(92) Hoang, K. First-Principles Theory of Doping in Layered Oxide Electrode Materials. *Phys. Rev. Mater.* **2017**, *1* (7), 075403.

(93) Caurant, D.; Baffier, N.; Garcia, B.; Pereira-Ramos, J. P. Synthesis by a Soft Chemistry Route and Characterization of $LiNi_xCo_{1-x}O_2$ ($0 \leq x \leq 1$) Cathode Materials. *Solid State Ionics* **1996**, *91* (1–2), 45–54.

(94) Tarascon, J. M.; Vaughan, G.; Chabre, Y.; Seguin, L.; Anne, M.; Strobel, P.; Amatucci, G. In Situ Structural and Electrochemical Study of $Ni_{1-x}Co_xO_2$ Metastable Oxides Prepared by Soft Chemistry. *J. Solid State Chem.* **1999**, *147* (1),

410–420.

(95) MacNeil, D. D.; Lu, Z.; Chen, Z.; Dahn, J. R. A Comparison of the Electrode/Electrolyte Reaction at Elevated Temperatures for Various Li-Ion Battery Cathodes. *J. Power Sources* **2002**, *108* (1–2), 8–14.

(96) Arai, H.; Okada, S.; Sakurai, Y.; Yamaki, J. Electrochemical and Thermal Behavior of $LiNi_{1-z}M_zO_2$ (M = Co, Mn, Ti). *J. Electrochem. Soc.* **1997**, *144* (9), 3117.

(97) Rossen, E.; Jones, C. D. W.; Dahn, J. R. Structure and Electrochemistry of $Li_xMn_yNi_{1-y}O_2$. *Solid State Ionics* **1992**, *57* (3–4), 311–318.

(98) Guilmard M.; Croguennec, L.; Denux, D.,; Delmas, C. Thermal Stability of Lithium Nickel Oxide Derivatives. Part I: $Li_xNi_{1.02}O_2$ and $Li_xNi_{0.89}Al_{0.16}O_2$ (x = 0.50 and 0.30). *Chem. Mater.* **2003**, *15* (23), 4476–4483.

(99) Gao, Y.; Yakovleva, M. V.; Ebner, W. B. Novel $LiNi_{1-x}Ti_{x/2}Mg_{x/2}O_2$ Compounds as Cathode Materials for Safer Lithium-Ion Batteries. *Electrochem. Solid-State Lett.* **1999**, *1* (3), 117.

(100) Zhang, J.-N.; Li, Q.; Ouyang, C.; Yu, X.; Ge, M.; Huang, X.; Hu, E.; Ma, C.; Li, S.; Xiao, R.; Yang, W.; Chu, Y.; Liu, Y.; Yu, H.; Yang, X.-Q.; Huang, X.; Chen, L.; Li, H. Trace Doping of Multiple Elements Enables Stable Battery Cycling of $LiCoO_2$ at 4.6 V. *Nat. Energy* **2019**, *4* (7), 594–603.

(101) Langdon, J.; Manthiram, A. A Perspective on Single-Crystal Layered Oxide Cathodes for Lithium-Ion Batteries. *Energy Storage Mater.* **2021**, *37*, 143–160.

(102) Li, F.; Kong, L.; Sun, Y.; Jin, Y.; Hou, P. Micron-Sized Monocrystalline $LiNi_{1/3}Co_{1/3}Mn_{1/3}O_2$ as High-Volumetric-Energy-Density Cathode for Lithium-Ion Batteries. *J. Mater. Chem. A* **2018**, *6* (26), 12344–12352.

(103) Xiong, X.; Wang, Z.; Yue, P.; Guo, H.; Wu, F.; Wang, J.; Li, X. Washing Effects on Electrochemical Performance and Storage Characteristics of $LiNi_{0.8}Co_{0.1}Mn_{0.1}O_2$ as Cathode Material for Lithium-Ion Batteries. *J. Power Sources* **2013**, *222*, 318–325.

2. Probing Dopant Redistribution, Phase Propagation, and Local Chemical Changes in the Synthesis of Layered Oxide Battery Cathodes

Zhijie Yang[1], Linqin Mu[1], Dong Hou[1], Muhammad Mominur Rahman[1], Zhengrui Xu[1], Jue Liu[2], Dennis Nordlund[3], Cheng-Jun Sun[4], Xianghui Xiao[5], Feng Lin[1]*

1. Department of Chemistry, Virginia Tech, Blacksburg, VA, 24061, USA
2. Oak Ridge National Laboratory, Oak Ridge, TN, 37831, USA
3. Stanford Synchrotron Radiation Lightsource, SLAC National Accelerator Laboratory, Menlo Park, CA, 94025, USA
4. Advanced Photon Source, Argonne National Laboratory, Argonne, IL, 60439, USA
5. National Synchrotron Light Source II, Brookhaven National Laboratory, Upton, NY, 11973, USA

Correspondence and requests for materials should be addressed to F.L. (email: fenglin@vt.edu)

2.1. Abstract

Achieving the targeted control of layered oxide properties calls for more fundamental studies to mechanistically probe their evolution during the synthesis. Herein, we investigate dopant distribution, phase propagation, and local chemical changes as well as their interplay in multielement-doped $LiNiO_2$ materials using spectroscopic, imaging, and scattering techniques. We show that dopants undergo dynamic redistribution in the $Ni(OH)_2$ host lattice at the early stage of calcination (below 300 °C). Such a redistribution behavior exhibits a strong dopant-dependent characteristic, allowing for the targeted surface and bulk doping control. The Ni oxidation process exhibits a depth-dependent characteristic and the most rapid Ni oxidation takes place between 300 °C and 700 °C. Using Ni oxidation state as the proxy for the phase transformation, we show the buildup of heterogeneous phase propagation in the early stage of calcination, especially along the radial direction of secondary particles. The radial heterogeneous phase distribution gradually decreases upon completing the calcination. However, a high degree of mosaic-like heterogeneity may still be present in the final product, departing from the perfect layered oxide. The present study advances fundamental insights into manipulating multiscale materials properties during calcination for obtaining stable, high-energy layered oxide cathodes.

2.2. Introduction

With the increasing demand for high energy batteries in applications such as electric vehicles, $LiNiO_2$ based layered cathode materials have received broad research attention in recent years.[1–3] In addition, the toxic, high-cost Co gives rise to the research interest in Co-free layered cathode materials. However, the thermal and chemical instability of $LiNiO_2$, especially at the deep-charged state, leads to severe safety issues and hinders its practical applications.[4] Recent studies have recognized the importance of elaborate synthetic control to obtain high performance $LiNiO_2$ based materials.[5–8] An ideal synthetic protocol should be capable of tailoring critical materials properties such as the dopant distribution at relevant length scales, extending from the surface to the bulk of cathode particles. However, achieving the targeted control of these properties calls for more fundamental studies to structurally and microscopically probe their evolution in the synthesis.

Cation doping is considered as an effective method to stabilize $LiNiO_2$ based cathodes by improving its bulk structural integrity as well as surface oxygen retention.[9–11] The doping effort has been extended to the multielement doping approach for simultaneously accessing the benefits of individual dopants.[12,13] In cathode materials with a low dopant concentration, especially in multielement-doped cathode materials, the dopant distribution pattern has been primarily understood through thermodynamics-based theoretical calculations.[14–17] Kinetically, the dopant redistribution during calcination may be governed by ion diffusion properties, which are intimately associated with ion diffusion coefficient, local environment of the host, and experimental conditions (e.g., temperature, atmosphere).[18–20] Therefore, understanding how dopants redistribute and change their local

chemical environments during calcination may provide a knob for improving the dopant functions in the bulk and at the surface of battery particles.

In addition to dopant distribution, phase propagation and local chemical changes during synthesis also play a significant role in ensemble-averaged battery performance. Many studies have gone beyond global crystal and electronic structures and revealed the importance of mesoscale chemical properties in the stability of layered oxide cathodes. For example, Mu *et al.* reported that the thermal degradation of charged layered oxides is governed by the local valence curvature of the layered to rocksalt phase propagation front.[21] In addition, the morphological defects at mesoscale that originate from local chemical and structural transformations, such as intergranular and intragranular cracks, are detrimental to the battery performance.[22] These chemomechanical breakdown of battery particles constitutes a frontier challenge in layered oxide cathodes and can be exacerbated by the heterogeneous charge distribution during charging and discharging of the particles.[23] The overcharged and undercharged nanodomains (i.e., charge heterogeneity) create undesired local stress fields, leading to the chemomechanical breakdown of battery particles and accelerating the performance degradation.[24] Xu *et al.* showed that charge distribution homogeneity and battery cycling stability can be enhanced by modulating the grain crystallographic orientation in polycrystalline battery materials.[25] The charge heterogeneity during battery cycling is associated with the local structural and chemical characteristics originating from the synthesis. The metal hydroxide precursor to layered oxide transition involves multiple steps of phase and chemical transformations, including dehydration of metal hydroxide precursors, lithiation of metal hydroxides, and crystallinity growth of oxides. Because of the intrinsic complexity of the calcination environment, these

transformations may exhibit a high degree of heterogeneity. For example, the 3D mapping of chemical states has exclusively shown that the transition metal (TM) oxidation states are heterogeneous even in commercial battery particles.[26,27] Many studies about the cathode formation process discussed how synthetic conditions, such as sintering temperature[5] and calcination atmosphere,[7] influence the battery performance. Regarding the cathode formation mechanism, the structural and chemical changes of several layered oxide cathodes are probed with X-ray diffraction (XRD) during the synthesis.[28,29] However, XRD can only provide the ensemble-averaged information, and there is a lack of the knowledge regarding how the local characteristics spatially transform along the calcination process.

Herein, we investigate the dopant redistribution, phase propagation, and local chemical changes of layered oxides at multiple length scales using a multielement-doped $LiNi_{0.96}Mg_{0.02}Ti_{0.02}$ (Mg/Ti-LNO) as a model platform.[12] The dopant redistribution takes place below 300 °C. There is no major dopant redistribution above 300 °C throughout the calcination process. Mg^{2+} rapidly diffuses into the $Ni(OH)_2$ matrix and forms a relatively uniform distribution in the final product, whereas Ti^{4+} exhibits a gradient distribution that is enriched at the surface. Globally, the phase transformation takes place from the initial mixed hydroxide phase to the layered phase through a metal oxide-liked intermediate phase. The mesoscale phase propagation and chemical changes show a high degree of three-dimensional (3D) heterogeneity, especially along the radial direction of secondary particles. Such 3D heterogeneity can be present in the final layered oxide product, albeit to a much lesser degree. These findings contribute to understanding the multiscale formation

of layered cathodes and potentially inform better design of cathode materials through controlling the thermal processing.

2.3. Materials and methods

Material Synthesis: The Mg/Ti-LNO was synthesized through a co-precipitation method and then calcined under specific temperature profiles to obtain the samples at various stages of calcination. Firstly, the starting solution (40 mL of NaOH and $NH_3 \cdot H_2O$ with a molar ratio of NaOH/ $NH_3 \cdot H_2O$ = 1/1.25) was prepared and the pH was adjusted to 11.0 by adding sulfuric acid. Secondly, the transition metal aqueous solution (100 mL of 0.096 M $NiSO_4 \cdot 6H_2O$, 0.002 M $MgSO_4 \cdot 7H_2O$, and 0.002 M $TiOSO_4$) and base solution (100 mL of NaOH and $NH_3 \cdot H_2O$ with a molar ratio of NaOH/ $NH_3 \cdot H_2O$ = 1/1.25) were added simultaneously into the starting solution obtained from the first step with a feed rate of 2 mL min^{-1} under constant stirring. The reaction was carefully controlled to keep the temperature at 55 °C and the pH at 11.0 ± 0.2 under N_2 flow protection. Thirdly, the precipitant obtained from the second step was washed with DI water, filtered, and dried in the vacuum oven at 105 °C for 12 hours. Finally, the as-prepared precursor from the third step was thoroughly mixed with LiOH (2% excess to compensate the Li loss during calcination), then the mixture was calcined at 460 °C for 2 h and then at 700 °C for 5 h under O_2 with a flow rate of 1.5 L min^{-1} to obtain the product. The samples at various intermediate states of calcination were prepared by interrupting the calcination at specific temperatures and time followed by cooling (Figure S2).

Electrochemical Characterization: To prepare the composite electrode slurry, poly(vinylidene difluoride, as the binder) (PVdF) was first dissolved into N-methyl-2-pyrrolidone, then the active material product obtained after calcination and the acetylene

carbon were added into the solution and thoroughly mixed, following the ratio of active material: PVdF: acetylene carbon = 90 wt %: 5 wt %: 5 wt %. The slurry was subsequently cast on the carbon-coated aluminum foil and dried at 120 °C for 12 h in a vacuum oven. The dry composite electrode was punched into disks of a diameter of 10 mm with a mass loading of ~1.4 mAh/cm^2. The obtained composite electrodes were used as cathode and the Li foils were used as the anode with the Whatman glass fiber (1827-047934-AH) as the separator to assemble the CR2032 coin cells in an Ar-filled glove box. The electrolyte is 1 M $LiPF_6$ in ethylene carbonate (EC) and ethyl methyl carbonate (EMC) with 2 wt % vinylene carbonate (VC). The coin cells were under galvanostatic discharge/charge in the cutoff voltage range of 2.5–4.4V at 22 °C and measured on the electrochemical workstation (Wuhan Land Company). 1C is defined as fully charging the cathode in 1 hour, which corresponds to the specific current rate of 200 mA g^{-1}.

Material Characterization: X-ray photoelectron spectroscopy (XPS) measurements were performed on the PHI VersaProbe III with a monochromatic Al K-alpha X-ray source (1486.6 eV). The samples for XPS were cooled to room temperature after calcination in oxygen and taken out from the furnace. Then the samples were ground for five minutes in the air and sealed for transfer and measurement. The sample exposure to air during sample collection and grinding gives rise to the Li carbonate formation. The full-field transmission X-ray microscopy (TXM) was performed at National Synchrotron Light Source II (NSLS- II) beamline 18-ID, Brookhaven National Laboratory. A python-based framework TomoPy was used to reconstruct the tomographic datasets,[30] and a commercial software Avizo was used for visualization. Soft XAS was performed at the Stanford Synchrotron Radiation Lightsource (SSRL) beamline 10-1, SLAC National

Accelerator Laboratory using a ring current of 350 mA and a 1000 L mm^{-1} spherical grating monochromator with 20 μm entrance and exit slits, providing ~10^{11} ph s^{-1} at 0.2 eV resolution in a 1 mm^2 beam spot. Data were acquired under ultrahigh vacuum (10^{-9} Torr) in a single load at room temperature using total electron yield (TEY), where the sample drain current was collected. The samples were mounted on an aluminum sample holder in an Ar-filled glove box and well-sealed for transfer. Hard XAS (XANES and EXAFS) measurement was performed using a Si (111) monochromator at the beamline 20-ID of the Advanced Photon Source (APS) at Argonne National Laboratory. The absorption energy calibration was based on the first inflection points of the Ni reference spectra that were collected from a Ni foil reference simultaneously with the samples. The samples of hard XAS and synchrotron XRD were sealed with Kapton tapes in the Ar-filled glove box for transfer and measurement. The synchrotron XRD patterns were collected at the beamline 11-3 of SSRL at SLAC National Accelerator Laboratory with the X-ray wavelength of 0.9762 Å. A LaB_6 sample was used to calibrate the diffraction configuration. The synchrotron XRD patterns were converted to the Cu K-α based XRD with the wavelength of 1.5406 Å. Neutron diffraction (ND) was performed on Nanoscale-Ordered Materials Diffractometer (NOMAD) BL-1B, Spallation Neutron Source (SNS) at Oak Ridge National Laboratory.[31,32] About 0.2-0.3 g powder sample was loaded into the quartz capillary (3mm) and each measurement took about 1 hour. The refinement of neutron diffraction patterns was conducted using the software GSAS EXPGUI.[33] For each sample, three histograms with different d-spacing range were used for refinement. The refinements for the other two histograms are shown in the Supporting Information. Thermogravimetric Analysis (TGA) was performed on TGA Q50 in the range of 250-750 °C at a temperature

ramping rate of 5 °C min^{-1} in air flow. The morphology of the particles during calcination was studied through scanning electron microscopy with the EDS performed at the acceleration voltage of 20 kV (ESEM, FEI Quanta 600 FEG).

2.4. Results

The hydroxide precursor of Mg/Ti-LNO is synthesized through a co-precipitation method.[12] The Mg/Ti-LNO material used in this study has better cycling stability than the baseline $LiNiO_2$ material, which is consistent with our previous study.[12] The electrochemical performance of Mg/Ti-LNO at 22 °C is evaluated in Li metal cells within a voltage window of 2.5-4.4 V vs. Li/Li^+. The initial discharge capacity is 220 mAh g^{-1} at C/10 which is comparable with the baseline $LiNiO_2$ (Figure S1a, Supporting Information).[12] The capacity retention after 60 cycles at C/10 is 93% and the capacity retentions after cycling for 100 times at C/2 and C/3 are both 94% (Figure S1b, Supporting Information). At a higher cycling rate as 3C, the capacity retention is 83% after 300 cycles (Figure S1c, Supporting Information). In this study, we probe the precursor-to-layered oxide transformation by characterizing the materials at different stages of the thermal calcination. Figure S2 shows the thermal profile of a typical calcination implemented in this study. The samples at different calcination stages were cooled to room temperature and prepared for *ex situ* characterizations.

The high specific capacity and cycling stability are attributed to the hierarchical distribution of Mg/Ti dual dopants in $LiNiO_2$.[12,17] Mg tends to homogeneously distribute throughout the individual $LiNiO_2$ primary particles, whereas Ti forms a gradient concentration distribution that is enriched at the surface.[12] The thermodynamics based density functional theory (DFT) calculations may predict what dopants are preferentially

enriched at the surface based on the energy difference between occupying the surface and in the bulk lattice.[14] However, theoretical calculations cannot account for the complex phase constituents at different stages of materials synthesis. Here we report that the dopant redistribution takes place long before the complete formation of the layered oxide phase, in sharp contrast to the models adopted by recent theoretical studies.[14,15]

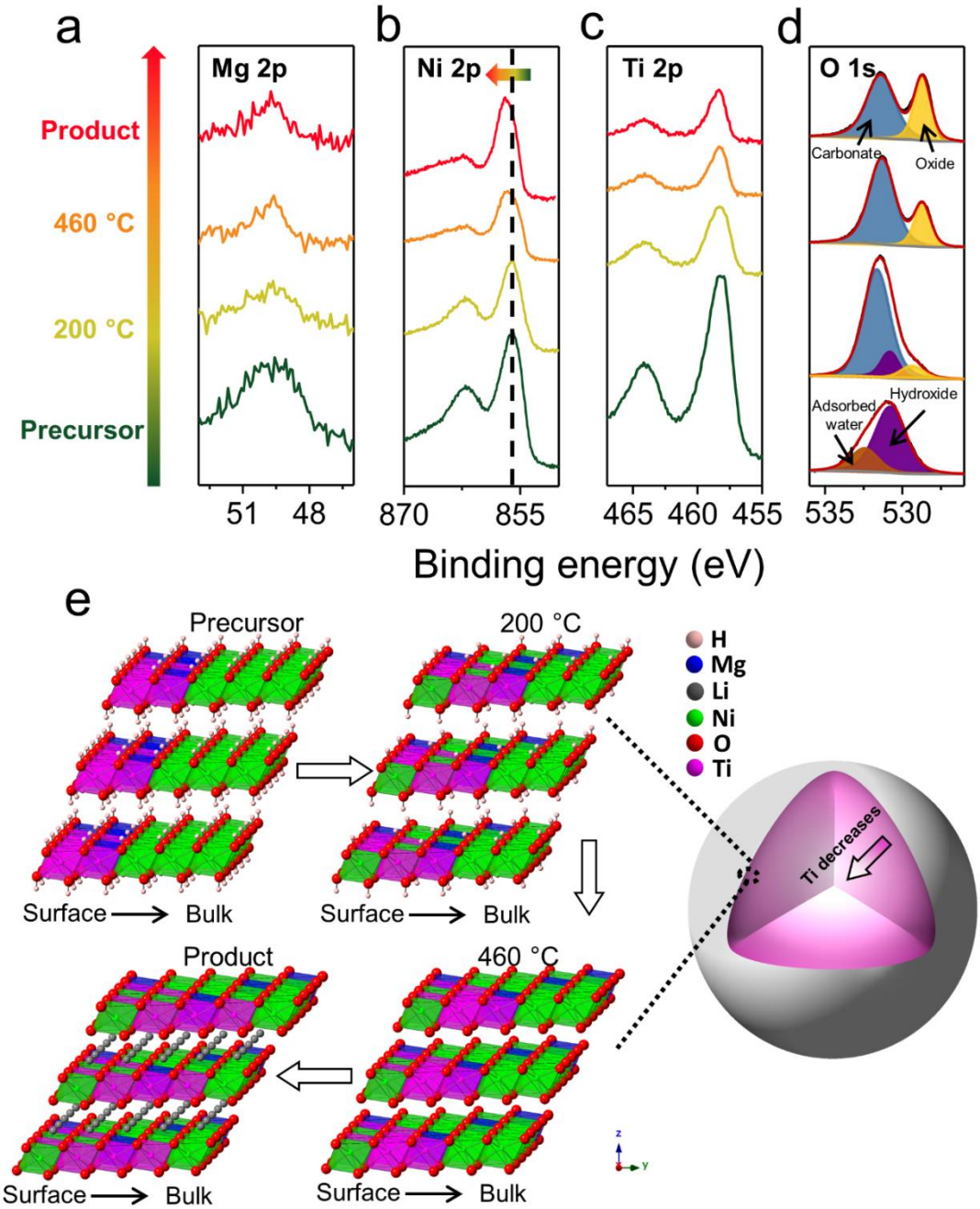

Figure 1. Element concentration changes at the surface upon calcination. a) Mg 2p, b) Ni 2p, c) Ti 2p, and d) O 1s XPS spectra of the samples at different stages of calcination, peak assignments are based on the references;[16, 17a] e) A scheme showing the dopant redistribution at the particle surface upon calcination. The number of different elements shown in the scheme does not indicate the exact elemental fraction but reflects the trend. Mg and Ti diffuse into the nickel hydroxide matrix during the early stage of calcination. Mg completes the redistribution at 200 °C, whereas Ti does not complete the redistribution even in the final product yielding a surface enriched Ti distribution.

We performed X-ray photoelectron spectroscopy (XPS) to understand the dopant redistribution at different stages of calcination. The irregular secondary particles are composed of numerous primary particles around hundreds of nanometers in size. The surface sensitive XPS can probe 3-6 nm into the particle surface and provide the chemical and electronic information of the particle surface.[34] The XPS binding energy calibration is based on the Mg 2p peak in this study (Figure 1a), as several studies have indicated that using C 1s for calibration is sometimes not robust.[35] The Ti oxidation state is relatively stable upon calcination (Figure 1c). As indicated by the O 1s spectra (Figure 1d**)**, the precursor is composed of chemisorbed/physisorbed water and metal hydroxide (Ni hydroxide predominantly). Upon heating to 200 °C, the adsorbed molecular water vanishes, and the metal hydroxide diminishes. Subsequently, metal oxide and carbonate start to grow (Figure 1d**)**. In the meantime, the elemental fractions of Ti and Mg at the surface decrease, which suggests the diffusion of dual dopants into the hydroxide matrix (Figure 1a,c, Table S1). The formation of carbonate species is usually inevitable in layered

oxide cathodes even with brief exposure to the ambient environment after calcination.[36,37] As the temperature increases to 460 °C, Ni at the surface is oxidized (Figure 1b). At 460 °C, no metal hydroxide is observed, and the concentration of metal oxide and carbonate at the surface increases and decreases, respectively (Figure S3, Supporting Information). The surface chemical composition is quantified using XPS (Table S1). The atomic concentration fraction of Ni: Mg: Ti changes from 80%: 5%: 15% (precursor) continuously to 90%: 3%: 7% (product). The scheme illustrates the diffusion of dopants during calcination (Figure 1e). In the precursor, both Mg and Ti are rich at the surface. Upon the early calcination, Ti and Mg diffuse from the surface into the bulk of the metal hydroxide matrix. Beyond 200 °C, Mg concentration at the surface becomes relatively stable and close to the value in the final product of Mg/Ti-LNO (2% Mg), which suggests Mg diffusion is almost completed at 200 °C. Although Ti concentration at the surface is also nearly stable, Ti continues diffusing in the bulk within 200-300 °C (Figure 4 d-e, discussed later). In the product, Mg distributes uniformly from the bulk to the surface while Ti remains rich at the surface, which is consistent with the elemental mapping.[12] The inward dopant diffusion is also consistent with what the literature reported. For example, calcining surface-coated cathode materials may facilitate the inward diffusion of the coating species (e.g., Zr^{4+},[38] Ti^{4+},[39] Ta^{5+},[40] Na^{+}[41]), potentially forming hybrid coating and doping, which is an effective strategy to modify the surface structure of Ni-rich layered cathodes and thus enhance the cycling stability.[42] It was predicted through computational methods that different dopants can have varied surface segregation tendencies thermodynamically depending on the surface segregation energy.[14] Our experimental results have shown that the dopant diffusion and redistribution are largely dependent on the initial distribution and the

subsequent calcination. The Mg/Ti dual dopants can diffuse from the surface into the bulk of cathode particles at the early stage of calcination, prior to the complete formation of the layered oxide (Figure 5a, discussed later). In addition, Mg completes redistribution ahead of Ti due to its kinetic advantage, potentially resulting from the weaker electrostatic interaction with the oxygen framework, and thus a favorable Mg ion diffusion coefficient. In addition to the pre-doped mixed metal hydroxide, mixing the cathode active materials with dopant-containing species, such as ZrO_2, followed by different calcination conditions may also give rise to different dopant distributions. Our analysis potentially has broad applicability because adding dopants in the precursor synthesis represents one of the most common methods to introduce dopants in the final oxides.

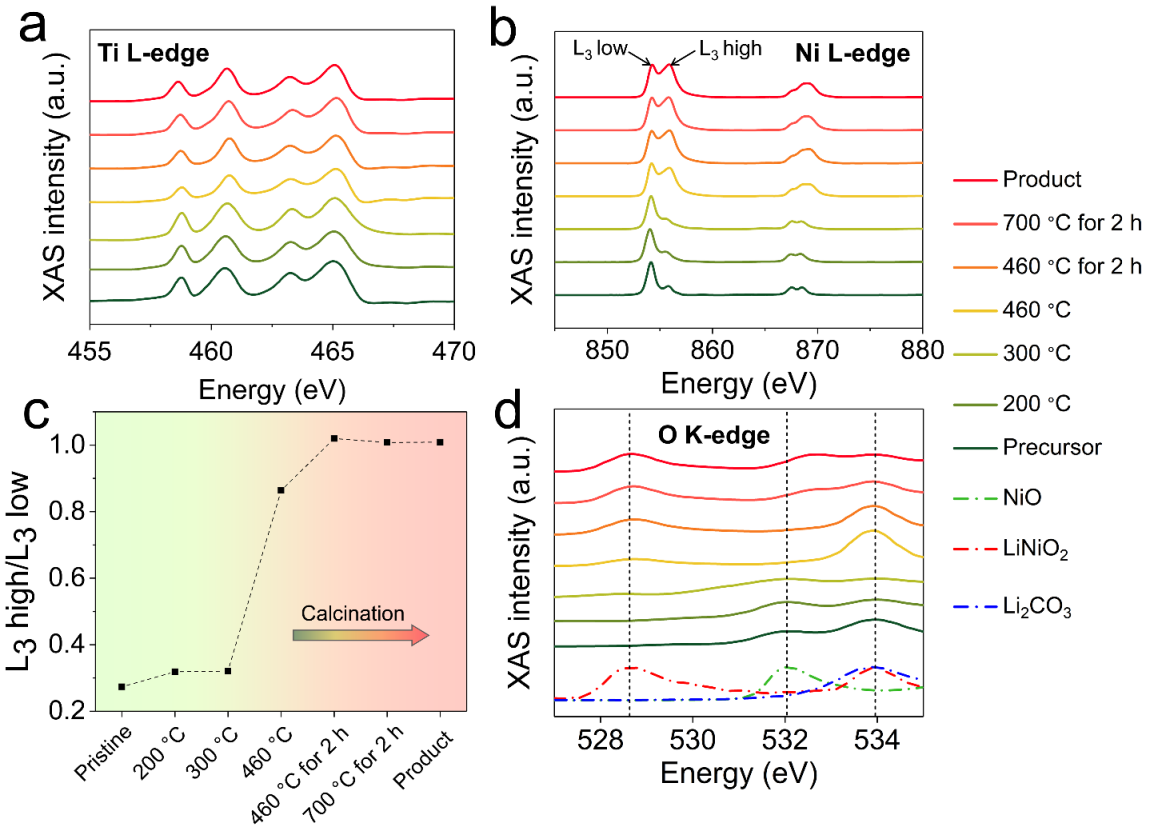

Figure 2. Electronic and chemical structure changes upon calcination. a) Ti L-edge b) Ni L-edge soft XAS spectra in the total electron yield (TEY) mode at different stages of

calcination; c) The values of L_3 high/L_3 low at different stages of calcination. The dashed line shows the trend upon calcination. d) O K-edge soft XAS spectra at different stages of calcination. The standard spectra are remade with the permission from ref.[43]

Next, we investigate how the global and local phase and chemical transformations take place during the calcination. A typical precursor-to-layered oxide calcination involves the mass transport across three different phases, namely, mixed metal hydroxides precursor, Li precursor (e.g., LiOH, Li_2CO_3), and O_2.[44] The uniformity of the three-phase interaction determines the phase and chemical homogeneity of the resulting layered oxides. Another unique aspect of the layered oxide formation is the synchronous changes of electronic and crystal structures, which allows us to use electronic structure as the proxy for the phase transformation during calcination.[21] The electronic structure can be studied using surface-sensitive and ensemble-averaged soft X-ray absorption spectroscopy (XAS), bulk sensitive and ensemble-averaged hard XAS as well as spatially resolved, 3D X-ray spectroscopic tomography. The combination of these techniques can non-destructively probe phase and chemical transformations covering nearly all relevant length scales in cathode particles. First, we performed soft XAS in the total electron yield (TEY) mode, which can probe up to 10 nm into the particle surface.[45] In Mg/Ti-LNO, Ti remains at the tetravalent state upon calcination (Figure 2a), consistent with the XPS result (Figure 1c). Ni L-edge spectra show an increasing intensity ratio between the high energy shoulder and low energy shoulder (L_3 high/L_3 low) at the L_3-edge, revealing the oxidation of Ni at the surface upon calcination (Figure 2b and 2c). The Ni surface oxidation is consistent with the XPS results (Figure 1b). Ni is at a relatively low oxidation state in the precursor and

remains at the low oxidation states during the early stage of calcination (< 300 °C). As the temperature increases to 460 °C when LiOH starts to melt, significant Ni oxidation at the surface is observed, indicated by a much higher L_3 high/L_3 low ratio.[46] The oxidation state of Ni continues to increase and becomes relatively stable after calcination at 460 °C for two hours, which is shown in the L_3 high/L_3 low trend (Figure 2c). Above 460 °C, there is no noticeable change in the Ni oxidation state, indicating that the surface Ni has completed oxidation much before the complete formation of the bulk layered oxide phase (Figure 2c and Figure 5a). To further demonstrate the Ni oxidation state change, the spectra of the intermediate calcination states are expressed as a linear combination of the spectra of the precursor (state 1) and the final layered oxide product (state 2) (Figure S4, Supporting Information). The result shows the continuous Ni oxidation before calcining at the 460 °C holding stage, which is revealed by less low oxidation state component (state 1) and more high oxidation state component (state 2) upon calcination. This result is in good agreement with the trend of the L_3 high/L_3 low change in Figure 2c. The O K-edge soft XAS is sensitive to the local environment change of coordinated transition metals. Specifically, the pre-edge region (< 535 eV) of O K-edge soft XAS spectra provides absorption features for the TM 3d-O 2p hybridization.[47] As shown in Figure 2d, the Ni^{3+} 3d-O 2p hybridization is strengthened while the Ni^{2+} 3d-O 2p hybridization is weakened upon calcination. The appearance of the Ni^{3+} 3d-O 2p hybridization at 460 °C is consistent with the Ni oxidation state change observed in the Ni L-edge spectra (Figure 2b). The peak at ~534 eV is attributed to carbonate species, which is also identified by XPS (Figure 1d).[43] These surface-sensitive characterizations suggest Ni oxidation at the surface completes at a

relatively low temperature (460 °C), without being interfered much by the subsequent phase transformation and local structure change at higher temperatures.

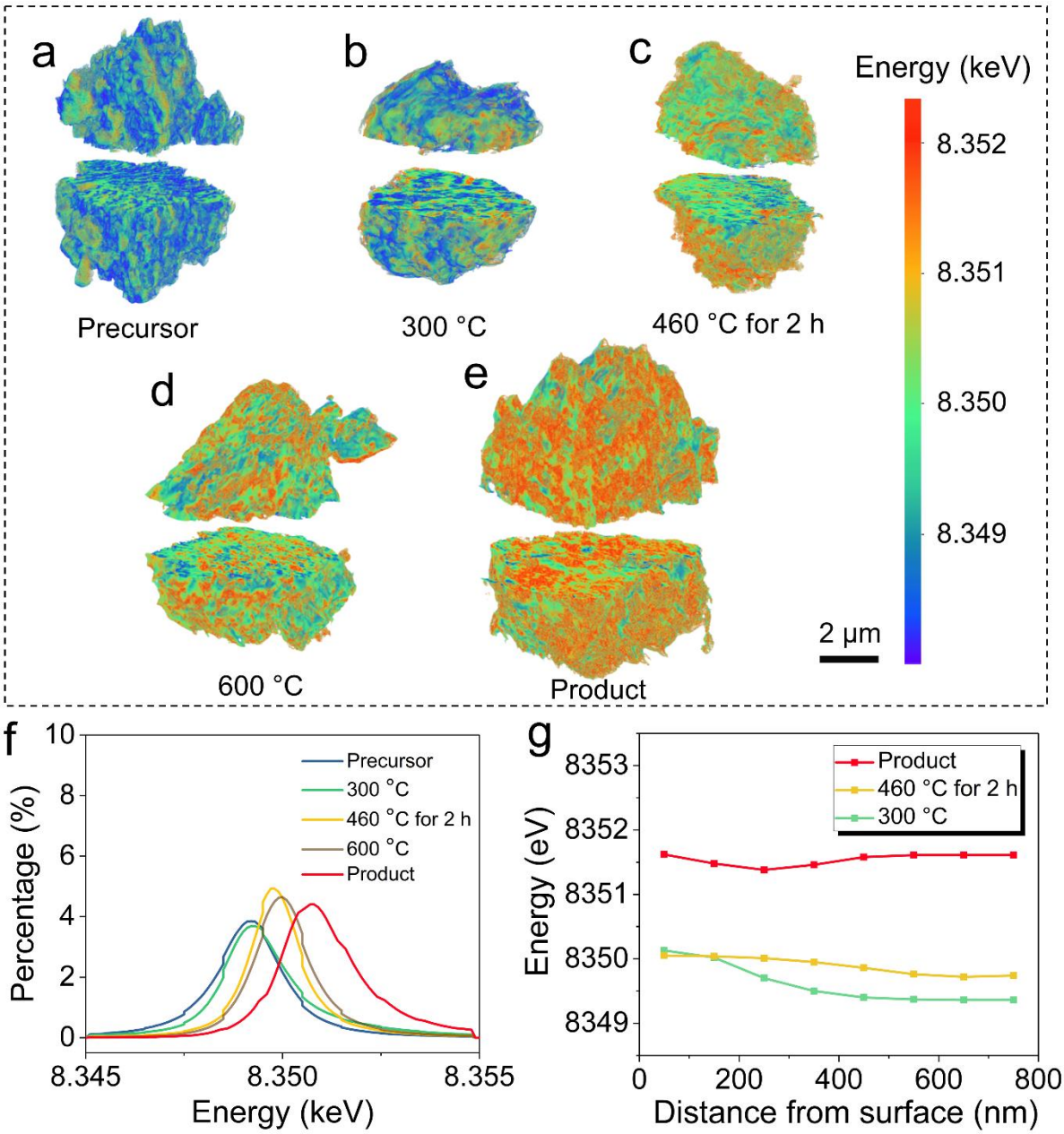

Figure 3. Electronic and chemical structure changes at particle scale upon calcination. Ni K-edge 3D TXM results for the samples a) at the pristine state; b) calcined at 300 °C; c) calcined at 460 °C for 2 hours; d) calcined at 600 °C; e) complete calcination; f) The Ni K-

edge white-line energy distribution of the samples at different stages of calcination; g) Ni K-edge white-line energy at different stages of calcination as a function of the distance from the particle surface. The energy is the mean value of the Ni K-edge white-line energy of all voxels with the same distance from the surface in the particle. Ni oxidation at the surface completes at 460°C. The Ni oxidation heterogeneity along the radial direction decreases upon calcination and becomes insignificant when calcination completes, while the mosaic-like heterogeneity remains throughout the whole calcination process.

To complement soft XAS at different length scales, we further performed 3D Ni K-edge full-field transmission X-ray microscopy (TXM) at different stages of calcination to visualize the Ni oxidation state evolution and distribution at the secondary particle scale (Figure 3a-e). The white-line energy continuously shifts from ~8.349 keV to ~8.351 keV upon calcination (Figure 3a-e), which indicates the continuous oxidation of Ni. Specifically, the dramatic change of Ni oxidation state takes place from 300 °C to 460 °C, and from 600 °C to the product. Therefore, the Ni oxidation behavior at the single particle level is different from that at the particle surface (Figure 2b). We notice that at each calcination stage there is a certain breadth of the white-line energy distribution, which signifies the heterogeneous precursor-to-layered oxide transformation at the mesoscale (Figure 3f). The mixed metal hydroxide particles exhibit a porous structure (Figure S5, Supporting Information). We hypothesize that the regions in the vicinity of pores complete the oxidation reaction earlier due to the rapid reaction with LiOH infiltrating through the pores. This hypothesis may be validated through a systematic study to establish the relationship between morphological characteristics (e.g., porosity) and local phase transformation, using the experimental approaches demonstrated in our recent studies.[24,25]

To further demonstrate the heterogeneity of Ni oxidation in secondary particles, we plot Ni K-edge white-line energy as a function of the distance from the particle surface at several calcination stages (Figure 3g). Mathematically, this is done by averaging the white-line energy for each shell at different distances from the particle surface (Figure S6, Supporting Information). At 300 °C, Ni oxidation shows a larger variation between the near-surface region (~500 nm from the surface) and the bulk region, i.e., radial heterogeneity. When the temperature increases to 460 °C, the energy difference in the radial direction of the cathode particle becomes smaller. As the temperature further increases to the completion of the calcination, the radial heterogeneity becomes insignificant. However, the mosaic-like heterogeneity is still present after calcination at 700 °C for five hours (Figure 3e). This observation is consistent with our recent studies on the pristine commercial NMC811 materials, where a discernible degree of Ni oxidation state heterogeneity was reported.[25,48] To verify the validity of 3D TXM results, we further performed 2D Ni K-edge TXM on a larger number of particles (Figure S6, Supporting Information) to statistically confirm the mosaic-like heterogeneity of Ni oxidation states in secondary particles. Overall, the oxidation pattern revealed by 2D Ni K-edge TXM is similar to that of 3D TXM (Figure S7, Supporting Information). It should be highlighted that the charge heterogeneity inside the cathode particles is not merely observed in the cathode formation process, it is also a major issue in the battery cycling, which can accumulate mechanical stress and lead to chemomechanical breakdown of battery particles.[49] In summary, the Ni oxidation in secondary particles takes place predominantly from 300 °C to the 460 °C holding stage, and from 600 °C to the final layered oxide product. Furthermore, we observe mosaic-like heterogeneity of Ni oxidation states throughout the calcination. However, the radial

heterogeneity dominates the early stage of calcination and becomes insignificant after the calcination is completed. Comparing soft XAS and TXM results, we report that the Ni oxidation behavior exhibits dependence on the geometric location in secondary particles, e.g., near-surface region *versus* bulk region.

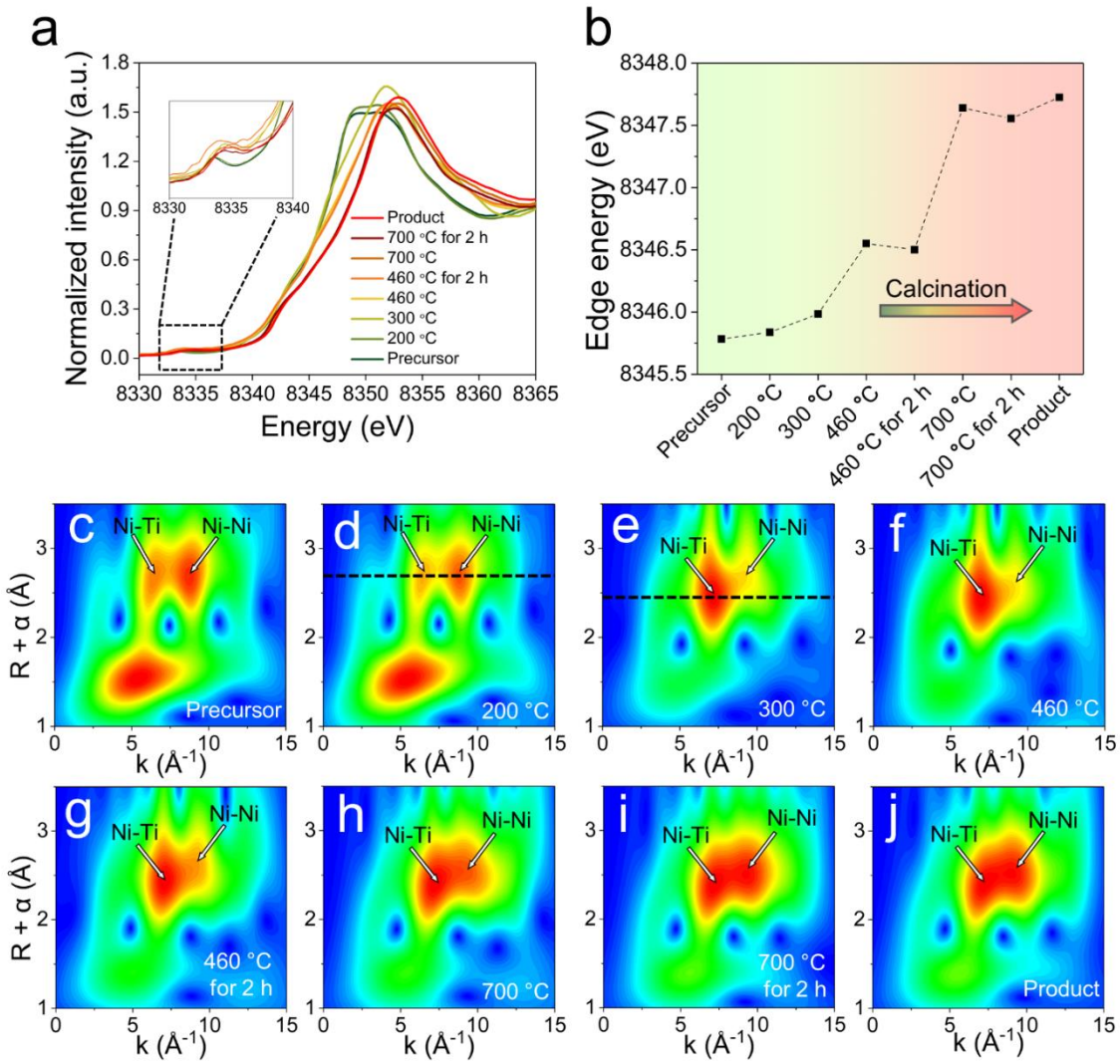

Figure 4. Ensemble-averaged characterization of electronic structure and local environment upon calcination. a) Ni K-edge XANES spectra at different stages of calcination; b) Evolution of edge energy calculated from the Ni K-edge XANES spectra, where the dashed line shows the trend upon calcination; Wavelet transformation of Ni K-

edge EXAFS for the samples c) at the pristine state; d) calcined at 200 °C; e) calcined at 300 °C; f) calcined at 460 °C; g) calcined at 460 °C for 2 h; h) calcined at 700 °C; i) calcined at 700 °C for 2 h; j) complete calcination. Ni oxidation in the bulk completes at 700 °C, which is later than that at the surface (460 °C, Figure 2b). Ti diffuses into the Ni hydroxide matrix predominantly between 200 °C and 300 °C, which is delayed compared to the surface probed by XPS (< 200 °C).

The above surface-sensitive XPS/XAS and 3D single-particle TXM measurements collectively provide depth-profiled analysis for Mg/Ti-LNO at different stages of calcination. The battery performance is also determined by the ensemble-averaged, collective behavior of many electrode particles. Therefore, probing the bulk-sensitive, ensemble-averaged electronic and chemical environments can not only improve the statistical relevance of the analytical results but also, more importantly, provide atomistic insights into the local coordination changes. Here, we further performed Ni K-edge X-ray absorption near edge structure (XANES) and extended X-ray absorption fine structure (EXAFS) to investigate the electronic structure and chemical environment. As shown in Figure 4a, the edge shifting toward higher energy implies the Ni oxidation. The overall trend of edge energy shift shows that the Ni oxidation in the bulk is not completed at 460 °C, and the prominent Ni oxidation is observed from 460 °C to 700 °C (Figure 4b). This observation, based on many particles, is consistent with the TXM results discussed above (Figure 3). To quantify the Ni oxidation state evolution, a calibration curve composed of estimated oxidation state as a function of edge energy was made based on standard spectra (Figure S8, Supporting Information). The Ni oxidation state estimated from the calibration

curve implies the Ni oxidation from the divalent state to the trivalent state upon calcination (Table S2). Furthermore, the same linear combination method used in soft XAS analysis is applied to analyze the Ni oxidation state change in the bulk XANES (Figure S9, Supporting Information). The result supports the trend in Figure 4b that an apparent Ni oxidation is observed from 460 °C to 700 °C. When the temperature reaches 700 °C, Ni stays at a relatively high oxidation state even after the calcination is extended to 5 hours. In comparison with Ni L-edge soft XAS spectra (Figure 2b), Ni shows delayed oxidation in the bulk during calcination. The top surface of the precursor is directly exposed to the O_2 atmosphere and in contact with LiOH, and thus the oxidation reaction is kinetically more favorable at the surface. The TXM result also confirms that the near-surface regions (~500 nm) are more oxidized at the same stage of calcination (Figure 3g). As an ensemble-averaged technique, XANES confirms the trend of Ni oxidation with statistical relevance, which is consistent with the 3D TXM at the single particle scale. Furthermore, the bulk-sensitive XANES well complements the surface-sensitive soft XAS and suggests the delayed Ni oxidation in the bulk.

To comprehensively understand the cathode formation regarding the correlation between electronic structure evolution and elemental diffusion, we further performed EXAFS to explore the local coordination change at the atomistic scale. The Fourier-transformed Ni K-edge EXAFS indicates that the precursor shows the characteristic of $Ni(OH)_2$, while the product shows the characteristic of $LiNiO_2$ (Figure S10, Supporting Information). An apparent shift of both Ni-O and Ni-metal (M) shells to lower R values is observed at 300 °C, indicating a decrease in the Ni-O and Ni-M interatomic distances. This decrease is associated with the dehydration of the $Ni(OH)_2$ below 300 °C. The dehydration

reaction produces a NiO-based rocksalt phase that has shorter Ni-O and Ni-M interatomic distances.[50] Next, we performed Ni K-edge EXAFS wavelet transform (WT) analysis to decompose the k-space and R-space to separate the backscattering atoms that are overlapped in the R-space.[51,52] As shown in Figure 4c-j, the WT maximum referring to Ni-metal in the second shell at ~2.5 Å (R+α) splits in the k-space. The left maximum at ~6 $Å^{-1}$ (k) is assigned to Ni-Ti scattering and the right maximum at ~8 $Å^{-1}$ (k) is assigned to Ni-Ni scattering.[53,54] The decrease of R distance for Ni-Ti scattering from 200 °C (Figure 4d) to 300 °C (Figure 4e) implies the decreasing Ni-Ti interatomic distance and thus the further Ti^{4+} diffusion into the matrix. The Ni-Ti interatomic distance remains nearly unchanged after 300 °C (Figure 4f-j). These results and XPS results collectively suggest that Ti diffusion at the surface is almost completed by 200 °C, but Ti continues diffusing in the bulk between 200 °C and 300 °C (Figure 1c and Table S1). In summary, the XANES and EXAFS results demonstrate that Ni oxidation is delayed in the bulk ensemble and is not completed until 700 °C, and that the Ti dopant diffuses into the matrix predominantly between 200 °C and 300 °C. Therefore, our results collectively suggest tailoring the dopant distribution can be best achieved at the early stage of the calcination during the dehydration of the mixed metal hydroxides. It is worth noting that different dopants may have varied redistribution behavior, depending on the dopant properties and dopant initial distribution in the precursor.

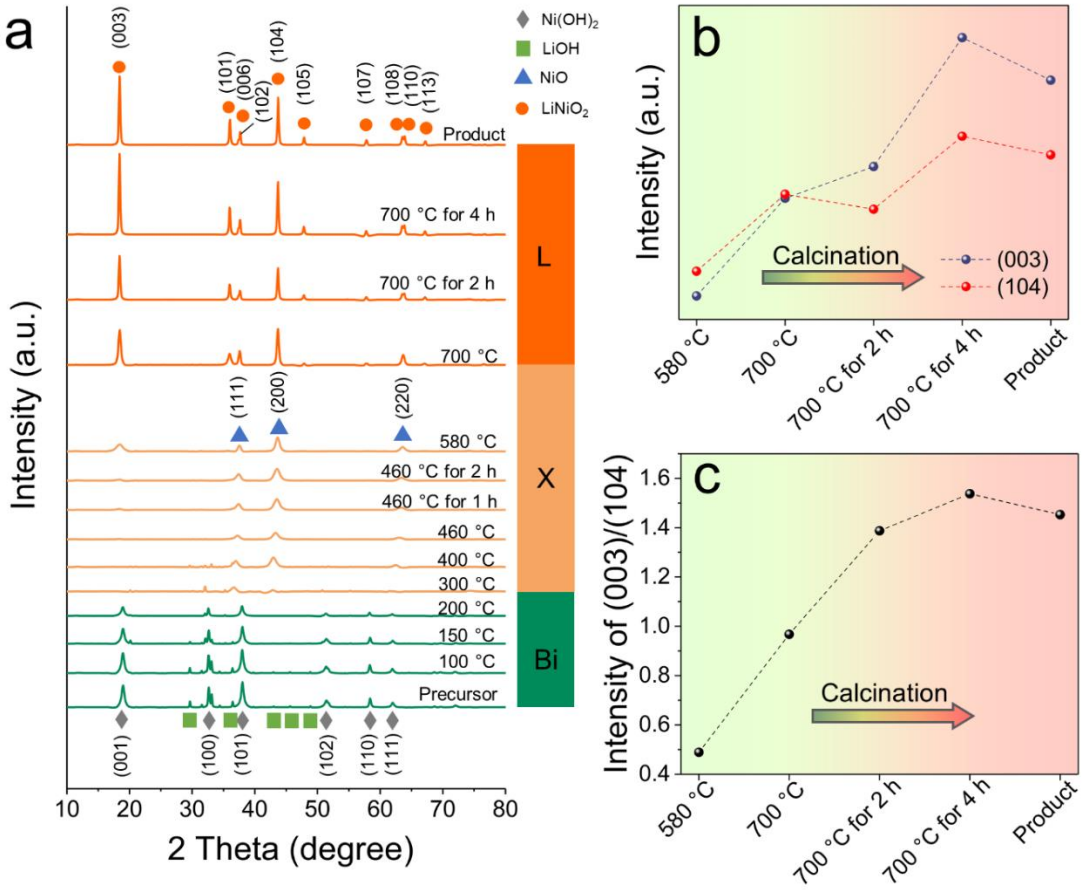

Figure 5. Global structural change and phase evolution upon calcination. a) XRD patterns at different stages of calcination; b) Evolution of the normalized intensity of (003) peak and (104) peak and c) the intensity ratio of (003) peak to (104) peak at different stages of calcination, where the dashed line shows the trend upon calcination. Phase transformation takes place from the mixed hydroxide bi-phase to the layered oxide L phase through an intermediate X phase, with Li intercalation and increasing crystallinity upon calcination.

The multiscale chemical transformations, especially the local coordination changes, collectively determine the global phase transformations that can be probed by XRD. Furthermore, XRD measurements at different stages of calcination can be utilized to

evaluate the statistical representativeness of the XPS, XAS, and TXM measurements. We performed synchrotron XRD at different stages of calcination to study the structural change and phase transformation (Figure 5a). The mixed metal hydroxide and LiOH are thoroughly mixed to prepare the precursor before calcination. Ni hydroxide predominates the metal hydroxide and the effect of Mg/Ti dopants on the diffraction pattern is trivial due to the low content. A mixture of LiOH phase and $Ni(OH)_2$ phase is observed from the diffraction peaks. As the temperature reaches 300 °C, the bi-phase gradually transforms to an intermediate phase X, where $Ni(OH)_2$ and LiOH characteristic peaks diminish and the rock-salt NiO-like characteristic peaks appear. When the temperature reaches 700 °C, several diffraction peaks of $LiNiO_2$ start to grow, which indicates the formation of a new phase named as L. As the temperature is held at 700 °C for a longer time, the intensity of $LiNiO_2$ diffraction peaks further increases, and the peaks become narrower due to the overall increased crystallinity and particle growth. The appearance of the (003) peak implies the formation of the layered structure. The overall increased intensity of (003) and (104) peaks and the (003)/(104) intensity ratio reveal less Ni/Li cation mixing and a better-defined layered structure (Figure 5b and 5c). Moreover, the (220) peak in the rock-salt NiO converts to (108) peak and (110) peak in the layered $LiNiO_2$ also suggests the formation of the layered structure.[55] The neutron diffraction patterns imply the co-existence of three phases at high temperature, i.e., layered $(Li_{1-x}Ni_x)(Ni_{0.96-x}Li_xMg_{0.02}Ti_{0.02})O_2$ phase, monoclinic Li rich phase and Li_2CO_3 phase (Figure 6).[56,57] From 600 °C to the 700 °C holding stage, the fraction of the layered oxide phase increases while the monoclinic Li rich phase diminishes and almost disappears at 700 °C (Table S3). Only a small degree of Li/Ni cation mixing is observed at 700 °C (Table S3), which is consistent with our earlier

publication.[5a] Both Mg and Ti remain on the Ni site after 600 °C until the formation of the cathode product (Figure 6). More detailed neutron diffraction refinement results are shown in Figure S11. Our results are consistent with the *in situ* XRD study of the $LiNiO_2$ formation reported by Bianchini *et al.*[29] Together with our XPS and XAS results, the XRD result further confirms that the metal hydroxide phase is still present at the temperature (below 300 °C) when Mg/Ti dopants diffuse into the matrix. To rationalize the dopant diffusion in the nickel hydroxide matrix, we hypothesize that the larger Ni-O and Ni-M distances in the metal hydroxide (larger lattice volume) result in lower energy barriers for dopants to diffuse (Figure 4c).[58] In addition, the co-dehydration of the mixed metal hydroxides can facilitate dopant diffusion into the Ni-O coordination environment (Figure S12, Supporting Information). In brief, phase transformation takes place from the mixed hydroxide bi-phase to the layered L phase through an intermediate metal oxide-like X phase, and dopants diffuse into the metal hydroxide matrix below 300 °C.

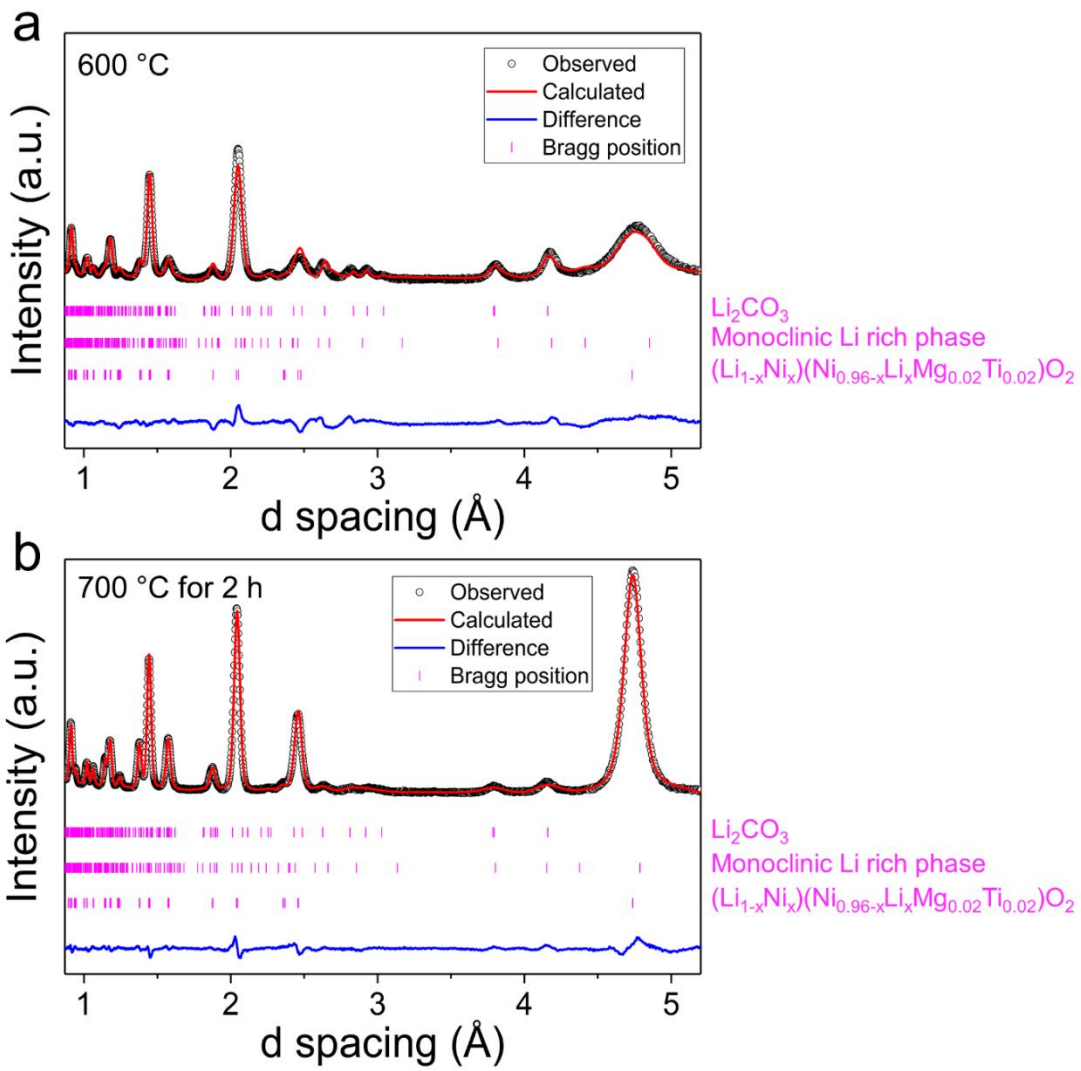

Figure 6. Neutron diffraction patterns and Rietveld refinement at a) 600 °C, and b) 700 °C for 2 h. R_{wp} for a) is 5.38% and R_{wp} for b) is 4.36%. More layered oxide phase is identified, and Li/Ni cation mixing is reduced from 600 °C to the 700 °C holding stage.

Based on the phase transformations during calcination identified by XRD, the reaction mechanism is proposed as the following two-step reactions (equation (1) and equation (2)) and overall reaction (equation (3), the potential presence of Li_2O and

intermediate lithium nickel oxide with varying compositions are not included for simplicity):

$$Ni(OH)_2 \rightarrow NiO + H_2O \quad (1)$$

$$NiO + LiOH + \frac{1}{4} O_2 \rightarrow LiNiO_2 + \frac{1}{2} H_2O \quad (2)$$

$$Ni(OH)_2 + LiOH + \frac{1}{4} O_2 \rightarrow LiNiO_2 + \frac{3}{2} H_2O \quad (3)$$

To further verify the reaction mechanism, we performed thermogravimetric analysis (TGA) (Figure S13, Supporting Information). The 8.37% weight loss below 100 °C refers to the volatilization of moisture.[59] The weight loss above 100 °C, mostly due to metal hydroxide dehydration and lithiation, is 15.07%, which is slightly lower than the theoretical value of 16.29% (equation 3). This can potentially be attributed to the inactive residuals in the sample such as Li_2CO_3, which does not participate in the reaction and thereby has no contribution to the reaction weight loss. The temperature range for the reaction is consistent with the appearance of the NiO-like phase at 300 °C (Figure 5a). To visualize the morphology evolution and the reaction that takes place during calcination, scanning electron microscopy (SEM) is performed (Figure S14a-f, Supporting Information). The secondary particles in the precursor consist of needle-like primary particles (Figure S14a, Supporting Information**)**, which evolves into gravel-like morphology in the layered oxide product (Figure S14f, Supporting Information). The lighter contrast in the highlighted regions in Figure S14c-d is partially mixed with the secondary particle. The energy dispersive X-ray spectroscopy (EDS) measurements show that Ni is abundant in the secondary particle but is hardly detected in the lighter contrast regions (Figure S15a-d, Supporting Information). We conjecture that the lighter contrast regions are attributed to the recrystallized LiOH during the cooling. The distribution of the LiOH is highly

heterogeneous, which potentially gives rise to the heterogeneous phase propagation identified by TXM (Figure 3). In summary, XRD and TGA results collectively confirm the two-step reaction mechanism, and the contact homogeneity of reactants can potentially determine the reaction homogeneity and phase distribution in cathode particles.

2.5. Discussion

Manipulating doping chemistry and the microstructure of cathodes are two of the most popular strategies adopted by the cathode community to enhance the battery performance. However, without a systematic investigation of the cathode synthesis, the fundamental understanding of dopant distribution and local environment evolution during cathode formation is limited. With a range of synchrotron diagnostic tools and complementary characterizations, we have probed the dopant redistribution, electronic and chemical structure evolution, and phase transformations at multiple length scales during the synthesis of the high energy Co-free layered cathode. We observed that the dopant redistribution pattern is largely dependent on the dopant properties, the initial distribution in the mixed metal hydroxides precursor, and the following calcination protocol. In addition, the local structure change and phase transformations are heterogeneous, depending on the geometric location in secondary particles and different calcination stages. Specifically, we have made the following observations and conclusions:

I. Ti and Mg dopants diffuse in the Ni hydroxide matrix at the early stage of calcination (below 300 °C), much before the formation of the layered oxide phase. Mg completes redistribution before Ti. Mg distribution is relatively uniform, while Ti is enriched at the particle surface.

II. Oxidation reaction is kinetically more favorable at the surface compared with that in the bulk. Ni oxidation at the surface completes at 460 °C before the bulk layered oxide phase forms, whereas we observed drastic Ni oxidation in the bulk from 300 °C to the 460 °C holding stage, and from 600 °C to the formation of layered oxide product.

III. At the mesoscale, the radial heterogeneity of electronic and chemical structure change decreases upon calcination and becomes insignificant after calcination completes. However, we still observe the mosaic-like heterogeneity in the product, similar to commercial Ni-rich NMC materials.

IV. Global phase transformation takes place from the mixed hydroxide phase to the intermediate metal oxide-like phase at around 300 °C, and the intermediate phase transforms to the layered oxide phase at about 700 °C. Higher crystallinity and less Li/Ni cation mixing are observed with a longer duration at 700 °C.

This study not only enriches the understanding of layered cathode formation at multiple length scales and potentially guides the high-energy cathode design such as dopant distribution and 3D chemical homogeneity, but also provides a systematic protocol that can be readily applied to explore the formation of other energy materials.

2.6. Acknowledgements

The work is supported by the U.S. Department of Energy's Office of Energy Efficiency and Renewable Energy (EERE) under the award number: DE-EE0008444. The use of the Stanford Synchrotron Radiation Lightsource, SLAC National Accelerator Laboratory, is supported by the U.S. Department of Energy, Office of Science, Office of Basic Energy Sciences under Contract No. DE-AC02-76SF00515. This research used

resources of the Advanced Photon Source, a U.S. Department of Energy (DOE) Office of Science User Facility operated for the DOE Office of Science by Argonne National Laboratory under Contract No. DE-AC02-06CH11357. The research used 18-ID of the National Synchrotron Light Source II, a U.S. Department of Energy (DOE) Office of Science User Facility operated for the DOE Office of Science by Brookhaven National Laboratory under Contract No. DE-SC0012704. The use of the Spallation Neutron Source at Oak Ridge National Laboratory is supported by the U.S. Department of Energy, Office of Science, Office of Basic Energy Sciences under Contract No. DE-AC05-00OR22725. This work was performed in part at the Surface Analysis Laboratory in Department of Chemistry at Virginia Tech, which is supported by the National Science Foundation under Grant No. CHE-1531834. This research was partially supported by Virginia Tech's Institute for Critical Technology and Applied Science through instruments provided by the Nanoscale Characterization and Fabrication Laboratory (NCFL). The authors acknowledge the assistance of Dr. Thomas W. Staley on the TGA experiment. The authors also acknowledge the assistance of Dr. Yijin Liu, Dr. Xu Feng and Dr. Chunguang Kuai on the data analysis. Z.Y. and F.L. thank Dr. Yijin Liu's research group for the initial proof-of-concept TXM studies. This report was prepared as an account of work sponsored by an agency of the United States Government. Neither the United States Government nor any agency thereof, nor any of their employees, makes any warranty, express or implied, or assumes any legal liability or responsibility for the accuracy, completeness, or usefulness of any information, apparatus, product, or process disclosed, or represents that its use would not infringe privately owned rights. Reference herein to any specific commercial product, process, or service by trade name, trademark, manufacturer, or otherwise does not

necessarily constitute or imply its endorsement, recommendation, or favoring by the United States Government or any agency thereof. The views and opinions of authors expressed herein do not necessarily state or reflect those of the United States Government or any agency thereof.

2.7. References

(1) Schipper, F.; Erickson, E. M.; Erk, C.; Shin, J.-Y.; Chesneau, F. F.; Aurbach, D. Review—Recent Advances and Remaining Challenges for Lithium Ion Battery Cathodes. *J. Electrochem. Soc.* **2017**, *164* (1), A6220–A6228.

(2) Xu, J.; Lin, F.; Doeff, M. M.; Tong, W. A Review of Ni-Based Layered Oxides for Rechargeable Li-Ion Batteries. *J. Mater. Chem. A* **2017**, *5* (3), 874–901.

(3) Liu, W.; Oh, P.; Liu, X.; Lee, M.-J.; Cho, W.; Chae, S.; Kim, Y.; Cho, J. Nickel-Rich Layered Lithium Transition-Metal Oxide for High-Energy Lithium-Ion Batteries. *Angew. Chemie Int. Ed.* **2015**, *54* (15), 4440–4457.

(4) Bianchini, M.; Roca-Ayats, M.; Hartmann, P.; Brezesinski, T.; Janek, J. There and Back Again-The Journey of $LiNiO_2$ as a Cathode Active Material. *Angew. Chemie Int. Ed.* **2019**, *58* (31), 10434–10458.

(5) Gover, R. K. B.; Kanno, R.; Mitchell, B. J.; Yonemura, M.; Kawamoto, Y. Effects of Sintering Temperature on the Structure of the Layered Phase $Li_x(Ni_{0.8}Co_{0.2})O_2$. *J. Electrochem. Soc.* **2000**, *147* (11), 4045.

(6) Zhao, J.; Zhang, W.; Huq, A.; Misture, S. T.; Zhang, B.; Guo, S.; Wu, L.; Zhu, Y.; Chen, Z.; Amine, K.; Pan, F.; Bai, J.; Wang, F. In Situ Probing and Synthetic Control of Cationic Ordering in Ni-Rich Layered Oxide Cathodes. *Adv. Energy Mater.* **2017**, *7* (3), 1601266.

(7) Shim, J. H.; Kim, C. Y.; Cho, S. W.; Missiul, A.; Kim, J. K.; Ahn, Y. J.; Lee, S. Effects of Heat-Treatment Atmosphere on Electrochemical Performances of Ni-Rich Mixed-Metal Oxide ($LiNi_{0.80}Co_{0.15}Mn_{0.05}O_2$) as a Cathode Material for Lithium Ion Battery. *Electrochim. Acta* **2014**, *138*, 15–21.

(8) Qian, G.; Zhang, Y.; Li, L.; Zhang, R.; Xu, J.; Cheng, Z.; Xie, S.; Wang, H.; Rao, Q.; He, Y.; Shen, Y.; Chen, L.; Tang, M.; Ma, Z. F. Single-Crystal Nickel-Rich Layered-Oxide Battery Cathode Materials: Synthesis, Electrochemistry, and Intra-Granular Fracture. *Energy Storage Mater.* **2020**, *27*, 140–149.

(9) Arai, H.; Okada, S.; Sakurai, Y.; Yamaki, J. I. Electrochemical and Thermal Behavior of $LiNi_{1-z}M_zO_2$ (M = Co, Mn, Ti). *J. Electrochem. Soc.* **1997**, *144* (9), 3117–3125.

(10) Pouillerie, C.; Croguennec, L.; Biensan, P.; Willmann, P.; Delmas, C. Synthesis and Characterization of New $LiNi_{1-y}Mg_yO_2$ Positive Electrode Materials for Lithium-Ion Batteries. *J. Electrochem. Soc.* **2000**, *147* (6), 2061–2069.

(11) Kim, J.; Amine, K. The Effect of Tetravalent Titanium Substitution in $LiNi_{1-x}Ti_xO_2$ ($0.025 \leqslant x \leqslant 0.2$) System. *Electrochem. commun.* **2001**, *3* (2), 52–55.

(12) Mu, L.; Zhang, R.; Kan, W. H.; Zhang, Y.; Li, L.; Kuai, C.; Zydlewski, B.; Rahman, M. M.; Sun, C.-J. J.; Sainio, S.; Avdeev, M.; Nordlund, D.; Xin, H. L.; Lin, F. Dopant Distribution in Co-Free High-Energy Layered Cathode Materials. *Chem. Mater.* **2019**, *31* (23), 9769–9776.

(13) Mu, L.; Kan, W. H.; Kuai, C.; Yang, Z.; Li, L.; Sun, C. J.; Sainio, S.; Avdeev, M.; Nordlund, D.; Lin, F. Structural and Electrochemical Impacts of Mg/Mn Dual Dopants on the $LiNiO_2$ Cathode in Li-Metal Batteries. *ACS Appl. Mater. Interfaces*

2020, *12* (11), 12874–12882.

(14) Shin, Y.; Kan, W. H.; Aykol, M.; Papp, J. K.; McCloskey, B. D.; Chen, G.; Persson, K. A.; Hay Kan, W.; Aykol, M.; Papp, J. K.; McCloskey, B. D.; Chen, G.; Persson, K. A. Alleviating Oxygen Evolution from Li-Excess Oxide Materials through Theory-Guided Surface Protection. *Nat. Commun.* **2018**, *9* (1), 1–8.

(15) Kim, Y. Effects and Distribution of Zr Introduced in Ni-Based Cathode Material for Li-Ion Batteries. *Phys. Chem. Chem. Phys.* **2019**, *21* (23), 12505–12517.

(16) Lin, R.; Hu, E.; Liu, M.; Wang, Y.; Cheng, H.; Wu, J.; Zheng, J. C.; Wu, Q.; Bak, S.; Tong, X.; Zhang, R.; Yang, W.; Persson, K. A.; Yu, X.; Yang, X. Q.; Xin, H. L. Anomalous Metal Segregation in Lithium-Rich Material Provides Design Rules for Stable Cathode in Lithium-Ion Battery. *Nat. Commun.* **2019**, *10* (1).

(17) Kong, D.; Hu, J.; Chen, Z.; Song, K.; Li, C.; Weng, M.; Li, M.; Wang, R.; Liu, T.; Liu, J.; Zhang, M.; Xiao, Y.; Pan, F. Ti-Gradient Doping to Stabilize Layered Surface Structure for High Performance High-Ni Oxide Cathode of Li-Ion Battery. *Adv. Energy Mater.* **2019**, *9* (41), 1901756.

(18) Mehrer, H. *Diffusion in Solids: Fundamentals, Methods, Materials, Diffusion-Controlled Processes*; Springer Berlin Heidelberg, 2007.

(19) Li, J.; Doig, R.; Camardese, J.; Plucknett, K.; Dahn, J. R. Measurements of Interdiffusion Coefficients of Transition Metals in Layered Li–Ni–Mn–Co Oxide Core–Shell Materials during Sintering. *Chem. Mater.* **2015**, *27* (22), 7765–7773.

(20) Zhao, Y.; Li, J.; Dahn, J. R. Interdiffusion of Cations from Metal Oxide Surface Coatings into $LiCoO_2$ During Sintering. *Chem. Mater.* **2017**, *29* (12), 5239–5248.

(21) Mu, L.; Yuan, Q.; Tian, C.; Wei, C.; Zhang, K.; Liu, J.; Pianetta, P.; Doeff, M. M.;

Liu, Y.; Lin, F. Propagation Topography of Redox Phase Transformations in Heterogeneous Layered Oxide Cathode Materials. *Nat. Commun.* **2018**, *9* (1), 2810.

(22) Mu, L.; Lin, R.; Xu, R.; Han, L.; Xia, S.; Sokaras, D.; Steiner, J. D.; Weng, T.-C.; Nordlund, D.; Doeff, M. M.; Liu, Y.; Zhao, K.; Xin, H. L.; Lin, F. Oxygen Release Induced Chemomechanical Breakdown of Layered Cathode Materials. *Nano Lett.* **2018**, *18* (5), 3241–3249.

(23) Xu, Z.; Rahman, M. M.; Mu, L.; Liu, Y.; Lin, F. Chemomechanical Behaviors of Layered Cathode Materials in Alkali Metal Ion Batteries. *J. Mater. Chem. A*, **2018**, *6*, 21859-21884.

(24) Yang, Y.; Xu, R.; Zhang, K.; Lee, S.; Mu, L.; Liu, P.; Waters, C. K.; Spence, S.; Xu, Z.; Wei, C.; Kautz, D. J.; Yuan, Q.; Dong, Y.; Yu, Y.; Xiao, X.; Lee, H.; Pianetta, P.; Cloetens, P.; Lee, J.; Zhao, K.; Lin, F.; Liu, Y. Quantification of Heterogeneous Degradation in Li-Ion Batteries. *Adv. Energy Mater.* **2019**, *9* (25), 1900674.

(25) Xu, Z.; Jiang, Z.; Kuai, C.; Xu, R.; Qin, C.; Zhang, Y.; Rahman, M. M.; Wei, C.; Nordlund, D.; Sun, C. J.; Xiao, X.; Du, X. W.; Zhao, K.; Yan, P.; Liu, Y.; Lin, F. Charge Distribution Guided by Grain Crystallographic Orientations in Polycrystalline Battery Materials. *Nat. Commun.* **2020**, *11* (1), 1–9.

(26) Gent, W. E.; Li, Y.; Ahn, S.; Lim, J.; Liu, Y.; Wise, A. M.; Gopal, C. B.; Mueller, D. N.; Davis, R.; Weker, J. N.; Park, J.-H.; Doo, S.-K.; Chueh, W. C. Persistent State-of-Charge Heterogeneity in Relaxed, Partially Charged $Li_{1-x}Ni_{1/3}Co_{1/3}Mn_{1/3}O_2$ Secondary Particles. *Adv. Mater.* **2016**, *28* (31), 6631–6638.

(27) Zhang, Y.; Yang, Z.; Tian, C. Probing and Quantifying Cathode Charge Heterogeneity in Li Ion Batteries. *J. Mater. Chem. A*, **2019**,*7*, 23628-23661.

(28) Hua, W.; Wang, K.; Knapp, M.; Schwarz, B.; Wang, S.; Liu, H.; Lai, J.; Müller, M.; Schökel, A.; Missyul, A.; Ferreira Sanchez, D.; Guo, X.; Binder, J. R.; Xiong, J.; Indris, S.; Ehrenberg, H. Chemical and Structural Evolution during the Synthesis of Layered Li(Ni,Co,Mn)O_2 Oxides . *Chem. Mater.* **2020**, *32* (12), 4984–4997.

(29) Bianchini, M.; Fauth, F.; Hartmann, P.; Brezesinski, T.; Janek, J. An in Situ Structural Study on the Synthesis and Decomposition of $LiNiO_2$. *J. Mater. Chem. A* **2020**, *8* (4), 1808–1820.

(30) Gürsoy, D.; De Carlo, F.; Xiao, X.; Jacobsen, C. TomoPy: A Framework for the Analysis of Synchrotron Tomographic Data. *J. Synchrotron Radiat.* **2014**, *21* (5), 1188–1193.

(31) Neuefeind, J.; Feygenson, M.; Carruth, J.; Hoffmann, R.; Chipley, K. K. The Nanoscale Ordered MAterials Diffractometer NOMAD at the Spallation Neutron Source SNS. *Nucl. Instruments Methods Phys. Res. Sect. B Beam Interact. with Mater. Atoms* **2012**, *287*, 68–75.

(32) Calder, S.; An, K.; Boehler, R.; Dela Cruz, C. R.; Frontzek, M. D.; Guthrie, M.; Haberl, B.; Huq, A.; Kimber, S. A. J.; Liu, J.; Molaison, J. J.; Neuefeind, J.; Page, K.; Dos Santos, A. M.; Taddei, K. M.; Tulk, C.; Tucker, M. G. A Suite-Level Review of the Neutron Powder Diffraction Instruments at Oak Ridge National Laboratory. *Review of Scientific Instruments* **2018**, 92, 92701.

(33) Toby, B. H. EXPGUI, a Graphical User Interface for GSAS. *J. Appl. Crystallogr.* **2001**, *34* (2), 210–213.

(34) Seah, M. P.; Dench, W. A. Quantitative Electron Spectroscopy of Surfaces: A Standard Data Base for Electron Inelastic Mean Free Paths in Solids. *Surf. Interface*

Anal. **1979**, *1* (1), 2–11.

(35) Greczynski, G.; Hultman, L. Compromising Science by Ignorant Instrument Calibration - Need to Revisit Half a Century of Published XPS Data. *Angew. Chemie* **2020**, ange.201916000.

(36) Mu, L.; Yang, Z.; Tao L.;Waters, K. C.; Xu, Z.; Li, L.; Sainio, S.; Du, Y.; Xin, H.L.; Nordlund, D.; Lin, F.. The Sensitive Surface Chemistry of Co-Free, Ni-Rich Layered Oxides: Identifying Experimental Conditions That Influence Characterization Results. *J. Mater. Chem. A* **2020**, *8* (34), 17487–17497.

(37) Zhang, M. J.; Hu, X.; Li, M.; Duan, Y.; Yang, L.; Yin, C.; Ge, M.; Xiao, X.; Lee, W. K.; Ko, J. Y. P.; Amine, K.; Chen, Z.; Zhu, Y.; Dooryhee, E.; Bai, J.; Pan, F.; Wang, F. Cooling Induced Surface Reconstruction during Synthesis of High-Ni Layered Oxides. *Adv. Energy Mater.* **2019**, *9* (43), 1901915.

(38) Schipper, F.; Bouzaglo, H.; Dixit, M.; Erickson, E. M.; Weigel, T.; Talianker, M.; Grinblat, J.; Burstein, L.; Schmidt, M.; Lampert, J.; Erk, C.; Markovsky, B.; Major, D. T.; Aurbach, D. From Surface ZrO_2 Coating to Bulk Zr Doping by High Temperature Annealing of Nickel-Rich Lithiated Oxides and Their Enhanced Electrochemical Performance in Lithium Ion Batteries. *Adv. Energy Mater.* **2018**, *8* (4), 1701682.

(39) Sun, H.; Cao, Z.; Wang, T.; Lin, R.; Li, Y.; Liu, X.; Zhang, L.; Lin, F.; Huang, Y.; Luo, W. Enabling High Rate Performance of Ni-Rich Layered Oxide Cathode by Uniform Titanium Doping. *Mater. Today Energy* **2019**, *13*, 145–151.

(40) Weigel, T.; Schipper, F.; Erickson, E. M.; Susai, F. A.; Markovsky, B.; Aurbach, D. Structural and Electrochemical Aspects of $LiNi_{0.8}Co_{0.1}Mn_{0.1}O_2$ Cathode Materials

Doped by Various Cations. *ACS Energy Lett.* **2019**, *4* (2), 508–516.

(41) Qing, R.-P.; Shi, J.-L.; Xiao, D.-D.; Zhang, X.-D.; Yin, Y.-X.; Zhai, Y.-B.; Gu, L.; Guo, Y.-G. Enhancing the Kinetics of Li-Rich Cathode Materials through the Pinning Effects of Gradient Surface Na^+ Doping. *Adv. Energy Mater.* **2016**, *6* (6), 1501914.

(42) Weber, D.; Tripković, Đ.; Kretschmer, K.; Bianchini, M.; Brezesinski, T. Surface Modification Strategies for Improving the Cycling Performance of Ni-Rich Cathode Materials. *Eur. J. Inorg. Chem.* **2020**, *2020* (33), 3117–3130.

(43) Tian, C.; Nordlund, D.; Xin, H. L.; Xu, Y.; Liu, Y.; Sokaras, D.; Lin, F.; Doeff, M. M. Depth-Dependent Redox Behavior of $LiNi_{0.6}Mn_{0.2}Co_{0.2}O_2$. *J. Electrochem. Soc.* **2018**, *165* (3), A696–A704.

(44) Ohzuku, T.; Ueda, A.; Nagayama, M. Electrochemistry and Structural Chemistry of $LiNiO_2$ (R3m) for 4 Volt Secondary Lithium Cells; *J. Electrochem. Soc.* **1993**, *140* (7), 1862.

(45) Yang, W.; Liu, X.; Qiao, R.; Olalde-Velasco, P.; Spear, J. D.; Roseguo, L.; Pepper, J. X.; Chuang, Y. De; Denlinger, J. D.; Hussain, Z. Key Electronic States in Lithium Battery Materials Probed by Soft X-Ray Spectroscopy. *J. Electron Spectros. Relat. Phenomena* **2013**, *190* (PART A), 64–74.

(46) Lin, F.; Markus, I. M.; Nordlund, D.; Weng, T.-C.; Asta, M. D.; Xin, H. L.; Doeff, M. M. Surface Reconstruction and Chemical Evolution of Stoichiometric Layered Cathode Materials for Lithium-Ion Batteries. *Nat. Commun.* **2014**, *5* (1), 3529.

(47) De Groot, F. M. F.; Grioni, M.; Fuggle, J. C.; Ghijsen, J.; Sawatzky, G. A.; Petersen, H. Oxygen 1s X-Ray-Absorption Edges of Transition-Metal Oxides. *Phys. Rev. B*

1989, *40* (8), 5715–5723.

(48) Jiang, Z.-S.; Li, S.-F.; Xu, Z.-R.; Nordlund, D.; Ohldag, H.; Pianetta, P.; Lee, J.-S.; Lin, F.; Liu, Y.-J. Revealing the Inhomogeneous Surface Chemistry on the Spherical Layered Oxide Polycrystalline Cathode Particles. *Chin. Phys. B* **2020**, *29* (2), 26103.

(49) Xia, S.; Mu, L.; Xu, Z.; Wang, J.; Wei, C.; Liu, L.; Pianetta, P.; Zhao, K.; Yu, X.; Lin, F.; Liu, Y. Chemomechanical Interplay of Layered Cathode Materials Undergoing Fast Charging in Lithium Batteries. *Nano Energy* **2018**, *53*, 753–762.

(50) Mansour, A. N.; Melendres, C. A. Analysis of X-Ray Absorption Spectra of Some Nickel Oxycompounds Using Theoretical Standards. *J. Phys. Chem. A* **1998**, *102* (1), 65–81.

(51) Funke, H.; Scheinost, A. C.; Chukalina, M. Wavelet Analysis of Extended X-Ray Absorption Fine Structure Data. *Phys. Rev. B - Condens. Matter Mater. Phys.* **2005**, *71* (9), 094110.

(52) Funke, H.; Chukalina, M.; Scheinost, A. C. A New FEFF-Based Wavelet for EXAFS Data Analysis. *J. Synchrotron Radiat.* **2007**, *14* (5), 426–432.

(53) Siebecker, M. G.; Sparks, D. L. Structural Differentiation between Layered Single (Ni) and Double Metal Hydroxides (Ni−Al LDHs) Using Wavelet Transformation. **2017**.

(54) Dong, J.; Zhu, H.; Xiang, Y.; Wang, Y.; An, P.; Gong, Y.; Liang, Y.; Qiu, L.; Zheng, A.; Peng, X.; Lin, M.; Xu, G.; Guo, Z.; Chen, D. Toward a Unified Identification of Ti Location in the MFI Framework of High-Ti-Loaded TS-1: Combined EXAFS, XANES, and DFT Study. **2016**.

(55) Levi, E.; Levi, M. D.; Salitra, G.; Aurbach, D.; Oesten, R.; Heider, U.; Heider, L.

Electrochemical and In-Situ XRD Characterization of LiNiO2 and LiCo0.2Ni0.8O2 Electrodes for Rechargeable Lithium Cells. *Solid State Ionics* **1999**, *126* (1–2), 97–108.

(56) Zhang, Y.-P.; Liang, E.-Q.; Wang, J.-X.; Yu, B.-J.; Wang, C.-Y.; Li, M.-W. Effect of Aluminum Doping on the Stability of Lithium-Rich Layered Oxide $Li[Li_{0.23}Ni_{0.15}Mn_{0.52}Al_{0.10}]O_2$ as Cathode Material. *Int. J. Electrochem. Sci* **2017**, *12*, 9051–9060.

(57) Wang, C. C.; Jarvis, K. A.; Ferreira, P. J.; Manthiram, A. Effect of Synthesis Conditions on the First Charge and Reversible Capacities of Lithium-Rich Layered Oxide Cathodes. *Chem. Mater.* **2013**, *25* (15), 3267–3275.

(58) Hall, D. S.; Lockwood, D. J.; Bock, C.; MacDougall, B. R. Nickel Hydroxides and Related Materials: A Review of Their Structures, Synthesis and Properties. *Proceedings of the Royal Society A: Mathematical, Physical and Engineering Sciences*. **2015**, *471*, 2174.

(59) Yan, W.; Jia, X.; Yang, S.; Huang, Y.; Yang, Y.; Yuan, G. Synthesis of Single Crystal $LiNi_{0.92}Co_{0.06}Mn_{0.01}Al_{0.01}O_2$ Cathode Materials with Superior Electrochemical Performance for Lithium Ion Batteries . *J. Electrochem. Soc.* **2020**, *167* (12), 120514.

(60) McCalla, E.; Carey, G. H.; Dahn, J. R. Lithium Loss Mechanisms during Synthesis of Layered $Li_xNi_{2-x}O_2$ for Lithium Ion Batteries. *Solid State Ionics* **2012**, *219*, 11–19.

2.8. Supplementary information

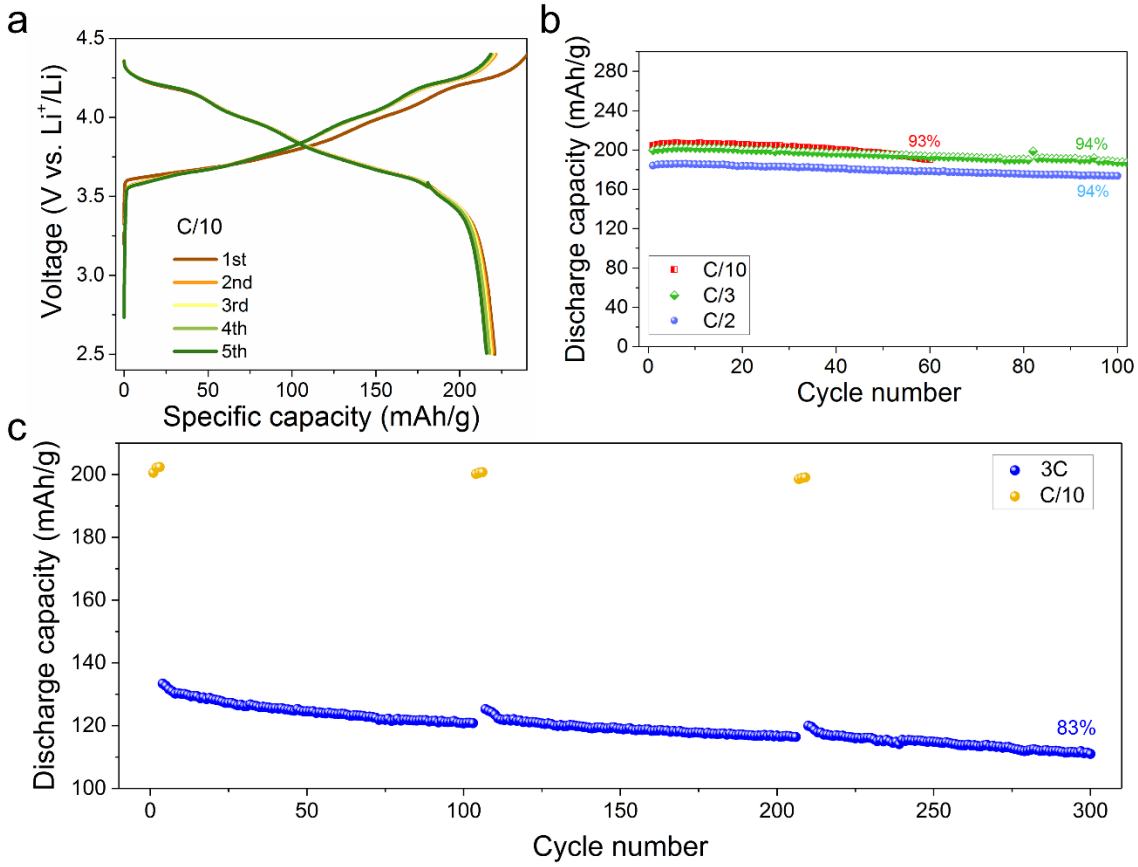

Figure S1. Electrochemical performance of the Li metal cells with the Mg/Ti-LNO cathode. a) Voltage profile of Mg/Ti-LNO in the first five cycles at C/10 within the voltage window of 2.5-4.4V vs. Li/Li^+; b) the capacity retention at different C-rates; c) the capacity retention after 300 cycles at 3C, three cycles at C/10 were applied in the beginning of every 100 cycles.

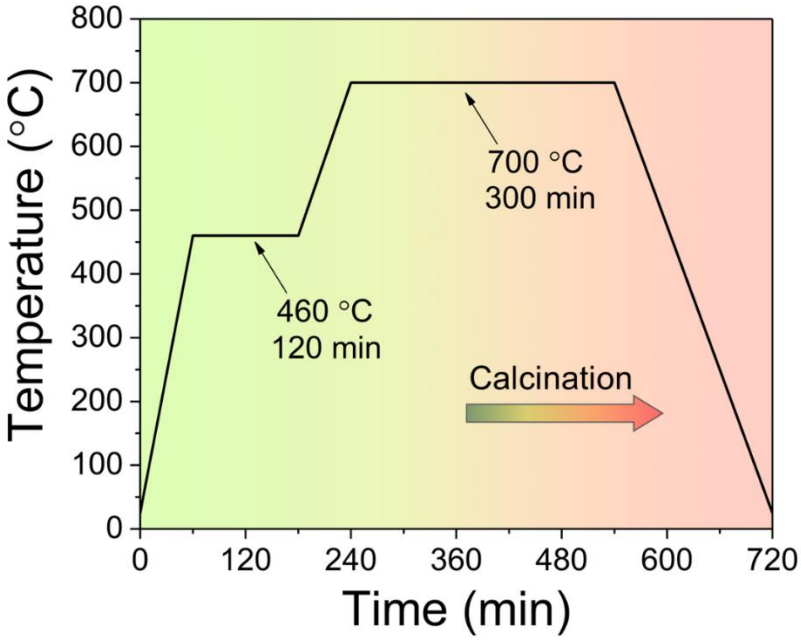

Figure S2. Thermal profile of a typical calcination process in this study showing the temperature as a function of calcination time. The temperature is increased from 25 °C to 460 °C in one hour (temperature ramping rate: 7.25 °C/min), then held at 460 °C for two hours. Subsequently, the temperature is increased from 460 °C to 700 °C in one hour (temperature ramping rate: 4 °C/min), then held at 700 °C for five hours, and followed by cooling for 3 hours (cooling rate: 3.75 °C/min).

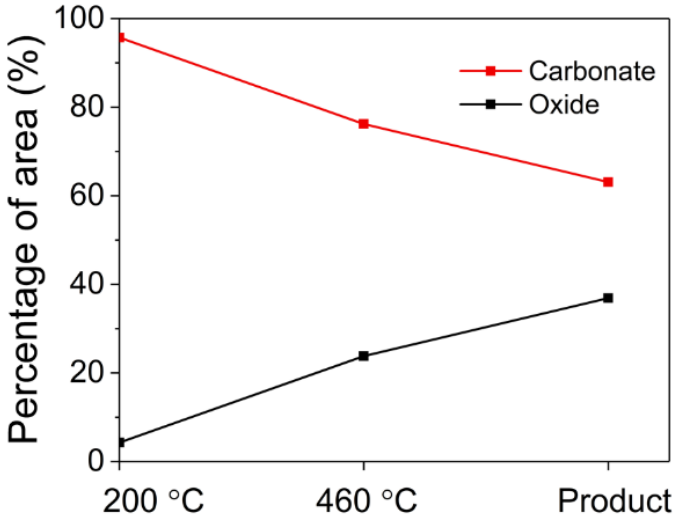

Figure S3. Percentage of carbonate peak and oxide peak areas in O 1s XPS spectra.

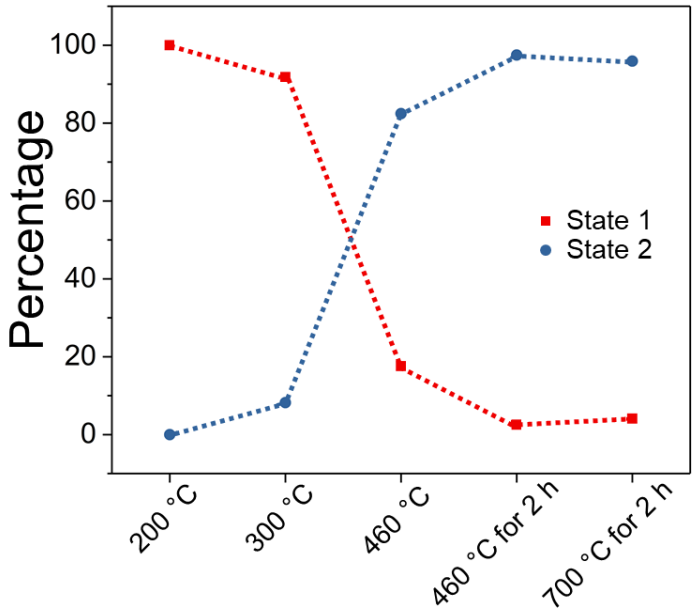

Figure S4. Linear combination result of the intermediate calcination stages showing the percentage of each component. The spectra of the precursor (state 1) and the product (state 2) represent the lowest and the highest oxidation states, respectively. Each intermediate state is expressed as a linear combination of state 1 and state 2. The fitting is based on Ni L_3-edge. The dash lines show the trend upon calcination.

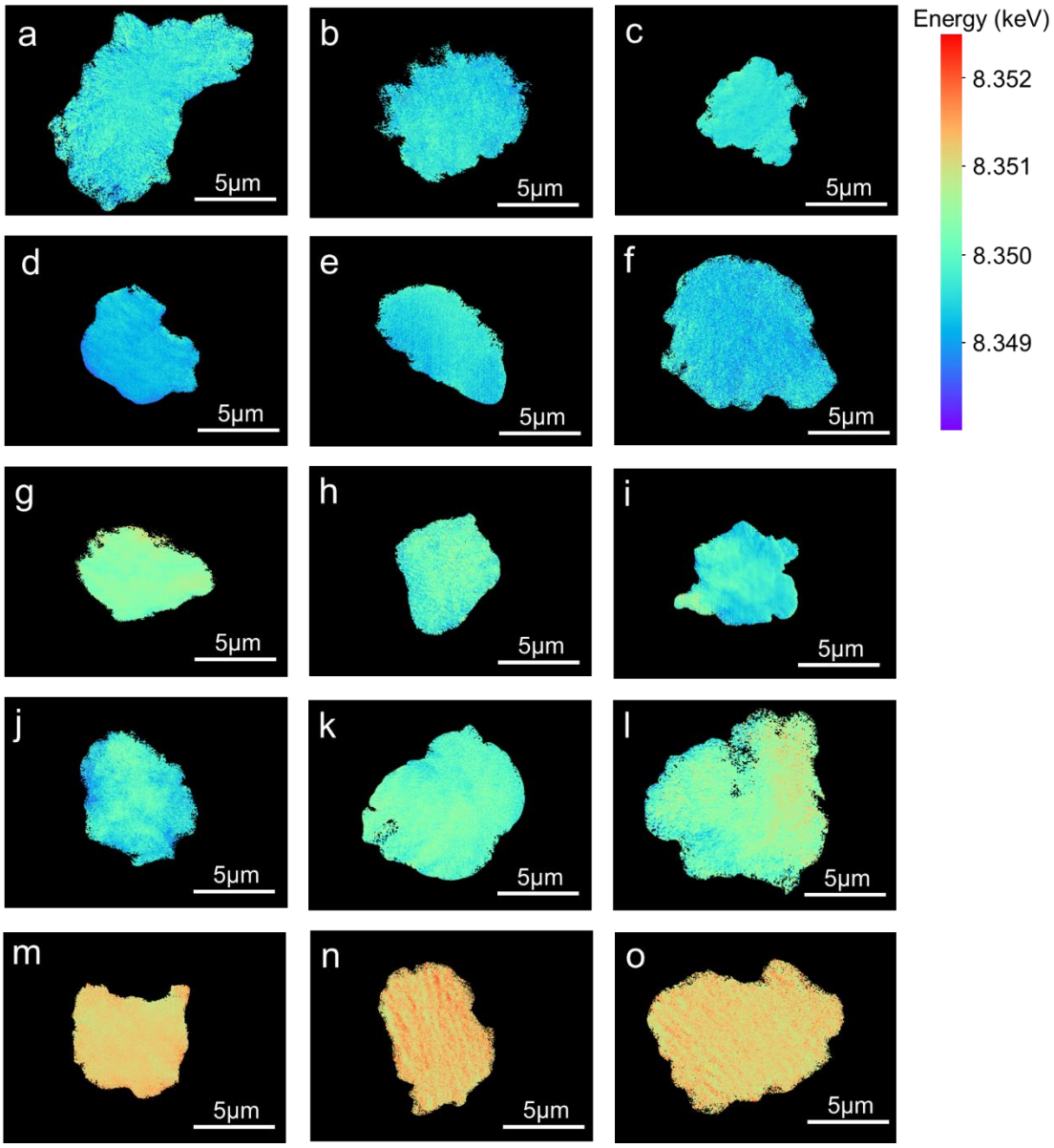

Figure S5. Ni K-edge 2D TXM images for the samples a-c) at pristine state; d-f) calcined at 300 °C; g-i) calcined at 460 °C for 2 hours; j-l) calcined at 600 °C; m-o) complete calcination.

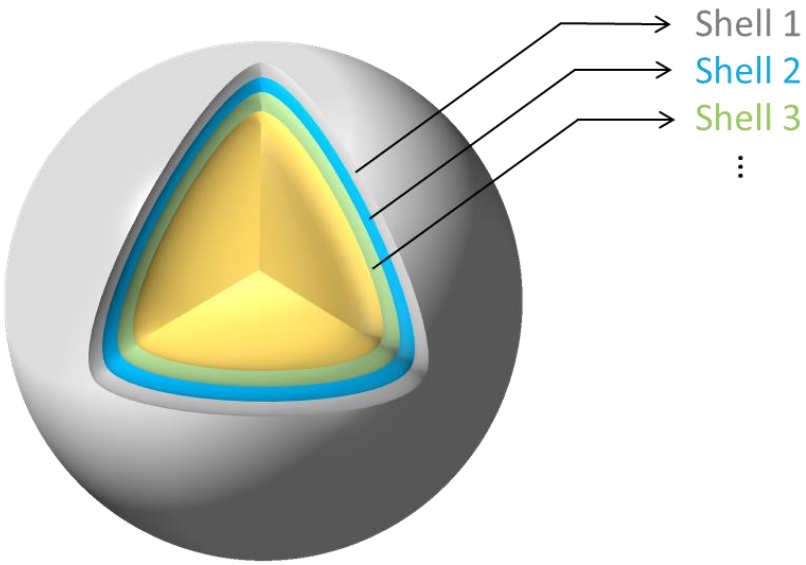

Figure S6. Schematic illustration of TXM depth profiling analysis. Each shell is 20 nm away from its outer shell. The energy of each shell is defined as the mean value of the Ni K-edge white-line energy of all voxels within the shell.

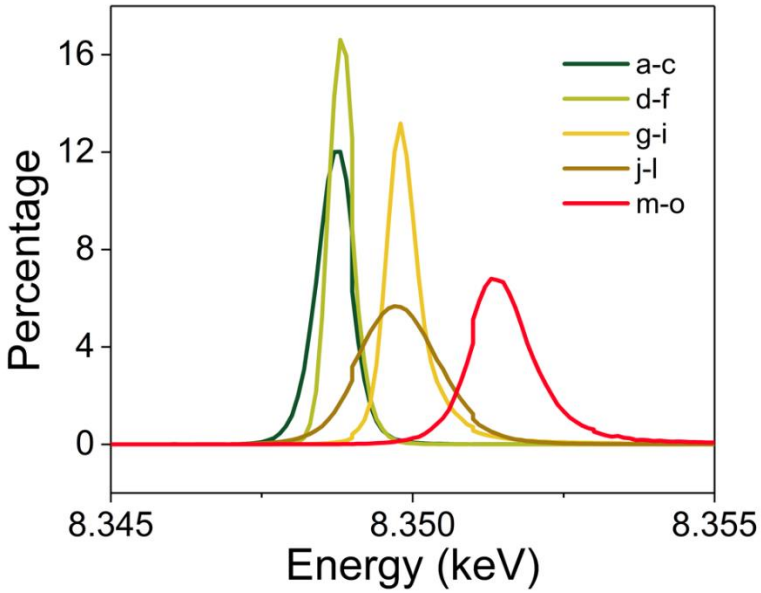

Figure S7. Ni K-edge energy histogram of the samples at different stages of calcination corresponding to Figure S5.

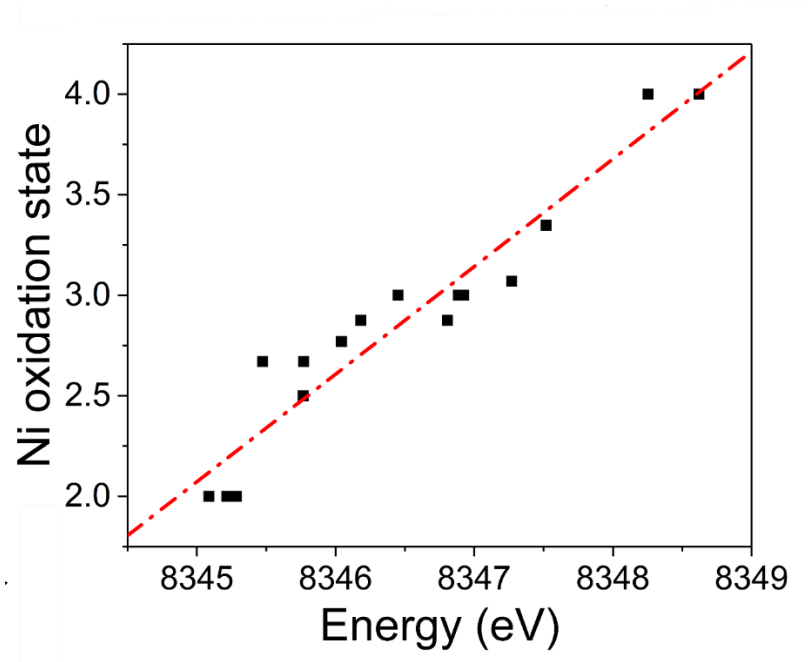

Figure S8. Estimated Ni oxidation state as a function of edge energy defined by the integration method. Different shapes of the spectra reported by different publications can lead to the variation of the integral and eventually the difference of estimated edge energy even at the same estimated oxidation state.

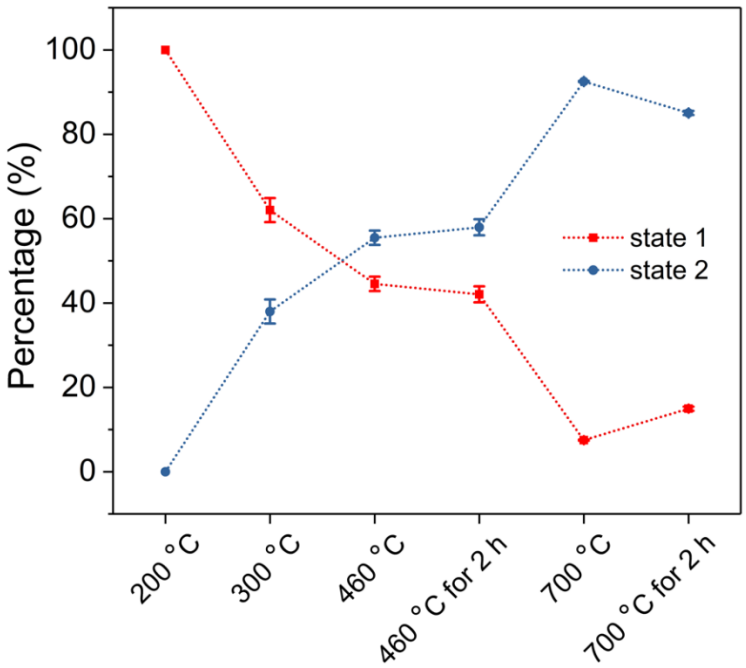

Figure S9. Linear combination result of the intermediate calcination stages showing the percentage of each component. The spectra of the precursor (state 1) and the product (state 2) represent the lowest and the highest oxidation states, respectively. Each intermediate state is expressed as a linear combination of state 1 and state 2. The dashed line shows the trend upon calcination. The error bars show the difference between different fitting methods, e.g., edge fitting, white-line fitting, and full-spectrum fitting. The slight decrease of Ni oxidation state for holding 2 hours at 700 °C can be possibly caused by the Li loss.[60]

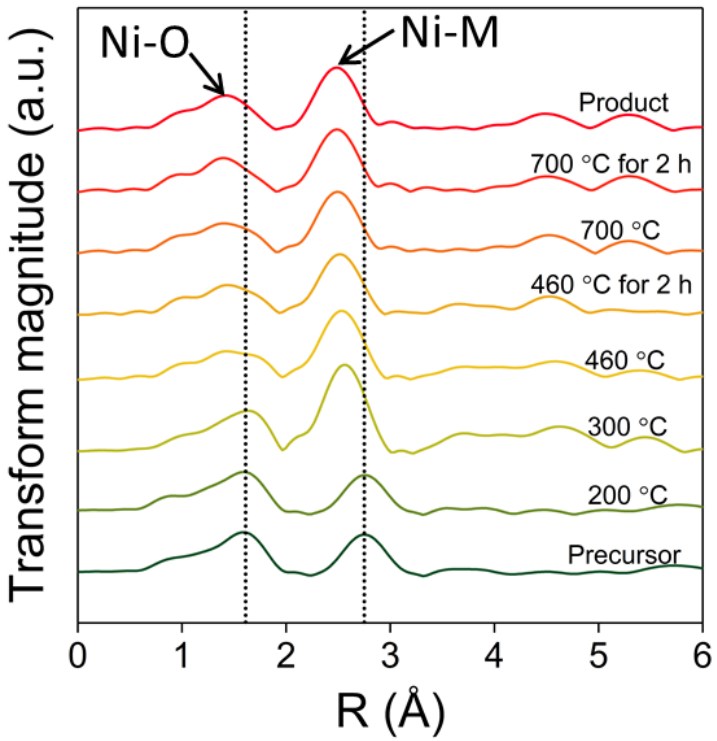

Figure S10. Ni K-edge Fourier transformed EXAFS at different stages of calcination. There is a sharp decrease of the Ni-M distance between 200 ºC and 300 ºC due to dopant redistribution.

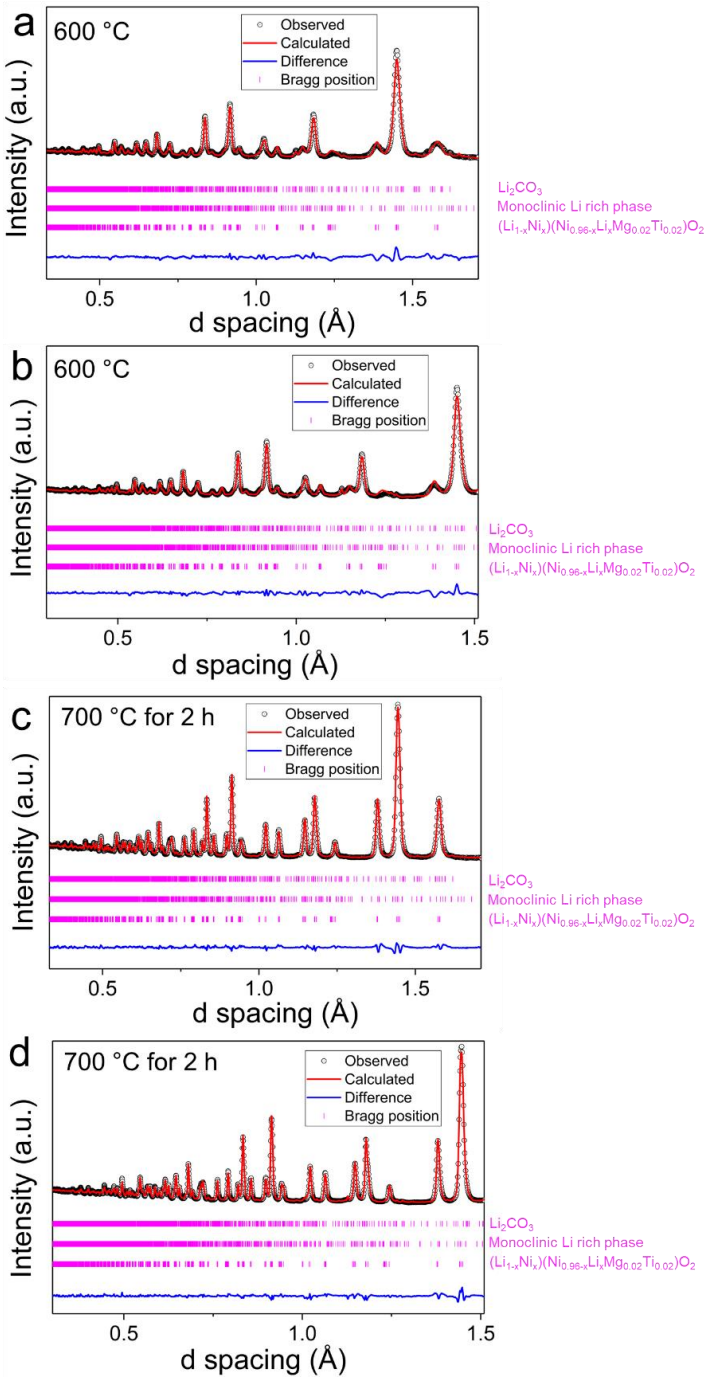

Figure S11. Neutron diffraction patterns and Rietveld refinement at different d-spacing ranges a-b) at 600 °C, and c-d) at 700 °C for 2 h. R_{wp} for a) to d) is 5.04 %, 4.87 %, 4.01 % and 4.36 %, respectively. More layered oxide phase is identified, and Li/Ni cation mixing is reduced from 600 °C to 700 °C for two hours.

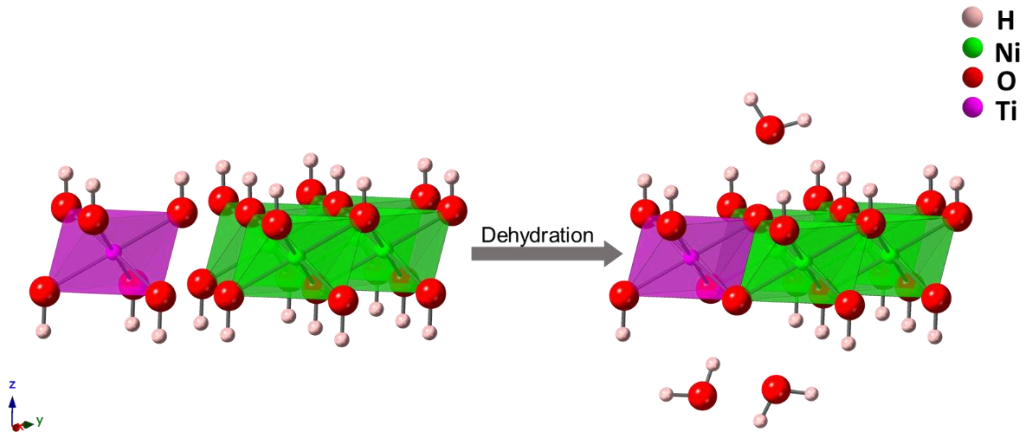

Figure S12. Schematic illustration of the dehydration reaction and dopant incorporation in the $Ni(OH)_2$ lattice at the early stage of calcination.

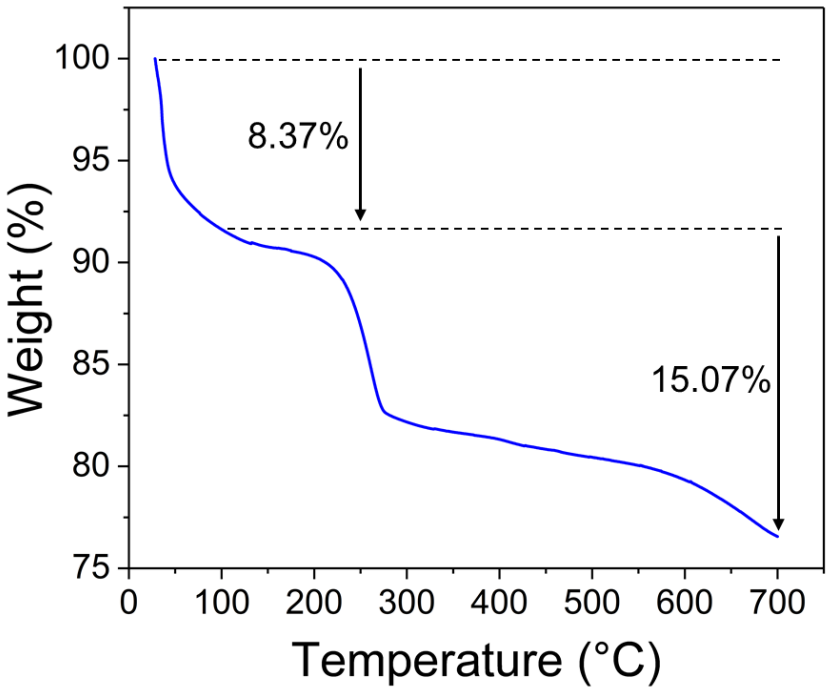

Figure S13. Thermogravimetric analysis (TGA) curve of the precursor heated from room temperature to 460 °C at a temperature ramping rate of 7.25 °C min^{-1}, and from 460 °C to 700 °C at a temperature ramping rate of 4 °C min^{-1} in oxygen flow (The same temperature ramping rate as the thermal profile shows in Figure S2).

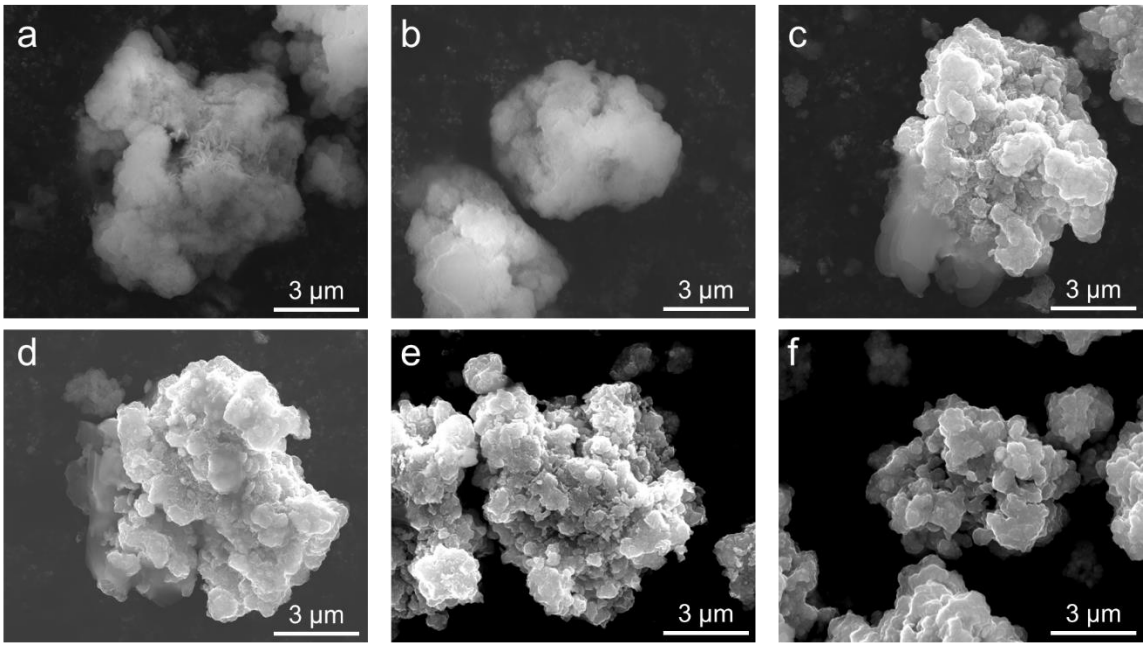

Figure S14. Scanning electron microscopy (SEM) images for the samples a) at the pristine state; b) calcined at 300 °C; c) calcined at 460 °C; d) calcined at 580 °C; e) calcined at 700 °C; f) complete calcination. The samples were heated to the designated temperature and cooled down at 3.75 °C min^{-1} to room temperature prior to the SEM measurement.

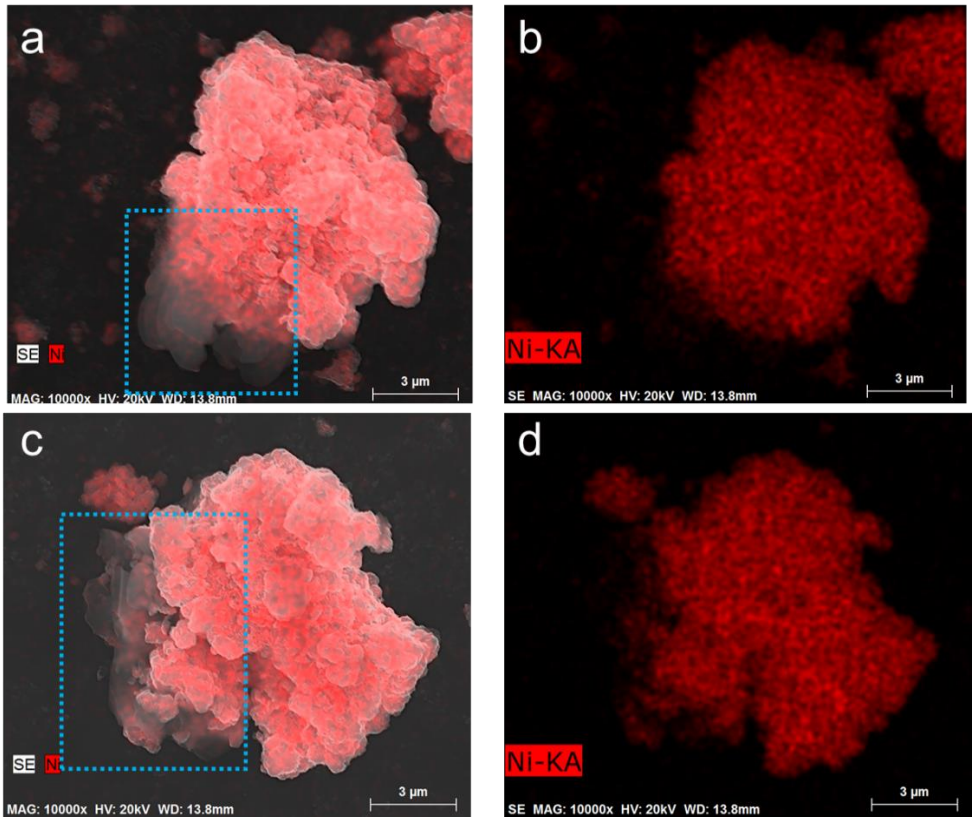

Figure S15. EDS mapping of the samples a-b) calcined at 460 °C and c-d) calcined at 580 °C. The highlighted lighter contrast regions are possibly recrystallized LiOH after cooling. The heterogeneous distribution of LiOH can potentially lead to the heterogeneous phase propagation.

Table S1. Elemental fractions at the particle surface at different stages of calcination based on peak fitting of XPS data.

	Ni (%)	Mg (%)	Ti (%)
Precursor	80	5	15
200 °C	89	3	8
460 °C	89	3	8
Product	90	3	7

Table S2. The estimated Ni oxidation state of the samples at different states of calcination based on Ni K-edge XANES. The deviation from the trivalent state of the Ni in the product is potentially caused by the off-stoichiometry of the product due to Li loss during calcination or experimental errors.

Sample	Precursor	200 °C	300 °C	460 °C	460 °C for 2 h	700 °C	700 °C for 2 h	Product
Edge energy/eV	8344.9	8345.1	8345.7	8345.9	8346.0	8346.8	8346.7	8347.0
Estimated Ni oxidation state	2.0	2.1	2.5	2.6	2.6	3.0	3.0	3.1

Table S3. Neutron diffraction Rietveld refinement results for samples at 600 °C and 700 °C for 2 h. X value represents the content of Ni in the Li layer and Li in the Ni layer in layered phase $(Li_{1-x}Ni_x)(Ni_{0.96-x}Li_xMg_{0.02}Ti_{0.02})O_2$, respectively. More layered phase and less Li/Ni cation mixing are observed from 600 °C to 700 °C for 2 h.

Sample	$(Li_{1-x}Ni_x)(Ni_{0.96-x}Li_xMg_{0.02}Ti_{0.02})O_2$ fraction	Monoclinic Li rich phase fraction	Li_2CO_3 fraction	x value
600 °C	83.11%	12.77%	4.12%	0.0492
700 °C for 2 h	96.83%	1.14%	2.03%	0.0051

3. Revealing and manipulating particle level Mn distribution upon thermal treatment in Ni-rich Co-free layered cathodes

Zhijie Yang[1], Dong Hou[1], Jungki Min[1], Zhengrui Xu[1], Dennis Nordlund[2], Chengjun Sun[3], Xianghui Xiao[4], Feng Lin[1*]

1. Department of Chemistry, Virginia Tech, Blacksburg, VA, 24061, USA
2. Stanford Synchrotron Radiation Lightsource, SLAC National Accelerator Laboratory, Menlo Park, CA, 94025, USA
3. Advanced Photon Source, Argonne National Laboratory, Argonne, IL, 60439, USA
4. National Synchrotron Light Source II, Brookhaven National Laboratory, Upton, NY, 11973, USA

Correspondence and requests for materials should be addressed to F.L. (email: fenglin@vt.edu)

3.1. Abstract

Ni-rich Co-free layered oxide cathodes have become one of the most promising candidates to enable high energy-density and sustainable Li-ion batteries (LIBs) in the approaching era of electric vehicles (EVs). However, these Ni-rich Co-free layered cathodes usually suffer from low interfacial and bulk stability, which can facilitate battery performance degradation. Several approaches have been widely applied to stabilize the cathode surface and bulk structure, such as surface coating, bulk doping, and concentration gradient distribution engineering. Essentially, these engineering approaches modify the cathode properties by manipulating the distribution of foreign or existing elements in the materials. However, the elemental distribution behavior during the synthesis has not been well understood. A systematic study of the elemental distribution is required to guide the cathode engineering approaches. Herein, we use Mn-coated single crystal $LiNiO_2$ (LNO) as the platform to investigate the elemental distribution, structural and chemical changes in cathode particles upon thermal treatment. With a combination of synchrotron X-ray scattering, spectroscopic, and microscopic measurements at multiple length scales, we find the evolution of the Mn diffusion layer towards the bulk of the cathode particle at different stages of heat treatment. Mn diffuses more rapidly with higher temperatures. In addition, the Mn diffusion rate increase and then decrease from the surface to the bulk of the cathode particle. Upon heating, Mn is oxidized and occupies the Ni site, forming a gradient Mn distribution. Ni is reduced and occupies the Li site within the Mn diffusion layer with an increasing level of Li/Ni cation mixing. This study can guide the cathode modification by precisely manipulating the ion distribution. A combination of coating, doping, and concentration gradient engineering can be potentially achieved to enable the efficient

utilization of foreign elements. This work provides insights into the solid-state ion diffusion at the microscale, and the methods demonstrated in this work can be applied to study a wide variety of solid-state materials besides batteries.

3.2. Introduction

Since 1991, the commercialization of Li-ion batteries (LIBs) has reshaped the daily lives of people. The revolution of smartphones can not be achieved without the support of LIBs. Another epoch-making revolution taking place at present that is promoted by the significant development of LIBs is electric vehicles (EVs). There is a worldwide trend of transiting from internal combustion engine vehicles (ICEVs) to EVs, yet two obstacles, i.e., cost and performance, faced by the EV industry impede the fast transition.[1] The most critical component determining EVs' cost and performance is LIBs.[1] Although LIB price has dropped by around 97% since its commercialization, the cost of LIBs in EVs needs to be further reduced to make it competitive with ICEVs.[1] In commercial graphite anode-based LIBs, cathode is the largest cost contributor and the bottleneck of the performance. Layered ternary oxide materials, i.e., $LiNi_xMn_yCo_{1-x-y}O_2$ (NMC) and $LiNi_xCo_yAl_{1-x-y}O_2$ (NCA), are among the most prevailing cathodes in EV LIBs. Co is the most expensive one among the metal elements because of its scarcity and uneven distribution. Around 70% of Co mineral extraction is from the Democratic Republic of the Congo (DRC).[1] The human rights issue during Co mining and unstable geopolitics in the DRC bring extensive challenges and uncertainties to the Co supply chain. Therefore, the battery community has been making tremendous efforts to eliminate Co in the cathode materials. Meanwhile, another trend of developing these layered ternary oxide materials is to increase Ni content in the chemical formula because Ni dominates the redox reaction and battery capacity, and

higher Ni content gives rise to higher energy density.[2] However, these Ni-rich Co-free cathodes usually suffer from low electrochemical and structural stability.[3]

Several approaches are generally adopted to enhance the stability of Ni-rich Co-free cathodes, i.e., bulk doping, surface coating, and surface-to-bulk concentration gradient strategies.[4,5] For example, Li *et al.* reported an Al-doped high-Ni Co-free $LiNi_{1-x-y}Mn_xAl_yO_2$ (NMA) cathode that outperforms its NMC and NCA counterparts with identical Ni content.[6] A large variety of dopants, such as Mg, Ti, Zr, and Ta, have been reported to be beneficial to cycling stability by enhancing the cathode bulk structural integrity.[7–10] Surface coating, such as metal oxides, can protect the cathode surface by mitigating the parasitic reactions with electrolytes, suppressing the active mass dissolution, blocking moisture in the ambient environment during storage, etc.[11] Sun *et al.* reported a full-gradient approach to enhance the cycling and thermal stability while maintaining high energy density by forming a decreasing Ni concentration and increasing Mn concentration from the center to the surface of cathode particles.[12] Although the studies reporting these strategies usually highlight the sole effect of one specific strategy, it is worth noting that the doping, coating, and concentration gradient phenomena are often intermixed and controlled by the kinetics of ion diffusion, considering the relatively short calcination time of cathode processing. Yoon *et al.* reported that the dopant Zr in bulk can diffuse to the surface upon calcination and spontaneously form a surface Li_2ZrO_3 coating layer.[13] Schipper *et al.* coated $LiNi_{0.8}Mn_{0.1}Co_{0.1}O_2$ (NMC811) with ZrO_2 and produced bulk doping of Zr^{4+} by inward diffusion with high temperature annealing.[14] Both studies achieved enhanced electrochemical performance with the coexistence of doping and coating, although from opposite directions of ion diffusion. It is reported that the

conversion of coating to doping for Nb and Al can be achieved by enhancing the calcination temperature.[15,16] Our recent study shows dopants Mg and Ti in the lattice can undergo dynamic redistribution at early stage of calcination (below 300 °C).[17] Eventually, the surface-enriched Ti gradient distribution can be achieved in the primary particle.[17,18] These studies show that the boundaries among doping, coating, and gradient distribution are not well defined. Instead, they can be converted and mixed to some extent to achieve better cathode performance. However, how to precisely control the ion diffusion behavior at the particle level from the synthesis aspect is still not well understood yet.

Probing the ion diffusion at the particle scale is challenging yet crucial to guide ion distribution engineering in practice. Dahn group has reported several studies that investigated cation interdiffusion.[19,20] Specifically, two pellets containing the cations of interest were compressed under high pressure followed by high-temperature sintering. Subsequently, they performed scanning electron microscopy (SEM) and energy dispersive spectroscopy (EDS) line scan at the cross-section of two pellets to estimate the interdiffusion coefficients. Although these studies provide valuable guidance on ion interdiffusion by mimicking the coating process, the ion diffusion behavior at the cathode particle scale could vary. The coating layer in cathodes is typically produced through chemical reaction or atomic layer deposition (ALD), which can induce different interfaces and the following diffusion from that obtained by high-pressure compressing.[21] Also, the diffusion of dopants or coating cations is normally one-way to the cathode lattice instead of interdiffusion. Furthermore, the sintering temperatures in these studies are higher than 800 °C, which is higher than the requirements of most doping or coating strategies.[19,20] Previous studies suggested that ion redistribution can take place at much lower

temperatures.[17] Therefore, more investigations are needed on the ion dynamic distribution in real cathode particles at lower temperatures. Herein, we synthesized $Mn(OH)_2$-coated single crystal $LiNiO_2$ (LNO) and used it as the platform to monitor the Mn redistribution and the structural and chemical evolution of the LNO cathode. We first used *in situ* transmission X-ray microscopy (TXM) to track the Mn tomography inside the LNO particle and Ni oxidation state evolution at various temperatures below 700 °C. We performed hard X-ray absorption spectroscopy (XAS) and soft XAS at different extents of Mn diffusion to reveal chemical changes in the bulk and at the surface of the cathode at ensemble-averaged scale, respectively. We further carried out synchrotron X-ray diffraction (XRD) and neutron diffraction (ND) to understand the structural evolution caused by Mn diffusion at various temperatures.

3.3. Materials and methods

Material synthesis:

The precursor $Ni(OH)_2$ was obtained through a co-precipitation reaction. Specifically, the starting solution (NaOH and $NH_3{\cdot}H_2O$ with a molar ratio of $NaOH/NH_3{\cdot}H_2O$ = 1/1.25) was prepared, and the pH was adjusted to 11.00 by adding sulfuric acid. $NiSO_4{\cdot}6H_2O$ solution and base solution (NaOH and $NH_3{\cdot}H_2O$ with a molar ratio of $NaOH/NH_3{\cdot}H_2O$ = 1/1.25) were added simultaneously into the starting solution obtained from the first step under constant stirring. The reaction was carefully controlled to keep the temperature at 50 °C and the pH at 11.00 ± 0.02 under N_2 flow protection at 0.1 L min^{-1}. The obtained precipitant was washed with deionized water and isopropyl alcohol (IPA), filtered and dried in the vacuum oven at 100 °C for 12 h. The single crystal LNO was synthesized through a molten-salt method. $Ni(OH)_2$ precursor was mixed

thoroughly with the $LiOH \cdot H_2O$ and KCl with a molar ratio of $Ni(OH)_2/LiOH \cdot H_2O/KCl$ = 1/2/1.5, followed by a calcination procedure at 900 °C for 3 h and 800 °C for 10 h under O_2 flow. The obtained product was washed with deionized water and IPA, filtered, and dried in the vacuum oven at 100 °C for 12 h. 10% additional LiOH was added to the product obtained from the last step and calcined at 675 °C for 6 h. 20% $Mn(OH)_2$-coated LNO was prepared for in situ heating TXM to ensure the LNO cathode particles were thoroughly coated. Noting that the Mn content in specific particles may vary. $Mn(OH)_2$ was coated by adding stoichiometric content of $MnSO_4 \cdot H_2O$ and $NaOH/NH_3 \cdot H_2O$ (molar ratio 1/1.25) to the single crystal LNO cathode and stirred overnight. The coated cathode was washed with deionized water and isopropyl alcohol (IPA), filtered and dried in the vacuum oven at 100 °C for 12 h. The samples with various Mn content were prepared with the same protocol but different reagent ratios.

Materials characterizations:

In situ heating full field TXM was performed at beamline 18-ID at National Synchrotron Light Source II (NSLS- II), Brookhaven National Laboratory. The experimental setup is illustrated in the previous report.[22] A python-based software TXM-Sandbox was used to reconstruct and analyze the tomographic datasets,[23,24] and a commercial software Avizo was used for data interpretation. Hard XAS (XANES and EXAFS) measurement was performed at the beamline 20-ID of the Advanced Photon Source (APS) at Argonne National Laboratory. The incident beam was monochromatized by using a Si (111) fixed-exit and a double-crystal monochromator. The absorption energy calibration was based on the first inflection points of the reference spectra that were collected from a metal foil reference simultaneously with the samples. The samples were

sealed with Kapton tapes in the Ar-filled glove box for transfer and measurement. Soft XAS measurements were performed at beamline 10-1 at Stanford Synchrotron Radiation Lightsource (SSRL) using a ring current of 350 mA and a 1000 L mm^{-1} spherical grating monochromator with 20 μm entrance and exit slits, providing ~10^{11} ph s^{-1} at 0.2 eV resolution in a one mm^2 beam spot. Data were acquired under ultrahigh vacuum (10^{-9} Torr) in a single load at room temperature, where the sample drain current was collected. Ni L-edge spectra were collected in total electron yield (TEY) and fluorescence yield (FY) mode. The powder samples were loaded in an Ar-filled glovebox before measurement. Synchrotron X-ray diffraction (XRD) was performed at beamline 28-ID at National Synchrotron Light Source II (NSLS- II), Brookhaven National Laboratory. The wavelength of the applied X-ray is 0.2437 Å. The Rietveld refinements were conducted using the software GSAS EXPGUI. The morphology of the cathode precursor, uncoated cathode, and coated cathode were studied through SEM with the EDS performed at the acceleration voltage of 20 kV (ESEM, FEI Quanta 600 FEG).

3.4. Results

We prepared transition metal hydroxide precursor through a co-precipitation method (Figure S1a-b). Next, we synthesized single crystal LNO with a $Mn(OH)_2$ coating layer on the cathode surface (Figure S1c-h), which is utilized as the platform to study the Mn diffusion inside the LNO cathode particle at various temperatures and holding time (Figure S2). First, we probed the elemental distribution of Mn and the oxidation state evolution of Ni in the cathode using *in situ* heating TXM (Figure 1a). Upon heating, Mn^{2+} is oxidized, and Ni^{3+} in LNO is reduced simultaneously. Therefore, we use the Ni oxidation state as an indicator for the elemental distribution of Mn inside the cathode particle. The

scheme in Figure 1b illustrates the experimental setup. The Mn-coated LNO sample was loaded in the sample holder and heated by the furnace. Meanwhile, three-dimensional (3D) TXM for Ni and Mn was performed at various temperatures and durations. Ni K-edge white-line energy is positively correlated with the Ni oxidation state.[25] At room temperature, the Ni oxidation state at the cathode particle surface is slightly higher, and its distribution is heterogeneous due to the anisotropic reaction upon synthesis (Figure 1a).[17] Upon heating to 300 °C and holding for one hour, the Ni at the surface is slightly reduced (Figure 1a). This indicates that Mn diffuses into the top surface of the LNO particle. At 500 °C and the holding stage, surface Ni is further reduced, indicating the continuous Mn inward diffusion (Figure 1a). At 700 °C, we observe the evolution of the surface Ni reduction layer towards the core of the LNO particle (Figure 1a,b). After holding at 700 °C for one hour, Ni is reduced throughout the particle (Figure 1a).

We plot the Ni K-edge white-line energy as a function of the distance from the particle surface to quantify the results (Figure 1c). There is a pronounced trend that the surface reduction layer becomes thicker and evolves to the bulk (Figure 1c). At room temperature, the slightly oxidized Ni at the surface is confirmed (Figure 1c). After holding at 300 °C for one hour, the surface Ni is reduced, and the reduction gradually evolves into the bulk until it forms a surface reduction layer of around 1 μm (Figure 1c). At the 500 °C holding stage, the surface is further reduced, and the reduction gradually extends to the core direction (Figure 1c). After holding at 700 °C for one hour, Ni in the particle is uniformly reduced, and the Ni oxidation state at the surface and in the bulk stays almost identical (Figure 1c). Figure 1d shows the histogram of energy distribution for the samples at various stages of heating. The symmetric energy distribution at room temperature

suggests that Ni oxidation state distribution is relatively homogeneous throughout the particle (Figure 1d). At 300 °C for one hour, the histogram becomes asymmetric, and the main peak position remains unchanged. However, the weight at the low-energy end is higher. Although the oxidation state of the majority Ni is stable, there is a slightly reduced region, which can be attributed to the surface reduction layer (Figure 1d). At 500 °C for one hour, the low energy portion of the histogram evolves into a peak and shows a bimodal feature. This means the contribution of the reduced region is larger, and this can be assigned to the growth and inward evolution of the surface reduction layer (Figure 1d). At 700 °C for one hour, the overall histogram has around 2 eV shift to lower energy, showing the overall reduction of Ni in the particle. The slight shoulder at the high energy end indicates there is a small portion of high Ni oxidation state region remaining in the particle (Figure 1d). The depth profiles and energy distribution histograms of all intermediate states are shown in Figure S3 and S4, respectively. The results show that the surface Ni reduction and growth of the reduction layer thickness is a continuous process throughout the heating. Overall, we have identified the Mn diffusion from the surface coating layer to the bulk of LNO particles upon heating to 700 °C using the Ni oxidation state as an indicator. Mn diffusion into LNO takes place at 300 °C or potentially lower temperatures. Upon heating, the surface Mn layer proceeds to the center direction until Mn fully diffuses in the LNO particle at 700 °C for one hour.

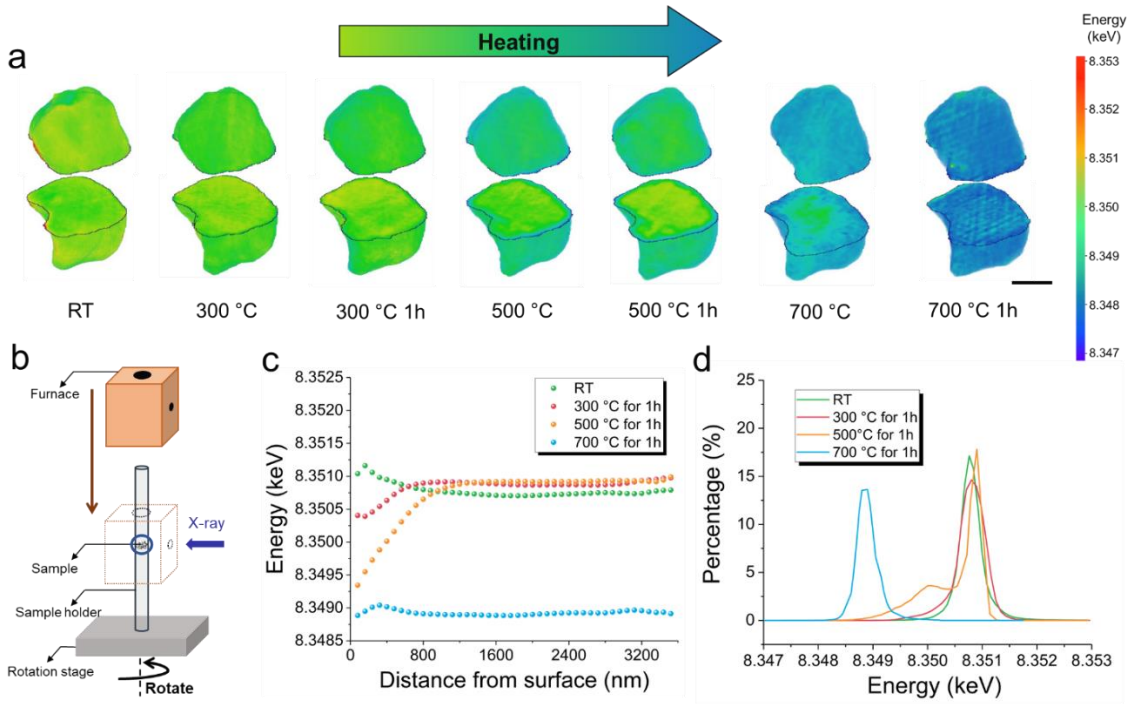

Figure 1. Electronic structure changes and elemental diffusion at the particle scale indicated by Ni K-edge TXM (a) Ni K-edge 3D TXM results for the samples at various stages of heating from room temperature (RT) to 700 °C for 1 h. Scale bar: 3 µm. (b) Schematic illustration of the *in situ* heating TXM experimental setup. (c) Ni K-edge white-line energy at different stages of heating as a function of the distance from the particle surface. The energy is the mean value of the Ni K-edge white-line energy of all voxels with the same distance from the surface of the particle. (d) The Ni K-edge white-line energy distribution of the samples at different stages of calcination.

To investigate the Mn diffusion behavior at various temperatures and holding stages, we reconstruct the 3D Mn tomography and align them with the LNO particle (Figure 2a). The cross-section images at different stages of heating show the inward diffusion of Mn inside the bulk of the LNO particle, which validates the 3D Ni K-edge TXM results (Figure 1,2a). We isolate the Mn diffusion layer in the LNO particle by

subtracting the Mn tomography at high temperatures from that of room temperature (Figure 2b). The diffusion frontier is defined as the inner-most layer with the Mn concentration above zero, as highlighted by the red circle (Figure 2b). Figure 2c shows the Mn concentration as a function of distance from the particle surface for Mn diffusion layers at various heating stages. The projection of the sloppy regions on the x-axis indicates the thickness of Mn diffusion layers (Figure 2c). The thickness of around 1 μm of the surface Mn diffusion layer at 300 °C and 500 °C is consistent with the results of the Ni K-edge TXM depth profile (Figure 1c,2c). In addition, the Mn diffusion layer has a concentration gradient of Mn from the surface to the center (Figure 2c). From 300 °C to 500 °C and the holding stage, the diffusion frontier barely evolves, meaning the thickness of the Mn diffusion layer remains almost identical (Figure 2c). However, Mn accumulates at the surface region as indicated by the increased Mn concentration, which explains the continuous Ni reduction at the surface at 500 °C (Figure 1c,2c). At 700 °C, the thickness of the Mn diffusion layer is doubled to around 2 μm, and the concentration of the diffused Mn significantly increases (Figure 2c). After holding at 700 °C for one hour, Mn diffuses to the center of the particle, and the concentration gradient of Mn from the surface to the core is maintained.

Next, we further study the effect of temperature on the distribution of Mn inside the LNO particle. We calculate the Mn concentration difference between the specific temperature and its holding stage at different depths (Figure 2d). The increased Mn concentration at the top surface due to one-hour of holding at 300 °C, 500 °C, and 700 °C is 0.05, 0.08, and 0.19, respectively (Figure 2d). This indicates a significantly higher Mn diffusion rate at higher temperatures. The Mn diffusion rate is not constant even at the same

temperature. Instead, it varies with different particle depths. From the surface to the core, the Mn diffusion rate undergoes an increase followed by a decrease for all samples (Figure 2d). The position of the highest Mn diffusion rate evolves deeper to the core with increasing temperature, as indicated by the arrow in Figure 2d. As Mn approaches the center of the particle, the Mn diffusion rate decreases gradually (Figure 2d). To validate the results, we have performed *in situ* heating 3D TXM on another Mn-coated LNO particle. The Ni oxidation state evolution shows the same trend as in the first particle upon heating (Figure S5). The depth profile confirms the gradual growth of surface reduction layer thickness and its extension to the center of the cathode particle with increasing temperature (Figure S6). The energy distribution histogram shows the overall shifting to lower energy throughout the heating process, and the intermediate states exhibit the bimodal feature or asymmetric peak shoulder (Figure S7). These results verify the repeatability of the discoveries from the first particle.

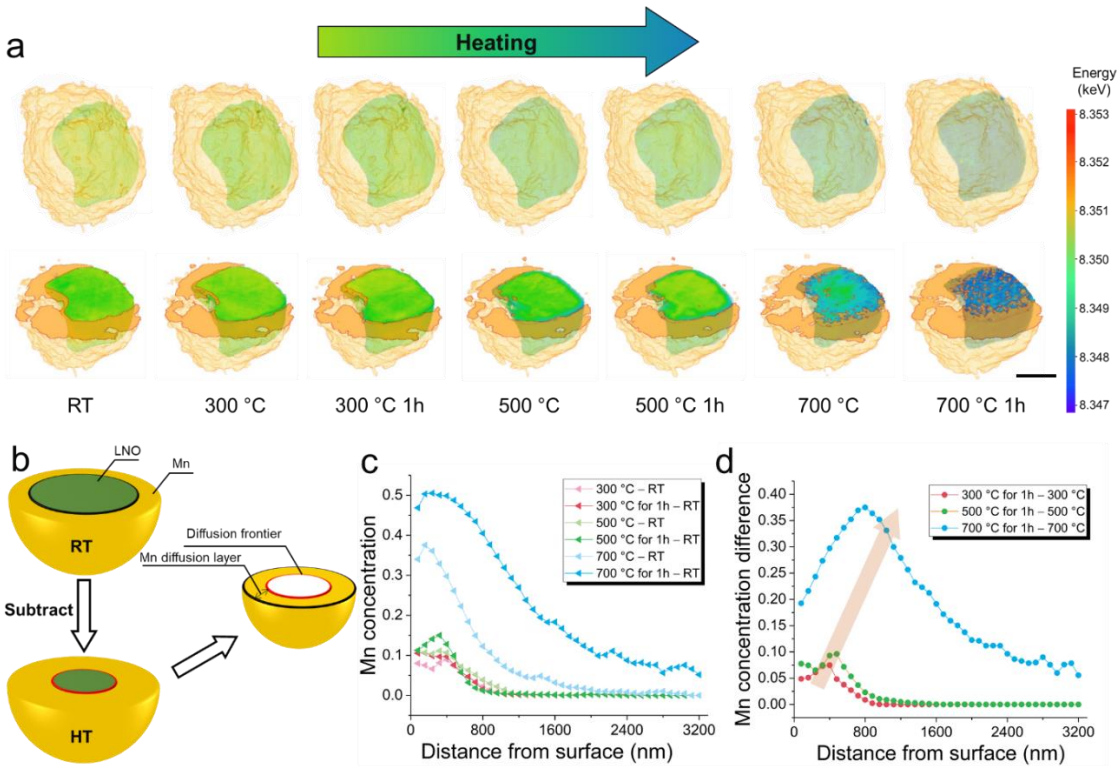

Figure 2. Electronic structure changes and elemental diffusion at the particle scale indicated by Mn K-edge TXM. (a) Aligned 3D Mn K-edge tomography with Ni K-edge TXM at various stages of heating from room temperature (RT) to 700 °C for 1 h. Scale bar: 3 µm. (b) Schematic illustration of the model to isolate the Mn diffusion layer. (c) Mn concentration at different stages of heating as a function of the distance from the particle surface. Mn concentration is defined as the ratio between the voxels with Mn K-edge absorption and all the voxels in the specific shells. (d) Mn concentration difference of the three intermediate states before and after holding at 300 °C, 500 °C, and 700 °C for 1 h as a function of the distance from the particle surface.

Beyond the particle level analyses, we further performed ensemble-averaged soft XAS and hard XAS measurements that are based on a large quantity of particles. Soft XAS is sensitive to the electronic and chemical structures of specific elements at the surface.[26]

With various detection modes, e.g., fluorescence yield (FY) and total electron yield (TEY), soft XAS is capable of probing around 50 nm and 10 nm deep into the surface, respectively.[26,27] The integrated intensity ratio of L_3 peak high energy shoulder (L_{3high}) to L_3 low energy shoulder (L_{3low}) for the Ni L-edge spectrum is positively correlated with the Ni oxidation state.[28] Ni L-edge spectra with FY mode show the L_{3high} to L_{3low} intensity ratio decreases with increasing temperature (Figure 3a). The integrated peak intensity ratio of L_{3high}/L_{3low} continuously decreases from 0.655 to 0.415 from room temperature to 700 °C for one hour, which means Ni at the surface is continuously reduced upon heating (Figure 3b). Ni L-edge spectra with TEY mode show minimal changes in the spectra and L_{3high} to L_{3low} intensity ratio, potentially due to the shallow probing depth of TEY mode and thick Mn coating layer (Figure S8-S9). In addition to surface evolution, the bulk properties usually play a vital role in determining cell performance. Hard XAS, including the X-ray near edge structure (XANES) and extended X-ray absorption fine structure (EXAFS), can resolve the electronic structure and local chemical environment inside the bulk of cathode particles.[26] Ni K-edge XANES spectra exhibit continuous shifts to lower energy at both half-intensity region and white-line region from room temperature to 700 °C for one hour, which indicates the continuous Ni reduction in the bulk upon heating (Figure 3c). Correspondingly, Mn undergoes oxidation upon heating, as indicated by the shift towards high energy of Mn K-edge spectra (Figure 3d). With higher temperatures, Ni K-edge and Mn K-edge EXAFS show slightly increased Ni-metal distance and decreased Mn-metal distance due to Ni reduction and Mn oxidation (Figure S10-S11). To further distinguish the local chemical environment of the transition metals, we performed an EXAFS wavelet transform (Figure 3e-h). Wavelet transform can differentiate the overlapped metal

coordination in R space by k space.[29–31] The wavelet transform maximum at around 2.5 Å (R + α) corresponds to the Mn-metal scattering in Mn K-edge EXAFS wavelet transform (Figure 3e-h). In k space, Mn-metal scattering is differentiated into Mn-Mn scattering and Mn-Ni scattering at around 7 $Å^{-1}$ (k) and 9 $Å^{-1}$ (k), respectively, due to different atomic masses (Figure 3e-h). Upon heating to 300 °C for one hour, Mn-Ni scattering starts to appear, indicating the initial diffusion of Mn in the LNO (Figure 3f). As heated to 500 °C for one hour, the signal of Mn-Ni scattering becomes more substantial (Figure 3g). From 500 °C to 700 °C for one hour, the Mn-Ni interatomic distance decreases, which implies that Mn further diffuses to the bulk of LNO (Figure 3g,h). In all, the ensemble-averaged soft XAS and hard XAS results confirm that the Mn diffusion behavior probed by 3D TXM is statistically representative.

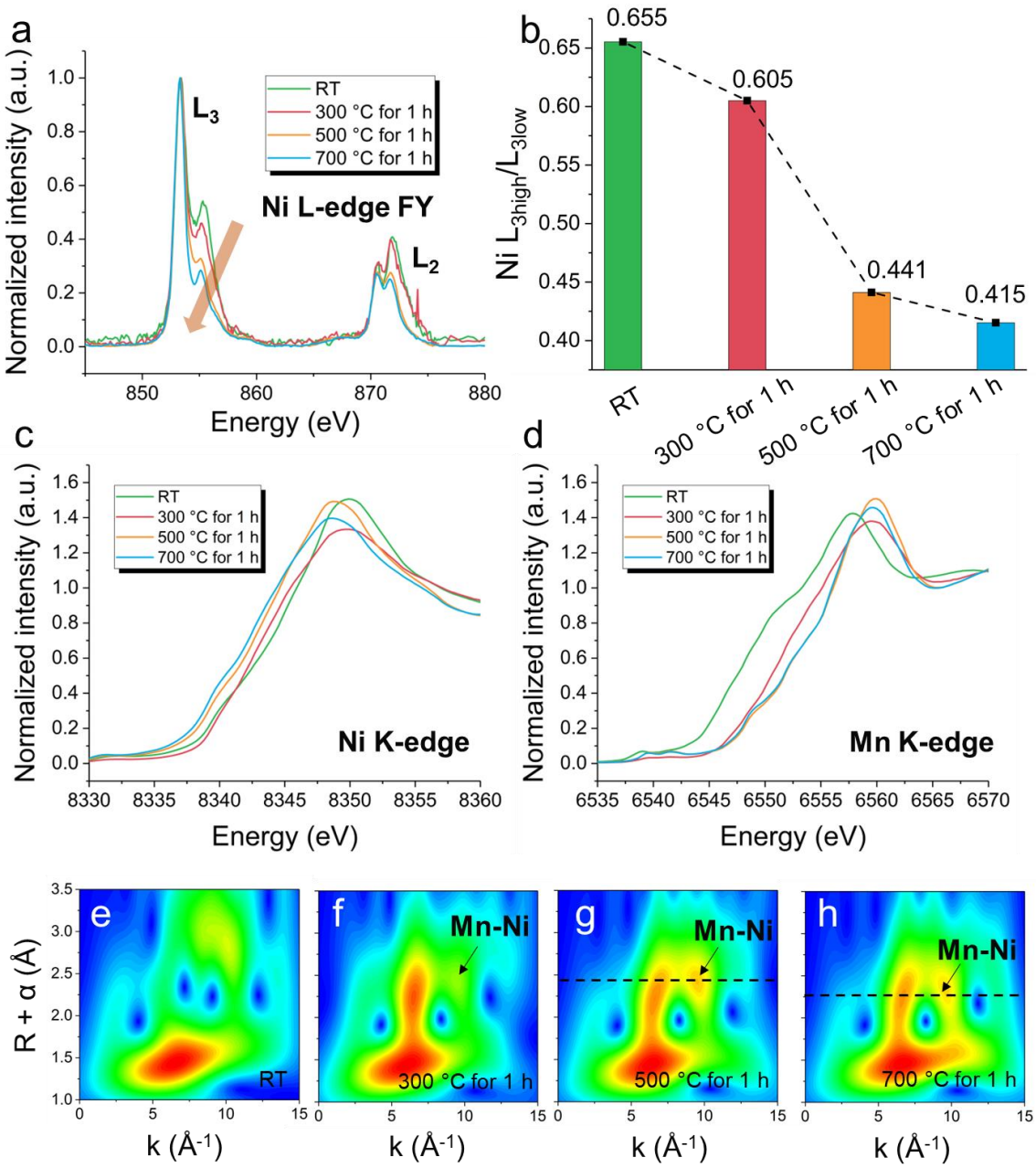

Figure 3. Electronic and chemical structure changes and elemental diffusion at the ensemble-averaged scale at various stages of heating. (a) Ni L-edge soft XAS spectra with the FY mode at different stages of heating. (b) The Ni L_{3high}/L_{3low}-edge values at different stages of heating for FY mode. (c) Ni K-edge and (d) Mn K-edge XANES spectra at different stages of heating. Wavelet transformation of Mn K-edge EXAFS for the samples

e) at room temperature (RT), (f) heated at 300 °C for 1 h, (g) heated at 500 °C for 1 h, (h) heated at 700 °C for 1 h.

Mn in the lattice can alter the crystal structure to different extents with various concentrations and distributions. We performed synchrotron XRD and Rietveld refinements for the Mn-coated LNO at different stages of heating (Figure 4). The pristine sample at room temperature exhibits a hexagonal α-$NaFeO_2$ layered structure with $R\bar{3}m$ space group (Figure 4a). The Li/Ni cation mixing level is 3.9% (Table S1). At 500 °C for one hour, Mn diffuses into LNO. We define the pure LNO phase as Phase 1 and a relatively Mn-rich layered phase $(Li_{0.6}Ni_{0.2})Ni_{0.8}Mn_{0.2}O_2$ as Phase 2 to perform the Rietveld refinement (Figure 4b). The Li/Ni cation mixing level increases to 5.1% (Table S1). The fraction of Phase 1 to Phase 2 is 0.75: 0.25 (Table S1). As the temperature further increases to 700 °C for one hour, the Li/Ni cation mixing becomes 8.9%. The weight of Phase 2 also increases by 2% with a Phase 1 to Phase 2 fraction of 0.73: 0.27 (Table S1). The lattice parameters and lattice volume of the LNO phase also increase slightly with increasing temperature (Table S1). Upon heating, Mn^{2+} is oxidized and occupies the Ni site in the LNO lattice. Meanwhile, Ni is reduced and occupies the Li site to form a new layered phase $(Li_{1-2x}Ni_x)Ni_{1-x}Mn_xO_2$ with Li loss taking place as shown in Reaction (1):

$$LiNiO_2 + x\ Mn(OH)_2 \rightarrow (Li_{1-2x}Ni_x)Ni_{1-x}Mn_xO_2 + 2x\ LiOH \qquad (1)$$

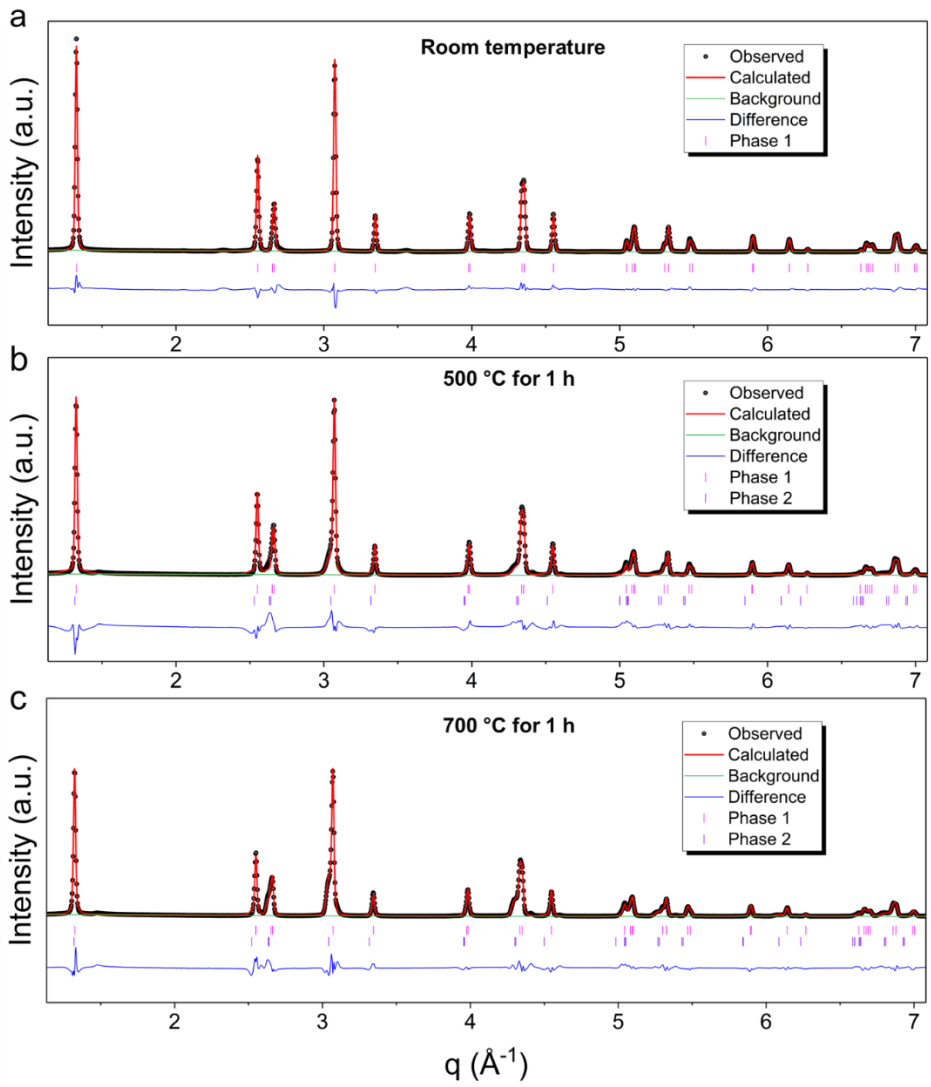

Figure 4. Global structural change and phase evolution upon Mn diffusion. XRD patterns and Rietveld refinement of the samples a) at room temperature (R_{wp} = 7.70%), (b) heated at 500 °C for 1 h (R_{wp} = 14.33%), (g) heated at 700 °C for 1 h (R_{wp} = 10.88%). Phase 1 is defined as the pure LNO phase, and Phase 2 is defined as $(Li_{0.6}Ni_{0.2})Ni_{0.8}Mn_{0.2}O_2$.

3.5. Discussion

This study investigates the elemental diffusion behavior and correlated chemical and structural changes within the cathode particles upon thermal treatment at multiple length scales using Mn-coated single crystal LNO as the platform. At pristine state, Ni is

slightly oxidized at some regions of the cathode surface because the cathode synthesis is anisotropic and non-uniform. Mn diffusion from the surface coating layer to the LNO particle has already taken place at 300 °C. After holding at 300 °C for one hour, the Mn diffusion layer within the LNO particle grows to around 1 μm. Ni within the Mn diffusion layer is reduced, and Mn is oxidized. In addition, Mn concentration is the highest at the top surface and the lowest at the diffusion frontier in the center, forming a Mn concentration gradient structure. Upon heating to 500 °C and holding for one hour, the thickness of the Mn diffusion layer remains almost unchanged. However, Mn concentration at the surface becomes higher, leading to continuous Ni reduction. At 700 °C, the thickness of the Mn diffusion layer increases to around 2 μm. Mn concentration in the Mn diffusion layer significantly increases. After holding at 700 °C for one hour, Mn diffuses to the center of the particle, and the concentration gradient of Mn from the surface to the core is maintained. Ni is reduced throughout the particle. We observed a significantly higher Mn diffusion rate with higher temperatures. Interestingly, our particle-level measurement reveals that the Mn diffusion rate varies with the depth, even at the same temperature. The diffusion rate of Mn increases first and then decreases from the particle surface to the bulk. The position of the highest Mn diffusion rate evolves to the core direction as temperature increases. The continuous reduction of Ni and oxidation of Mn are verified by soft XAS and hard XAS at the ensemble-averaged scale. Mn K-edge EXAFS wavelet transform shows the incorporation of Mn into the LNO lattice upon heating. Our structural characterizations reveal that the Li/Ni cation mixing level increases, and the fraction of the Mn-rich phase increases upon heating. Combined with the chemical structure analyses, we propose that Mn^{2+} is oxidized and occupies the Ni site in the LNO lattice during the inward

diffusion process. Meanwhile, Ni is reduced and occupies the Li site to form a new layered phase $(Li_{1-2x}Ni_x)Ni_{1-x}Mn_xO_2$ with Li loss taking place.

This work first probed the real-time transition metal ion diffusion inside the cathode particle at the particle scale complemented by the characterizations from multiple length scales. We found that the coating element does not solely remain on the surface of the cathode with the heat treatment at around 500 °C, as widely adopted in coating approaches. In contrast, the coating element can diffuse in the cathode lattice and forms a gradient distribution. Therefore, a combination of coating, doping, and concentration gradient at various extents can be potentially achieved by tuning the heating condition to modify the materials properties and achieve better performance. Noting that the method demonstrated in this work can be widely applied to study ion diffusion in solid-state materials, although the diffusion behavior of specific elements may vary with their properties, such as oxidation state, ionic radius, and concentration.

3.6. Acknowledgements

The work is supported by the U.S. Department of Energy's Office of Energy Efficiency and Renewable Energy (EERE) under the award number: DE-EE0008444. The use of the Stanford Synchrotron Radiation Lightsource, SLAC National Accelerator Laboratory, is supported by the U.S. Department of Energy, Office of Science, Office of Basic Energy Sciences under Contract No. DE-AC02-76SF00515. This research used resources of the Advanced Photon Source, a U.S. Department of Energy (DOE) Office of Science User Facility operated for the DOE Office of Science by Argonne National Laboratory under Contract No. DE-AC02-06CH11357. The research used 18-ID of the National Synchrotron Light Source II, a U.S. Department of Energy (DOE) Office of

Science User Facility operated for the DOE Office of Science by Brookhaven National Laboratory under Contract No. DE-SC0012704. This research was partially supported by Virginia Tech's Institute for Critical Technology and Applied Science through instruments provided by the Nanoscale Characterization and Fabrication Laboratory (NCFL).

3.7. References

(1) Yang, Z.; Huang, H.; Lin, F.; Yang, Z.; Lin, F.; Huang, H. Sustainable Electric Vehicle Batteries for a Sustainable World: Perspectives on Battery Cathodes, Environment, Supply Chain, Manufacturing, Life Cycle, and Policy. *Adv. Energy Mater.* **2022**, *12* (26), 2200383.

(2) Xu, J.; Lin, F.; Doeff, M. M.; Tong, W. A Review of Ni-Based Layered Oxides for Rechargeable Li-Ion Batteries. *J. Mater. Chem. A* **2017**, *5* (3), 874–901.

(3) Liu, W.; Oh, P.; Liu, X.; Lee, M.-J.; Cho, W.; Chae, S.; Kim, Y.; Cho, J. Nickel-Rich Layered Lithium Transition-Metal Oxide for High-Energy Lithium-Ion Batteries. *Angew. Chemie Int. Ed.* **2015**, *54* (15), 4440–4457.

(4) Bianchini, M.; Roca-Ayats, M.; Hartmann, P.; Brezesinski, T.; Janek, J. There and Back Again—The Journey of $LiNiO_2$ as a Cathode Active Material. *Angew. Chemie Int. Ed.* **2019**, *58* (31), 10434–10458.

(5) Manthiram, A.; Knight, J. C.; Myung, S. T.; Oh, S. M.; Sun, Y. K. Nickel-Rich and Lithium-Rich Layered Oxide Cathodes: Progress and Perspectives. *Adv. Energy Mater.* **2016**, *6* (1), 1501010.

(6) Li, W.; Lee, S.; Manthiram, A. High-Nickel NMA: A Cobalt-Free Alternative to NMC and NCA Cathodes for Lithium-Ion Batteries. *Adv. Mater.* **2020**, *32* (33), 2002718.

(7) Pouillerie, C.; Croguennec, L.; Delmas, C. The $Li_xNi_{1-y}Mg_yO_2$ (y=0.05, 0.10) System: Structural Modifications Observed upon Cycling. *Solid State Ionics* **2000**, *132* (1–2), 15–29.

(8) Kim, J.; Amine, K. The Effect of Tetravalent Titanium Substitution in $LiNi_{1-x}Ti_xO_2$ ($0.025 \leq x \leq 0.2$) System. *Electrochem. commun.* **2001**, *3* (2), 52–55.

(9) Yoon, C. S.; Choi, M.-J.; Jun, D.-W.; Zhang, Q.; Kaghazchi, P.; Kim, K.-H.; Sun, Y.-K. Cation Ordering of Zr-Doped $LiNiO_2$ Cathode for Lithium-Ion Batteries. *Chem. Mater.* **2018**, *30* (5), 1808–1814.

(10) Weigel, T.; Schipper, F.; Erickson, E. M.; Susai, F. A.; Markovsky, B.; Aurbach, D. Structural and Electrochemical Aspects of $LiNi_{0.8}Co_{0.1}Mn_{0.1}O_2$ Cathode Materials Doped by Various Cations. *ACS Energy Lett.* **2019**, *4* (2), 508–516.

(11) Manthiram, A.; Song, B.; Li, W. A Perspective on Nickel-Rich Layered Oxide Cathodes for Lithium-Ion Batteries. *Energy Storage Mater.* **2017**, *6*, 125–139.

(12) Sun, Y.-K.; Chen, Z.; Noh, H.-J.; Lee, D.-J.; Jung, H.-G.; Ren, Y.; Wang, S.; Yoon, C. S.; Myung, S.-T.; Amine, K. Nanostructured High-Energy Cathode Materials for Advanced Lithium Batteries. *Nat. Mater.* **2012**, *11* (11), 942–947.

(13) Yoon, C. S.; Kim, U.-H.; Park, G.-T.; Kim, S. J.; Kim, K.-H.; Kim, J.; Sun, Y.-K. Self-Passivation of a $LiNiO_2$ Cathode for a Lithium-Ion Battery through Zr Doping. *ACS Energy Lett.* **2018**, *3* (7), 1634–1639.

(14) Schipper, F.; Bouzaglo, H.; Dixit, M.; Erickson, E. M.; Weigel, T.; Talianker, M.; Grinblat, J.; Burstein, L.; Schmidt, M.; Lampert, J.; Erk, C.; Markovsky, B.; Major, D. T.; Aurbach, D. From Surface ZrO_2 Coating to Bulk Zr Doping by High Temperature Annealing of Nickel-Rich Lithiated Oxides and Their Enhanced

Electrochemical Performance in Lithium Ion Batteries. *Adv. Energy Mater.* **2018**, *8* (4), 1701682.

(15) Xin, F.; Zhou, H.; Zong, Y.; Zuba, M.; Chen, Y.; Chernova, N. A.; Bai, J.; Pei, B.; Goel, A.; Rana, J.; Wang, F.; An, K.; Piper, L. F. J.; Zhou, G.; Whittingham, M. S. What Is the Role of Nb in Nickel-Rich Layered Oxide Cathodes for Lithium-Ion Batteries? *ACS Energy Lett.* **2021**, *6* (4), 1377–1382.

(16) Riesgo-González, V.; Hall, D. S.; Märker, K.; Slaughter, J.; Wright, D. S.; Grey, C. P. Effect of Annealing on the Structure, Composition, and Electrochemistry of NMC811 Coated with Al_2O_3 Using an Alkoxide Precursor. *Chem. Mater.* **2022**.

(17) Yang, Z.; Mu, L.; Hou, D.; Rahman, M. M.; Xu, Z.; Liu, J.; Nordlund, D.; Sun, C.; Xiao, X.; Lin, F. Probing Dopant Redistribution, Phase Propagation, and Local Chemical Changes in the Synthesis of Layered Oxide Battery Cathodes. *Adv. Energy Mater.* **2020**, 2002719.

(18) Mu, L.; Zhang, R.; Kan, W. H.; Zhang, Y.; Li, L.; Kuai, C.; Zydlewski, B.; Rahman, M. M.; Sun, C.-J. J.; Sainio, S.; Avdeev, M.; Nordlund, D.; Xin, H. L.; Lin, F. Dopant Distribution in Co-Free High-Energy Layered Cathode Materials. *Chem. Mater.* **2019**, *31* (23), 9769–9776.

(19) Zhao, Y.; Li, J.; Dahn, J. R. Interdiffusion of Cations from Metal Oxide Surface Coatings into $LiCoO_2$ During Sintering. *Chem. Mater.* **2017**, *29* (12), 5239–5248.

(20) Li, J.; Doig, R.; Camardese, J.; Plucknett, K.; Dahn, J. R. Measurements of Interdiffusion Coefficients of Transition Metals in Layered Li–Ni–Mn–Co Oxide Core–Shell Materials during Sintering. *Chem. Mater.* **2015**, *27* (22), 7765–7773.

(21) Herzog, M. J.; Gauquelin, N.; Esken, D.; Verbeeck, J.; Janek, J. Facile Dry Coating

Method of High-Nickel Cathode Material by Nanostructured Fumed Alumina (Al_2O_3) Improving the Performance of Lithium-Ion Batteries. *Energy Technol.* **2021**, *9* (4), 2100028.

(22) Antonelli, S.; Ronne, A.; Han, I.; Ge, M.; Layne, B.; Shahani, A. J.; Iwamatsu, K.; Wishart, J. F.; Hulbert, S. L.; Lee, W. K.; Chen-Wiegart, Y. C. K.; Xiao, X. Versatile Compact Heater Design for in Situ Nano-Tomography by Transmission X-Ray Microscopy. *J. Synchrotron Radiat.* **2020**, *27* (3), 746–752.

(23) Xiao, X.; Xu, Z.; Lin, F.; Lee, W. K. TXM-Sandbox: An Open-Source Software for Transmission X-Ray Microscopy Data Analysis. *J. Synchrotron Rad.* **2022**, *29* (1), 266–275.

(24) Xiao, X.; Xu, Z.; Hou, D.; Yang, Z.; Lin, F. Rigid Registration Algorithm Based on the Minimization of the Total Variation of the Difference Map. *J. Synchrotron Radiat.* **2022**, *29* (4), 1085–1094.

(25) Kuppan, S.; Xu, Y.; Liu, Y.; Chen, G. Phase Transformation Mechanism in Lithium Manganese Nickel Oxide Revealed by Single-Crystal Hard X-Ray Microscopy. *Nat. Commun.* **2017**, *8* (1).

(26) Lin, F.; Liu, Y.; Yu, X.; Cheng, L.; Singer, A.; Shpyrko, O. G.; Xin, H. L.; Tamura, N.; Tian, C.; Weng, T.-C.; Yang, X.-Q.; Meng, Y. S.; Nordlund, D.; Yang, W.; Doeff, M. M. Synchrotron X-Ray Analytical Techniques for Studying Materials Electrochemistry in Rechargeable Batteries. *Chem. Rev.* **2017**, *117* (21), 13123–13186.

(27) Lin, F.; Nordlund, D.; Markus, I. M.; Weng, T.-C. C.; Xin, H. L.; Doeff, M. M. Profiling the Nanoscale Gradient in Stoichiometric Layered Cathode Particles for

Lithium-Ion Batteries. *Energy Environ. Sci.* **2014**, *7* (9), 3077–3085.

(28) Lin, F.; Markus, I. M.; Nordlund, D.; Weng, T.-C.; Asta, M. D.; Xin, H. L.; Doeff, M. M. Surface Reconstruction and Chemical Evolution of Stoichiometric Layered Cathode Materials for Lithium-Ion Batteries. *Nat. Commun.* **2014**, *5* (1), 3529.

(29) Funke, H.; Scheinost, A. C.; Chukalina, M. Wavelet Analysis of Extended X-Ray Absorption Fine Structure Data. *Phys. Rev. B - Condens. Matter Mater. Phys.* **2005**, *71* (9), 094110.

(30) Funke, H.; Chukalina, M.; Scheinost, A. C. A New FEFF-Based Wavelet for EXAFS Data Analysis. *J. Synchrotron Radiat.* **2007**, *14* (5), 426–432.

(31) Xia, Z.; Zhang, H.; Shen, K.; Qu, Y.; Jiang, Z. Wavelet Analysis of Extended X-Ray Absorption Fine Structure Data: Theory, Application. *Phys. B Condens. Matter* **2018**, *542*, 12–19.

3.8. Supplementary information

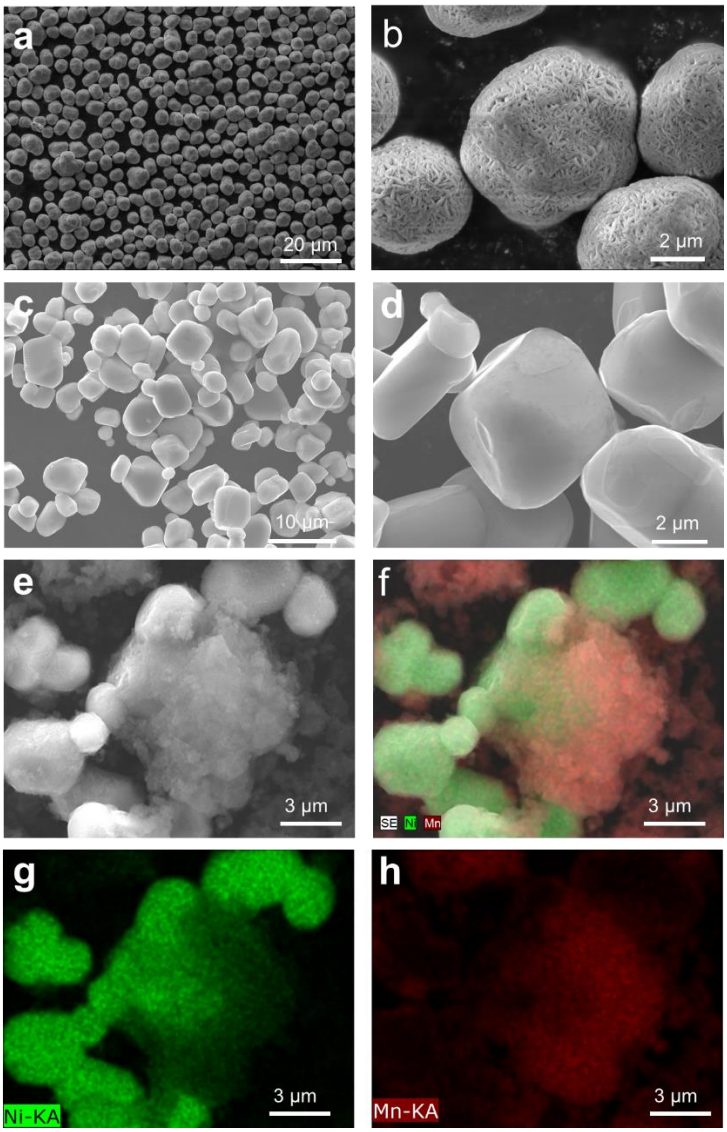

Figure S1. Scanning electron microscopy (SEM) images of (a-b) $Ni(OH)_2$ precursor at different length scales, (c-d) pristine single crystal $LiNiO_2$ (LNO) at different magnifications, (e) Mn-coated LNO. Energy dispersive X-ray spectroscopy (EDS) mapping of (f) Mn-coated LNO, (g) Ni elemental distribution in (f) and (h) Mn elemental distribution in (f).

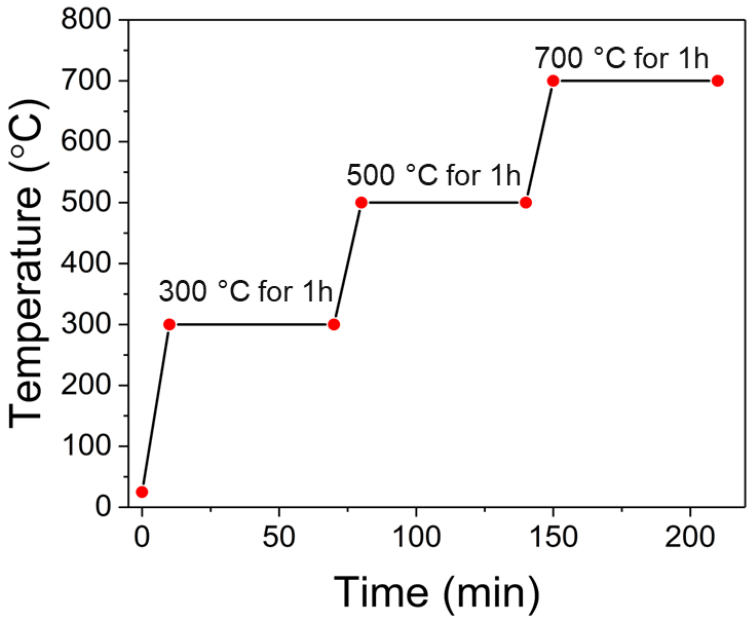

Figure S2. Thermal profile applied in this study.

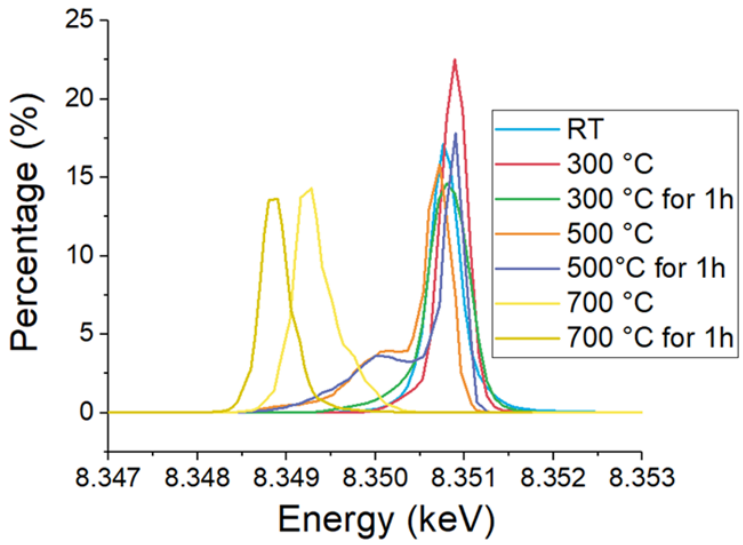

Figure S3. Ni K-edge white-line energy distribution of the samples at all stages of calcination.

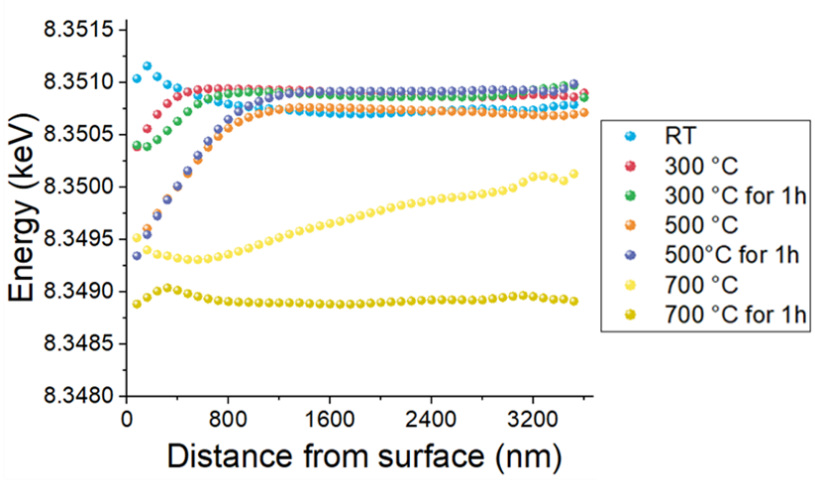

Figure S4. Ni K-edge white-line energy at all stages of heating as a function of the distance from the particle surface. The energy is the mean value of the Ni K-edge white-line energy of all voxels with the same distance from the surface in the particle.

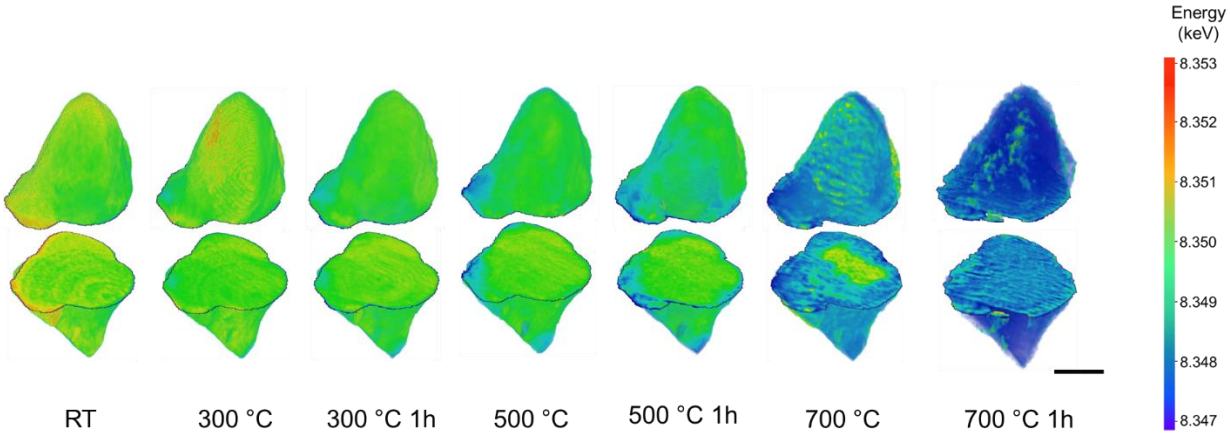

Figure S5. Ni K-edge 3D TXM results for the second particle at various stages of heating from room temperature (RT) to 700 °C for 1 h

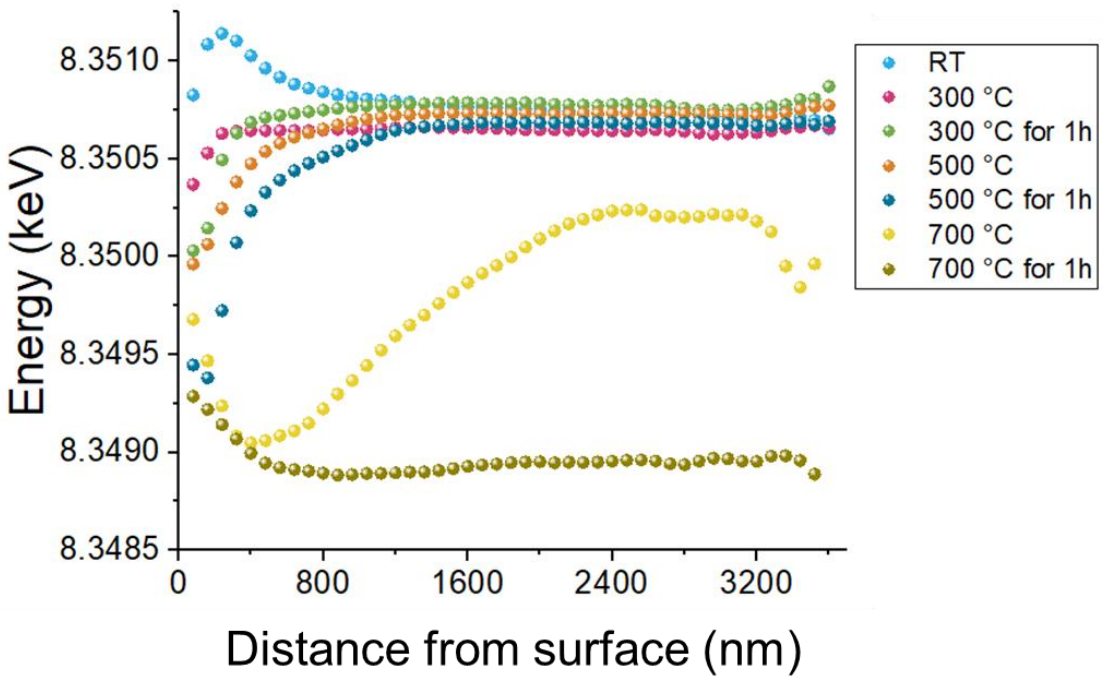

Figure S6. Ni K-edge white-line energy at all stages of heating as a function of the distance from the particle surface for the second particle. The energy is the mean value of the Ni K-edge white-line energy of all voxels with the same distance from the surface in the particle.

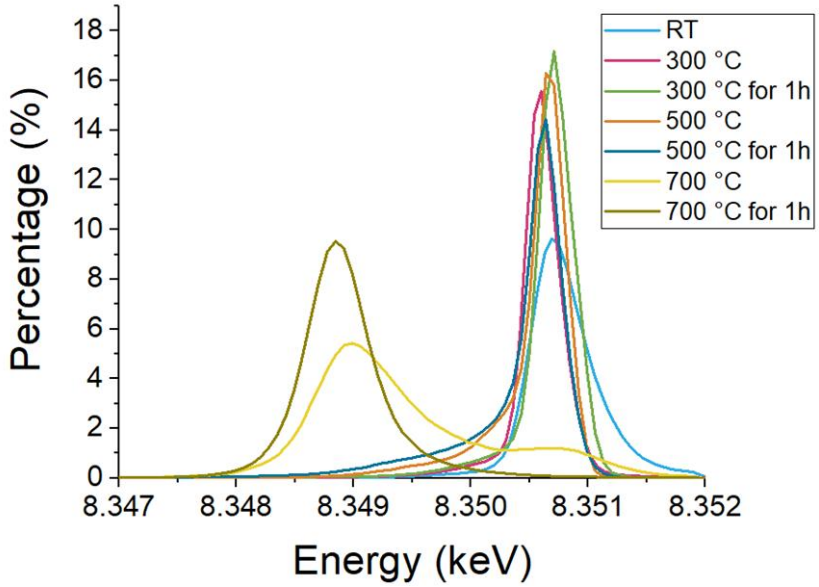

Figure S7. Ni K-edge white-line energy distribution of the samples at all stages of calcination for the second particle.

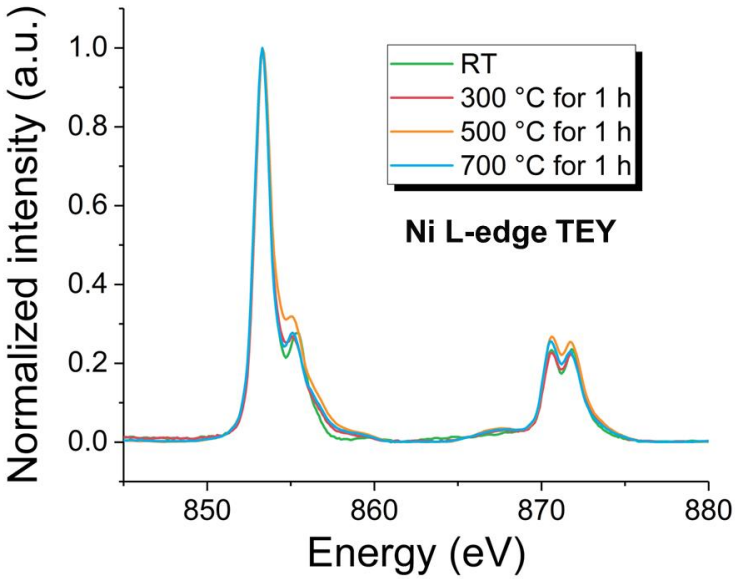

Figure S8. Ni L-edge soft XAS spectra with the TEY (total electron yield) mode at different stages of heating.

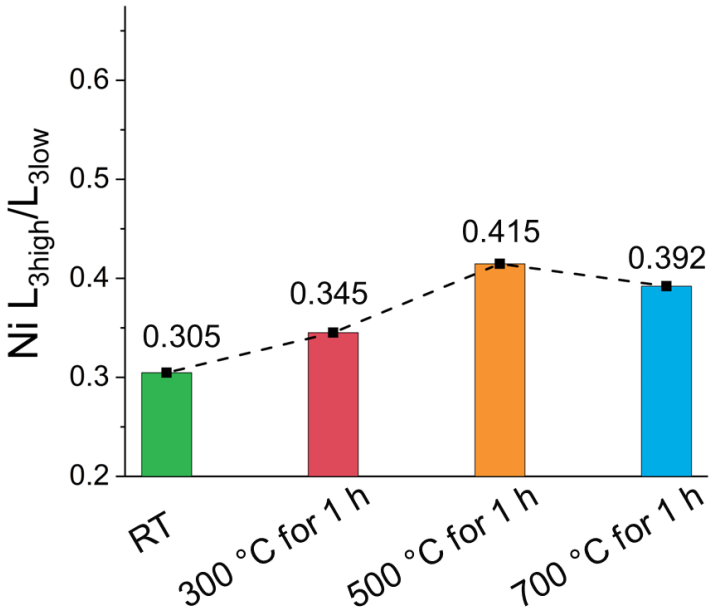

Figure S9. The Ni L_{3high}/L_{3low}-edge values at different stages of heating for TEY (total electron yield) mode.

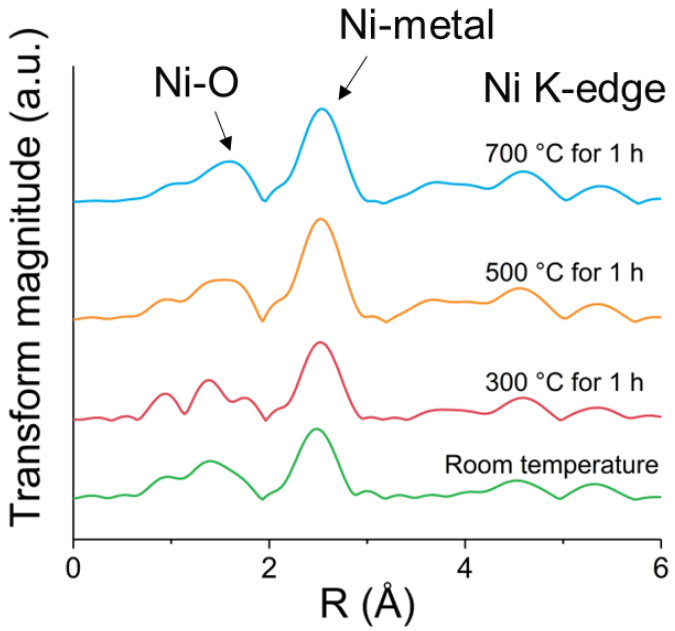

Figure S10. Ni K-edge Fourier transformed EXAFS at different stages of calcination.

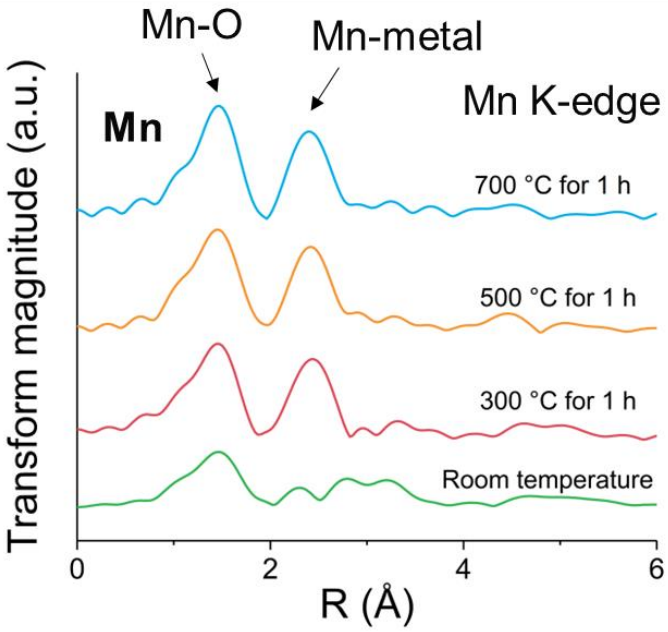

Figure S11. Mn K-edge Fourier transformed EXAFS at different stages of calcination.

Table S1. Structural parameters of the samples at different stages of heating determined from Rietveld refinement of X-ray diffraction data.

Sample	a, b (Å)	c (Å)	Volume ($Å^3$)	Li/Ni cation mixing	Phase 1:Phase 2 fraction
Room temperature	2.8858	14.2145	102.513	0.039	1:0
500 °C for 1 h	2.8884	14.2259	102.781	0.051	0.75:0.25
700 °C for 1 h	2.8883	14.2225	102.752	0.089	0.73:0.27

4. Surface layer formation enabling high interfacial stability and homogeneous charge distribution in Ni-rich layered oxides

*Zhijie Yang[1#], Huabin Sun[1,2#], Anyang Hu[1], Yuxin Zhang[1], Jue Liu[3], Chengjun Sun[4], Sami Sainio[5], Dennis Nordlund[5], Xianghui Xiao[6], Yijin Liu[5], Wei Luo[2], Yunhui Huang[2], Feng Lin[1]**

1. Department of Chemistry, Virginia Tech, Blacksburg, VA, 24061, USA
2. Institute of New Energy for Vehicles, Shanghai Key Lab. of D&A for Metal-Functional Materials, School of Materials Science and Engineering, Tongji University, Shanghai 201804, China
3. Oak Ridge National Laboratory, Oak Ridge, TN, 37831, USA
4. Advanced Photon Source, Argonne National Laboratory, Argonne, IL, 60439, USA
5. Stanford Synchrotron Radiation Lightsource, SLAC National Accelerator Laboratory, Menlo Park, CA, 94025, USA
6. National Synchrotron Light Source II, Brookhaven National Laboratory, Upton, NY, 11973, USA

Correspondence and requests for materials should be addressed to F.L. (email: fenglin@vt.edu)

# equal contributions

4.1. Abstract

Ni-rich layered oxide cathodes have drawn extensive interest due to their high energy density, which corresponds to the long driving range of electric vehicles (EVs) as the EV industry demands. However, the structural and electrochemical instability issues of these Ni-rich layered cathodes impede their further applications. The materials degradation usually initiates at the cathode-electrolyte interface due to parasitic reactions and proceeds in the bulk of cathode particles. Therefore, enhancing the cathode surface stability is vital to improve the overall battery cycle life. Multiple materials modification approaches have been applied, such as surface coating and core-shell structure fabrication. Nevertheless, these methods usually require additional processing steps that can raise energy consumption and cost. Herein, we developed a facile quenching approach to creating a surface passivation layer on the cathode during the synthesis. We investigated the evolution of crystal structure and the chemical environment with a series of characterization tools from various length scales. We found that surface passivation layer formation can enhance the cycling stability of NMC cathodes by promoting cathode and electrolyte interfacial stability and homogeneous charge distribution. This study contributes to the understanding of surface passivation layer-induced cathode chemical and structural changes and guides the surface engineering of Ni-rich layered oxide cathodes to enable high-energy next-generation Li-ion batteries.

4.2. Introduction

With the increasing demand for higher energy density in Li-ion battery applications, particularly electric vehicles, the development of Ni-based layered oxide cathode materials has been focused on increasing the Ni content. However, the lifetime and thermal stability

of these Ni-rich cathodes decrease with higher Ni content due to more severe surface degradation and lower bulk structure robustness.[1] The performance degradation of the Ni-rich cathodes usually initiates at the cathode surface, such as the parasitic reactions with electrolytes, cathode surface lattice structure reconstruction, and metal cations dissolution.[2–4] Upon extensive cycles of Li-ion intercalation and deintercalation, the effect of these surface degradation becomes more pronounced. Although battery performance is generally a bulk electrochemical process, the surface reaction largely leverages the interface reaction followed by bulk structure evolution. The surface side reactions can result in cathode bulk deterioration, such as crack formation, which can eventually lead to cell-level resistance growth and capacity fade.[5] Therefore, protecting the cathode surface is vital to promote the overall cell stability of Ni-rich cathodes.

Several approaches have been widely applied to address the cathode surface instability issue, such as surface coating, elemental concentration gradient or core-shell structure engineering, and artificial cathode electrolyte interface (CEI) fabrication.[6–11] These methods can build a less reactive protection layer at the cathode surface to mitigate the parasitic reactions with the electrolyte and undesired phase transformations. For instance, Monhanty *et al.* reported that Al_2O_3 and TiO_2 coating layers on Ni-rich cathodes by atomic layer deposition (ALD) could significantly enhance the cell cycling stability with lower charge transfer impedance.[12] However, these approaches usually require additional processing steps, such as adding coating species to the as-synthesized cathode, followed by heating, to form the surface layer.[6] In addition, it is not well understood how the surface layer impacts charge distribution and lattice structure changes in the bulk.

Herein, we fabricate a surface passivation layer for NMC particles through a facile quenching approach during the synthesis of the cathode. We studied lattice structure change and redox chemistry using a combination of bulk and surface structural characterization methods, i.e., soft X-ray absorption spectroscopy (XAS), and hard XAS. We further resolved the charge distribution at the single particle level through full-field transmission X-ray microscopy (TXM). The surface layer can leverage the bulk chemistry, including valence state and charge distribution. We found that surface passivation layer formation can enable high interfacial stability and homogeneous charge distribution, impelling superior electrochemical performance of NMC cathode materials. The facile approach to fabricating the surface passivation layer of NMC particles in this study can enhance electrochemical properties, especially cycling stability. This work provides insights into the underlying mechanism of the surface layer effect and sheds light on the optimization of high-capacity cathodes in LIBs through surface engineering.

4.3. Materials and methods

Material synthesis:

The precursor of $Ni_{0.8}Mn_{0.1}Co_{0.1}(OH)_2$ (Shuangdeng Group Co, Ltd.) was thoroughly ground with LiOH for one hour. 5 mol% excess Li was added to compensate for the Li loss during high-temperature calcination. The obtained powder was calcined at 460 °C for two hours, followed by 750 °C for six hours with a temperature ramping rate of 3 °C/min. Subsequently, two protocols of cooling were performed to obtain the $LiNi_{0.8}Mn_{0.1}Co_{0.1}O_2$ cathode with and without surface modification: (1) slow cooling under constant oxygen flow (denoted as NMC); (2) swiftly moving the powder outside the furnace and quenching in the air (denoted as NMC-L).

Materials characterizations:

Synchrotron X-ray diffraction (XRD) was performed at the beam line 11-3 of Stanford Synchrotron Radiation Lightsource (SSRL). The wavelength of the applied X-ray is 0.976 Å. Neutron diffraction (ND) was performed on Nanoscale-Ordered Materials Diffractometer (NOMAD) BL-1B, Spallation Neutron Source (SNS) at Oak Ridge National Laboratory. About 0.2-0.3 g powder sample was loaded into the quartz capillary (3mm) and each measurement took about 1 hour. The refinement of neutron diffraction patterns was conducted using the software GSAS EXPGUI to identify the lattice structure and Li/Ni cation mixing in NMC and NMC-L samples. The morphology of the NMC and NMC-L powder was performed by scanning electron microscopy (SEM, FEI Quanta 600 FEG). Hard XAS (XANES and EXAFS) measurement was performed using a Si (111) monochromator at the beamline 20-ID of the Advanced Photon Source (APS) at Argonne National Laboratory. The absorption energy calibration was based on the first inflection points of the Ni, Mn, and Co reference spectra that were collected from a Ni foil reference simultaneously with the samples. X-ray photoelectron spectroscopy (XPS) measurements were performed on the PHI VersaProbe III with a monochromatic Al K-alpha X-ray source (1486.6 eV). Soft XAS was performed at the Stanford Synchrotron Radiation Lightsource (SSRL) beamline 10-1, SLAC National Accelerator Laboratory using a ring current of 350 mA and a 1000 L mm^{-1} spherical grating monochromator with 20 μm entrance and exit slits, providing ~10^{11} ph s^{-1} at 0.2 eV resolution in a 1 mm^2 beam spot. Data were acquired under ultrahigh vacuum (10^{-9} Torr) in a single load at room temperature using total electron yield (TEY), where the sample drain current was collected. The samples were mounted on an aluminum sample holder in an Ar-filled glove box and well-sealed for transfer. The full-

field transmission X-ray microscopy (TXM) was performed at beamline 18-1D at National Synchrotron Light Source II (NSLS-II), Brookhaven National Laboratory. A python-based software TXM-Sandbox was used to reconstruct and analyze the tomographic datasets,[13,14] a commercial software Avizo was used for visualization. To identify charge distribution in NMC and NMC-L particles, the 2D nanodomain valence gradient vectors were calculated by adding two partial valence gradient vectors. The vector direction presents the local distribution of Ni valence states and the vector magnitude is proportional to the local valence states gradient. The definition of 3D nanodomain valence gradient vectors was discussed in our earlier publication and are referenced here.[15]

Electrochemical measurements:

The NCM and NMC-L electrodes were prepared with the same procedure. To prepare the composite electrode slurry, poly(vinylidene difluoride, as the binder) (PVdF) was first dissolved into N-methyl-2-pyrrolidone, then the active material product obtained after calcination and the acetylene carbon were added into the solution and thoroughly mixed, following the ratio of active material: PVdF: acetylene carbon = 90 wt %: 5 wt %: 5 wt %. The slurry was subsequently cast on the carbon-coated aluminum foil and dried at 120 °C for 12 h in a vacuum oven. The dry composite electrode was punched into disks of a diameter of 10 mm with a mass loading of ~1.4 mAh/cm^2. The obtained composite electrodes were used as cathode and the Li foils were used as the anode with the Whatman glass fiber (1827-047934-AH) as the separator to assemble the CR2032 coin cells in an Ar-filled glove box. The electrolyte is 1 M $LiPF_6$ in ethylene carbonate (EC) and ethyl methyl carbonate (EMC) with 2 wt % vinylene carbonate (VC). All coin cells were cycled using a LAND battery testing system from 2.8 to 4.5 V vs. Li/Li$^+$. For

galvanostatic charge/discharge experiments, cells were cycled at 0.5C and 1C, with a definition of 1C as fully charging a cathode in 1 hour, corresponding to a specific current density of 200 mAh/g. The electrochemical impedance spectroscopy (EIS) was examined by applying an AC voltage of 5 mV over the frequency range of 0.01 Hz to 100 kHz of coin cells at fully discharged at 0.5C after 1 cycle and 10 cycles.

4.4. Results

4.4.1. Surface layer formation on NMC particles

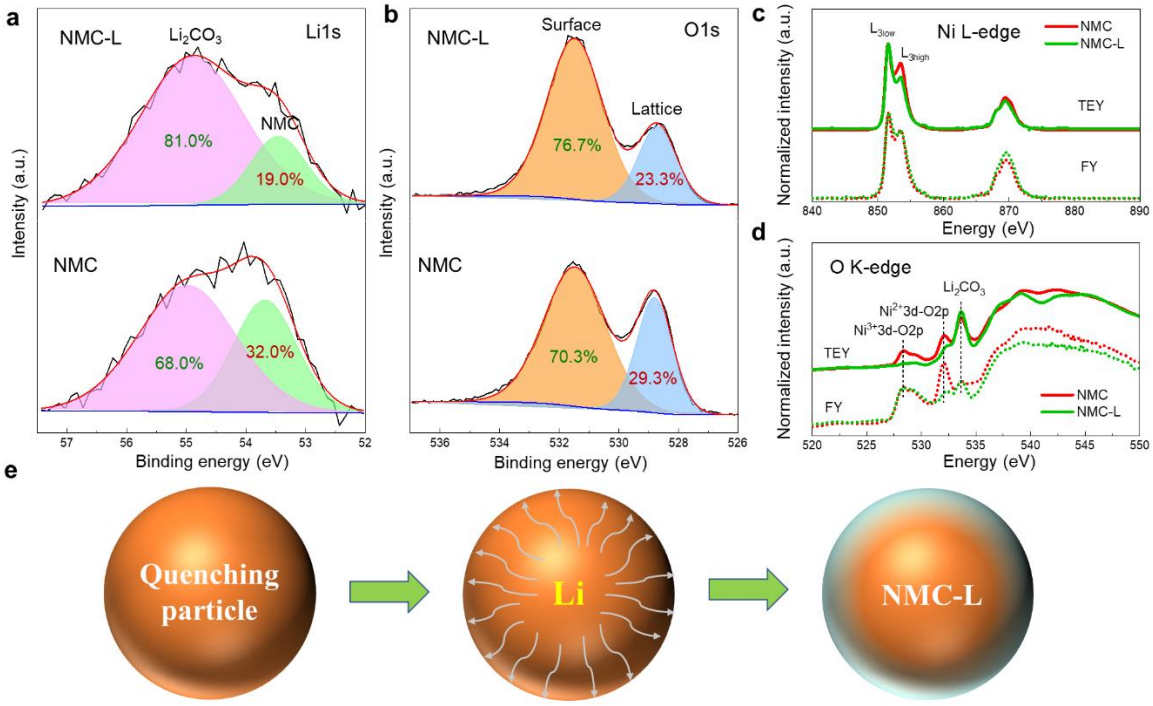

Figure. 1. The surface structural and chemical properties of NMC and NMC-L pristine materials. XPS spectra of (a) Li 1s and (b) O 1s for NMC and NMC-L pristine powders. Li 1s spectra that are deconvoluted into Li_2CO_3 and NMC, and O 1s spectra that are deconvoluted into surface and lattice oxygen (Li-O and Ni-O). Soft XAS (c) Ni L-edge and

(d) O K-edge spectra in the TEY and FY mode for NMC and NMC-L in the pristine state. (e) Schematic illustration of surface layer formation during the quenching process.

The conventional solid-state method for synthesizing layered cathodes is to calcine the precursor at high temperatures followed by natural cooling to room temperature.[16] In this work, we followed the same heating procedure as conventional cathode synthesis but quenched the cathode instead of slow cooling after high-temperature holding stage. The quenching process can result in a different cathode surface structure and surface Li-containing species formation. Therefore, we performed X-ray photoelectron spectroscopy (XPS), soft X-ray absorption spectroscopy (XAS) and full-field transmission X-ray microscopy (TXM) techniques to study the surface evolution for quenched sample (NMC-L) and naturally cooled sample (NMC). Li 1s XPS spectra are deconvoluted into Li_2CO_3 peak with a lower binding energy and Li in the lattice of NMC cathodes with a higher binding energy (Figure 1a).[17,18] The Li_2CO_3 content at the surface of NMC-L is 81.0%, which is much higher than 68.0% in the slow-cooled NMC. Accordingly, the Li at the surface of NMC-L lattice is 19.0% and lower than 32.0% in the slow-cooled NMC. O 1s spectra were further deconvoluted to differentiate the surface and lattice O species (Figure 1b). We found that the surface O assigned to lithium-containing species increases from 70.3% to 76.7% by quenching (Figure 1b).

Next, we performed soft XAS to further investigate the impact of quenching on the surface chemical structure of NMC. Soft XAS is sensitive to the oxidation states and electronic configurations of transition metals at the surface.[19] Herein, we applied two detection modes, i.e., total electron yield (TEY) and fluorescence yield (FY), to probe the

surface and subsurface information at ~10 nm and ~50 nm, respectively.[19,20] The peak intensity ratio between the high energy shoulder (L_{3high}) and low energy shoulder (L_{3low}) of L_3-edge is positively correlated to the oxidation state.[2] At ~10 nm deep detected by TEY mode, the quenched sample NMC-L shows a lower L_{3high}/L_{3low} ratio and thereby a lower Ni oxidation state than NMC (Figure 1c). In contrast, the Ni oxidation state remains nearly the same at ~50 nm deep for NMC and NMC-L based on the results of FY (Figure 1c). The pre-edge of O K-edge spectra can be attributed to Ni^{3+} 3d-O 2p (~528 eV) and Ni^{2+} 3d-O 2p (~531 eV), and the peak at ~534 eV corresponds to Li_2CO_3 (Figure 1d). The O K-edge spectra in TEY mode show higher intensity of Li_2CO_3 in NMC-L than that in NMC, which is consistent with the XPS results (Figure 1a,b,d). The pre-edge of O K-edge spectra shows a lower Ni oxidation state in NMC-L, which is also supported by Ni L-edge spectra (Figure 1c,d). O K-edge in FY mode indicates negligible changes besides slightly less Ni reduction after quenching (Figure 1d). Overall, the complementary results from XPS and XAS indicate the formation of a surface passivation layer, which can be attributed to the transportation of lattice Li to the surface due to a sudden decrease of temperature as illustrated in the scheme (Figure 1e).

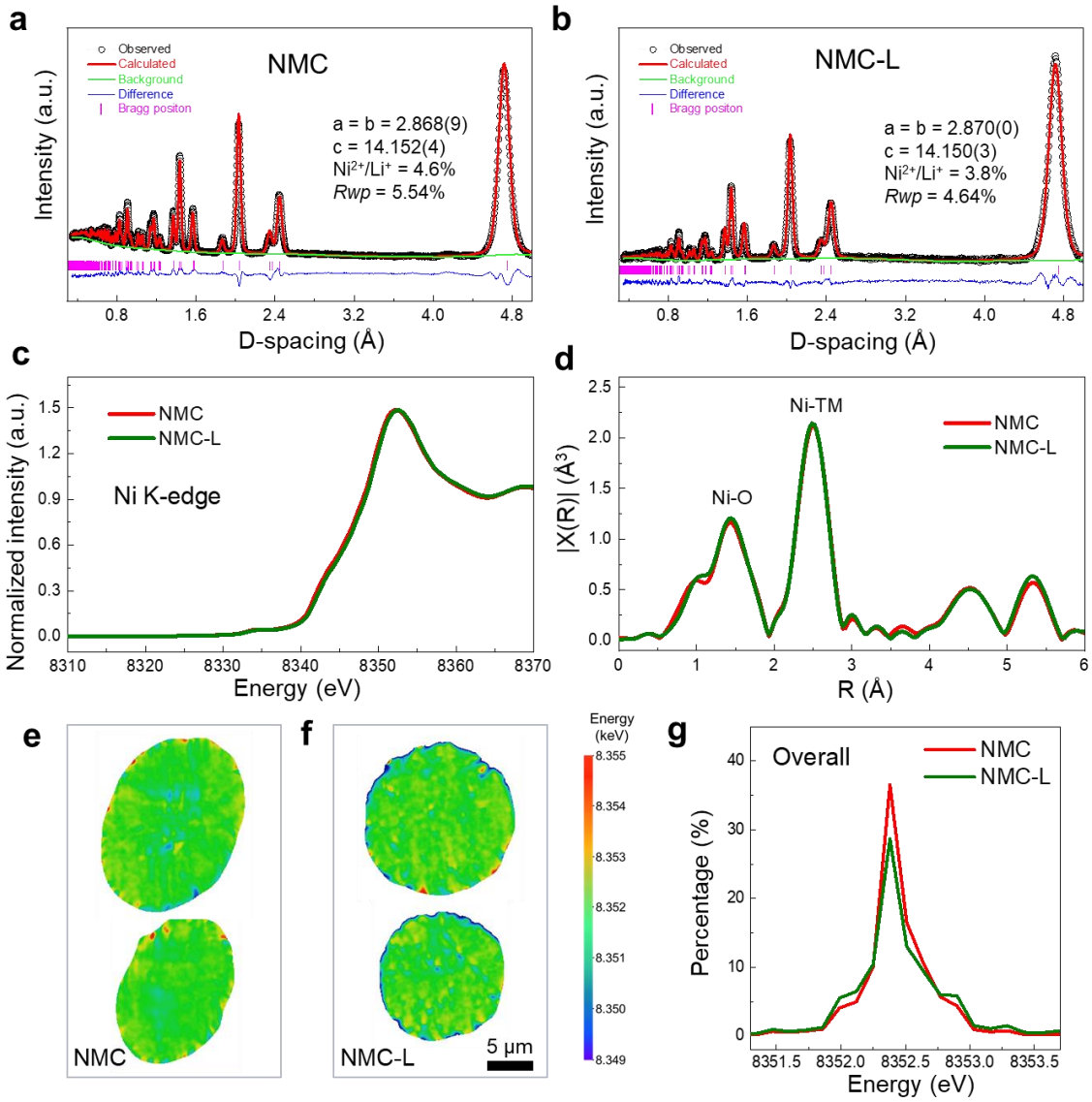

Figure 2. The bulk structural and chemical properties of NMC and NMC-L pristine materials. Rietveld refinement neutron diffraction patterns of the powder samples by (a) NMC and (b) NMC-L. The red dots, black line, blue line, and pink vertical tick marks represent the observed, calculated, difference pattern, and Bragg peaks, respectively. Hard XAS Ni K-edge (c) XANES, (d) EXAFS spectra of NMC and NMC-L samples. Cross-sectional 3D TXM images of (e) NMC and (f) NMC-L cathode materials. (g) Ni K-edge energy distribution in the whole particle of NMC and NMC-L at the pristine state.

4.4.2. Similarity of bulk properties on NMC and NMC-L materials.

Although intercalation and deintercalation of Li^+ initiate at the cathode surface, the overall electrochemical performance of the cathode involves the particle bulk properties eventually. Therefore, probing the bulk properties is equally important. XRD patterns of both NMC-L and NMC show that they both have a hexagonal α-$NaFeO_2$ layered structure with $R\bar{3}m$ space group and no impurity phases are observed (Figure S1). The peak positions and shape of NMC-L are consistent with NMC, revealing a similar crystal structure and crystallinity after natural cooling and quenching. We further performed neutron diffraction (ND) and Rietveld refinements for NMC-L and NMC (Figure 2a,b and Figure S2). The degree of Ni^{2+}/Li^+ cation mixing and lattice parameters are similar for NMC-L and NMC, suggesting minimal bulk structure changes induced by quenching.

To probe the transition metal electronic structure and local chemical environment in bulk, we performed hard XAS that includes the X-ray near edge structure (XANES) and extended X-ray absorption fine structure (EXAFS). Ni K-edge XANES spectra show well-aligned shape and nearly no shift of the pre-edge and edge positions for NMC-L and NMC, indicating similar Ni oxidation state in the two samples (Figure 2c). In addition, Ni K-edge EXAFS for NMC-L and NMC almost overlaps with each other, which means the interatomic distances of Ni-O and Ni-M and the atomic environment of Ni are nearly identical for the two samples (Figure 2d). The similarity of Mn and Co XANES and EXAFS results further confirms that different cooling protocols barely lead to the bulk chemical environment variance (Figure S3). We further examine the morphology of the two samples through scanning electron microscopy (SEM). Both NMC-L and NMC

possess a spherical polycrystalline particle morphology with around ten μm diameter (Figure S4). No crack formation is observed in either sample, suggesting a minimal effect of cooling protocol on the particle morphology (Figure S4).

Charge heterogeneity is strongly correlated with the redox behavior within the cathode particles, which can lead to a variation of polarization and performance degradation upon cycling.[15,21,22] To complement the surface-sensitive soft XAS and ensemble-averaged hard XAS, we further performed the full field TXM at single particle scale for NMC and NMC-L at the pristine state. TXM is a powerful technique that can non-invasively reconstruct the bulk structure of particles with a spatial resolution down to ~30 nm and provide chemical information, such as oxidation states. From the cross-section of three-dimensional (3D) TXM images for NMC (Figure 2e) and NMC-L (Figure 2f), we observe similar Ni K-edge energy level and overall uniform distribution, indicating similar Ni oxidation state and distribution inside the particles at pristine state. We further plot the energy distribution histogram, which shows similar average Ni K-edge absorption energy at around 8352.4 eV for both samples (Figure 1g). The similar bulk Ni oxidation state in the particles is consistent with the hard XAS results (Figure 1c,d). To resolve the spatial details of energy distribution, we did depth-dependent analyses (Figure S5). Shell 1 is the outmost shell at the particle surface with a thickness of 20 nm (Figure S5a). Each shell with increasing numbers is 20 nm away from its outer shell (Figure S5a). We plot the energy distribution within Shell 1 for NMC-L and NMC (Figure S5b). The histogram of NMC-L entirely shifts to lower energy compared to that of NMC, which indicates the Ni oxidation state of NMC-L is overall lower than that of NMC at the top 20 nm surface (Figure S5b). We further average the energy in each shell and plot the energy as a function of distance

from the particle surface (Figure S5c). The results confirm that Ni is reduced at the surface of NMC-L but not in NMC, while the energy level in the bulk is similar for the two samples (Figure S5c). These results are consistent with the trend revealed by soft XAS and hard XAS and demonstrate the formation of a surface layer (Figure 1c,d and Figure 2c,d)

4.4.3. Enhanced cycling stability by a passivation layer on NMC surface

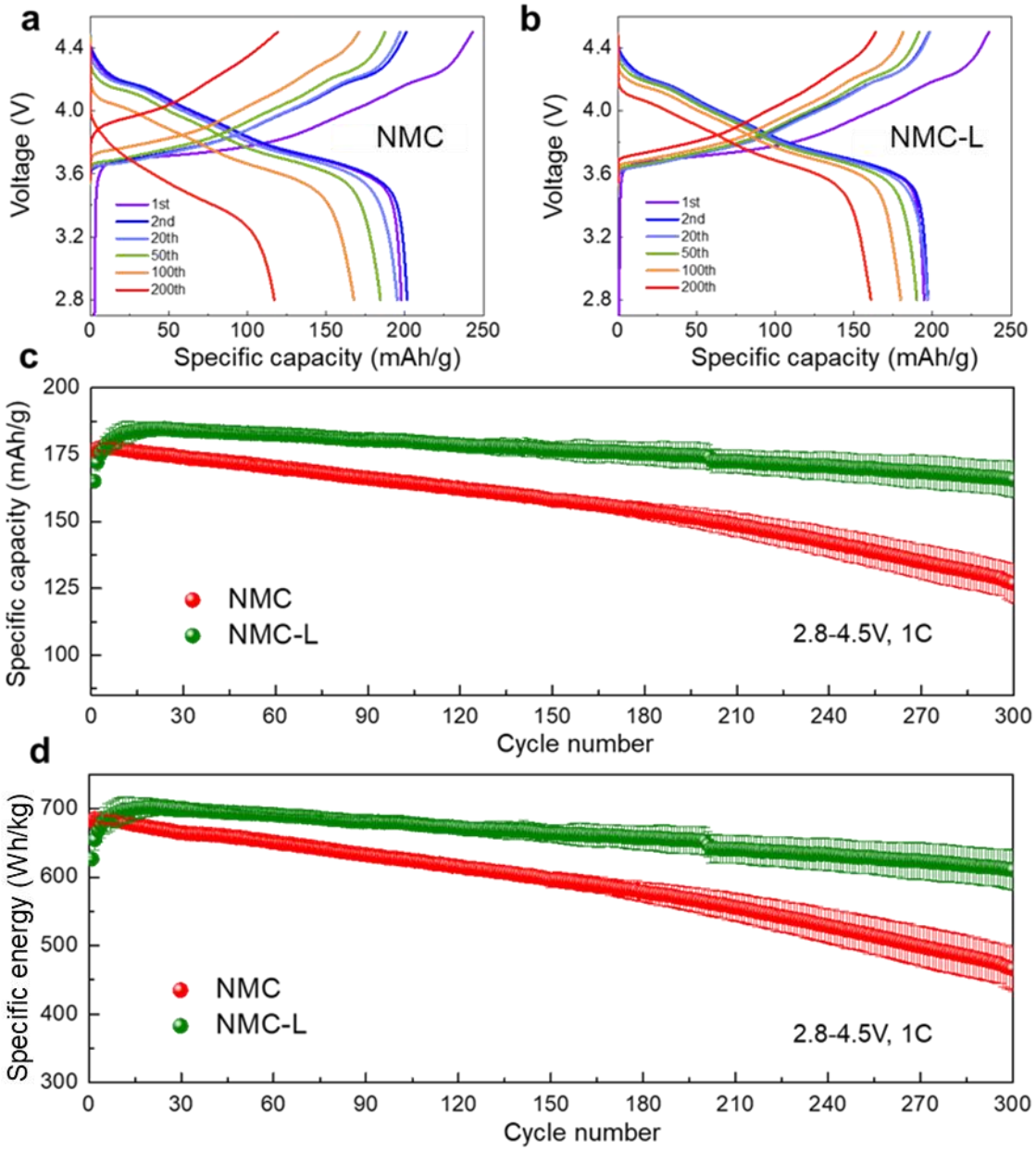

Figure 3. Electrochemical cycling performance of NMC and NMC-L measured in half-cell. The charge/discharge profiles of (a) NMC, (b) NMC-L for 1st, 2nd, 20th, 50th, 100th and 200th cycle at 0.5C with a voltage range of 2.8-4.5 V. (c) The discharge capacity of the NMC and NMC-L at 1C at 22 °C based on three coin cells and error bars are included. (d) The corresponding specific energy of the same cells shown in (c).

We examine the effect of the surface passivation layer on the electrochemical performance. NMC-L and NMC are paired with Li metal anode and cycled within the voltage window of 2.8-4.5 V at 22 °C. The initial specific discharge capacity of NMC-L and NMC at 0.5C is 194.7 mAh/g and 197.8 mAh/g, respectively (Figure 3a,b). After 200 cycles, the capacity retention of NMC-L is much higher than that of NMC, showing enhanced stability of NMC-L by the passivation layer. When increasing the charging rate to 1C, the specific discharge capacity for NMC-L and NMC is 181.1 mAh/g and 176.3 mAh/g. The capacity retention of NMC-L after 300 cycles at 1C is 90%, which is much higher than 72% of NMC under the same conditions (Figure 3c). NMC-L also delivers higher specific energy of 702 Wh/kg than 673 Wh/kg of NMC and exhibits better energy retention (Figure 3d). We want to point out that the calculation of specific capacity and energy retention was based on the division of final value by the highest value after the first several activation cycles. We further compare the cell resistance of NMC-L and NMC using electrochemical impedance spectroscopy (EIS). Figure S6 shows that the charge transfer resistance of NMC-L after one cycle and after 50 cycles are both lower than that of NMC due to the enhanced surface stability.

4.4.4. Better interfacial stability NMC-L upon cycling.

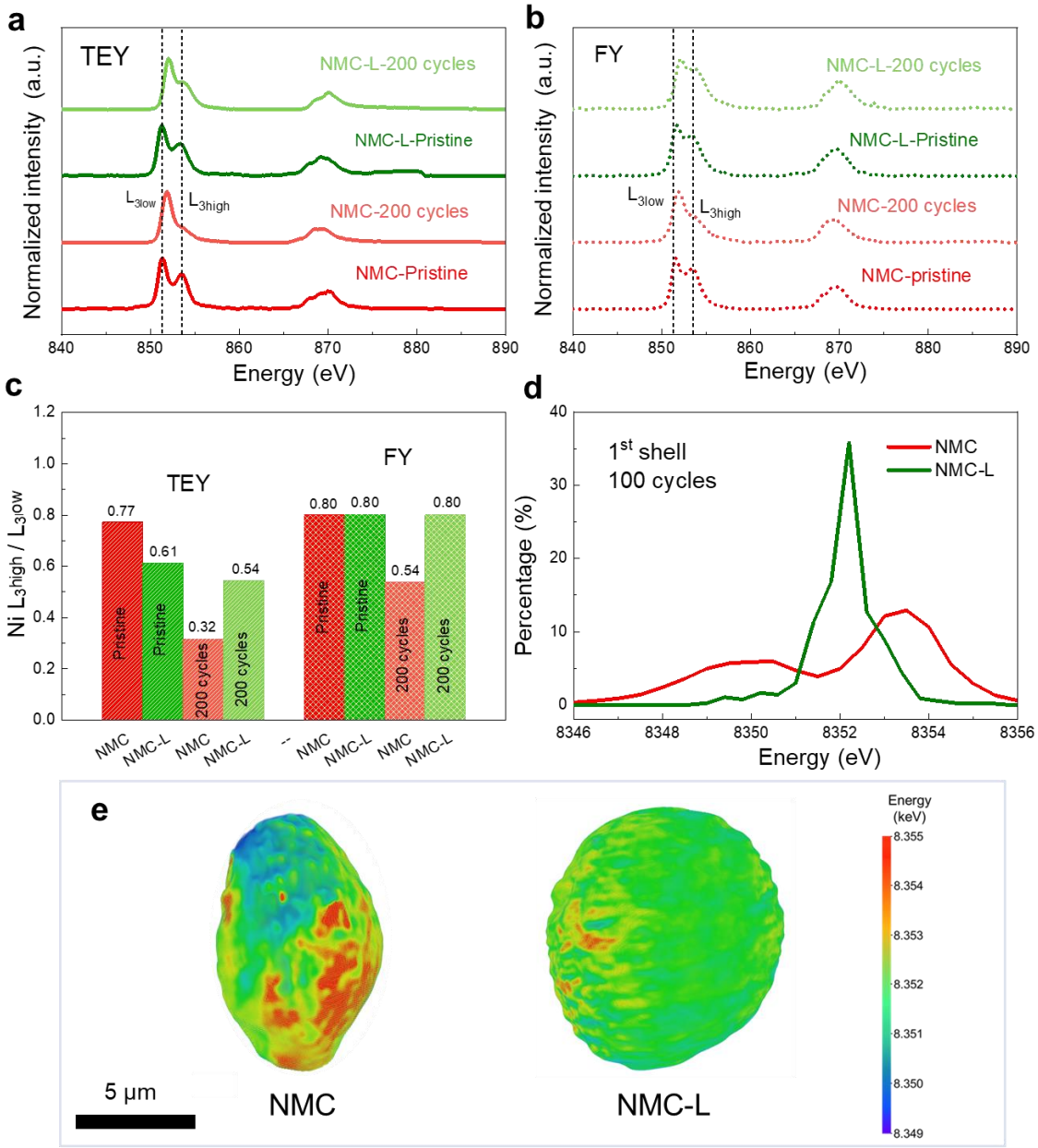

Figure 4. The surface chemical and structural evolution of NMC and NMC-L after cycling. Soft XAS (a) Ni L-edge (TEY mode), and (b) Ni L-edge (FY mode) of the NMC and NMC-L in the pristine state and after 200 cycles. (c) The Ni L_{3high}/L_{3low}-edge values in TEY mode and FY mode of NMC and NMC-L for the pristine state and after 200 cycles. (d) The first

shell (20 nm away from particle surface) Ni K-edge energy distribution and (e) 3D TXM images of NMC and NMC-L particles after 100 cycles.

To investigate the origin of the enhanced cycling stability and the evolution of the surface layer in NMC-L, we performed soft XAS for NMC and NMC-L at the pristine state and after 200 cycles (Figure 4a,b). The peak intensity ratio Li_{3high}/L_{3low} of NMC-L shows little change after 200 cycles, whereas the NMC samples experience profound Ni reduction at the surface based on both TEY and FY modes (Figure 4a,b). These results show that NMC-L demonstrates superior interfacial structural stability. We further quantify the L_3 edge peak intensity ratio L_{3high}/L_{3low} for the two samples at the pristine state and after 200 cycles (Figure 4c). L_{3high}/L_{3low} of NMC-L slightly decreases from 0.61 to 0.54 with TEY mode while remaining 0.80 with FY mode after 200 cycles (Figure 4c). In contrast, the value for NMC has a sharp decrease from 0.77 to 0.32 with TEY mode and from 0.80 to 0.54 with FY mode upon 200 cycles, which can be attributed to more severe surface structural distortion (Figure 4c). We further perform TXM on NMC-L and NMC after 100 cycles and plot the Ni K-edge energy distribution in Shell 1 (Figure 4d). The histogram of NMC-L is sharp, and the energy distributes in a relatively small range, indicating a more uniform Ni oxidation state distribution at the top surface of NMC-L (Figure 4d). In contrast, the energy distribution of NMC is broader and exhibits a bimodal feature (Figure 4d). The low energy peak indicates a large portion of Ni at the top surface of NMC is reduced (Figure 4d). Ni is the primary charging compensating element; thus, the oxidation or reduction of Ni can be utilized as an indicator for delithiation or lithiation. 3D Ni K-edge TXM shows the charge distribution at the surface of NMC is significantly more heterogeneous than that

of NMC-L upon extensive cycles. The results of soft XAS and TXM collectively show that the surface passivation layer in NMC-L promotes the charge homogeneity at the cathode surface and the interfacial stability, which can lead to less cathode-electrolyte parasitic reactions and enhance cycling stability.

4.4.5. Homogeneous charge distribution in NMC-L particles after long-term cycling.

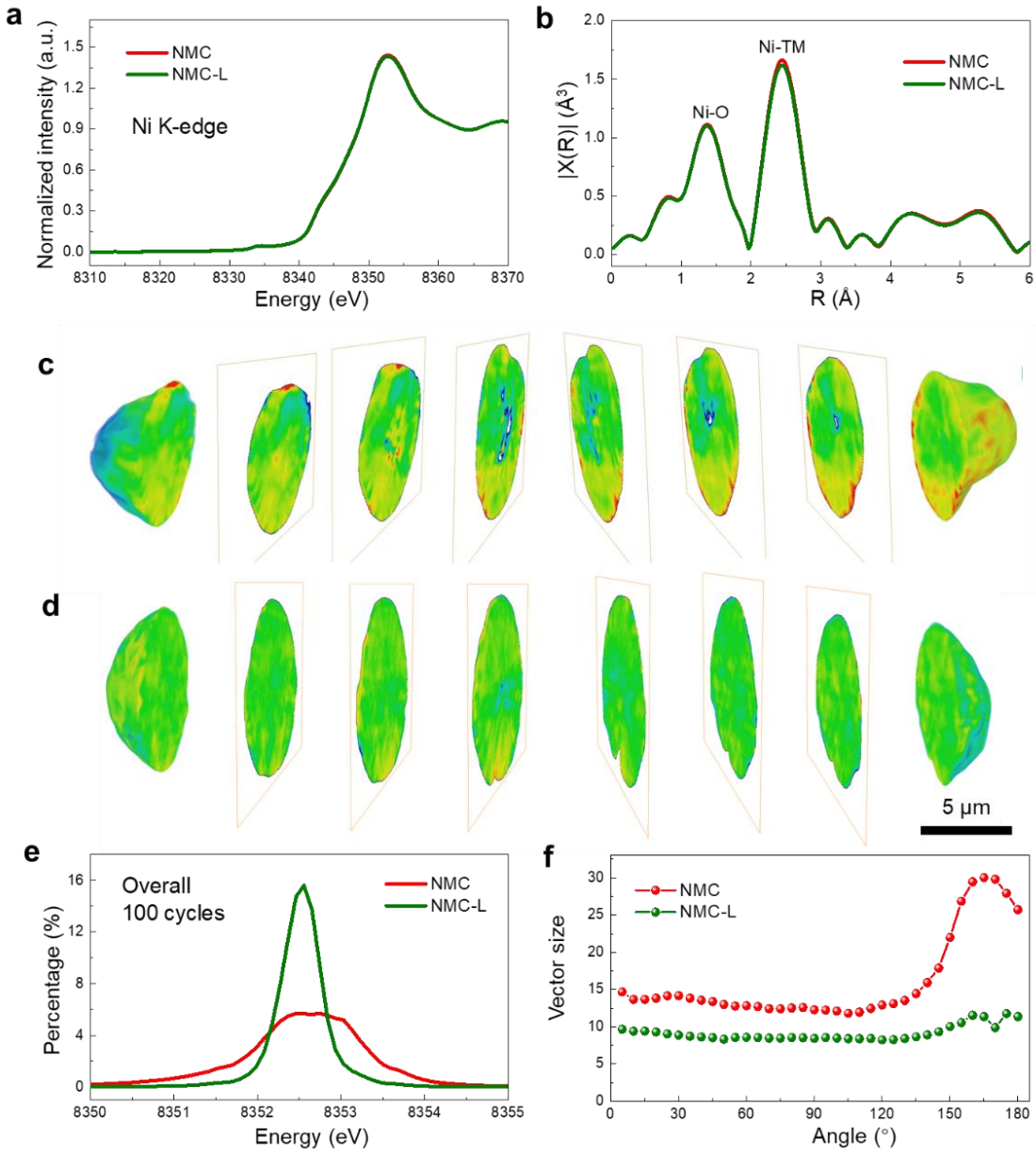

Figure 5. The bulk chemical and structural evolution of NMC and NMC-L after cycling. (a) hard XAS and (b) EXAFS spectra of Ni K-edge after 100 cycles. 3D rendering of the tomographic data over the (c) NMC and (d) NMC-L particle with the perspective views of a few virtual slices through different displayed in the center. (e) Ni K-edge energy distribution in the whole particle of NMC and NMC-L after 100 cycles. (f) The average valence gradient vector size as a function of θ where 0°-180° were divided to 36 intervals.

We further study the evolution of bulk structure upon cycling using hard XAS and TXM. Ni K-edge XANES (Figure 5a) and EXAFS (Figure 5b) results show minimal difference between NMC-L and NMC after 100 cycles, which indicates Ni oxidation state, Ni-O and Ni-M interatomic distances, and the local environment of Ni are similar in NMC-L and NMC at ensemble-averaged scale. Co K-edge and Mn K-edge XANES and EXAFS spectra in Figure S7 show similar peaks intensity and shape without energy shift for NMC-L and NMC, further confirming similar Co and Mn oxidation states and bulk structural stability. However, the particle scale analyses from 3D TXM show large differences between NMC-L and NMC (Figure 5c,d). The 3D TXM cross-sectional tomographic images of NMC show large charge distribution heterogeneity (Figure 5c), whereas the charge distribution within NMC-L particle is relatively homogeneous (Figure 5d). Ni K-edge energy distribution further confirms that NMC-L has a more uniform charge and oxidation state distribution than NMC due to a narrower peak (Figure 5e). We further plot the average valence gradient vector size as a function of vector angle θ based on our previous study.[15] The overall smaller vector size of NMC-L confirms that the charge heterogeneity of NMC-L is smaller.

4.5. Discussion

In this work, we enhance the cycling stability of NMC811 cathode materials by modifying the surface structure through a facile quenching approach. We further investigate the effect of the modified surface layer on the long-term cycling performance using a combination of synchrotron microscopic and spectroscopic techniques at various length scales. We synthesize two NMC811 cathodes, denoted as NMC-L and NMC, using the traditional solid-state calcination method but followed by quenching and natural cooling, respectively. NMC-L delivers a relatively high discharge capacity of 185 mAh/g and a high energy density of 702 Wh/kg at 1C charging and discharging rate. Upon 300 cycles at 1C, the capacity retention of NMC-L is 90% and higher than 72% of NMC. The enhanced electrochemical performance of NMC-L can be attributed to the stable surface structure, which can not only mitigate the parasitic reactions between cathode and electrolyte, but also alleviate interface impendence growth during cycling. The particle scale analyses show that the charge homogeneity in the bulk is significantly promoted in the quenched NMC-L sample. Therefore, Li transportation upon cycling is more effective.

4.6. Acknowledgements

The work was supported by the National Science Foundation (NSF) under Grant no. DMR-1832613. The use of the Stanford Synchrotron Radiation Lightsource, SLAC National Accelerator Laboratory, is supported by the U.S. Department of Energy, Office of Science, Office of Basic Energy Sciences under Contract No. DE-AC02-76SF00515. This research used resources of the Advanced Photon Source, a U.S. Department of Energy (DOE) Office of Science User Facility operated for the DOE Office of Science by Argonne National Laboratory under Contract No. DE-AC02-06CH11357. The research used 18-ID

of the National Synchrotron Light Source II, a U.S. Department of Energy (DOE) Office of Science User Facility operated for the DOE Office of Science by Brookhaven National Laboratory under Contract No. DE-SC0012704. The use of the Spallation Neutron Source at Oak Ridge National Laboratory is supported by the U.S. Department of Energy, Office of Science, Office of Basic Energy Sciences under Contract No. DE-AC05-00OR22725. This research was partially supported by Virginia Tech's Institute for Critical Technology and Applied Science through instruments provided by the Nanoscale Characterization and Fabrication Laboratory (NCFL).

4.7. References

(1) Noh, H. J.; Youn, S.; Yoon, C. S.; Sun, Y. K. Comparison of the Structural and Electrochemical Properties of Layered $Li[Ni_xCo_yMn_z]O2$ (x = 1/3, 0.5, 0.6, 0.7, 0.8 and 0.85) Cathode Material for Lithium-Ion Batteries. *J. Power Sources* **2013**, *233*, 121–130.

(2) Lin, F.; Markus, I. M.; Nordlund, D.; Weng, T.-C.; Asta, M. D.; Xin, H. L.; Doeff, M. M. Surface Reconstruction and Chemical Evolution of Stoichiometric Layered Cathode Materials for Lithium-Ion Batteries. *Nat. Commun.* **2014**, *5* (1), 3529.

(3) Zhang, S. S. Problems and Their Origins of Ni-Rich Layered Oxide Cathode Materials. *Energy Storage Mater.* **2019**.

(4) Liang, L.; Zhang, W.; Zhao, F.; Denis, D. K.; Zaman, F. uz; Hou, L.; Yuan, C. Surface/Interface Structure Degradation of Ni-Rich Layered Oxide Cathodes toward Lithium-Ion Batteries: Fundamental Mechanisms and Remedying Strategies. *Adv. Mater. Interfaces* **2020**, *7* (3), 1901749.

(5) Xu, Z.; Rahman, M. M.; Mu, L.; Liu, Y.; Lin, F. Chemomechanical Behaviors of

Layered Cathode Materials in Alkali Metal Ion Batteries. *J. Mater. Chem. A* **2018**, *6* (44), 21859–21884.

(6) Chen, Z.; Qin, Y.; Amine, K.; Sun, Y. K. Role of Surface Coating on Cathode Materials for Lithium -Ion Batteries. *J. Mater. Chem.* **2010**, *20* (36), 7606–7612.

(7) Sun, Y.-K.; Myung, S.-T.; Park, B.-C.; Prakash, J.; Belharouak, I.; Amine, K. High-Energy Cathode Material for Long-Life and Safe Lithium Batteries. *Nat. Mater.* **2009**, *8* (4), 320–324.

(8) Li, J.; Camardese, J.; Shunmugasundaram, R.; Glazier, S.; Lu, Z.; Dahn, J. R. Synthesis and Characterization of the Lithium-Rich Core-Shell Cathodes with Low Irreversible Capacity and Mitigated Voltage Fade. *Chem. Mater.* **2015**, *27* (9), 3366–3377.

(9) Kim, U.-H.; Lee, E.-J.; Yoon, C. S.; Myung, S.-T.; Sun, Y.-K.; Kim, U.-H.; Lee, E.-J.; Sun, Y.-K.; Yoon, C. S.; Myung, -T S. Compositionally Graded Cathode Material with Long-Term Cycling Stability for Electric Vehicles Application. *Adv. Energy Mater.* **2016**, *6* (22), 1601417.

(10) Koenig, G. M.; Belharouak, I.; Deng, H.; Sun, Y. K.; Amine, K. Composition-Tailored Synthesis of Gradient Transition Metal Precursor Particles for Lithium-Ion Battery Cathode Materials. *Chem. Mater.* **2011**, *23* (7), 1954–1963.

(11) Liang, J. Y.; Zhang, X. D.; Zeng, X. X.; Yan, M.; Yin, Y. X.; Xin, S.; Wang, W. P.; Wu, X. W.; Shi, J. L.; Wan, L. J.; Guo, Y. G. Enabling a Durable Electrochemical Interface via an Artificial Amorphous Cathode Electrolyte Interphase for Hybrid Solid/Liquid Lithium-Metal Batteries. *Angew. Chemie* **2020**, *132* (16), 6647–6651.

(12) Mohanty, D.; Dahlberg, K.; King, D. M.; David, L. A.; Sefat, A. S.; Wood, D. L.;

Daniel, C.; Dhar, S.; Mahajan, V.; Lee, M.; Albano, F. Modification of Ni-Rich FCG NMC and NCA Cathodes by Atomic Layer Deposition: Preventing Surface Phase Transitions for High-Voltage Lithium-Ion Batteries. *Sci. Reports* **2016**, *6* (1), 1–16.

(13) Xiao, X.; Xu, Z.; Lin, F.; Lee, W. K. TXM-Sandbox: An Open-Source Software for Transmission X-Ray Microscopy Data Analysis. *J. Synchrotron Rad.* **2022**, *29* (1), 266–275.

(14) Xiao, X.; Xu, Z.; Hou, D.; Yang, Z.; Lin, F. Rigid Registration Algorithm Based on the Minimization of the Total Variation of the Difference Map. *J. Synchrotron Rad.* **2022**, *29* (4), 1085–1094.

(15) Xu, Z.; Jiang, Z.; Kuai, C.; Xu, R.; Qin, C.; Zhang, Y.; Rahman, M. M.; Wei, C.; Nordlund, D.; Sun, C. J.; Xiao, X.; Du, X. W.; Zhao, K.; Yan, P.; Liu, Y.; Lin, F. Charge Distribution Guided by Grain Crystallographic Orientations in Polycrystalline Battery Materials. *Nat. Commun.* **2020**, *11* (1), 83.

(16) Yang, Z.; Mu, L.; Hou, D.; Rahman, M. M.; Xu, Z.; Liu, J.; Nordlund, D.; Sun, C.; Xiao, X.; Lin, F. Probing Dopant Redistribution, Phase Propagation, and Local Chemical Changes in the Synthesis of Layered Oxide Battery Cathodes. *Adv. Energy Mater.* **2020**, 2002719.

(17) Mu, L.; Yang, Z.; Tao L.;Waters, K. C.; Xu, Z.; Li, L.; Sainio, S.; Du, Y.; Xin, H.L.; Nordlund, D.; Lin, F.. The Sensitive Surface Chemistry of Co-Free, Ni-Rich Layered Oxides: Identifying Experimental Conditions That Influence Characterization Results. *J. Mater. Chem. A* **2020**, *8* (34), 17487–17497.

(18) Zhang, M. J.; Hu, X.; Li, M.; Duan, Y.; Yang, L.; Yin, C.; Ge, M.; Xiao, X.; Lee, W. K.; Ko, J. Y. P.; Amine, K.; Chen, Z.; Zhu, Y.; Dooryhee, E.; Bai, J.; Pan, F.; Wang,

F. Cooling Induced Surface Reconstruction during Synthesis of High-Ni Layered Oxides. *Adv. Energy Mater.* **2019**, *9* (43), 1901915.

(19) Lin, F.; Liu, Y.; Yu, X.; Cheng, L.; Singer, A.; Shpyrko, O. G.; Xin, H. L.; Tamura, N.; Tian, C.; Weng, T.-C.; Yang, X.-Q.; Meng, Y. S.; Nordlund, D.; Yang, W.; Doeff, M. M. Synchrotron X-Ray Analytical Techniques for Studying Materials Electrochemistry in Rechargeable Batteries. *Chem. Rev.* **2017**, *117* (21), 13123–13186.

(20) Lin, F.; Nordlund, D.; Markus, I. M.; Weng, T.-C. C.; Xin, H. L.; Doeff, M. M. Profiling the Nanoscale Gradient in Stoichiometric Layered Cathode Particles for Lithium-Ion Batteries. *Energy Environ. Sci.* **2014**, *7* (9), 3077–3085.

(21) Yang, Z.; Lin, F. Heterogeneous, Defect-Rich Battery Particles and Electrodes: Why Do They Matter, and How Can One Leverage Them? *J. Phys. Chem. C* **2021**, *125* (18), 9618–9629.

(22) Zhang, Y.; Yang, Z.; Tian, C. Probing and Quantifying Cathode Charge Heterogeneity in Li Ion Batteries. *J. Mater. Chem. A,* **2019**,*7,* 23628-23661.

4.8. Supplementary information

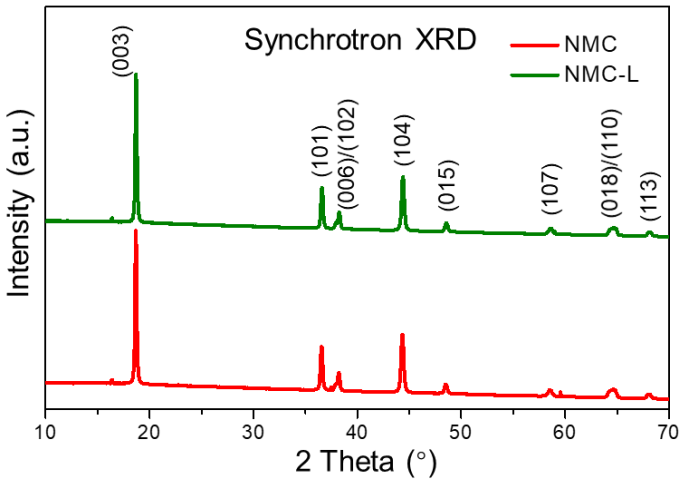

Figure S1. Synchrotron XRD for NMC and NMC-L powder.

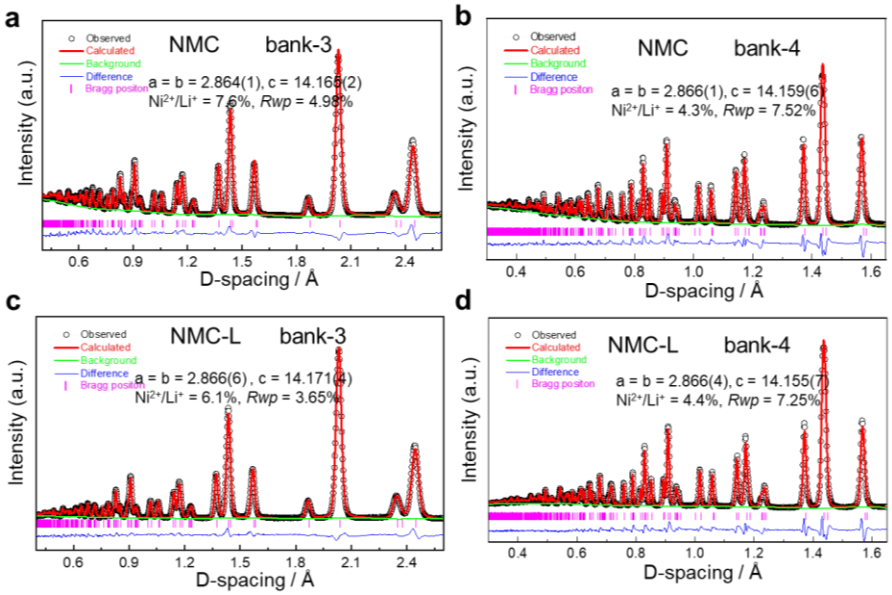

Figure S2. Neutron patterns for NMC and NMC-L powder in different banks. Bank 3 for (a) NMC and (c) NMC-L; bank 4 for (b) NMC and (d) NMC-L.

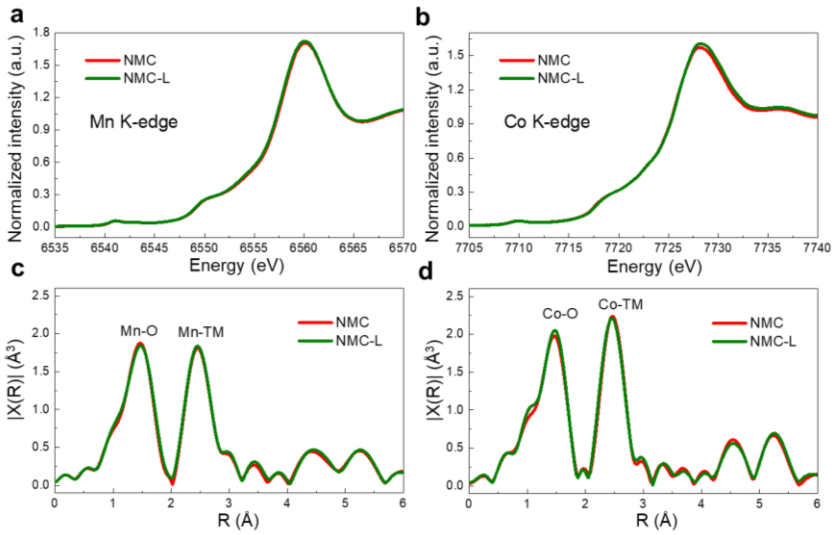

Figure S3. Hard XAS XANES spectra for (a) Mn K-edge and (b) Co K-edge. EXAFS spectra of (c) Mn K-edge and (d) Co K-edge for NMC and NMC-L powders.

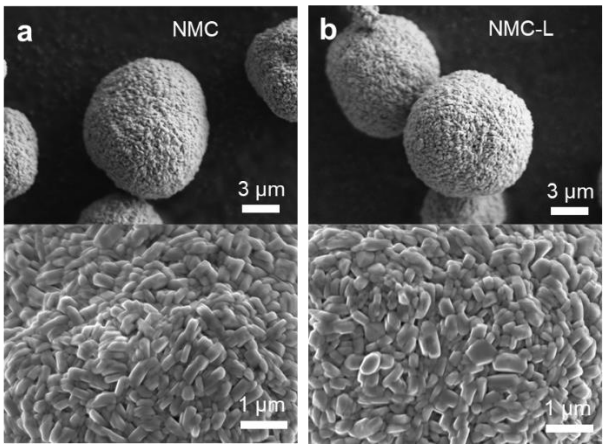

Figure S4. SEM images for (a) NMC and (b) NMC-L powders in various magnification.

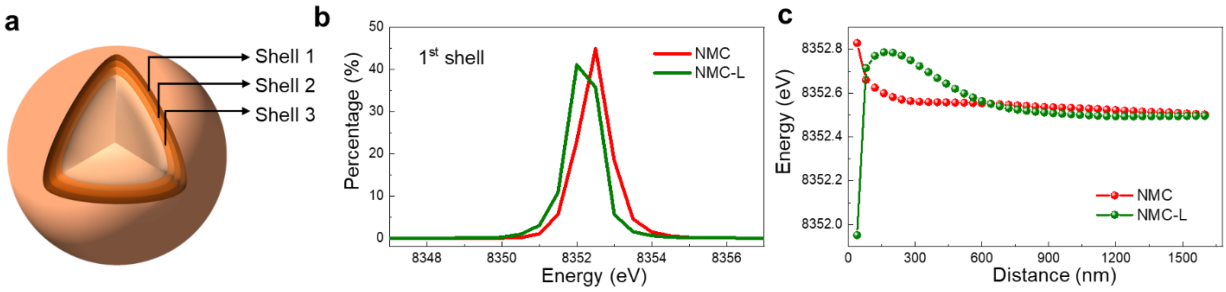

Figure S5. (a) Schematic illustration of TXM depth profiling analysis. Each shell is 20 nm away from its outer shell. (b) The first shell (20 nm away from particle surface) Ni K-edge energy distribution of NMC and NMC-L in the pristine state. (c) Ni K-edge energy of NMC and NMC-L as a function of the distance from the particle surface. The energy is defined as the mean value of the Ni K-edge energy of all voxel with the same shell, meaning the same distance from the particle surface.

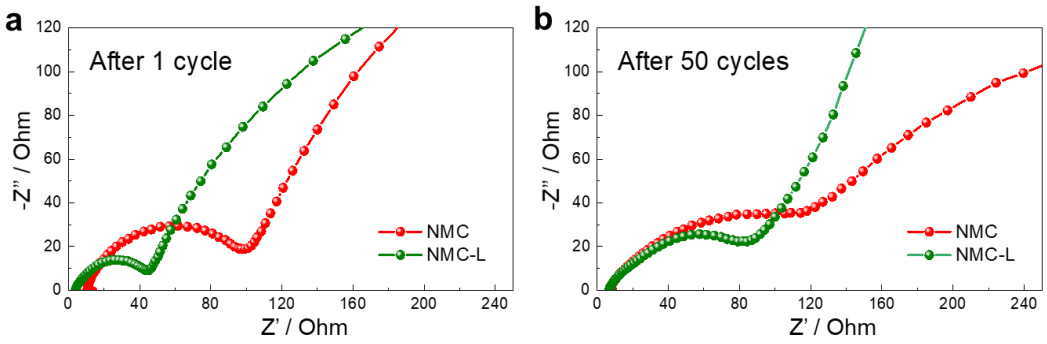

Figure S6. Nyquist plot of EIS performed with fully discharged cells at 0.5C after (a) 1 cycle and (b) 50 cycles of NMC and NMC-L cathodes.

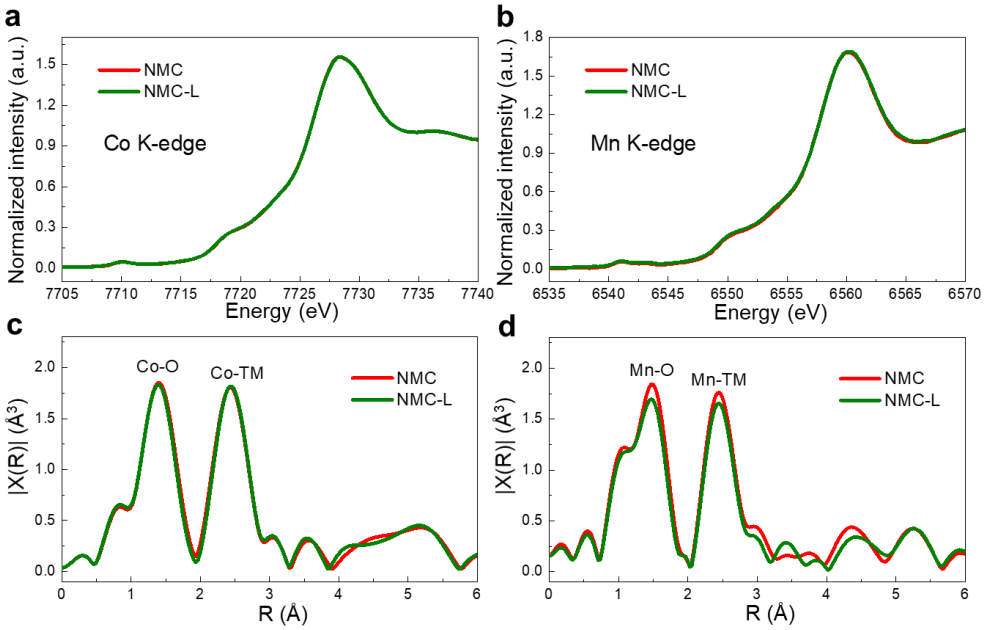

Figure S7. Hard XAS spectra of (a) Co K-edge and (b) Mn K-edge for NMC and NMC-L after 100 cycles. EXAFS spectra of (c) Co K-edge and (d) Mn K-edge for NMC and NMC-L after 100 cycles

5. Synthesis and Size Control of Single Crystal Ni-Rich Layered Oxide Cathodes Using Statistical Analysis-Guided Molten Salt Method

Zhijie Yang[1], Dajun Yu[2], Dong Hou[1], Ryan Ragasa[3], Paul Roark[1], Jue Liu[4], Feng Lin[1]*

1. Department of Chemistry, Virginia Tech, Blacksburg, VA, 24061, USA

2. Department of Food Science and Technology, Virginia Tech, Blacksburg, VA, 24061, USA

3. Department of Chemical Engineering, Virginia Tech, Blacksburg, VA, 24061, USA

4. Oak Ridge National Laboratory, Oak Ridge, TN, 37831, USA

Correspondence and requests for materials should be addressed to F.L. (email: fenglin@vt.edu)

5.1. Abstract

$Li(Ni_{1-x-y}Mn_xCo_y)O_2$ (NMC) is one of the most successful commercial cathodes with various transition metal (Ni, Mn, and Co) ratios. Higher Ni content in the composition of NMC gives rise to higher energy density but at the price of structural and thermal stability. Recently, synthesizing single-crystal cathode particles has been extensively investigated as a strategy to enhance the stability of NMC cathodes. Most commercial NMC cathode particles possess a polycrystalline structure, which is prone to induce intergranular cracking and parasitic reactions with the electrolyte upon cycling due to grain boundaries and large surface area. In contrast, single crystal NMC cathodes show higher cycling stability than their polycrystalline counterparts. However, the synthesis of single crystals normally requires higher temperatures and longer calcination duration than that of the polycrystalline counterparts for solid-state synthesis. Alternatively, molten salt synthesis of single crystals is less energy-intensive and capable of tuning particle morphology and size. However, there is not yet a systematic guideline for the molten salt synthesis of single crystal Ni-rich NMC cathodes. Herein, we studied the effect of different synthetic parameters on the performance of single crystal Ni-rich NMC cathodes. We applied statistical analysis tools to correlate the synthetic conditions with cathode properties and optimized the synthetic parameters. Furthermore, we investigated the effect of single crystal size on the cathode performance. Our findings provided new insights into the synthesis and understanding of single crystal Ni-rich cathodes.

5.2. Introduction

Li-ion batteries (LIBs) have been extensively used in daily lives, such as electric vehicles (EVs), grid energy storage, and portable electronic devices. To address the growing energy and environmental concerns, many countries have announced the goals of transiting to cleaner energy sources and achieving carbon neutrality by the middle of this century.[1] Shifting from internal combustion engine vehicles (ICEVs) to EVs has been adopted by more and more countries to reduce carbon emissions. Previous studies have shown that the lifetime greenhouse gas (GHG) emission of EVs is lower than that of ICEVs even considering the carbon emissions during vehicle and LIB production.[1] Upon the massive adoption of EVs, LIBs play a vital role because they are the most significant cost contributor to EVs, and the supply chain of LIBs largely determines the EV market. Cathode is an essential component of LIBs that currently governs the performance of commercial LIBs using graphite anode. $LiNi_xCo_yMn_{1-x-y}O_2$ (NMC) is one family of cathodes that are widely applied in the prevailing commercial LIBs.[2,3] With the increasing demand for longer driving ranges from EVs, the development of NMC cathodes is in the direction of high energy density and capacity. Ni redox couples govern the electrochemical activity of NMC cathodes. Therefore, increasing the Ni content in NMC cathodes can enhance the capacity of LIBs upon electrochemical cycling.[4] However, there is a trade-off between energy density and cycling stability as the Ni content increases and Co and Mn content decreases.[5] To enhance the stability of Ni-rich NMC cathodes, the battery community has been modifying the materials with multiple approaches, such as doping, surface coating, and crystallographic engineering. [6–13]

Nowadays, commercial NMC cathodes are primarily based on the morphology of polycrystalline particles. These polycrystalline secondary particles are composed of numerous primary single crystal grains, which give rise to a relatively high specific surface area.[14] The high specific surface area leads to severe parasitic reactions between the cathode surface and electrolyte, causing the battery performance degradation.[15,16] Additionally, the crystallographic orientation of these primary grains is generally random if without intentional control. The electrochemical reaction inside the secondary particles is heterogeneous, and the full capacity of each cathode particle is not efficiently utilized.[14,17,18] Furthermore, stress accumulates at the single grain and grain boundaries due to phase transformations and volume changes upon electrochemical cycling.[19] Intergranular cracks can readily form in the polycrystalline secondary particles because of the stress accumulation.[20] The cracks not only result in worse electronic and ionic conduction, but also expose more fresh surfaces and lead to more severe parasitic reactions with the electrolyte.[21,22] These drawbacks facilitate the degradation of battery performance.

In addition to the aforementioned methods that are used to resolve the instability issues of these polycrystalline NMC cathodes, another approach is to synthesize single crystal cathodes instead of modifying polycrystalline materials.[15,16,23,24] Contrasting to the polycrystalline counterparts, single crystal NMC cathodes have lower specific surface area and less prominent parasitic reactions with electrolytes. In addition, the structural integrity of single crystal cathodes can be better maintained upon cycling without any grain boundaries and intergranular crack issues.[15,16,23,24] However, the synthetic conditions of single crystal cathodes are stricter than their polycrystalline counterparts, especially for Ni-rich NMC cathodes. High-temperature synthesis and molten salt synthesis are two of the

mainstream single crystal synthesis methods.[15] Increasing the calcination temperature can enhance ion mobility and thus facilitate grain growth.[25] However, the formation of agglomerations at high temperatures is a typical issue, which normally requires additional pulverization and sieving.[26] In addition, the thermal stability of NMC decreases with increasing Ni content.[5] The synthesis temperature of Ni-rich NMC cathodes is generally lower to mitigate Li loss, Li/Ni cation mixing, and surface rocksalt phase formation.[5,27,28] These limitations make it more challenging to synthesize single crystal Ni-rich cathodes using high-temperature synthesis method. On the other hand, molten salt synthesis adopts specific salts, which melt at relatively low temperatures and provide liquid media for the single crystal to grow.[29] The morphology and preferred surface facets of single crystals can be changed by tuning the synthetic conditions.[24,29,30] Nevertheless, the performance of single crystal Ni-rich NMC cathodes is significantly determined by the molten salt synthesis conditions, and multiple synthetic parameters can synergistically make an impact. To the best of our knowledge, there is not yet a systematic study investigating the synthetic parameters for the synthesis of Ni-rich NMC cathodes using the molten salt method.

Herein, we use statistical tools to identify the significance of multiple synthetic parameters upon the molten salt synthesis of single crystal Ni-rich NMC cathodes, i.e., O_2 atmosphere, recalcination, salt ratio, Li ratio, calcination temperature, and calcination time. Based on a large set of controlled experiments, we created a prediction model to forecast the performance of synthesized single crystal Ni-rich NMC cathodes from the input of synthetic parameters with relatively high prediction accuracy. By tuning the synthetic conditions, we synthesized single crystal $LiNi_{0.9}Co_{0.05}Mn_{0.05}O_2$ (SC-N90) with different

particle sizes. We found that large SC-N90 (L-N90) showed worse capacity and cycle life than small SC-N90 (S-N90) due to slower Li kinetics, especially at a high current rate. We further identified the Li diffusion coefficient of L-N90 and S-N90 is at a similar scale. Therefore, the slower Li conduction for L-N90 is mainly attributed to longer Li traveling distances upon charge and discharge cycles. The statistical and prediction models developed in this study can guide the molten salt synthesis of Ni-rich cathodes and simplify the optimization of synthetic parameters. The findings of particle size effect on the performance provide insights into size engineering while developing next-generation single crystal Ni-rich NMC cathodes.

5.3. Materials and methods

Material synthesis

The $Ni_{0.9}Mn_{0.05}Co_{0.05}O_2$ precursor was synthesized through a co-precipitation method. The starting solution (NaOH and $NH_3{\cdot}H_2O$ with a molar ratio of NaOH/$NH_3{\cdot}H_2O$ = 1/1.25) was prepared, and the pH was adjusted to 11.00 by adding sulfuric acid. The transition metal aqueous solution ($NiSO_4{\cdot}6H_2O$/$CoSO_4{\cdot}7H_2O$/$MnSO_4{\cdot}H_2O$ in the molar ratio of 0.9/0.05/0.05) and base solution (NaOH/$NH_3{\cdot}H_2O$ in the molar ratio of 1/1.25) were added simultaneously into the starting solution under constant stirring. The reaction was maintained at 50 °C and at the pH of 11.00 ± 0.02 under N_2 flow protection at 0.1 L min^{-1}. The obtained precipitant was washed with deionized water and isopropyl alcohol (IPA), filtered and dried in the vacuum oven at 100 °C for 12 h. The single crystal N90 cathodes with various particle sizes were synthesized through a molten-salt method with different temperature profiles. $Ni_{0.9}Mn_{0.05}Co_{0.05}O_2$ precursor, $LiOH{\cdot}H_2O$ and KCl with a molar ratio of 1/2/1.5 were mixed thoroughly. For S-N90, the mixed reagents were calcined

at 550 °C for 3 h followed by 800 °C for 10 h. L-N90 was prepared by calcination at 550 °C for 3 h followed by 900 °C for 10 h. The obtained product was washed with deionized water and IPA, filtered and dried in the vacuum oven at 100 °C for 12 h. 10% additional LiOH was added to the product obtained from the last step and calcined at 460 °C for 2 h followed by 700 °C for 5 h. The samples for statistical analyses are calcined within the temperature range of 700 °C-1000 °C. The calcination time ranges from 5 h to 20 h. The molar ratio of Li salt/transition metal precursor ranges from 1.1 to 5. The molar ratio of molten salt/transition metal precursor ranges from 1.5 to 4.

Statistical analyses

All discharge capacities are measured at least three times, and all values are used in the statistical analysis. Student's t-test and one-way Analysis of Variance (ANOVA) were performed using GraphPad Prism 8.3.0. The *p*-value is set as 0.05. CART analysis was performed using IBM SPSS Modeler 18.0. The data set was randomly divided into training and testing sets (4:1). The input is the synthetic conditions, including O_2 atmosphere, recalcination, salt ratio, Li ratio, calcination temperature, and calcination time. The output is the capacity.

Materials characterizations

Neutron diffraction (ND) was performed on Nanoscale-Ordered Materials Diffractometer (NOMAD) BL-1B, Spallation Neutron Source (SNS) at Oak Ridge National Laboratory.[31,32] About 0.2–0.3 g powder sample was loaded into the quartz capillary (3 mm) and each measurement took about 1 h. The refinement of neutron diffraction patterns was conducted using the software GSAS EXPGUI. Lab XRD was performed conducted using a Rigaku MiniFlex II diffractometer with Cu K-α radiation (λ =

1.54 Å). SEM was conducted on FEI Quanta 600 FEG ESEM. DSC measurement was performed using a DSC-Q20 equipment at a scan rate of 10 °C/min in the range of 40 °C to 300 °C under N_2 flow. The charged cathodes were collected and sealed in an Ar-filled glovebox. During the DSC measurement, 10 μL of electrolyte was added to the cathode and then sealed in a stainless steel pan.

Electrochemical measurements

The electrode slurry was prepared by mixing S-N90 or L-N90 cathodes, polyvinylidene difluoride (PVdF), acetylene carbon in *N*-methyl-2-pyrrolidone in the weight ratio of 90:5:5. The slurry was subsequently cast on the carbon-coated aluminum foil and dried at 120 °C for 12 h in a vacuum oven. The dry composite electrode was punched into disks with a mass loading of around 9 mg cm^{-2}. The obtained composite electrodes were used as the cathode, and the Li foils were used as the anode with the Whatman glass fiber (1827-047934-AH) as the separator to assemble the CR2032 coin cells in an Ar-filled glove box. The electrolyte was 1 M $LiPF_6$ in ethylene carbonate (EC) and ethyl methyl carbonate (EMC) with 2 wt% vinylene carbonate (VC). The coin cells were under galvanostatic discharge/charge in the cutoff voltage range of 2.5−4.5 V at about 20 °C and measured on the Neware electrochemical workstation. 1 C was defined as fully charging the cathode in 1 h, which corresponded to the specific current rate of 200 mA g^{-1}. The cyclic voltammetry (CV) and electrochemical impedance spectroscopy (EIS) were performed on a BioLogic electrochemical workstation.

The diffusion coefficient D of Li from GITT is based on the equation (1):

$$D = \frac{4}{\pi\tau}\left(\frac{m_B V_M}{M_B S}\right)^2\left(\frac{\Delta E_S}{\Delta E_\tau}\right)^2 \quad (1)$$

where τ is the pulse duration (in this case it was 1 hour), m_B and M_B are the active mass and molar

mass of the active material, V_M is the molar volume (we employed 21.55 cm^3 mol^{-1}), and S is the active surface area of the electrode (S-N90 is 0.66 m^2 g^{-1} and L-N90 is 0.55 m^2 g^{-1}). ΔE_S and ΔE_τ can be obtained from the GITT curves. V_M = density/N_A. S = (mass loading) × (specific surface area)

The diffusion coefficient of Li from CV is based on the Randles-Sevcik equation (2) at 25 °C:

$$i_P = (2.69 \times 10^5) n^{1.5} S D_{Li}^{0.5} C_{Li} \nu^{0.5} \quad (2)$$

where i_P is current maximum, n is number of electrons transferred (n = 1), C_{Li} is molar volume density of Li (0.052 mol cm^{-2}), S is active surface area of the electrode, D_{Li} is Li diffusion coefficient, and ν is scan rate. We estimated D_{Li} from the slope of the fitted line. S = (mass loading) × (specific surface area)

5.4. Results

5.4.1. Statistical analyses and model for performance prediction

To identify how significantly each synthetic parameter can impact the performance of the cathode product, we applied statistical analysis tools, i.e., Student's t-test and Analysis of Variance (ANOVA).[33] Six key synthetic parameters are selected to correlate with the battery performance, i.e., O_2 atmosphere during the calcination, recalcination after the first calcination and water washing, the mole ratio of molten salt to transition metal precursor (salt ratio), the mole ratio of Li source to transition metal precursor (Li ratio), calcination temperature, and calcination time. We use initial discharge capacity in this study as an indicator of the pristine cathode performance to screen the cathode materials

with different synthetic conditions. First, we kept five of the six synthetic parameters consistent with only the remaining one parameter of interest varied for multiple control groups of synthesis. Each of the synthesized cathode products was assembled into Li metal half cells with the same assembly procedure, followed by electrochemical cycling with the same cycling conditions (cutoff voltage windows and cycling rate). Subsequently, the performances with varied parameters of interest were correlated to identify if this specific parameter can induce a significance difference in performance. Student's t-test is a powerful statistical analysis method to identify if two sets of data are significantly different from each other by comparing the means of the two variables. Specifically, a t-value can be obtained for each control group with varied parameter of interest based on Equations (3) and (4):

$$t = \frac{\bar{x}_1 - \bar{x}_2}{\sqrt{s^2\left(\frac{1}{n_1} + \frac{1}{n_2}\right)}} \tag{3}$$

$$s^2 = \frac{\sum_{i-1}^{n_1}(x_i - \bar{x}_1)^2 + \sum_{j-1}^{n_2}\left(x_j - \bar{x}_2\right)^2}{n_1 + n_2 - 2} \tag{4}$$

where $\bar{x}$ is the means of specific sample, n is the sample size, s is the standard deviation, and the subscripts 1 and 2 refer to the controlled samples. Each t-value obtained corresponds to a specific p-value, which is the probability that the results not occurring by chance.[34] Lower than the threshold value of 0.05 for p-value can indicate a 95% plus confidence to state that the two groups of data are significantly correlated. Similarly, ANOVA can identify if there is a significant difference among three or more data sets.

Herein, we applied Student's t-test to identify the contribution of performance variation from O_2 atmosphere, recalcination, and other parameters that have two groups of data for correlation. We applied ANOVA to identify the difference among three or more

data sets for other synthetic parameters. For example, p-values of all three control groups for recalcination in Table 1 are smaller than 0.05, which means the performance of the group with recalcination and the group without recalcination significantly varies. In other words, recalcination can significantly lead to performance differences. We did inductively coupled plasma mass spectrometry (ICP-MS) to quantify the Li content in two single crystal cathodes with different Ni contents. We found that the Li content increased from 0.957 mol to 1.003 mol in single crystal Mg-doped $LiNiO_2$ cathode (SC-LNO-Mg), and increased from 0.904 mol to 0.970 mol in single crystal $LiNi_{0.8}Co_{0.1}Mn_{0.1}O_2$ (SC-NMC811) after recalcination (Table 2). The enhanced performance can be potentially attributed to the increased Li content closer to stoichiometry. Based on Student's t-test analysis, we found that O_2 atmosphere during calcination is also necessary to reach good performance, because O_2 gives rise to significant performance difference as indicated by the small p-values that are greatly smaller than 0.05 (Table 1). We found that changing the salt ratio in the given range of 1.5 to 4.0 and the Li ratio in the range of 1.1 to 2.0 do not induce significant performance variance (Table 1). The impact of temperature on the performance largely depends on the temperature range. We did not observe significant differences in the performance if the calcination temperature variation is smaller than 50 °C (Table 1). However, the temperature can significantly affect the performance when the temperature variation among the groups is larger than 150 °C (Table 1). In addition, the calcination time can also be a factor that significantly determines the performance difference. We want to highlight that the correlation results are dependent on the data range. However, the correlation method can be universally applied to more materials systems to identify the contribution of each synthetic parameter to the product properties.

Table 1. Student's t-test and ANOVA correlation p values of six synthetic parameters

	Recalcination	O_2	Salt ratio	Li ratio	Temperature	Time
Significantly different ($P < 0.05$)?	Yes	Yes	No	No	N/A	Yes
P-value1	0.0042	0.0002	0.0791	0.9617	0.0616 (50 °C variation)	0.0019
P-value2	0.0011	0.0046	0.3671	0.96	0.1645 (50 °C variation)	0.0133
P-value3	0.0183	/	/	0.6418	<0.0001 (150 °C variation)	0.0002

Table 2. Moles of various elements in the two cathodes from ICP-MS

Sample	Li (mol)	Ni (mol)	Mn (mol)	Co (mol)	Mg (mol)
SC-LNO-Mg before recalcination	0.957203	1	/	/	0.002196
SC-LNO-Mg after recalcination	1.003133	1	/	/	0.002707
SC-NMC811 before recalcination	0.903796	0.8	0.099099	0.103921	/
SC-NMC811 after recalcination	0.970399	0.8	0.098637	0.102795	/

After identifying the significance of each synthetic parameter, we want to further predict the battery performance from the input of synthetic conditions. We created a classification and regression tree (CART) model and trained the model hundreds of times with a large set of performance data obtained from various synthetic conditions. Figure 1 shows the scheme of the workflow for the CART model. First, N_1 of performance data are categorized into good (>150 mAh g^{-1}), fair (100-150 mAh g^{-1}), and poor (<100 mAh g^{-1}).

At node 1, one of the six synthetic parameters is randomly chosen to classify N_1 further into good, fair, and poor. A and B conditions indicate yes, no, or specific values. For example, if node 1 represents recalcination, the branch with A condition (Yes) means N_2 of samples are recalcined, which are further classified into good (x_2%), fair (y_2%), and poor (z_2%). In contrast, the branch with B condition indicates (N_1-N_2) samples do not undergo recalcination, and the samples are classified into good (x_3%), fair (y_3%), and poor (z_3%). At the next node 2, one of the remaining five synthetic parameters is chosen for further classification. A and B can be one of multiple values, such as 800 °C, 2.0, 10 hours, if the synthetic parameter is chosen from salt ratio, Li ratio, calcination temperature, and calcination time. Similarly, a synthetic parameter is chosen at each of the following nodes for classification. This procedure is repeated hundreds of times with various synthetic parameters at each node every time. We use 44 groups of data to perform training for the CART model, and the prediction success rate for the trained samples is 88.64% (Table 3). Next, we tested the trained CART model with another 11 groups of data, and the accuracy of prediction on the performance is 81.82% (Table 3). In summary, we have identified the significance of six synthetic parameters to the final cathode performance based on the analyses of Student's t-test and ANOVA. Recalcination, O_2 atmosphere, and calcination time show a significant impact on the performance. The effect of calcination temperature depends on the temperature range selected. Salt ratio and Li ratio have less impact on the performance in this study. We further created a predictive CART model for performance prediction with the input of synthetic parameters and achieved a relatively high accuracy of 81.82%. These findings can provide guidance for synthetic parameter screening to optimize performance.

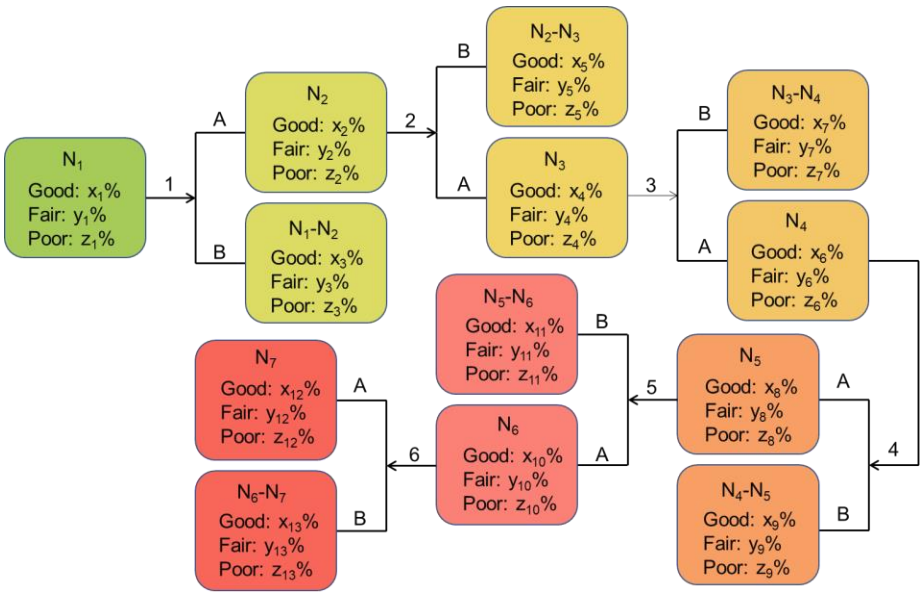

Figure 1. Scheme of classification and regression tree (CART) model workflow. 1 to 6 correspond to the six synthetic parameters, i.e., recalcination, O_2, salt ratio, Li ratio, temperature, time. A represents yes or values, and B represents no or values. x_n, y_n, and z_n are percentage ($x_n + y_n + z_n = 100$, n = 1, 2, …, 12). N_a is sample size (a = 1, 2, …, 7).

Table 3. Performance prediction accuracy of training samples and testing samples in the classification and regression tree (CART) model.

	Training	Rate	Testing	Rate
Correct	39	88.64%	9	81.82%
Wrong	5	11.36%	2	18.18%
Total	44	100.00%	11	100.00%

5.4.2. Morphology and performance

We have synthesized two types of SC-N90 with smaller grain sizes ranging from 1 µm to 2 µm (S-N90, Figure 2a) and larger grain sizes ranging from 3 µm to 4 µm (L-N90, Figure 2b) using the molten salt method. We performed X-ray diffraction (XRD) on both S-N90 and L-N90. Figure 2c shows that both S-N90 and L-N90 have a pure layered phase with the space group of R$\bar{3}$m. Li/Ni cation mixing can be present in as-synthesized Ni-rich layered cathodes due to similar ionic radii of Ni^{2+} and Li^{+}, which is detrimental to cell performance.[35] Therefore, we have performed neutron diffraction (ND) and Rietveld refinement for S-N90 to resolve the site occupancy. We found that there is only 2.1% of Li/Ni cation mixing in S-N90, which can potentially contribute to good performance (Figure 2d and Figure 3).

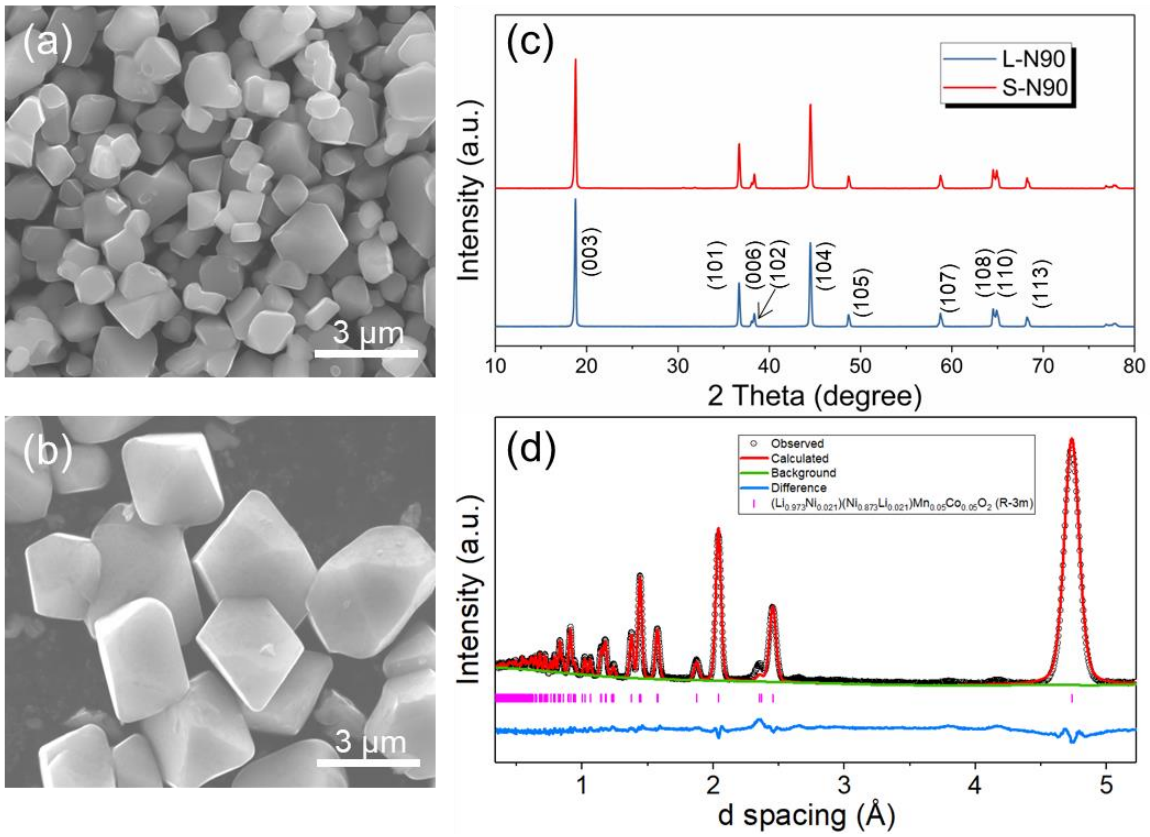

Figure 2. SEM images for the (a) S-N90 and (b) L-N90; (c) XRD patterns of L-N90 and S-N90; (d) ND pattern of S-N90 and Rietveld refinement. R_{wp} = 7.36%.

We evaluated the electrochemical performances of S-N90 and L-N90 in Li metal cell within the cutoff voltage window of 2.5 to 4.5 V versus Li/Li^+ at 20 °C (Figure 3). At C/10 charging and discharging, the specific discharge capacity of S-N90 is 201 mAh g^{-1} after formation, which is higher than 194 mAh g^{-1} of L-N90 (Figure 3a). After 80 cycles, the capacity retention of S-N90 and L-N90 is 90.37% and 69.01%, respectively, indicating significantly higher cycling stability of S-N90 (Figure 3a). At C/3, the specific discharge capacity of S-N90 and L-N90 is 183 mAh g^{-1} and 178 mAh g^{-1}, and the capacity retention is 86.48% and 48.75%, respectively (Figure 3b). The charge and discharge profile of S-N90 is smoother than L-N90, indicating that the phase transformations are mitigated in S-N90 (Figure 3c). The larger overpotential and more irreversible capacity in L-N90 can be potentially attributed to its higher resistance and slower Li conduction, leading to worse performance especially at high current rate. Thermal stability is another important aspect of battery performance. We further compared the thermal stability of S-N90 and L-N90 using differential scanning calorimetry (DSC). The cells using both S-N90 and L-N90 cathodes were charged to 70% state-of-charge (SoC) and then disassembled to collect the cathode powder. 10 µL of the baseline electrolyte was added during the DSC measurement. Figure 3d shows that the onset temperature of exothermic reaction for L-N90 is about 5 °C higher than that of S-N90. The temperature of exothermic peak for L-N90 is 4.2 °C higher than that of S-N90. In addition, the heat release of S-N90 (24.9 W g^{-1}) is nearly 2.5 times larger than that of L-N90 (9.3 W g^{-1}). The DSC results suggest higher thermal stability of L-N90 than S-N90, potentially due to smaller specific surface area of L-N90 (0.55 m^2/g)

than S-N90 (0.66 m^2/g) and less severe surface reaction. Overall, S-N90 demonstrated higher specific capacity and cycling stability, whereas the thermal stability is inferior. We want to further investigate the effects of single crystal size on the performance difference.

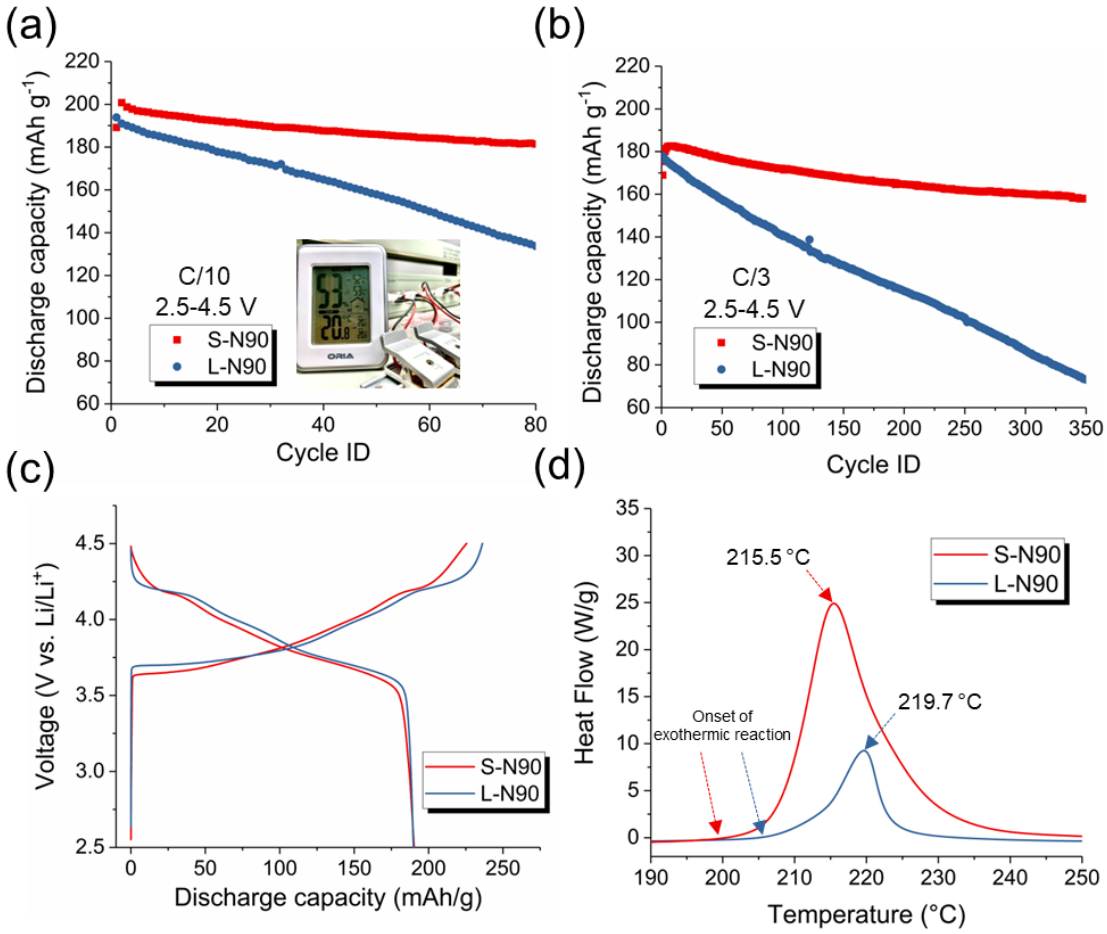

Figure 3. Electrochemical performance and thermal stability of S-N90 and L-N90. Specific discharge capacity retention within 2.5-4.5 V at ~20 °C at (a) C/10 (20 mA g^{-1}) and (b) C/3 (67 mA g^{-1}). (C) Voltage profiles of S-N90 and L-N90 at C/10. (d) DSC profile of charged S-N90 and L-N90. The two cells with S-N90 and L-N90 were both charged to 70% state of charge (SoC). 10 µL electrolyte was added to the charged cathode.

5.4.3. Origin of size effect on the performance difference

We performed electrochemical impedance spectroscopy (EIS) to investigate the cell resistance at different cycles (Figure 4a,b). An equivalent circuit in Figure 4a was used to fit the obtained spectra. In the equivalent circuit, R_e represents the electrolyte ohmic resistance. R_i represents the interfacial resistance at the solid electrolyte interface (SEI) as indicated by the left semicircle at high frequency. R_{ct} indicates the charge transfer resistance reflected by the right semicircle at low frequency. Z_w is the Warburg resistance that reflects the Li diffusion in the bulk electrode. We identified that the initial interfacial resistance and charge transfer resistance of L-N90 at the first cycle is around 50 Ohm and 100 Ohm, which increased to about 70 Ohm and 190 Ohm after ten cycles, respectively (Figure 4a). In contrast, the initial interfacial resistance and charge transfer resistance of S-N90 at the first cycle is only around 10 Ohm and 50 Ohm (Figure 4b). After ten cycles, the interfacial resistance remained around 10 Ohm, and the charge transfer resistance increased to around 90 Ohm but was still much lower than that of L-N90 (Figure 4b). Therefore, the lower initial and after-cycling resistance can contribute to better performance of S-N90 than L-N90.

To investigate the kinetics of Li transport, we performed cyclic voltammetry (CV) at a series of scan rates for L-N90 (Figure 4c) and S-N90 (Figure 4d) to estimate the Li-ion diffusion coefficient. Two major peaks $\#_1$ and $\#_2$ were selected to represent the oxidation reaction during charging and the reduction reaction during discharging (Figure 4c). Based on the Randles-Sevcik equation (2), the Li-ion diffusion coefficient can be estimated from the slope of the fitted line in the plot of current as a function of the square root of the scan rate (Figure 4e,f). We found that the Li-ion diffusion coefficient of L-N90 and S-N90 is at

the same magnitude. Specifically, the apparent Li-ion diffusion coefficient for L-N90 and S-N90 during discharging is 1.49×10^{-13} cm^2 s^{-1}, 2.56×10^{-13} cm^2 s^{-1} and during charging is 4.69×10^{-13} cm^2 s^{-1}, 4.72×10^{-13} cm^2 s^{-1}, respectively.

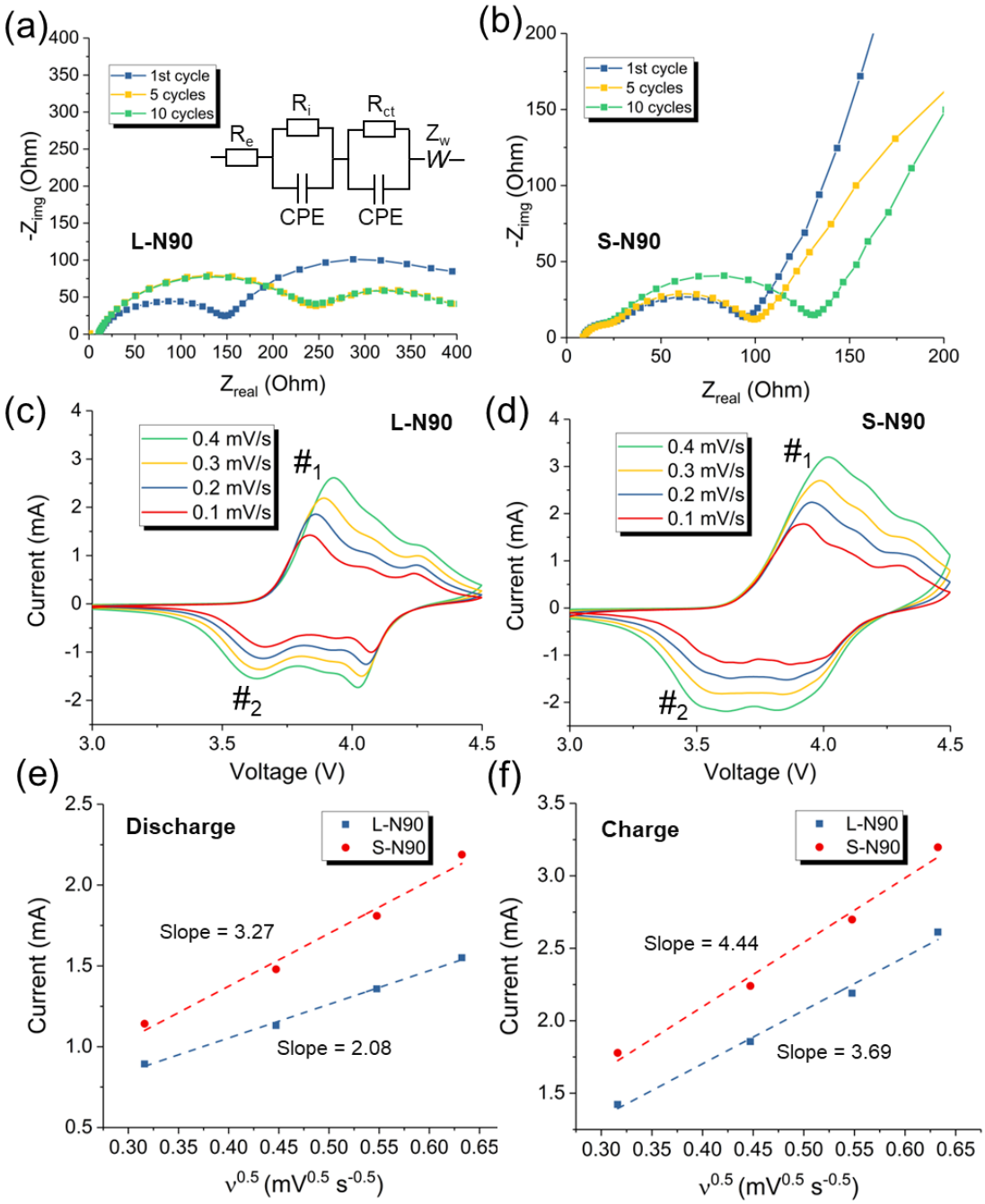

Figure 4. Nyquist plots of the half cells containing the (a) L-N90 and (b) S-N90 cathodes at the 1st cycle, 5 cycles, and 10 cycles at discharged state. The insert shows the equivalent circuit used to fit the curves. Cyclic voltammogram at the continuously increasing scan rates from 0.1 to 0.4 mV/s for (c) L-N90 and (d) S-N90. The current intensity as a function

of the squire root of scan rates for (e) the redox peaks $\#_2$ during discharging and (f) the redox peaks $\#_1$ during charging.

To verify the calculated Li-ion diffusion coefficient, we further carried out the galvanostatic intermittent titration technique (GITT) for L-N90 (Figure 5a) and S-N90 (Figure 5b) to investigate the Li kinetics. The hysteresis for both L-N90 and S-N90 is around 50 mV, which is reflected by the difference between the charged open circuit voltages (OCVs) and discharge OCVs (Figure 5a,b). The Li-ion diffusion coefficient at different SoC was calculated for both L-N90 and S-N90 during charging (Figure 5c) and discharging (Figure 5d). We found that the diffusion coefficients of L-N90 and S-N90 are very close, which is consistent with the results from CV. The sudden drop of Li-ion diffusion coefficient at high SoC is potentially due to the phase transformation from the H2 to the H3 phase.[36] In all, the Li-ion diffusion coefficients of L-N90 and S-N90 are close. The slower Li conduction in L-N90 can be potentially attributed to the longer Li traveling path in large grain.

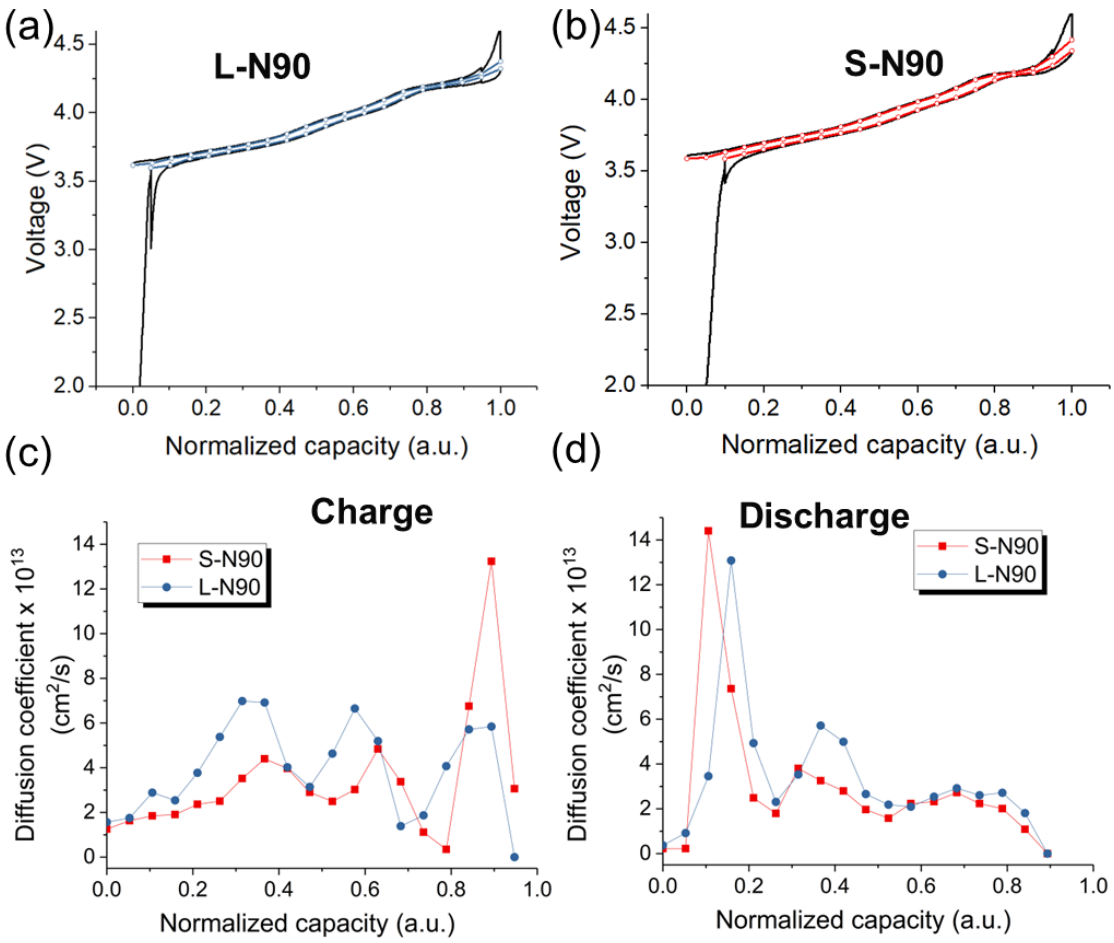

Figure 5. Kinetics performance of the half cells containing the S-N90 and L-N90 cathode. GITT curves at the second cycle of (a) L-N90 and (b) S-N90 and their derived open circuit voltage (OCV) curve of the cell upon charging/discharging at C/20 for 1 h and following with 6 h rest. The apparent chemical diffusion coefficient as a function of normalized capacity derived from the GITT curves during (c) charging and (d) discharging.

5.5. Discussion

In this work, we have synthesized over 50 single crystal Ni-rich layered oxide cathodes (Ni ≥ 80%) with various conditions using the molten salt method. We created correlation models to study how significantly each synthetic parameter can impact the

cathode performance. We found that recalcination after water washing and O_2 environment during calcination are essential to obtain high initial capacity. The temperature range has a great impact on cell performance. The performance does not exhibit a significant difference when the calcination temperature variation is smaller than 50 °C. However, a temperature variation larger than 150 °C leads to significant performance differences. The calcination time is also strongly correlated with performance. On the other hand, the salt ratio and Li ratio do not show a significant correlation with the performance within the selected range in this study, which are 1.5 to 4.0 and 1.1 to 2.0, respectively. Noting the correlation identified may depend on the specific range chosen in this work, but the model can be universally applied to other synthetic systems. We also created a prediction model to forecast the performance based on the input of 44 groups of synthetic conditions and performance correlations. We tested the model with 11 groups of data and achieved an 81.82% prediction rate. We further synthesized single crystal L-N90 and S-N90 with the same composition but different particle sizes. L-N90 shows worse capacity and cycle life than S-N90 due to slower Li kinetics. We identified that the Li diffusion coefficient of L-N90 and S-N90 is at the same magnitude based on CV and GITT. The worse Li kinetics in L-N90 can be potentially attributed to the longer Li transport distance. The thermal stability of L-N90 is higher than that of S-N90 potentially due to the smaller specific surface area of L-N90. In all, we have identified the particle size effect on the performance of single crystal Ni-rich layered cathodes. This work provides guidance for the synthesis of single crystal Ni-rich layered cathodes using the molten salt method with statistical correlation and prediction models.

5.6. Acknowledgements

The work is supported by the US Department of Energy's Office of Energy Efficiency and Renewable Energy (EERE) under the award number: DE-EE0008444. The use of the Spallation Neutron Source at Oak Ridge National Laboratory is supported by the US Department of Energy, Office of Science, Office of Basic Energy Sciences under Contract No. DE-AC05-00OR22725. This research was partially supported by Virginia Tech's Institute for Critical Technology and Applied Science through instruments provided by the Nanoscale Characterization and Fabrication Laboratory (NCFL). ZY also acknowledges the assistance of Yue Zhang on the BET surface area measurement.

5.7. References

(1) Yang, Z.; Huang, H.; Lin, F.; Yang, Z.; Lin, F.; Huang, H. Sustainable Electric Vehicle Batteries for a Sustainable World: Perspectives on Battery Cathodes, Environment, Supply Chain, Manufacturing, Life Cycle, and Policy. *Adv. Energy Mater.* **2022**, *12* (26), 2200383.

(2) Yoshio, M.; Noguchi, H.; Itoh, J. ichi; Okada, M.; Mouri, T. Preparation and Properties of $LiCo_yMn_xNi_{1-x-y}O_2$ as a Cathode for Lithium Ion Batteries. *J. Power Sources* **2000**, *90* (2), 176–181.

(3) Lu, Z.; MacNeil, D. D.; Dahn, J. R. Layered $Li[Ni_xCo_{1-2x}Mn_x]O_2$ Cathode Materials for Lithium-Ion Batteries. *Electrochem. Solid-State Lett.* **2001**, *4* (12), A200.

(4) Xu, J.; Lin, F.; Doeff, M. M.; Tong, W. A Review of Ni-Based Layered Oxides for Rechargeable Li-Ion Batteries. *J. Mater. Chem. A* **2017**, *5* (3), 874–901.

(5) Noh, H. J.; Youn, S.; Yoon, C. S.; Sun, Y. K. Comparison of the Structural and Electrochemical Properties of Layered $Li[Ni_xCo_yMn_z]O_2$ (x = 1/3, 0.5, 0.6, 0.7, 0.8

and 0.85) Cathode Material for Lithium-Ion Batteries. *J. Power Sources* **2013**, *233*, 121–130.

(6) Bianchini, M.; Roca-Ayats, M.; Hartmann, P.; Brezesinski, T.; Janek, J. There and Back Again—The Journey of $LiNiO_2$ as a Cathode Active Material. *Angew. Chemie Int. Ed.* **2019**, *58* (31), 10434–10458.

(7) Manthiram, A.; Knight, J. C.; Myung, S. T.; Oh, S. M.; Sun, Y. K. Nickel-Rich and Lithium-Rich Layered Oxide Cathodes: Progress and Perspectives. *Adv. Energy Mater.* **2016**, *6* (1), 1501010.

(8) Chen, Z.; Qin, Y.; Amine, K.; Sun, Y. K. Role of Surface Coating on Cathode Materials for Lithium -Ion Batteries. *J. Mater. Chem.* **2010**, *20* (36), 7606–7612.

(9) Sun, Y.-K.; Myung, S.-T.; Park, B.-C.; Prakash, J.; Belharouak, I.; Amine, K. High-Energy Cathode Material for Long-Life and Safe Lithium Batteries. *Nat. Mater.* **2009**, *8* (4), 320–324.

(10) Li, J.; Camardese, J.; Shunmugasundaram, R.; Glazier, S.; Lu, Z.; Dahn, J. R. Synthesis and Characterization of the Lithium-Rich Core-Shell Cathodes with Low Irreversible Capacity and Mitigated Voltage Fade. *Chem. Mater.* **2015**, *27* (9), 3366–3377.

(11) Kim, U.-H.; Lee, E.-J.; Yoon, C. S.; Myung, S.-T.; Sun, Y.-K.; Kim, U.-H.; Lee, E.-J.; Sun, Y.-K.; Yoon, C. S.; Myung, -T S. Compositionally Graded Cathode Material with Long-Term Cycling Stability for Electric Vehicles Application. *Adv. Energy Mater.* **2016**, *6* (22), 1601417.

(12) Koenig, G. M.; Belharouak, I.; Deng, H.; Sun, Y. K.; Amine, K. Composition-Tailored Synthesis of Gradient Transition Metal Precursor Particles for Lithium-Ion

Battery Cathode Materials. *Chem. Mater.* **2011**, *23* (7), 1954–1963.

(13) Liang, J. Y.; Zhang, X. D.; Zeng, X. X.; Yan, M.; Yin, Y. X.; Xin, S.; Wang, W. P.; Wu, X. W.; Shi, J. L.; Wan, L. J.; Guo, Y. G. Enabling a Durable Electrochemical Interface via an Artificial Amorphous Cathode Electrolyte Interphase for Hybrid Solid/Liquid Lithium-Metal Batteries. *Angew. Chemie* **2020**, *132* (16), 6647–6651.

(14) Yang, Z.; Lin, F. Heterogeneous, Defect-Rich Battery Particles and Electrodes: Why Do They Matter, and How Can One Leverage Them? *J. Phys. Chem. C* **2021**, *125* (18), 9618–9629.

(15) Langdon, J.; Manthiram, A. A Perspective on Single-Crystal Layered Oxide Cathodes for Lithium-Ion Batteries. *Energy Storage Mater.* **2021**, *37*, 143–160.

(16) Qian, G.; Zhang, Y.; Li, L.; Zhang, R.; Xu, J.; Cheng, Z.; Xie, S.; Wang, H.; Rao, Q.; He, Y.; Shen, Y.; Chen, L.; Tang, M.; Ma, Z. F. Single-Crystal Nickel-Rich Layered-Oxide Battery Cathode Materials: Synthesis, Electrochemistry, and Intra-Granular Fracture. *Energy Storage Mater.* **2020**, *27*, 140–149.

(17) Xu, Z.; Jiang, Z.; Kuai, C.; Xu, R.; Qin, C.; Zhang, Y.; Rahman, M. M.; Wei, C.; Nordlund, D.; Sun, C. J.; Xiao, X.; Du, X. W.; Zhao, K.; Yan, P.; Liu, Y.; Lin, F. Charge Distribution Guided by Grain Crystallographic Orientations in Polycrystalline Battery Materials. *Nat. Commun.* **2020**, *11* (1), 83.

(18) Li, J.; Sharma, N.; Jiang, Z.; Yang, Y.; Monaco, F.; Xu, Z.; Hou, D.; Ratner, D.; Pianetta, P.; Cloetens, P.; Lin, F.; Zhao, K.; Liu, Y. Dynamics of Particle Network in Composite Battery Cathodes. *Science.* **2022**, *376* (6592), 517–521.

(19) Xu, Z.; Rahman, M. M.; Mu, L.; Liu, Y.; Lin, F. Chemomechanical Behaviors of Layered Cathode Materials in Alkali Metal Ion Batteries. *J. Mater. Chem. A* **2018**,

6 (44), 21859–21884.

(20) Li, G.; Zhang, Z.; Huang, Z.; Yang, C.; Zuo, Z.; Zhou, H. Understanding the Accumulated Cycle Capacity Fade Caused by the Secondary Particle Fracture of $LiNi_{1-x-y}Co_xMn_yO_2$ Cathode for Lithium Ion Batteries. *J. Solid State Electrochem.* **2017**, *21* (3), 673–682.

(21) Xu, K. Electrolytes and Interphases in Li-Ion Batteries and Beyond. *Chem. Rev.* **2014**, *114* (23), 11503–11618.

(22) Watanabe, S.; Kinoshita, M.; Hosokawa, T.; Morigaki, K.; Nakura, K. Capacity Fade of $LiAl_yNi_{1-x-y}Co_xO_2$ Cathode for Lithium-Ion Batteries during Accelerated Calendar and Cycle Life Tests (Surface Analysis of $LiAl_yNi_{1-x-y}Co_xO_2$ Cathode after Cycle Tests in Restricted Depth of Discharge Ranges). *J. Power Sources* **2014**, *258*, 210–217.

(23) Fan, X.; Hu, G.; Zhang, B.; Ou, X.; Zhang, J.; Zhao, W.; Jia, H.; Zou, L.; Li, P.; Yang, Y. Crack-Free Single-Crystalline Ni-Rich Layered NCM Cathode Enable Superior Cycling Performance of Lithium-Ion Batteries. *Nano Energy* **2020**, *70*, 104450.

(24) Zhu, J.; Chen, G. Single-Crystal Based Studies for Correlating the Properties and High-Voltage Performance of $Li[Ni_xMn_yCo_{1-x-y}]O_2$ Cathodes. *J. Mater. Chem. A* **2019**, *7* (10), 5463–5474.

(25) German, R. M. Coarsening in Sintering: Grain Shape Distribution, Grain Size Distribution, and Grain Growth Kinetics in Solid-Pore Systems. *Critical Reviews in Solid State and Materials Sciences* **2010**, *35* (4), 263–305.

(26) Li, J.; Li, H.; Stone, W.; Weber, R.; Hy, S.; Dahn, J. R. Synthesis of Single Crystal

$LiNi_{0.5}Mn_{0.3}Co_{0.2}O_2$ for Lithium Ion Batteries . *J. Electrochem. Soc.* **2017**, *164* (14), A3529–A3537.

(27) Liu, W.; Oh, P.; Liu, X.; Lee, M.-J.; Cho, W.; Chae, S.; Kim, Y.; Cho, J. Nickel-Rich Layered Lithium Transition-Metal Oxide for High-Energy Lithium-Ion Batteries. *Angew. Chemie Int. Ed.* **2015**, *54* (15), 4440–4457.

(28) Malik, M.; Chan, K. H.; Azimi, G. Review on the Synthesis of $LiNi_xMn_yCo_{1-x-y}O_2$ (NMC) Cathodes for Lithium-Ion Batteries. *Mater. Today Energy* **2022**, *28*, 101066.

(29) Kim, Y. Lithium Nickel Cobalt Manganese Oxide Synthesized Using Alkali Chloride Flux: Morphology and Performance as a Cathode Material for Lithium Ion Batteries. *ACS Appl. Mater. Interfaces* **2012**, *4* (5), 2329–2333.

(30) Spence, S. L.; Xu, Z.; Sainio, S.; Nordlund, D.; Lin, F. Tuning the Morphology and Electronic Properties of Single-Crystal $LiNi_{0.5}Mn_{1.5}O_{4-\delta}$: Exploring the Influence of LiCl-KCl Molten Salt Flux Composition and Synthesis Temperature. *Inorg. Chem.* **2020**, *59* (15), 10591–10603.

(31) Neuefeind, J.; Feygenson, M.; Carruth, J.; Hoffmann, R.; Chipley, K. K. The Nanoscale Ordered MAterials Diffractometer NOMAD at the Spallation Neutron Source SNS. *Nucl. Instruments Methods Phys. Res. Sect. B Beam Interact. with Mater. Atoms* **2012**, *287*, 68–75.

(32) Calder, S.; An, K.; Boehler, R.; Dela Cruz, C. R.; Frontzek, M. D.; Guthrie, M.; Haberl, B.; Huq, A.; Kimber, S. A. J.; Liu, J.; Molaison, J. J.; Neuefeind, J.; Page, K.; Dos Santos, A. M.; Taddei, K. M.; Tulk, C.; Tucker, M. G. A Suite-Level Review of the Neutron Powder Diffraction Instruments at Oak Ridge National Laboratory. *Review of Scientific Instruments* **2018**, 92, 92701.

(33) Mishra, P.; Singh, U.; Pandey, C. M.; Mishra, P.; Pandey, G. Application of Student's t-Test, Analysis of Variance, and Covariance. *Ann. Card. Anaesth.* **2019**, *22* (4), 407.

(34) Modell, W. CRC Handbook of Tables for Probability and Statistics. *Clin. Pharmacol. Ther.* **1966**, *7* (4), 560–561.

(35) Li, J.; Liang, G.; Zheng, W.; Zhang, S.; Davey, K.; Pang, W. K.; Guo, Z. Addressing Cation Mixing in Layered Structured Cathodes for Lithium-Ion Batteries: A Critical Review. *Nano Mater. Sci.* **2022**.

(36) de Biasi, L.; Schiele, A.; Roca-Ayats, M.; Garcia, G.; Brezesinski, T.; Hartmann, P.; Janek, J. Phase Transformation Behavior and Stability of $LiNiO_2$ Cathode Material for Li-Ion Batteries Obtained from In Situ Gas Analysis and Operando X-Ray Diffraction. *ChemSusChem* **2019**, *12* (10), 2240–2250.

6. Conclusions and future perspective

6.1. Conclusions

Ni-rich layered oxide cathodes have been becoming one of the most promising cathode chemistries to enable the next generation high-energy LIBs. However, the low chemical and structural stability of Ni-rich cathodes are the major bottlenecks that impede their further applications. In addition, these Ni-rich cathodes usually contain Co to enhance the structural stability, whereas Co raises concerns of sustainability, cost, and human rights issues. Our studies provide insights in the design and synthesis of Ni-rich and low/no-Co layered oxide cathodes through surface and bulk modification to enhance the battery cycling stability.

In Chapter 2, we use a 3D doping strategy to synthesize the Ni-rich Co-free layered cathode $LiNi_{0.96}Mg_{0.02}Ti_{0.02}O_2$. 3D refers to the dopant distribution in cathode particles, where Ti is enriched at cathode surface to mitigate the surface oxygen loss, and Mg distributes homogeneously throughout the cathode particle to achieve bulk structural integrity. In this work, we probed the dopant redistribution, electronic and chemical structure evolution, and phase transformations at multiple length scales during the synthesis. Ti and Mg dopants diffuse in the Ni hydroxide matrix at the early stage of calcination (below 300 °C), much before the formation of the layered oxide phase. Mg completes redistribution before Ti. Mg distribution is relatively uniform, while Ti is enriched at the particle surface. The local structure change and phase transformations are heterogenous, depending on the geometric location in secondary particles and different calcination stages. This study enriches the understanding of Ni-rich Co-free cathode formation mechanism and provides guidance for cathode modification through 3D doping

approach. The protocol established in this work can also be applied to study the formation mechanism of other energy materials.

Doping, surface coating, and concentration gradient engineering are several approaches widely adopted by the battery community to enhance the cathode stability. In Chapter 3, we investigate the elemental diffusion behavior at multiple length scales using Mn-coated $LiNiO_2$ as the platform. We found that the coating element does not solely remain on the surface of the cathode with the heat treatment at around 500 °C as coating approaches widely adopt. In contrast, the coating element can diffuse in the cathode lattice and forms a gradient distribution. Mn diffusion rate is significantly higher with higher temperatures. Our particle-level measurement reveals that Mn diffusion rate varies with the depth even at the same temperature. A combination of coating, doping, and concentration gradient at various extents can be potentially obtained by tuning the heating condition to modify the materials properties and achieve better performance.

The cathode engineering approaches, such as doping and coating, usually require addition processing that can raise the cost and energy consumption. In Chapter 4, we propose a facile quenching approach during the synthesis of cathodes, which requires no additional steps or introduction of foreign elements, to form a surface passivation layer that stabilizes the cathode surface. We use the state-of-the-art commercial cathode $LiNi_{0.8}Mn_{0.1}Co_{0.1}O_2$ (NMC811) to demonstrate the method. The modified NMC811 delivers relatively high discharge capacity of 185 mAh/g and high energy density of 702 Wh/kg at 1C charging and discharging rate. Upon 300 cycles at 1C, the capacity retention of modified NMC811 is 90% and higher than 72% of pristine NMC811. The enhanced electrochemical performance can be attributed to the stable surface structure, which can

not only mitigate the parasitic reactions between cathode and electrolyte, but also alleviate interface impendence growth during cycling. Charge distribution is more homogeneous in the modified NMC811, so Li transportation upon cycling is more effective.

The aforementioned cathode engineering approaches are based on polycrystalline particle morphology. In contrast, single crystal cathodes have higher structural integrity and cycling stability than their polycrystalline counterparts. In Chapter 5, we have synthesized over 50 single crystal Ni-rich layered oxide cathodes (Ni ≥ 80%) with various conditions using molten salt method. We use statistical tools to identify the significance of each synthetic parameters upon molten salt synthesis. Based on a large set of controlled experiments, we created a prediction model to forecast the performance of synthesized single crystal Ni-rich NMC cathodes from the input of synthetic parameters with an 81.82% prediction accuracy. By tuning the synthetic conditions, we synthesized single crystal $LiNi_{0.9}Co_{0.05}Mn_{0.05}O_2$ (SC-N90) with different particle sizes. We found that large SC-N90 (L-N90) showed worse capacity and cycle life especially at high current rate than small SC-N90 (S-N90) due to slower Li kinetics. This work provides guidance for the synthesis of single crystal Ni-rich layered cathodes using molten salt method with statistical correlation and prediction models.

6.2. Perspective of future work

Our studies have investigated a series of approaches to enhancing the stability of Ni-rich and low/no-Co layered oxide cathodes, including 3D doping, elemental distribution engineering, surface passivation layer formation, and single crystal synthesis. We revealed the dopant redistribution, electronic and chemical structure evolution, and phase transformations during the formation of the Ni-rich Co-free layered cathode

$LiNi_{0.96}Mg_{0.02}Ti_{0.02}O_2$. We also studied the elemental diffusion within cathode particles and the corresponding chemical and structural changes at different extent of diffusion using Mn-coating $LiNiO_2$ as the platform. These studies lay the groundwork for cathode synthesis and modification through ion distribution control and demonstrate a systematic method to probe such doped or coated cathodes. However, the diffusion behavior may vary with the diffusion coefficients of specific elements and the properties of cathode matrix. More research efforts are in demand to probe a large variety of elements in more materials systems to identify the universal patterns of ion diffusion in solid materials. Our study has demonstrated the feasibility for combing doping, coating, and concentration gradient engineering to maximize the elemental utilization efficiency. Next, optimizing the extent of mixing the three approaches by manipulating the elemental distribution is needed to enhance the battery performance in more cathode materials.

Our work demonstrates a facile quenching approach in air to forming a surface passivation layer that can stabilize the cathode surface without the any post-treatment after synthesis. More research work can be performed to further optimize the composition and thickness of the surface layer by tuning the quenching conditions, such as the species and partial pressure of gases and quenching duration. Although the synthetic protocol for commercial layered oxide cathodes is relatively mature at industrial scale, optimizing the precursor synthesis and calcination thermal profile can further promote the mechanical robustness and charge homogeneity of the cathodes. For instance, our preliminary results indicate that the size of the secondary polycrystalline cathode particles can be controlled by tuning the condition of co-precipitation precursor synthesis. The size and shape of the primary single grain can be modified by changing the temperature profile of calcination. It

is reported that an optimization of grain orientation in the polycrystalline particles can suppress the propagation of microcracks thus enhance the battery cycle life.[1,2] The grain microstructure can also impact the thermal stability.[3] Therefore, more research work can be carried out to optimize the synthesis of the polycrystalline layered cathodes regarding the shape, size, and arrangement of the primary particles and secondary particles.

In parallel to polycrystalline Ni-rich layered oxide cathodes, we also design and synthesize their single crystal counterparts that have higher structural stability. We have established molten-salt synthesis protocols for single crystal Ni-rich cathodes with the assistance of statistical analysis tools. Our study also identified the effect of single crystal size on the performance of the battery. However, more investigations are needed to identify the optimal sizes for different compositions and materials systems. Based on our synthetic protocols, single crystal Ni-rich cathodes with different particle sizes can be obtained. Relatively small single crystal cathodes can be mixed with the large polycrystalline particles to fill in the pores and further enhance the energy density. The size of the single crystal particles and the ratio between the single crystal and polycrystalline cathodes need more investigation to achieve optimal electrochemical performance of the hybrid cathode. The synthesis of single crystal layered cathodes can be further optimized. Programmable heating and quenching (PHQ) is one of the promising approaches to achieving efficient cathode synthesis, although the method has not been demonstrated in cathode synthesis yet.[4] PHQ is based on Joule-heating that enables fast heating and quenching switch in milliseconds and reduces the cost of energy and time, which is substantially more efficient than the conventional high temperature synthesis.[4] An additional pulse high temperature sintering (PHTS) step to conventional high temperature synthesis is reported to achieve

single crystal cathode formation.[5] The rapid high temperature heating step can promote the grain growth with minimal Li loss. The heating temperature and duration of the PHQ method in cathode synthesis needs to be optimized in future studies. Molten salt can be added to the synthesis to control the morphology and lower the single crystal formation temperature.

Solid-state electrolytes (SSEs) can achieve higher cell-level energy density and safety for Ni-rich cathodes. However, the understanding of the cathode-SSE interface is still limited. Considering the various cathode engineering approaches, such as different surface coating, the understanding of the modified cathode-SSE interface is even more rare. Therefore, more potential future work can be performed to study the compatibility of Ni-rich cathode and SSE especially at the interface.

6.3. Perspective of future battery and electrical vehicle evolution

LIBs have reshaped the way we transport and connect with each other since the first commercialization. In the past decade, LIBs have played a significant role in the revolution of smartphones. In recent years, LIBs have demonstrated remarkable success in EVs for a greener automotive industry. In the next few decades, LIBs will not only experience expeditious growth but also promote the construction of associated infrastructures. LIBs will shape the world into a more interconnected and smarter place with the rise of the 5G networks. Herein, we envision the potential development of energy storage technologies and EV charging infrastructures in the future (Figure 1). In the short-term scenario that requires relatively less technology advancement, EVs running out of electricity can be charged *via* peer-to-peer car charging (P2C2) by other vehicles (Figure 1a). The P2C2 requires low-battery EVs to be plugged into full-battery vehicles.[6] Low-

battery EVs can also be charged during driving by the mobile charging stations, which are portable and temporarily installed in the EVs.[6] However, the weight of the portable charging stations may potentially lead to a low efficiency in vehicle mobility. Service vehicles will be on duty to provide P2C2 services or mobile charging stations. These charging methods are potentially not appropriate for routine charging but can offer rescue to EVs in an emergency. In the regions that receive sufficient sunshine, solar panel charging can be integrated on EVs to provide auxiliary support to the battery system. Sono Motors has announced their solar cell integrated EV Sion, which utilizes solar power.[7] Regarding the infrastructure, more charging stations can be constructed along the highways. More entertainment facilities will accompany the charging stations, such as restaurants and shopping malls, which can serve the people waiting for charging and boost the local economy. To summarize, we proposed several approaches to modifying the current EV charging methods based on relatively mature technologies. In addition, we conceived the long-term scenario that involves relatively significant adjustments to the current charging methods and infrastructures.

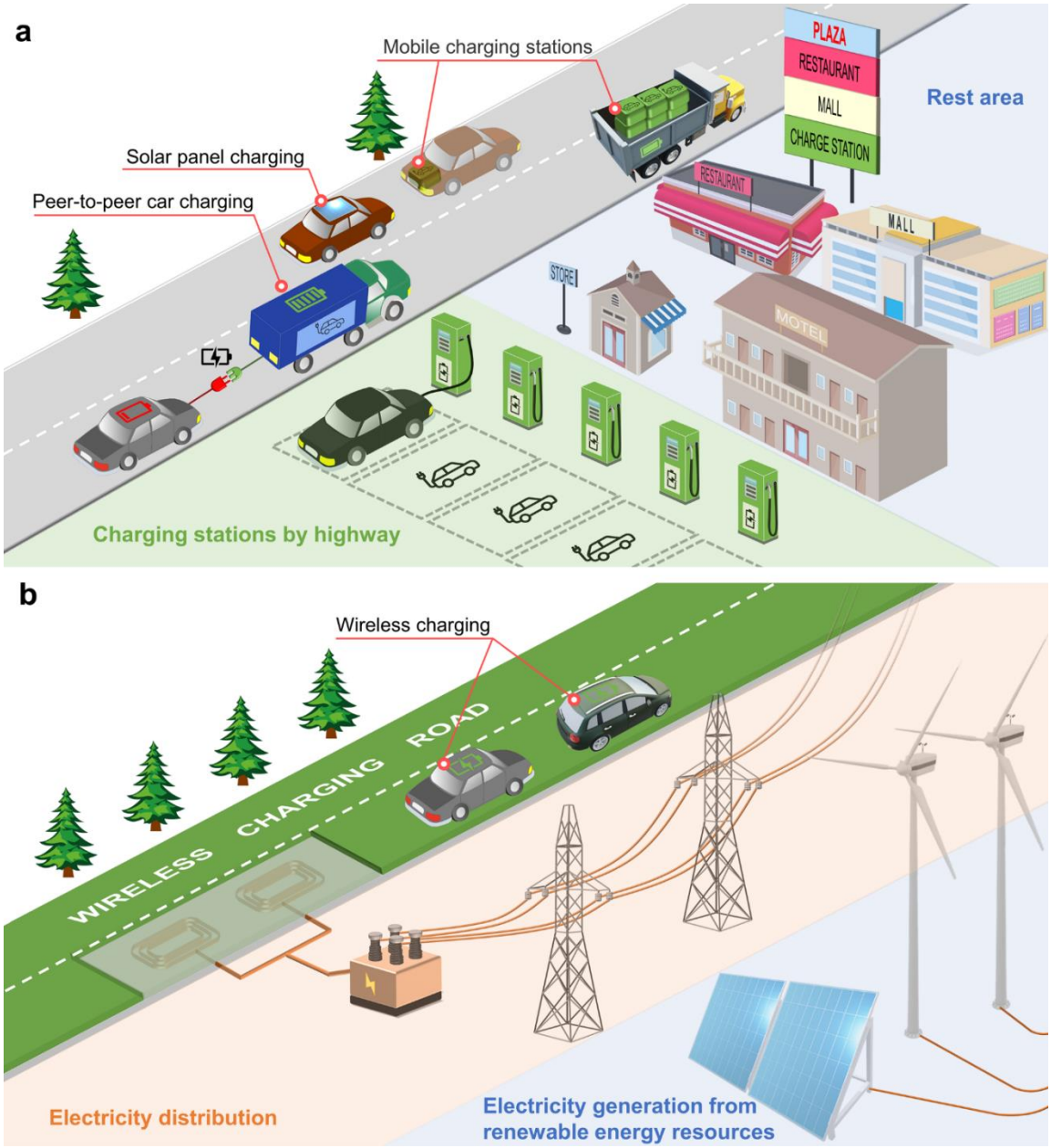

Figure 1. Scheme of visionary charging infrastructures in the future. (a) Short-term scenario that requires less technology advancement. (b) Long-term scenario that requires more technology advancement.

In the long-term scenario, both EVs and infrastructures will experience more technical breakthroughs, and there will be more interactions between them. Smart roads

can be constructed to combine wireless charging with various functions, such as ice melting in winter and traffic condition monitoring (Figure 2b). EVs can be charged on the roads during driving, which will alleviate the anxiety of mileage. In addition, energy harvesting technologies, such as piezoelectric systems, can be integrated into smart roads to generate electricity based on the stress and motion of vehicles, which can enhance the energy utilization efficiency.[8] Several projects of smart roads integrated with wireless charging have been demonstrated in Europe and the US by Electreon Wireless Ltd and Integrated Roadways.[9,10] This approach might open the door to a broader range of automotive batteries with lower energy density but superior economic and environmental benefits. During the transition period, the roads can be partially reconstructed to accommodate one or two wireless charging lanes based on established infrastructures. Vehicle-to-everything (V2X) communication will be strengthened significantly thanks to the high-speed 5G network that is undergoing rapid development.[11] V2X can create an information network by exchanging data between vehicles and traffic systems. As a result, a smarter, safer, and more efficient traffic ecosystem will become a reality, including more mature autonomous driving, collision avoidance, and traffic jam forecast and reduction. The breakthrough on electricity generation is also expected for the greener long-term scenario. Electricity generation using fossil fuels is still a significant source of carbon emissions today. More renewable energy sources, such as wind and solar energy, will be applied in suitable regions for future electricity generation. Electricity distribution stations can be constructed accordingly along with the charging infrastructures to achieve more flexible and convenient charging. In all, we anticipate that EVs will be more interconnected to other

facilities in the long-term scenario. The innovation of charging methods will also provide more room for battery materials development.

It is the worst of times when resources on the earth are becoming more limited, and the human society is facing energy crises and environmental degradation. It is the best of times when people are actively seeking strategies to address energy and environmental challenges with advanced and sustainable energy storage technologies. LIBs have changed and will continue to change the lifestyle of people and the ecosystem in the twenty-first century. In the upcoming decades, LIBs at the materials level will gradually shift to more sustainable chemistries. With extensive financial and strategic support from governments around the world, the LIB manufacturing and associated infrastructure construction will undergo a rapid growth. Climate issues can be alleviated by substituting ICEVs with EVs. Recycling will occupy a larger portion of the market and in turn enhance the economic and environmental efficiency of the battery production. The healthy growth of the LIB industry can never be solely accomplished by one specific field. We believe that building the synergies between different fields surrounding the LIB industry will greatly promote the development of LIBs for a more sustainable society. This Perspective aims to inspire more interdisciplinary discussion and investigations on the advancement of LIBs.

6.4. References

(1) Park, G. T.; Ryu, H. H.; Noh, T. C.; Kang, G. C.; Sun, Y. K. Microstructure-Optimized Concentration-Gradient NCM Cathode for Long-Life Li-Ion Batteries. *Mater. Today* **2022**, *52*, 9–18.

(2) Ryu, H. H.; Park, N. Y.; Noh, T. C.; Kang, G. C.; Maglia, F.; Kim, S. J.; Yoon, C. S.; Sun, Y. K. Microstrain Alleviation in High-Energy Ni-Rich NCMA Cathode for

Long Battery Life. *ACS Energy Lett.* **2021**, *6* (1), 216–223.

(3) Hou, D.; Xu, Z.; Yang, Z.; Kuai, C.; Du, Z.; Sun, C. J.; Ren, Y.; Liu, J.; Xiao, X.; Lin, F. Effect of the Grain Arrangements on the Thermal Stability of Polycrystalline Nickel-Rich Lithium-Based Battery Cathodes. *Nat. Commun. 2022 131* **2022**, *13* (1), 1–11.

(4) Dong, Q.; Yao, Y.; Cheng, S.; Alexopoulos, K.; Gao, J.; Srinivas, S.; Wang, Y.; Pei, Y.; Zheng, C.; Brozena, A. H.; Zhao, H.; Wang, X.; Toraman, H. E.; Yang, B.; Kevrekidis, I. G.; Ju, Y.; Vlachos, D. G.; Liu, D.; Hu, L. Programmable Heating and Quenching for Efficient Thermochemical Synthesis. *Nat.* **2022**, *605* (7910), 470–476.

(5) Huang, H.; Zhang, L.; Tian, H.; Yan, J.; Tong, J.; Liu, X.; Zhang, H.; Huang, H.; Hao, S. meng; Gao, J.; Yu, L.; Li, H.; Qiu, J.; Zhou, W. Pulse High Temperature Sintering to Prepare Single-Crystal High Nickel Oxide Cathodes with Enhanced Electrochemical Performance. *Adv. Energy Mater.* **2022**, 2203188.

(6) Chakraborty, P.; Parker, R.; Hoque, T.; Cruz, J.; Bhunia, S. P2C2: Peer-to-Peer Car Charging. *IEEE Veh. Technol. Conf.* **2020**.

(7) Sono Motors. *Driven by the Sun* . https://sonomotors.com/ (accessed 2022-01-27).

(8) Wang, H.; Jasim, A.; Chen, X. Energy Harvesting Technologies in Roadway and Bridge for Different Applications – A Comprehensive Review. *Appl. Energy* **2018**, *212*, 1083–1094.

(9) Electreon. *Projects*. https://www.electreon.com/projects (accessed 2022-01-27).

(10) Integrated Roadways. *Say Hello to the Real Information Super Highway*. https://integratedroadways.com/#News (accessed 2022-01-27).

(11) Statista. *In-depth Report: eMobility 2021*. https://www.statista.com/study/49240/emobility/ (accessed 2022-01-10).